Politecnico di Torino

ScuDo
Scuola di Dottorato ~ Doctoral School
WHAT YOU ARE, TAKES YOU FAR

Doctoral Dissertation
Doctoral Program in Electrical, Electronics and Communications Engineering
(36^{th}cycle)

Modeling and Simulation Strategies for Advancing Molecular FCN

Pioneering Design Rules Toward Implementation from Molecules to Devices

By

Giuliana Beretta

******

Supervisor(s):
Prof. Gianluca Piccinini, Supervisor, Politecnico di Torino
Prof. Guido Masera, Co-Supervisor, Politecnico di Torino

Doctoral Examination Committee:
Prof. Konrad Walus, Referee, University of British Columbia
Prof. Andrea Vezzoli, Referee, University of Liverpool

Politecnico di Torino
2024

Declaration

I hereby declare that the contents and organization of this dissertation constitute my own original work and do not compromise in any way the rights of third parties, including those relating to the security of personal data.

Giuliana Beretta
2024

* This dissertation is presented in partial fulfillment of the requirements for **Ph.D. degree** in the Graduate School of Politecnico di Torino (ScuDo).

To the true spirit warriors

Acknowledgements

I would like to thank the constellation of kindred spirits, whose orbits intertwined with mine over the past years, igniting sparks of inspiration that illuminated the winding road of this odyssey.

Thanks to my unwavering support system, whose belief in me has been the compass guiding this journey. You stood by me through the toughest times, offering consistent relief that kept me moving forward, always reminding me of the greater purpose and guiding me through the obstacles, ensuring I never lost sight of the journey ahead and behind. You taught me how to be serene in accepting things I cannot change, to be courageous in changing the things I can, and to be wise in knowing the difference. Your encouragement is etched into the very fabric of this dissertation, and this achievement is as much yours as it is mine.

Abstract

Molecular Field-Coupled Nanocomputing (molFCN) represents a paradigm shift in computational technology, exploiting the unique properties of molecules to revolutionize information processing. In this paradigm, information is encoded in the charge distribution on suitable molecules, and propagation is sustained by Coulomb's force through electrostatic coupling. Logic elaboration is obtained by positioning molecules according to specific layouts. Being a current-less paradigm, molFCN offers extremely low-power and high-frequency operations. Compared to other implementations, having molecules as unit elements offers the advantage of working at room temperature. Despite these noteworthy advantages, obtaining a working prototype requires effort in multiple research areas, slowing down the development of the technology over the last two decades.

This thesis aims to facilitate the future development of experimental validations and a working prototype. It explores different characteristics of the technology with the goal of defining design rules and properties for molecules and circuits, driving future research on the topic.

The proposed goal is addressed by decomposing the problem into subsequent abstraction levels, each one based on the previous finding, and hiding the non-relevant details as a matryoshka. Each abstraction level requires its own theory and simulation tools.

The first layer is composed of molecules, being the unit elements. This work analyzes various candidates and defines a set of parameters identifying the behavior to be provided to chemists to drive ad-hoc syntheses. Adopting DFT simulations and the MoSQuiTo methodology, this work also analyzes a case study to investigate the direct effects of multiple molecular modifications on its electrostatic behavior.

Based on the analyses performed in the previous layer, the second step treats molecules as simplified electrostatic devices composed of a set of point charges.

This modeling enables the study of molecule ensembles through the application of electrostatic fundamentals and the SCERPA simulator. The work analyzes the fundamental interactions found in molFCN devices using different electrostatic molecular footprints to test their impact. Consequently, the design of tailored molecular transcharacteristics enables the successful realization of new functions, such as a fully electrostatic solution for in-plane information crossover.

As an outer layer, this work proposes a methodology to model entire logic gates and develops an automatic tool named BBchar to create a library comprising the input/output behavior of fundamental gates and interconnections. The possibility to simulate circuits composed of multiple gates without focusing on the internal behavior of each of them enables a strong simulation speed-up, moving from hours or days down to a few milliseconds. Moreover, the proposed methodology is designed to consider the actual physical behavior of the technology, resulting in a 99.99% accuracy of the proposed model.

The final point of the present work proposes a modification of the paradigm that aims to simplify the reading of the information at the laboratory level and on-circuit data conversion. The paradigm has been named bend-boosted molFCN to highlight the property of including molecule bending in the charge-encoded information. Through DFT and dynamic simulation, this work demonstrates its correct working principle, and the offered read-out capabilities.

Overall, this thesis contributes to the advancement of molFCN technology by providing insights into molecular behavior, developing efficient simulation methodologies and tools, and proposing innovative device architectures that simplify data sensing and conversion. It lays the groundwork for future research in this field and offers a pathway toward the unprecedented realization of a working prototype.

Contents

List of Figures

List of Tables

List of Acronyms

AC Aggregated Charge

AIMD Ab Initio Molecular Dynamics

B3LYP Becke3 Lee–Yang–Parr

BBchar Block-Based characterization

BDL Binary Dot Logic

BF Bistable Factor

CAD Computer-Aided Design

CHELPG CHarges from ELectrostatic Potentials using a Grid

CMOS Complementary Metal-Oxide-Semiconductor

CUT Cell Under Test

DB Dangling Bonds

DFT Density Functional Theory

DrC Driver Cell

DSOA Device Safe-Operating Area

DUT Device Under Test

EBL Electron Beam Lithography

EDA Electronic Design Automation

ESP ElectroStatic Potential

FCN Field-Coupled Nanocomputing

FEM Finite Element Method

FIB Focused Ion-Beam

H-Si Hydrogen-terminated Silicon

HF Hartree-Fock

iNML In-plane Nano Magnetic Logic

LUT Look-Up Table

MBPT Many-Body Perturbation Theory

MD Molecular Dynamics

molFCN molecular Field-Coupled Nanocomputing

MoSQuiTo Molecular Simulator Quantum-dot cellular automata Torino

MUT Molecule Under Test

MV Majority Voter

NEGF Non-Equilibrium Green's Functions

QCA Quantum-dot Cellular Automata

RT-TDDFT Real-Time Time-Dependent Density Functional Theory

SAM Self-Assembled Monolayers

SCERPA Self-Consistent ElectRostatic Potential Algorithm

SET Single-Electron tunneling Transistor

SiDB Silicon Dangling Bonds

STM Scanning Tunnelling Microscope

TJ Tunnel Junction

TP Transmission Pathways

UHV Ultra-High Vacuum

UKS Unrestricted Kohn-Shann

VACT V_{in}-AC transcharacteristic

VHDL VLSI Hardware Description Language

Preface

The research presented in this thesis explores the fascinating world of molecular Field-Coupled Nanocomputing (molFCN), a field positioned at the intersection of molecular electronics, nanotechnology, and computational science. This endeavor has been a labor of passion, curiosity, and intellectual pursuit, and it is with great pleasure that I present the culmination of my research efforts in this document. Over the course of my doctoral studies, I have delved deep into the exploration of molecular-scale devices and their potential applications and integration in computing.

The primary objective of this research is to investigate the potential of molFCN as a promising paradigm for next-generation electronics. By leveraging the unique properties of molecules, nanoscale devices, and ultra-low power consumption, this study aims to reduce the distance from a prototypal validation of the technology. The major challenge is tightly linked with the need for expertise in various technical areas, such as molecular synthesis, 2D deposition, and nanofabrication. The ultimate goal is to develop a framework that enables simulations at different abstraction levels, providing valuable insights to experts in low-level technology requirements, and offering engineers a tool to work with the technology without necessarily needing to understand the underlying physics.

The research presented in this thesis adopts a multidisciplinary approach, drawing on principles from computational chemistry, molecular electronics, computational modelling, and algorithm development. Investigations are complemented by computational simulations, theoretical modeling, and data analysis to explore underlying mechanisms and validate theoretical predictions.

It is important to note that while this research represents a significant step forward in advancing our understanding of molFCN, it is not without limitations. Challenges such as device scalability, fabrication reproducibility, and reliability remain areas of

ongoing research and development. Additionally, the scope of this study is focused on specific architectures and ideal practical implementations.

In conclusion, I am sincerely grateful for the opportunity to embark on this intellectual adventure and to contribute to the ongoing pursuit of knowledge in the field of molecular field-coupled nanocomputing. It is my hope that this work will inspire further exploration and collaboration among different research entities, fostering innovation for a transformative future.

Outline of Chapters

This thesis is organized into the following chapters:

Chapter 1 - Introduction and context The chapter provides an overview of various field-coupled nanocomputing implementations, discussing their fundamental concepts, advantages, and current challenges. It concludes by outlining the motivation for the present work and explaining the justification behind choosing molecular implementations over other alternatives.

Chapter 2 - Molecules design principles This chapter explores the crucial role of molecules in molFCN, detailing how their composition and arrangement shape device behavior. It examines theoretical methods, structural characteristics, and key molecules in the field. Finally, it concludes with a detailed case study analyzing the impact of modifications on device performance metrics.

Chapter 3 - Molecules electrostatics and environment This chapter explores the significance of intra-molecular interactions and electrostatic footprints in molFCN, focusing on how molecular charge distributions influence information propagation. By analyzing different molecular species and their electrostatic behaviors, the chapter investigates their impact on logic computation and explores strategies for enhancing circuit capabilities through the integration of diverse molecules. Additionally, it discusses the feasibility of achieving coplanar crossover interconnections using purely electrostatic solutions.

Chapter 4 - Device modeling The chapter outlines a methodology for developing physically accurate models of entire devices using a hierarchical approach, validated against Self-Consistent ElectRostatic Potential Algorithm (SCERPA)

simulations for accuracy. It provides a tool to handle devices easily, facilitating investigations into the computational potential and scope of the technology.

Chapter 5 - Interface with the external world This chapter highlights the challenges of experimental validation due to difficulties in measuring molecule charges and introduces a novel bend-boosted molFCN paradigm, demonstrating its feasibility through Density Functional Theory (DFT) simulations. Additionally, it discusses compatibility with existing charge-based molFCN, paving the way for experimental validation and integration with CMOS technology.

Chapter 6 - Conclusion and future perspective The conclusion chapter summarizes the key findings and contributions of the research, highlighting the advancements made in understanding and modeling molecular field-coupled nanocomputing. It reflects on the challenges encountered, the implications of the proposed solutions, and the potential future directions for further exploration and development in the field.

Chapter 1

Introduction and context

Since its establishment, modern digital electronics has experienced a remarkable evolution thanks to the use of Complementary Metal-Oxide-Semiconductor (CMOS) technology, which has dominated the semiconductor industry for several decades. In the past two decades, the limitations of CMOS technology have become increasingly evident. The continuous demand for higher performance, lower power consumption, and more complex functionalities poses significant challenges for CMOS. These challenges include power dissipation, scaling limits, and the increasing complexity of manufacturing processes. Consequently, there is a growing need to explore alternative solutions that can push the boundaries of what is achievable in digital electronics. In response to these challenges, researchers and industry leaders are actively exploring a diverse range of options, from novel materials like graphene and carbon nanotube [1, 2] to different computation approaches [3, 4].

In the last two decades, two main approaches have been identified, namely "More than Moore" and "Beyond CMOS" [5]. The "More than Moore" concept acknowledges that further advancements in electronic technology cannot solely rely on shrinking transistor sizes as predicted by Moore's Law [6]. Instead, it emphasizes diversifying and integrating new functionalities into microelectronics, including sensors, power management, and embedded components [5]. On the other hand, the "Beyond CMOS" movement explores alternative technologies to CMOS, which is approaching its physical scaling limits. These novel technologies enclose a broad spectrum of approaches, such as DNA nanocomputing [7], spintronics [8], and photonic computing [9], offering the potential for enhanced performance, energy

efficiency, and functionality. Under the definition of "Beyond CMOS" solutions, the Field-Coupled Nanocomputing (FCN) emerges [10], offering the possibility to perform computation in a transistor-less environment and not exploiting charge transfer, preferring the local interaction of some fields.

The following sections discuss the four different technological implementations of the FCN paradigm, introducing the fundamental concepts of information encoding and propagation. The implementations are compared, and advantages and current challenges are presented. The chapter ends with the motivation of the present work.

1.1 Field-coupled nanocomputing implementations

The FCN paradigm exploits an innovative concept for computing at the nanoscale and finds a realization in different technologies. The basic idea is to use a field-based control, e.g., electric or magnetic, to drive the behavior of nanoscale components. This innovative approach aims to overcome some of the limitations of traditional semiconductor-based computing, such as power consumption and scalability [10]. Indeed, one of the primary advantages of FCN is its potential for significantly reduced power consumption because of the use of coupling fields instead of an electric current. Nevertheless, each specific implementation comes with its own advantages and challenges.

The following paragraphs discuss the leading implementations of the FCN paradigm, which are the metallic Quantum-dot Cellular Automata (QCA), the semiconductive QCA, the In-plane Nano Magnetic Logic (iNML), and the molecular Field-Coupled Nanocomputing (molFCN).

1.1.1 Metallic quantum dots

The principal approach investigated for the paradigm realization is called QCA [11]. A fundamental QCA unit comprises a square arrangement of four quantum dots interacting by tunneling. Fig. 1.1a illustrates a QCA cell with the four sites highlighted, where t indicates the tunneling energy between adjacent sites [12]. When two additional electrons are introduced into the unit, their Coulombic repulsion forces them to occupy dots on opposite corners. Fig. 1.1b shows the two resulting

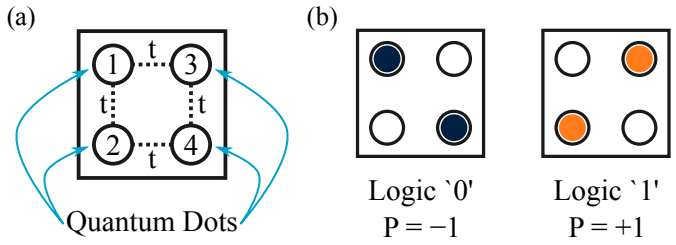

Fig. 1.1 Quantum-dot Cellular Automata (QCA). (a) Unit cell composed of four quantum dots interacting by tunneling, where numbers identify the position of the site in the cell and t is the tunneling energy linking two sites. (b) Resulting state configurations obtained by adding two electrons to the cell, represented as colored dots. The two distinct cells encode the logic values '0' and '1' and are associated with a cell polarization value of $P = -1$ and $P = +1$.

distinct state configurations. The two states are energetically equivalent and can be designated as logic '0' and '1'. A useful quantity describing the charge arrangement of the cell is the so-called cell polarization P, defined as

$$P = \frac{(\rho_2 + \rho_3) - (\rho_1 + \rho_4)}{\rho_1 + \rho_2 + \rho_3 + \rho_4} \tag{1.1}$$

where ρ_i is the electronic charge of the dot i. The cases corresponding to the two logic values are associated with $P = -1$ and $P = 1$ as reported in Fig. 1.1b. Besides, for an isolated cell, the ground state is an equal combination of these two states and, therefore, has a net polarization of zero.

Cells interaction: information propagation and elaboration

In a system of several cells, it is assumed that electrons can tunnel between the sites within the same cell, whereas electrons are prevented from tunneling between distinct cells. This restriction is achieved by maintaining a greater distance between dots in different cells compared to the spacing within the same cell, given that the probability of tunneling decays exponentially with distance. So, separate cells interact through the coupling of Coulomb interactions. Considering a system of two cells like the one in Fig. 1.2a, if we fix the polarization of the cell on the left, it is possible to predict the charge distribution of the cell on the right [11]. Ideally, the minimum energy configuration is the one for which the two cells encode the same information [11], as shown in Fig. 1.2b for both logic '0' and logic '1'. The steepness of the two-cell

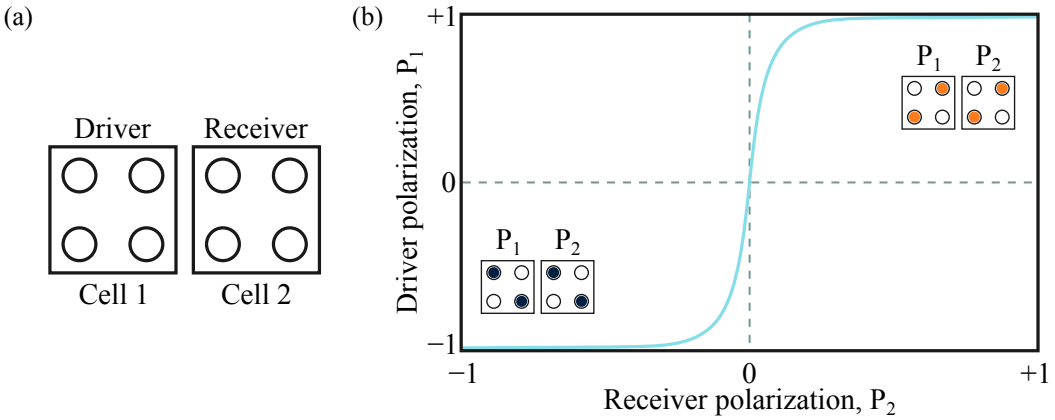

Fig. 1.2 Quantum-dot Cellular Automata (QCA) two-cells system. (a) Scheme and nomenclature for a system composed of two adjacent QCA cells. (b) Cell-to-cell response showing the variation of the receiver polarization versus the driver polarization.

polarization curve mainly depends on the tunneling energy between the dots and the Coulomb energy for electrons on different sites [11].

The same principle of information copying is at the basis of information propagation [13]. By placing several cells in a row, the value forced at the beginning propagates through all the cells through electrostatic coupling. Fig. 1.3a illustrates the ground state for a wire with a logic '0' forced as input, and for a wire propagating a logic '1'. From a logical point of view, the wire just described can be seen as a sequence of drivers copying the input information. By rotating the cell 45°, nearby cells assume opposite configurations, thus creating a wire of inverting cells, as shown in Fig. 1.3b [13].

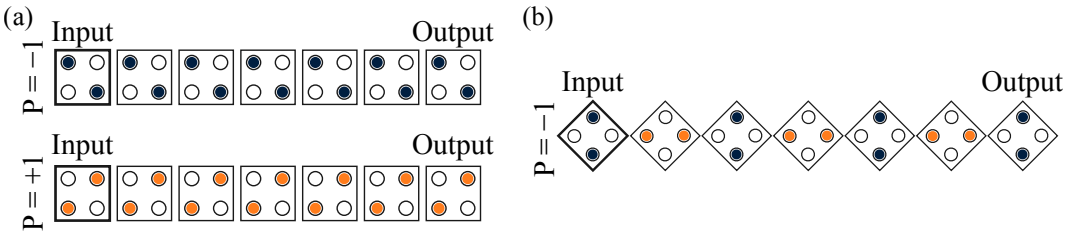

Fig. 1.3 Quantum-dot Cellular Automata (QCA) information propagation. (a) Propagation through electrostatic coupling of adjacent cells for the two logic values. (b) Inverting propagation through electrostatic coupling of cells rotated by 45°.

Since the interaction is based on electrostatic interaction, the outcome of a cell depends on the superposition of all the nearby cells. Considering the arrangement of Fig. 1.4a, the polarization of the computing cell depends on the polarization of

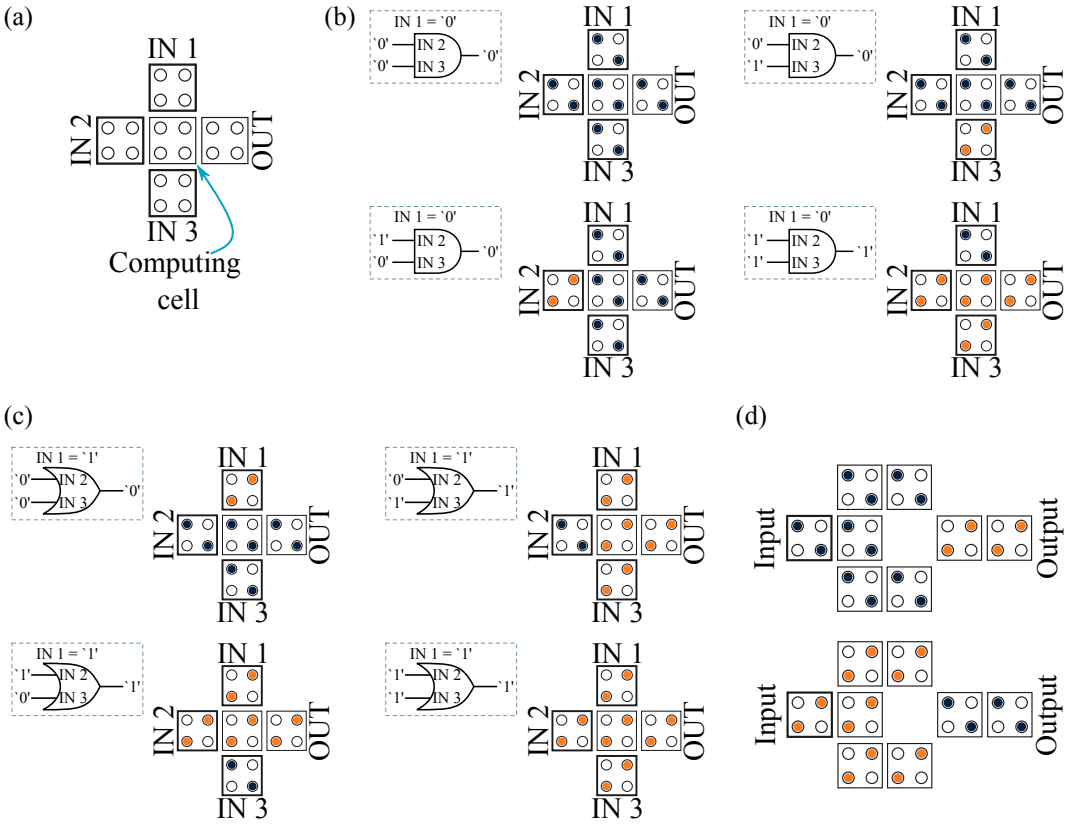

Fig. 1.4 Quantum-dot Cellular Automata (QCA) fundamental gates. (a) Majority voter (MV) layout with cells name highlighted. (b) Charge configuration of the MV with IN1 fixed to '0' implementing a two input AND gate between IN2 and IN3. (d) Charge configuration of the MV with IN1 fixed to '1' implementing a two input OR gate between IN2 and IN3. (d) Inverter layout and charge distribution for the two possible input values.

all three input cells [14]. Specifically, this layout implements the majority voting function, whose truth table is Table 1.1. In the Majority Voter (MV) gate, the polarization of the computing cell equals the same assumed by most of the input cells. The same layout can also work as a programmable gate implementing an AND or an OR gate between the remaining inputs [13, 15], as observable in Fig. 1.4b and reported in Table 1.1. Fig. 1.4b shows the charge configuration of a MV where IN1 has been fixed to implement the AND operation between the remaining inputs. Similarly, Fig. 1.4c shows the charge configuration of a MV where IN1 has been fixed to implement the logic OR. The union of the configurations shown in Fig. 1.4b and Fig. 1.4c represents the possible charge distribution in a generic 3-input MV.

Playing with the cell arrangement makes it possible to obtain other fundamental logic operations, such as the inverter shown in Fig. 1.4d for both the logic configu-

Table 1.1 Truth table of a three-input majority voter gate. Note that the top half of the table corresponds to an AND gate between IN2 and IN3, keeping IN1 fixed, whereas the bottom half identifies an OR gate in the same conditions.

IN 1	IN 2	IN 3	OUT
0	0	0	0
0	0	1	0
0	1	0	0
0	1	1	1
1	0	0	0
1	0	1	1
1	1	0	1
1	1	1	1

rations. In this case, the laying principles are the vertical copying mechanism and the diagonal interaction. Indeed, cells are equal on each side, making it possible to replicate the information in any direction. On the contrary, diagonal interaction behaves similarly to rotated cell propagation, generating an inversion on the output cell.

The clocking necessity

We mentioned that the two logic states correspond with two energy minima, meaning that information is potentially stable even without a power supply. If we want to change the state encoded by a cell, an external force is needed to reduce the energy barrier existing between the two states. To address this problem, six-dot cells and the application of an external electric field have been proposed [16, 17].

Fig. 1.5a shows the six-dot unit cell in the two logic states and the added state used to erase the information before switching to the new logic. The third created state is named 'NULL' to highlight that it does not encode any information. The external field is called *clock field*, and is a signal that enables the quasi-adiabatic switching between the possible cell configurations. The clock field provides energy to the system cyclically to enable electrons to move and varies smoothly enough for the system to stay close to its equilibrium ground state configuration during the switching [18]. Fig. 1.5b shows the accepted trapezoidal clock waveform and the name of the phase sequence. Fig. 1.5b also shows the equivalent potential profile

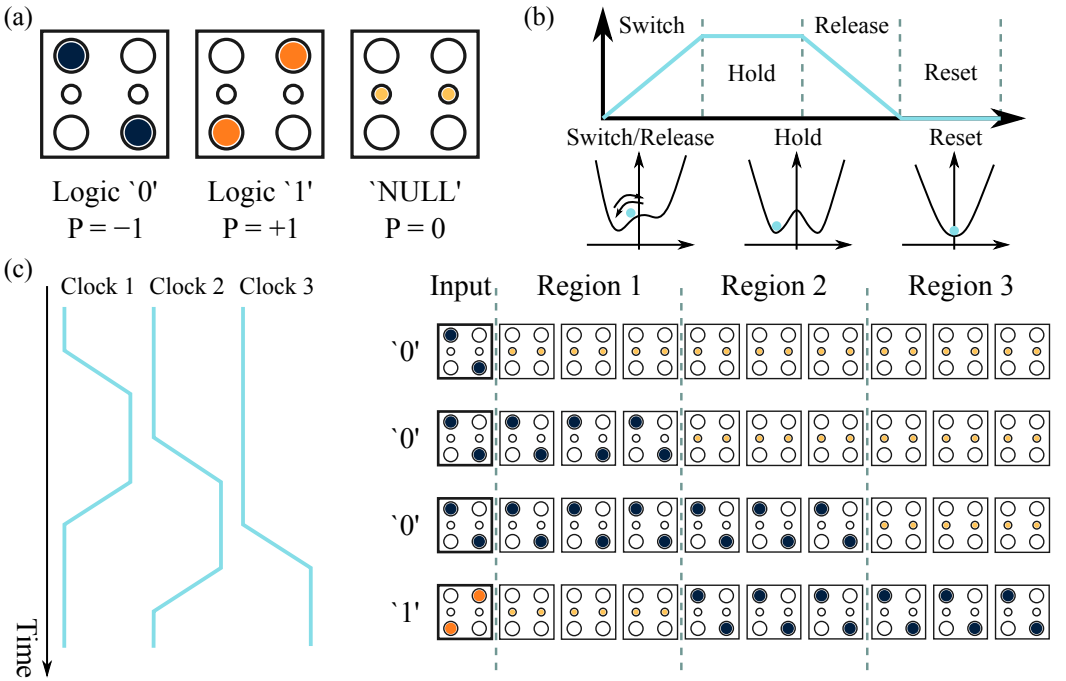

Fig. 1.5 Clocked Quantum-dot Cellular Automata (QCA). (a) Unit cells composed of six quantum dots and state configurations obtained by adding two electrons to the cell. (b) Typical period of the trapezoidal clock signal highlighting the name of each phase and energy-coordinate scheme for each of them showing the schematic potential profile. (c) Propagation example in a clocked wire divided into three regions subjected to out-of-phase clock signals. The sequential activation of the regions guides the propagation direction.

in the various phases versus the coordinate, and the blue circle is the particle in the system [18].

In addition, the electrostatic interaction fundamental for propagating information is not directional, meaning that a driving cell influences all the surrounding cells, losing the concept of the direction of propagation. By dividing the circuit into zones to which we provide out-of-phase clocking signals, we can force the information to follow specific paths to guarantee the synchronous operation of QCA devices. Fig. 1.5c shows an example of a wire divided into three regions. After each time step, information is guided from the input to the output thanks to the sequential activation of the clocking scheme [19].

Clocking in QCA introduces a unique advantage concerning energy efficiency. QCA devices only consume energy during state transitions, minimizing overall power consumption and potentially addressing the growing concerns associated with energy efficiency in modern computing [18].

Fabrication experiments

The fabrication of metal dots involves techniques employed to produce arrays of dots on a substrate. The precise placement and spacing of these dots are critical to the functioning of the QCA system, as they define the logic states and interactions [20]. Few experiments have been carried out using aluminum dots and aluminum-oxide tunnel junctions, demonstrating the possibility of switching cells [21, 22].

Metal dots are typically in the order of a few tens of nanometers [23, 18] and offer several benefits, including a comparatively high fabrication yield and consistent electrical behavior [10]. This consistency implies that the energy needed to introduce each subsequent electron into the dot remains relatively constant, even as numerous electrons are added. Such uniform behavior simplifies the process of loading the QCA cell with the precise number of electrons and facilitates biasing the cell to ensure that the two polarizations possess equivalent energy levels [24].

Regarding the clock signal generation, it is accepted to use metal rods beneath the circuit level to generate the potential associated with the clocking signal [17].

While these fabrication and modeling procedures are considered feasible, the main challenges are represented by scaling and the necessity of operating at cryogenic temperatures [25, 15].

1.1.2 Semiconductive quantum dots

In semiconductive QCA, the quantum dots themselves are made from semiconductor materials, such as silicon or gallium arsenide [26]. This choice of material offers several benefits, including compatibility with existing semiconductor fabrication processes and the potential for integration with current electronic devices [27]. By utilizing semiconductor quantum dots, semiconductive QCA systems seek to overcome some of the challenges associated with purely quantum-based QCA, such as scalability or operation at extremely low temperatures [27].

Silicon Dangling Bonds (SiDB) is a FCN implementation exploiting the properties of passivated silicon surfaces and manipulating unpaired electrons on these surfaces [28]. SiDB can be implemented following the QCA paradigm [29], even if the most studied implementation is referred to as Binary Dot Logic (BDL) [30].

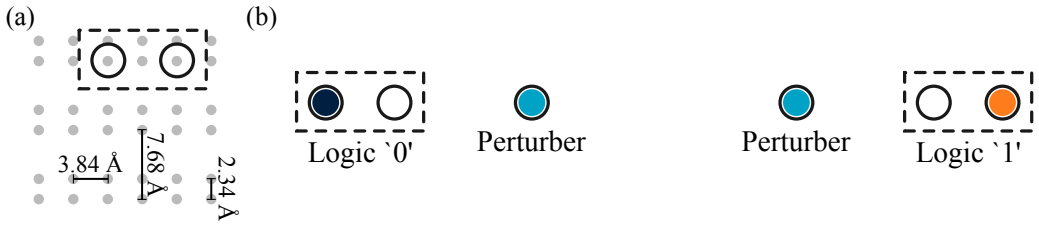

Fig. 1.6 Silicon Dangling Bonds (SiDB) in the binary dot logic. (a) Schematic representation of a pair of dangling bonds (DBs)on a Hydrogen-terminated Silicon (H-Si). (b) Resulting charge configurations obtained by placing a third DB near the pair. The two distinct cells encode the logic values ‘0’ and ‘1’, and colored dots are associated with the DB occupation by the electron.

In the SiDB technology, quantum dots are realized through dangling bonds in Hydrogen-terminated Silicon (H-Si), pursuing the ultimate miniaturization in technology. SiDB on H-Si can exhibit three charge states [31]: positive, neutral, and negative. The charge state of a Dangling Bonds (DB) is determined by the number of electrons it holds. Specifically, positive charge states (+) hold zero electrons, neutral charge states (0) occur when the DB holds one electron, and negative charge states (-) are associated with the dangling bond holding two electrons. By placing two DB away by two lattice sites, a DB pair is formed, as shown in Fig. 1.6a [31]. It has been experimentally demonstrated that at specific applied bias, the pair has one net negative charge and, from an electrostatic point of view, it behaves as an isolated DB presenting fluctuations between left and right dots [30, 31].

Introducing a third DB to the pair demonstrates a clear contrast between DBs. As Fig. 1.6b shows, the charge is biased to stay on one DB in the pair, creating a binary charge configuration that we can associate with logic ‘0’ and logic ‘1’. The isolated DB added to the system to force a logic state is typically called *perturber*.

A line composed of multiple paired SiDB forms a binary wire, schematically shown in Fig. 1.7a. Experimentally, it has been demonstrated that the wire states can be manipulated by placing a perturber at one end of the line or the other [30]. Also, the wire becomes self-polarized without any external electrostatic input if the perturber is missing.

In BDL, the easiest device to design is the OR gate, which has been also demonstrated experimentally [30]. Fig. 1.7b illustrates the two-input OR layout and the four possible combinations. A complete library of working devices has been proposed and validated through simulations in [32]. Even SiDB circuits need the presence of a

clock that helps the synchronization and information guidance. So far, no complete studies have addressed the influence of an external field on the physical behavior of DB or the maximum clock region dimension that must be satisfied to guarantee the correct functioning [33]. Anyway, a tool based on Finite Element Method (FEM) simulations has been developed in [34] to evaluate the clock potential generated by metal rods similar to those proposed in [17].

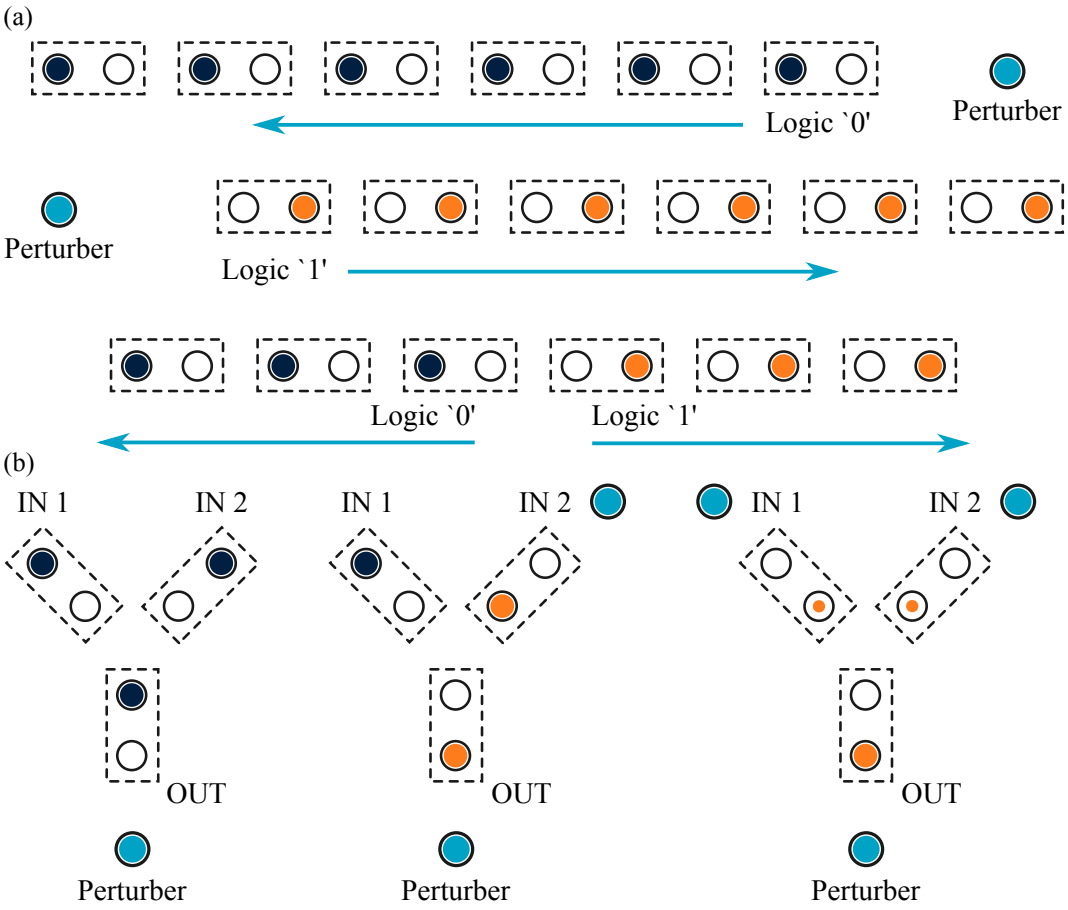

Fig. 1.7 Silicon Dangling Bonds (SiDB) propagation and fundamental gate. (a) Binary wire in different situations: with a perturber on each side of the wire, and in the case of self-polarization. (b) Combinations of a two-input OR gate.

Besides the experimental effort made to assess the technology [30, 29], a lot of investigation on the power of the implementation comes from the simulation of circuits and the possibility of automating the design phase through Computer-Aided Design (CAD) tools [35, 36]. The main challenges are related to the development of

input/output interfaces that will permit the removal of the perturbers, which are now fundamental for the functioning of circuits.

1.1.3 In-plane Nano Magnetic Logic

In-plane Nano Magnetic Logic (iNML) technology represents another implementation of FCN, exploiting single-domain nanomagnets as the holders of binary information [37]. As Fig. 1.8a shows, these nanomagnets are characterized by stable magnetizations parallel or antiparallel to the easy (longest) axis and encode logic '1' and '0' states. The technology capitalizes on the shape anisotropy of rectangular magnets, with typical dimensions of a few tens of nanometers [38]. If magnets are correctly designed, magnetization vectors are stable, meaning there's no standby power consumption, and magnets serve as both memory and logic elements.

A magnetic wire is constructed by cascading an even number of nanomagnets. Information propagates through the magnetic coupling of neighboring magnets. Fig. 1.8b shows that if magnets are juxtaposed facing the easy axis, then the coupling is antiferromagnetic. On the contrary, if magnets are aligned facing the hard (shortest) axis, information is coupled ferromagnetically.

If we change the input information by changing the magnetization vector of the initial magnet, a cascading effect is expected, causing all the subsequent magnets in the wire chain to flip in a domino-like manner [39]. Nevertheless, the energy barrier associated with the shape of the magnets that guarantee the information stability is too elevated to be overcome by the dipole-dipole energy provided by the input magnet only [40]. As shown inFig. 1.8c, an external clock field becomes necessary to induce a 90° rotation of the magnetization vector along the short axis, facilitating information propagation in iNML [41]. However, thermal noise limits the number of magnets that can be cascaded above a clocked zone, typically to 4 or 6 [42, 38]. Various clocking schemes have been proposed to ensure data flow direction and correct information propagation [19].

The potential for constructing magnetic circuits is related to the possibility of aligning magnets in various ways. The resulting iNML gates, depicted in Fig. 1.8d, form the basic building blocks, which have been proved through simulations and experimental validation [43, 38]. The MV is efficiently designed even in this implementation. Nevertheless, it is possible to build two-input AND and OR gates

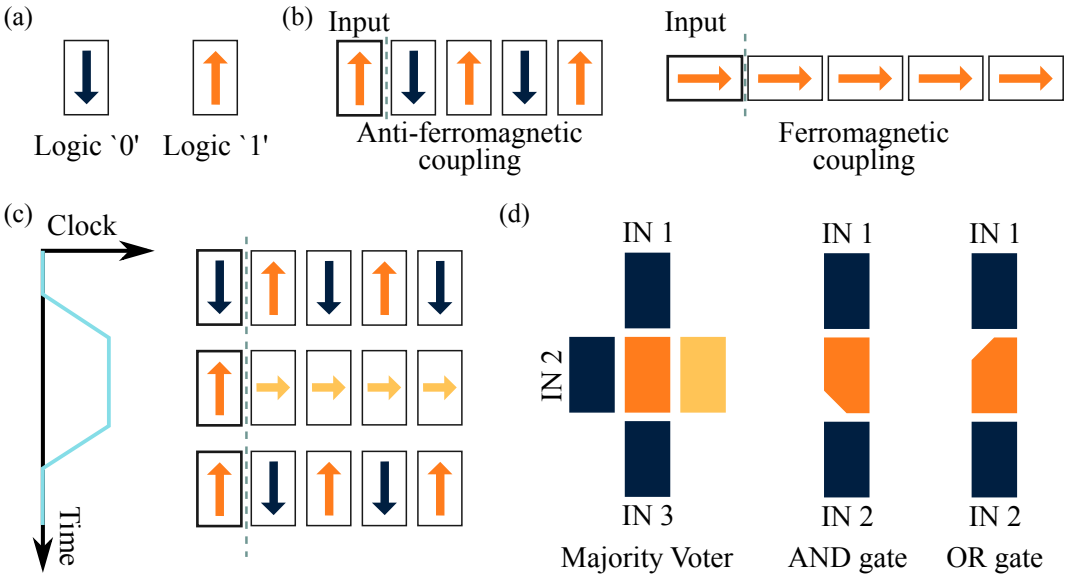

Fig. 1.8 In-plane Nano Magnetic Logic (iNML) logic, propagation, and fundamental gates. (a) Elementary cell composed of a rectangular magnet highlighting the magnetization vector. (b) Information propagation through antiferromagnetic and ferromagnetic coupling. (c) Effect of applying a clocking signal on the magnets of a wire, resetting the information before changing the input value. (d) iNML fundamental gates: majority voter, two-input AND gate, and two-input OR gate.

without using a MV by exploiting magnets with a cut on one angle. The cut favors the magnetization vector pointing toward the cut itself [44]. Since the horizontal propagation is anti-ferromagnetic, an odd number of magnets following the input will make an inversion of the information, and it's possible to balance length by adjusting the width of the magnets forming the inverter.

Standard tools like low-level and high-level simulators are used to study iNML devices at different abstraction layers. Micromagnetic simulators like oommf [45] and mumax^3 [46] are employed for accurate magnetic behavior simulations. The limitations of low-level simulators, such as being time-consuming for large architectures, and the drawbacks of high-level simulators, which result in losing physical information, led to the development of ToPoliNano [47]. This tool follows a top-down approach, allowing the description of circuits in VLSI Hardware Description Language (VHDL), automatic generation of optimized layouts, fast and accurate simulations, consideration of fabrication process faults, and flexibility for extension to other emerging technologies.

1.1.4 Molecular implementation

Another way to implement FCN is to use the molecule to implement a QCA cell or, more often, a half cell where redox-active molecular sites replace general dots [48]. Fig. 1.9a shows the thiolated-carbazole linked bisferrocenes molecule (bisferrocene for short) that we use throughout this work for the simulations [49]. The coordinates of the molecule are reported in Appendix A. The molecule comprises two ferrocenes connected to a carbazole in a 'V' shape. The carbazole is itself linked to a thiol, forming a 'Y' shaped molecule. The functional groups of the molecule are usually referred to as *dots*. The two ferrocenes, i.e., dot 1 and dot 2, are also named logic or active dots. Similarly, the union of dot 3 and dot 4 is called reset dot.

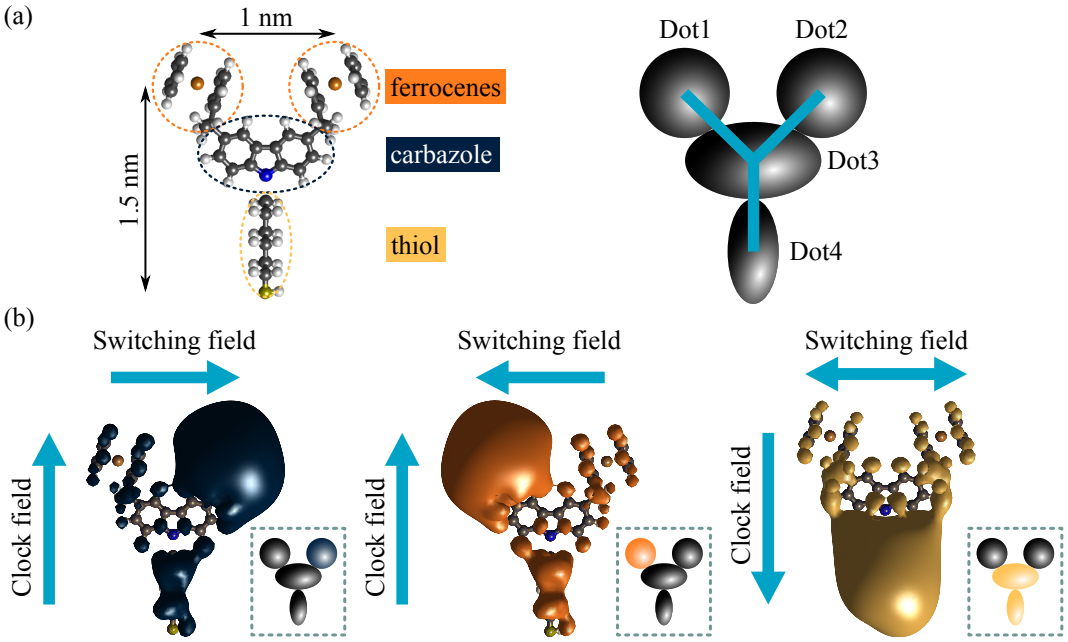

Fig. 1.9 Molecular Field-Coupled Nanocomputing (molFCN). (a) Geometry of the thiolated-carbazole linked bisferrocenes molecule, highlighting the functional groups and the extension. The figure on the right shows a schematic representation of the molecule. (b) The application of electric fields across the molecule changes the electronic distribution, represented as a colored cloud. Combining the clock field and the switching field generates three different charge configurations. Atoms in figure are colored as follows: H = white, C = charcoal, N = blue, S = yellow, Fe = orange.

Applying electric fields across the molecule moves the charge distribution in different molecule regions. Fig. 1.9b shows the isopotential surface on the bisferrocene in different situations, corresponding to three distinctive charge localization. In particular, the clock field is applied along the longitudinal axes and can move

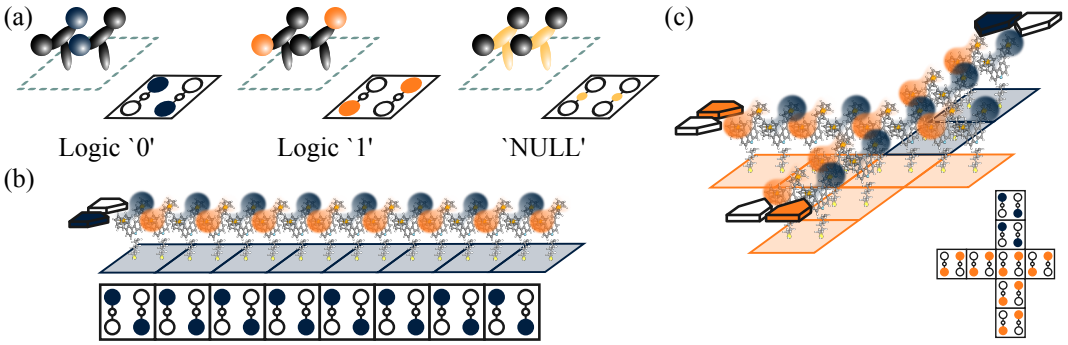

Fig. 1.10 Molecular Field-Coupled Nanocomputing (molFCN) information encoding and propagation. (a) Molecular cell composed of two juxtaposed molecules encoding the logic states '0', '1', and 'NULL'. The molecular cells are linkable to 6-dots QCA cells. (b) Molecular wire composed of 8 cells propagating a logic '0'. (c) Majority voter with the top input equal to '0' and the other inputs encoding a logic '1'.

the charge between the ferrocene and the carbazole/thiol group [50]. When the clock field moves the charge in the ferrocenes, the switching field applied across the molecule transversal axis forces the charge on one of them.

Different charge configurations are possible by placing two of those molecules side-by-side and depending on the applied clock field. When the clock field favors the presence of the charge in the ferrocenes (*hold state*), the charge clouds on the molecules maximize the distance for Coulombic repulsion, and two energy-equivalent configurations are possible. Fig. 1.10a shows the schematic molecular cells composed of two molecules in the mentioned configurations associated with logic '0' and '1'. Fig. 1.10a also shows the molecular cell when the clock favors the presence of the charge in dot 3 and dot 4. In that case, the molecular cell is associated with the 'NULL' state, where no information is encoded. Fig. 1.10a also illustrates that the molecular cells can be associated with a 6-dots QCA cell.

In molecular FCN (molFCN), the information propagation principle is the same as general QCA: the localized charge in a cell influences nearby cells, and the clock signal drives the information along the desired path. Fig. 1.10b shows a molFCN wire of 8 cells propagating a logic '0' and the schematic QCA view that simplifies the representation. In molFCN, fundamental gates are designed by playing with cell displacement, and the way to obtain AND and OR gates is by using the MV, shown in Fig. 1.10c when the top input equals '0' and the other two encode a logic '1'.

1.2 Molecular field-coupled nanocomputing

Using molecules as unit elements provides some unique advantages. Typical molecules proposed for molFCN are nanometric sized, and devices are built with few of them, allowing for highly compact and densely packed circuits [51]. The inherent nature of QCA and molFCN, that is, utilizing charge configurations and Coulombic interactions, allows for energy-efficient computation [52, 53]. Information propagates without charge transfer, requiring only the switching within each cell, whose energy has been studied and is of the order of 10^{-20} J [53]. To have an idea, the switch for a transistor requires a minimum energy of the orders of 10^{-18} J, so two orders of magnitude bigger [54]. Then, the Coulomb force between neighboring cells generates an interaction, letting molFCN work at room temperature [55, 56].

Alongside molecules being complex systems, it is not likely to treat several molecules as they are in a molFCN circuit. We need to define ad-hoc models and make specific considerations. Two main approaches exist in the literature to describe a molecule in a FCN environment: one focused on a theoretical quantomechanic description and the other based on data extrapolation from computational chemistry simulations. The following paragraphs describe the main concepts of the two approaches.

1.2.1 Theoretical approach: three-state approximation

The theoretical model has been introduced in [51] and describes a two-dot QCA half-cell using a double-well system. The cell binary information is encoded by the localization of a mobile charge in one of two wells. The entire four-dot cell can be viewed as a pair of half-cells with alternating polarizations. This model is named two-state approximation and describes electron transfer dynamics in a two-dimensional Hilbert space. The electron transfer in a cell is described in the context of interaction with a neighboring molecule, emphasizing Coulomb interactions. The work in [51] outlines a simplified electrostatic model for intermolecular interactions, considering two neighboring molecules with four dots forming a square, as in the general QCA paradigm. The cell–cell response function is used as a tool to evaluate molFCN functionality in relation to molecular structure, incorporating structural elements such as the electron transfer matrix element and the distance between redox centers [51].

The three-state approximation is a natural evolution of the model including an effective description for a clocked molFCN cell [57]. In this model, the Hamiltonian of a cell is constructed from basis vectors corresponding to the charge configurations of three logic states: the null state and two completely polarized states. Cell-to-cell interactions are characterized by the intercellular Hartree approximation, treating Coulombic interactions with a mean-field approach [57].

For molFCN half-cells represented by three stable charge configurations, the strategy involves conducting high-level *ab initio* calculations on single molecules to determine energies corresponding to the '0', '1', and 'NULL' states. The 3×3 model Hamiltonian constructed with the three-state approximation is given by

$$H = \begin{bmatrix} E_0 - e\varepsilon d/2 & -\gamma & 0 \\ -\gamma & E_0 + E_c & -\gamma \\ 0 & -\gamma & E_0 + e\varepsilon d/2 \end{bmatrix} \tag{1.2}$$

where E_0 is the energy of each state, E_c is the energy provided by the clock, ε is the switching field from neighboring molecules, and d and γ are the effective distance and tunneling energy between central and edge dots [58]. The Hamiltonian's two zeros correspond to the spatial separation between the two edge dots.

A tool named QCADesigner has been developed following this theoretical description for the simulation of molFCN, and QCA in general, circuits [59, 60].

1.2.2 Simulative approach: from *ab initio* to electrical devices

An alternative method for investigating molFCN employs *ab initio* simulations. While this serves as a reference and initial step, crucial for validating the system under examination, it comes with certain limitations. Firstly, these simulations demand substantial computational resources and extensive memory. Additionally, outcomes like molecular orbitals and atomic charge distribution are challenging to interpret from a device-level perspective. Controlling biasing conditions, such as input electric field, clock electric field, or technological parameters, proves complex. In response to these challenges, an approach named Molecular Simulator Quantum-dot cellular automata Torino (MoSQuiTo) has been introduced [61]. This approach, organized into three stages, involves analyzing the molecule through *ab initio* simulations, post-processing the obtained results to generate new figures of merit and device

characteristics, and finally implementing a higher-level algorithm to simulate the circuit and interactions among its elements.

First stage

The depiction of molecules involves using the Z-matrix or the coordinates, serving as the starting point for each *ab initio* simulation. Subsequently, biasing conditions are applied to consider elements such as the electric field generated by an input driver, a clock signal, or the presence of other molecules simulated through point charges [61]. The orientation of each field is specified, and the magnitude is systematically varied across a relevant range. The outcomes typically derived from these simulations include potential surfaces and the distribution of charges associated with each atom.

Second stage

The second stage is employed to analyze the information obtained in the preceding step and formulate novel metrics that characterize the molecule at a higher level of abstraction, sufficient to enclose the characteristics functional for FCN computation [62]. By using Fig. 1.11 as a reference, the principal metrics are the following [62].

Aggregated Charge (AC) is calculated as the sum of all the charges belonging to a functional group or a dot and is centered on a point of interest. Rather than collecting information on atomic charges, having information related to each dot is simpler.

Input voltage V_{in} is the integral of the electric field computed along the segment that connects the active dots (Dot 1 and Dot 2) of the Molecule Under Test (MUT).

Voltage at the receiver V_{out} is the integral of the electric field generated by the MUT, computed using the AC, on the segment that connects the receiver active dots when the receiver is placed at a distance $d = w$, where w is the distance between the MUT active dots. The same electric field that is related to the information encoding is usually named *switching field*.

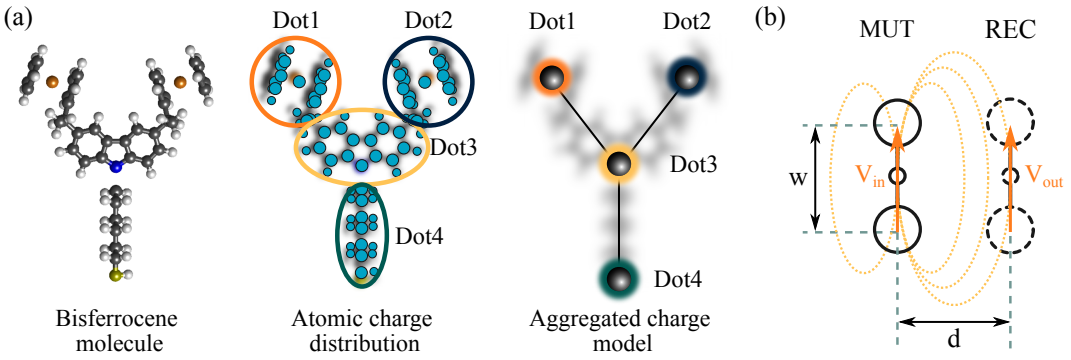

Fig. 1.11 Fundamental figures of merit defined in the Molecular Simulator Quantum-dot cellular automata Torino (MoSQuiTo) methodology. (a) Schematic representation of the aggregated charges obtained by the sum of the atomic charges for each dot. (b) Definition of the input voltage on the Molecule Under Test (MUT) and the voltage at the receiver (REC) evaluated at a distance $d = w$. Atoms in figure are colored as follows: H = white, C = charcoal, N = blue, S = yellow, Fe = orange.

By their associations, we define the V_{in}-V_{out} transcharacteristic (VVT) relating the output voltage generated on a dummy receiver molecule to the input voltage of a driving molecule, and the V_{in}-AC transcharacteristic (VACT) relating the AC of a molecule to a specific input voltage and a clock field.

The behavior of a molFCN cell can be linked to the general QCA paradigm by combining the QCA polarization expressed in equation (1.1) and the molecule AC. Fig. 1.12a shows the molecular cell composed by two molecules $M1$ and $M2$, whose logic dot charges are $Q_{M1,1}$ and $Q_{M1,2}$, $Q_{M2,1}$ and $Q_{M2,2}$, respectively. The polarization of the cell can be defined as in equation (1.3), according to the QCA paradigm.

$$P = \frac{(Q_{M1,2} - Q_{M1,1}) - (Q_{M2,2} - Q_{M2,1})}{Q_{M1,1} + Q_{M1,2} + Q_{M2,1} + Q_{M2,2}} \tag{1.3}$$

In particular, considering a maximum switching AC equal to 1 a.u. for each molecule, the cells with polarizations $P = -1$ and $P = +1$ are those propagating logic values '0' and '1', respectively. Fig. 1.12b shows these two simplistic cases encoding the two logic states, with the entire charge of each molecule on one of the two logic dots.

Third stage

In this stage, all the necessary elements for formulating an algorithm to simulate interaction have been established, giving rise to Self-Consistent ElectRostatic Potential

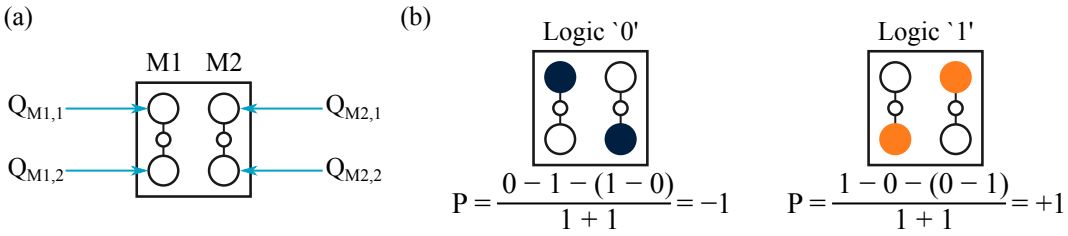

Fig. 1.12 Definition of the cell polarization for molFCN to associate it with the QCA paradigm. (a) Molecular cell composed of two molecules, $M1$ and $M2$, with a highlight on the names of logical dot charges. (b) Association of two cell polarization values to the logic states.

Algorithm (SCERPA) [63, 64]. SCERPA is an iterative algorithm designed to assess information propagation in molFCN circuits. In a molecular system, each molecule generates and responds to electric fields induced by other molecules or electrodes, defining different system states. Given the circuit description and information obtained from previous MoSQuiTo stages, SCERPA determines the relative effects of all the molecules in a self-consistent procedure. Upon reaching convergence, SCERPA provides information on the charge distribution of each molecule in the circuit for a specific clock/input combination.

1.2.3 Fabrication ideas

Most of the work in the last years focused on theoretical analysis and simulations. Unlike the other FCN implementations, an experimental demonstration of propagation or elaboration in molFCN is still missing. From the technological point of view, some works proposed molecules that hold the properties described for molFCN [49, 65, 66]. Regarding the possibility of fabricating a device, few studies proposed using a substrate onto which molecules attach employing a tile [49, 67, 68].

The primary challenge arises from molecules typically having dimensions in the range of 1–2 nm. Consequently, using lithography-based technology to achieve wires with comparable dimensions takes time and effort [69]. Additionally, regardless of size, precision in constructing angles is especially crucial for a cross structure like that of the MV. Once the nanopatterned substrate is defined, one valid approach proposed for molecule deposition involves using Self-Assembled Monolayers (SAM) [70–72]. It comes by itself that to obtain regular SAM, the nanopatterned substrate must be

precisely built. Any imprecision at the atomic level of the substrate may reflect in shifted, tilted, rotated, or misaligned molecules [67, 61].

Managing the generation of electric fields essential for computation, including the clock field and the switching field of input molecules, introduces another complexity requiring additional wires. The clock electrodes can be buried under the molecule deposition level [68] or on the edge of a trench [73]. Achieving precision at the level of few molecules is challenging. The dimension of the electrodes determines the number of molecules affected by the generated field, and inside this region, propagation must guaranteed. Information write-in is achieved with the same concept, forcing an electric field on the input molecules that behave as molecules in a nanogap [67].

1.3 Motivations of the work in the FCN panorama

Besides the concepts behind each implementation being the same, each implementation comes with its own advantages and challenges to overcome. In all the implementations, the power consumption was reduced thanks to the principle of no-current flowing to propagate information, which is the red thread of the paradigm.

First of all, the importance of the clock has already emerged as a character helping information switching and propagation along the desired paths. The general concept of the clock is to vary the potential barrier of unit elements, such as molecules or magnets, to erase the information, then by releasing the clock, depending on the surrounding fields, the unit element switches to a specific logic state.

The switching dynamic also depends on the working temperature since the presence of thermal noise can superpose to signal fields, possibly inducing an error. The metal QCA is restricted to work at cryogenic temperatures to prevent information loss [25]. Those temperatures reduce the impact of thermal noise, but the power consumption to keep the system at such low temperatures increases. In SiDB, circuits present errors at a few tens of kelvin, depending on the circuit [74]. Magnetic coupling in iNML is strong enough to work at room temperature [37, 40]. However, the presence of high thermal noise forces designers to shrink the maximum length of clock regions to a few magnets, implying a fine control of the clock network [75]. Even in molFCN thermal noise induces oscillation in the charge occupation of the

molecule dots [55, 56]. At room temperature, oscillations of the aggregated charge stay around the equilibrium point, and their amplitude is not sufficient to induce an encoding error [56].

The minimum dimension for information encoding is small in all the implementations. Indeed molFCN and SiDB unit elements extend below 1 nm [49, 30], whereas iNML and metal QCA need few tens of nanometer for the fundamental cell [40, 18].

Reduced minimum dimensions combined with the need for a few unit elements to build logic gates result in highly dense circuits. However, the small dimensions and the need for punctual control of the clock system make the fabrication of prototypes challenging. Except for molFCN, the other implementations have been experimentally validated. The fabrication of metal QCA exploits a top-down approach and requires a few process steps, using standard techniques such as Electron Beam Lithography (EBL), double layer resist development, and metal evaporation and oxidation [18]. Magnets in iNML can be defined through Focused Ion-Beam (FIB) lithography, a technique that can also be used for local manipulation of dot magnetic properties [38]. Currently, SiDB are created on top of a hydrogen-passivated silicon surface, using an artifact-free tip of a Scanning Tunnelling Microscope (STM) in a Ultra-High Vacuum (UHV) chamber at cryogenic temperature [30].

Writing and reading the information are typically two distinct problems in all the implementations. Writing data means applying a controlled field locally in a specific region of a circuit, not very different from the application of the clock field. The write-in system in iNML can be a magnetic Tunnel Junction (TJ) or a spin valve [38]. Metal QCA are metal TJs that can be driven by an external voltage applied through a coupling capacitance [18]. Molecules are sensitive to electric fields that can be applied by nanoelectrodes, as the ends of a nanogap with the molecule inside the gap itself [67, 76], or be light-induced [77]. A CMOS driver/inverter configuration can be used to drive the signal for inputs, as well as for cells with fixed polarization [78]. For SiDB, up to now, information is written using directly the STM tip, by creating single DBs that hold an electron, generating the electric field used as input [30]. Using a fixed DB enables the laboratory-level prototype validation, yet investigations are missing on a controllable runtime solution without the need for a STM tip.

Reading the information in iNML for its integration into transistor-based systems needs a magnetoelectric interface. The magnetic field encoding the information is used to induce a magnetization of a magnetic TJ, and then the magnetoresistance

phenomenon enables to read the information [38]. Detecting the position of the electron in metal QCA is a critical operation. The natural implementation proposed is the use of a Single-Electron tunneling Transistor (SET) placed next to the dot we are interested in sensing [79]. As for information writing in SiDB, even the output reading is performed through scanning microscopy [30]. This technique enables validation at the laboratory level but can't be used as a charge-sensing technique in the integration with transistor-based systems. Scanning microscopy techniques are also compatible with measuring information stored in molecules as a charge distribution [80, 81]. One particular challenge for the measurement is the ability to build a precise prototype.

FCN is an active research and development area, and each implementation still faces challenges. Among them, molFCN offers a unique combination of both room-temperature operation and miniaturization. The price to pay is the complexity of the fabrication that involves several actors: chemists for molecule syntheses and deposition, technology experts for the creation of nanopatterned hosting structures, and physicists for the measurement step. All these actors must cooperate in all the stages, and still the required techniques are very advanced in all those aspects.

Given the difficulty of conducting experiments, simulations become crucial to establish the behavior of systems, helping the prediction of their functioning, and driving focused experiments. Knowing in advance what to expect from a molecule or how a molecular system interacts with the surroundings becomes crucial to understanding how such systems could be realized technologically. Simulations are used to justify potential investments at the experimental level, demonstrating specific advantages over one implementation or another. The present work aims to provide considerations and design rules for molFCN systems. By starting from the investigation and the analysis of single molecules, the work focuses on the electrostatic interaction at the device level, especially describing how this can be used as a design parameter. Then, the work defines device modeling rules that can be used by CAD and Electronic Design Automation (EDA) tools to simulate large systems. The ability to design large circuits, proving them advantageous to other technologies, motivates the interest in the experimental validation of the technology. Finally, this work proposes a couple of alternatives for information reading again intending to facilitate the experimental proof.

Chapter 2

Molecules design principles

The role of molecules in the context of molecular Field-Coupled Nanocomputing (molFCN) is multifaceted; their composition dictates the electronic structure and quantum characteristics of the molecular cell, thereby shaping the behavior and functionality of the molFCN devices.

The selection of appropriate molecules becomes a critical aspect of molFCN design, as it directly influences the electrostatic effects that underlie the computational processes. The tailored arrangement of molecules for controlled manipulation of charge states offers a means to control and process information at the nanoscale. Furthermore, the engineering of molecule properties introduces the potential for tunability and customization, allowing researchers to fine-tune the performance characteristics of molFCN devices to meet specific computational requirements. This nuanced understanding of the molecular feature not only contributes to the optimization of molFCN technology but also opens avenues for exploring novel applications in quantum information processing and beyond, such as neural computation.

The next sections discuss molecules for molFCN, starting from the theoretical methods that can be used to study them and some core features that are of interest for molFCN applications. Then, a list of structural characteristics a molecule must have to be suitable for information propagation, before briefly describing the most studied molecules from the literature. Finally, the chapter analyzes in detail a case of study. We start with a molecule, and then various parts are modified to validate their effect on the valuable figures of merit for the molFCN.

2.1 Methods for studying molecules

Ab initio calculations and Density Functional Theory (DFT) are both approaches used in quantum mechanics to model the electronic structure and properties of molecules [82]. However, they differ in their underlying principles and computational methods.

Ab initio simulations represent a powerful computational approach for materials science and quantum chemistry, providing an accurate and detailed understanding of the properties and behavior of matter from first principles. Unlike empirical methods that rely on experimental data, *ab initio* simulations directly use quantum mechanical principles to predict the electronic structure and properties of molecules, starting with fundamental physical equations, one for all the Schrödinger equation

$$H\Psi = E\Psi \tag{2.1}$$

and solving them numerically to predict material properties.

Since this equation has an exact solution only for the hydrogen atom, some mathematical approximations are needed for any other molecules or systems: the nature of the necessary approximations determines the level of the calculation. *Ab initio* computations are based mainly on the laws of quantum mechanics and a set of physical constants (the speed of light, masses and charges of electrons and nuclei, Plank's constant).

One of the key strengths of *ab initio* simulations is their versatility, allowing researchers to investigate a variety of materials, from simple elements to complex compounds. These simulations play a crucial role in designing and analyzing novel materials or molecules with tailored properties, being general and theoretically reliable. It's important to note that ab initio simulations can be computationally demanding, requiring substantial computational resources. Nevertheless, advancements in computer power have significantly mitigated these drawbacks. The increase in computational speed over the years has transformed ab initio calculations from being considered impractical for molecules with more than 20 electrons to now routinely handling molecules with 100 electrons, demonstrating the remarkable progress in computational capabilities.

Unlike traditional ab initio methods, DFT doesn't attempt to directly solve the complex many-body Schrödinger equation. Instead, it focuses on the electron density, a key factor in determining the behavior of a quantum system. It aims to find the electronic density that minimizes the total energy of the system.

The core foundation of DFT lies in the Hohenberg-Kohn theorems [83], which assert that the ground-state electron density uniquely determines the potential energy of a system and, consequently, all other observables [82]. This theoretical principle enables a shift from dealing with many interacting electrons to a problem involving a single electron moving in an effective potential. The Kohn-Sham equations, a set of auxiliary non-interacting electron equations, are introduced to emulate the behavior of the real interacting system [83]. The challenge then becomes finding the exchange-correlation functional, a term accounting for the elusive electron-electron interactions.

It's important to note that the accuracy of DFT predictions is influenced by the choice of functionals and basis sets since both play a central role in approximating and describing the electronic structure of molecules and materials.

A functional in the context of quantum chemistry refers to a mathematical expression that associates a corresponding total energy with each possible electron density [82]. The exchange-correlation functional encapsulates the intricate electron-electron interactions that are challenging to account for explicitly. Various forms of exchange-correlation functionals exist, each designed to strike a balance between computational efficiency and accuracy in predicting molecular properties. Researchers continually refine and develop new functionals to improve the overall performance of DFT across a diverse range of systems and interactions.

Basis sets are sets of mathematical functions used to represent the spatial distribution of electrons within a molecule [82]. They serve as a foundation for expressing molecular orbitals, which are solutions to the Schrödinger equation. The choice of basis set significantly impacts the accuracy of quantum chemical calculations. Generally, larger basis sets with more functions provide a more accurate representation of electronic structure, but they come at the cost of increased computational complexity. Basis sets can be categorized into several types, such as minimal, double-zeta, and triple-zeta, each offering a trade-off between accuracy and computational efficiency.

DFT provides an excellent framework for accurate partial charge calculations as it accounts for the electronic correlation effects that influence the charge distribution

within a molecule. The choice of the exchange-correlation functional is crucial in ensuring the reliability of the results. Hybrid functionals, which combine Hartree-Fock exchange with DFT exchange-correlation functionals, are often employed for improved accuracy in describing charge distribution.

2.1.1 Partial charges calculation

As mentioned in subsection 1.2.2, DFT is used to obtain the data set for figures of merit extraction. The main interesting property is the charge distribution inside a molecule in response to external perturbations provided by electrodes or other molecules. The way to obtain such information is the use of partial charges.

DFT provides an excellent framework for accurate partial charge calculations as it accounts for the electronic correlation effects that influence the charge distribution within a molecule. The choice of the exchange-correlation functional is crucial in ensuring the reliability of the results. Hybrid functionals, which combine Hartree-Fock exchange with DFT exchange-correlation functionals, are often employed for improved accuracy in describing charge distribution.

Partial charges are a concept in chemistry that arise when atoms within a molecule share electrons unevenly [84]. In a covalent bond, where two atoms share electrons, the electronegativity of each atom determines how strongly it attracts the shared electrons. Electronegativity is a measure of an atom's ability to attract and hold onto electrons.

When two atoms with different electronegativities form a covalent bond, the electrons are not shared equally. The more electronegative atom attracts the electrons more strongly, leading to an uneven distribution of electron density. As a result, the atom with higher electronegativity acquires a partial negative charge $(\delta-)$ because it has a greater share of the electron density, while the atom with lower electronegativity acquires a partial positive charge $(\delta+)$.

Partial charge calculation is a critical aspect of understanding the electronic distribution within molecules, and DFT serves as a powerful tool for carrying out such calculations. In the context of DFT, partial charges are used to quantify the electron density distribution across different atoms within a molecular system. In DFT, the electron density is represented as a continuous distribution rather than discrete electron positions. Different methods have been proposed to calculate partial

charges or net atomic charges. Mulliken, Löwdin, and ElectroStatic Potential (ESP) derived charges are different methods used to calculate partial charges on atoms within a molecule. These methods provide different approaches to estimating how electrons are distributed among atoms in a molecular system.

The concept of Mulliken charges is rooted in the idea that the electron density around an atom is related to its electronegativity and, therefore, influences the charge distribution within a molecule [85, 86]. The calculation of Mulliken charges involves determining the average electron density of an atom within a molecule and then comparing it to the electron density of the isolated atom in its ground state. The difference between these values provides an estimate of the partial charge on the atom.

Mathematically, Mulliken charges (Q) are often expressed as follows:

$$Q_i = Z_i - \frac{1}{2}\sum_j P_{ij}S_{ij} \tag{2.2}$$

where Q_i is the Mulliken charge on atom i, P_{ij} is the off-diagonal element of the density matrix, and S_{ij} is the overlap matrix element. The summation is over all atoms j in the molecule.

While Mulliken charges are relatively straightforward to compute, they have some limitations. They can be sensitive to the choice of the basis set used in quantum mechanical calculations, and they may not always provide physically meaningful values, especially in cases where electron delocalization and resonance effects play a significant role [87].

Löwdin charges represent another approach to estimating partial charges on atoms within a molecule. Löwdin charges are derived from the density matrix and aim to provide a more physically meaningful description of the electron distribution than Mulliken charges [88]. Calculating Löwdin charges involves diagonalizing the overlap matrix (S) between atomic orbitals to obtain a set of orthogonalized orbitals. The density matrix elements (P) are then transformed to this new basis, and the trace of the resulting matrix provides the Löwdin charges for each atom [89].

Löwdin charges are considered to be more physically meaningful than Mulliken charge schemes. Nevertheless, even Löwdin charges can eventually become unstable with large basis sets [87].

ESP derived charges consider the electrostatic potential surrounding a molecule [90]. Among ESP-derived charge methods, the CHarges from ELectrostatic Potentials using a Grid (CHELPG) scheme is noteworthy for its effectiveness. The CHELPG method employs quantum chemical calculations to generate the molecular ESP. This potential is determined by solving the Poisson equation, considering the charge distribution of the atoms within the molecular system. The molecular ESP is then used to derive partial charges on individual atoms.

The fundamental idea behind CHELPG is to fit point charges onto the molecular surface in a way that reproduces the calculated electrostatic potential as closely as possible. The point charges are adjusted iteratively until the molecular ESP is well-matched. The resulting set of point charges represents the partial charges on each atom in the molecule.

The CHELPG method is widely used in quantum chemistry and molecular modeling because it provides accurate and physically meaningful partial charges. It accounts for the effects of nearby atoms and the overall molecular environment, making it especially valuable for studying molecular interactions and other properties that involve charge distribution. ESP-derived charges, particularly those obtained using the CHELPG method, are significantly more systematic and predictable behavior than the methods based on an analysis of the wave function or the electron density topology.

In summary, while Mulliken and Löwdin charges are older and more straightforward methods, ESP charges are generally more accurate and robust for calculating partial charges in molecular systems [91]. Researchers often choose the method based on the specific requirements of their studies and the level of accuracy needed for their calculations.

2.1.2 Molecular polarizability

Molecular polarizability is a fundamental concept in chemistry and physics that describes the ability of a molecule to respond to an external electric field by inducing a temporary dipole moment [92, 93]. This phenomenon arises from the redistribution of electrons within the molecule in response to the applied electric field.

Molecular polarizability is typically represented by the symbol α and quantifies how easily the electron cloud of a molecule can be distorted. Higher polarizability

values indicate that the molecule's electron cloud is more easily deformed, suggesting greater flexibility in its electronic structure. The molecular polarizability (α) is mathematically described by the equation:

$$\alpha = \frac{\mu}{E} \tag{2.3}$$

where μ is the induced dipole moment and E is the magnitude of the applied electric field.

The magnitude of the molecular polarizability depends on several factors, including the size and shape of the molecule, the distribution of electron density within the molecule, and the nature of the chemical bonds present. Generally, larger and more elongated molecules tend to have higher polarizability values due to the increased flexibility of their electron clouds.

The ORCA package offers three methods to calculate polarizability: analytic calculation, numeric differentiation of dipole moments, and fully numeric second derivatives.

In analytic calculation, the polarizability tensor is derived analytically from the electronic structure of the molecule using quantum mechanical methods such as Hartree-Fock (HF) theory, DFT, or Many-Body Perturbation Theory (MBPT). This method involves solving the electronic Schrödinger equation to obtain wavefunctions and energies, from which analytical expressions for the polarizability tensor components are derived.

With the numeric differentiation of dipole moments approach, the polarizability tensor is calculated numerically by perturbing the molecule's electronic structure with an external electric field and computing the resulting change in the dipole moment. The polarizability tensor components are obtained by numerically differentiating the dipole moment with respect to the electric field strength along different directions.

The fully numeric second derivatives method involves numerically computing the second derivatives of the molecular electronic energy with respect to atomic displacements induced by an external electric field. The polarizability tensor components are obtained from these second derivatives using finite difference or numerical differentiation methods.

Analytic calculation offers accuracy and efficiency for small to medium-sized molecules, while numeric methods provide flexibility and applicability to larger or

more complex systems at the cost of increased computational resources and potential numerical errors. In the following sections, the polarizability is calculated using analytic calculations.

2.2 Molecule requirements from a structural standpoint

Molecules for the molFCN technology need to have some characteristics to ensure the correct information treatment and the feasibility of a prototype. The requirements are strictly related to both the geometry of the system and the electrostatic behavior of the molecule. This section focuses more on aspects related to the space occupation, whereas chapter 3 deals in detail with the electrostatics of the molecules.

In the thesis, the molecules are treated as static entities to simplify the computational models and focus on fundamental interactions and behaviors. However, it is crucial to acknowledge that molecules are inherently dynamic, undergoing various vibrational modes and conformational changes. These dynamics can significantly influence the electrostatic interactions that are pivotal for molFCN. Recent studies have preliminarily investigated the impact of vibrations due to different working temperatures using Ab Initio Molecular Dynamics (AIMD) [56]. A recent work has also started investigating the dynamic behavior of molecules for molFCN using Real-Time Time-Dependent Density Functional Theory (RT-TDDFT) [94]. These types of simulations provide information to eventually improve the model of single molecules and are also compatible with the modular Molecular Simulator Quantum-dot cellular automata Torino (MoSQuiTo) methodology.

2.2.1 The bistability specifications

A vital aspect of molFCN is the requirement for bistable propagation [95, 66, 96]. Ideally, we have bistable propagation if adjacent molecules have the charge localized in the opposite part of the molecule and the amount of localized charge does not tend to zero going onward the wire/device.

Fig. 2.1(a) shows the charge along a wire and the associated dipole moment on a perfect bistable propagation: the charge and the dipole moment oscillate between

two constant values that do not vary along the wire. If the propagation is not bistable, information vanishes and gets lost after a few molecules. Ultimately, bistability depends on the molecule characteristics, and a parameter called Bistable Factor (BF) has been proposed to relate the possibility of having bistable propagation to the molecule features [96]. Considering the system shown in Fig. 2.1(b), composed of the driver molecule (DR) and the Molecule Under Test (MUT), the BF is defined as

$$BF_0(d, w, \alpha) = \frac{\alpha}{2\pi\varepsilon_0 w^2}\left(\frac{1}{d} - \frac{1}{\sqrt{d^2+w^2}}\right) \tag{2.4}$$

where d is the distance between the driver and the MUT (i.e., the intermolecular distance), w is the distance between the center of the groups involved in the logic encoding in the MUT (i.e., the molecular width), and α is the molecule polarizability.

In a system composed of N molecules, the bistable factor is computed by the following equation

$$BF_N = \sum_{i=1}^{N} (-1)^{\left(\frac{d_i}{d}+1\right)} BF_0(d_i, w, \alpha) \tag{2.5}$$

Bistable propagation occurs when $BF \geq 1$. However, if the BF surpasses a certain threshold, molecules polarize more rapidly, increasing the likelihood of errors during propagation. For instance, in the presence of thermal noise while working at room temperature, a small surrounding disturbance would be enough to polarize the molecule with a random value. This leads to the need for controlling the clock regions' dimensions: the larger the clock zones, the later the domino effect of the driving signal would cross the region, as already demonstrated for In-plane Nano Magnetic Logic (iNML) [75].

Here, we analyze the BF while varying the molecule width w and the polarizability α to determine the molecular safe-operating area. In the images displayed in the right column of Fig. 2.1c, the colored regions represent the molecular safe-operating area, with the gradient indicating the degree of BF satisfaction. Conversely, by adjusting the intermolecular distance d, a technology parameter, we delineate the technological safe-operating area, as illustrated in the images in the left column of Fig. 2.1c.

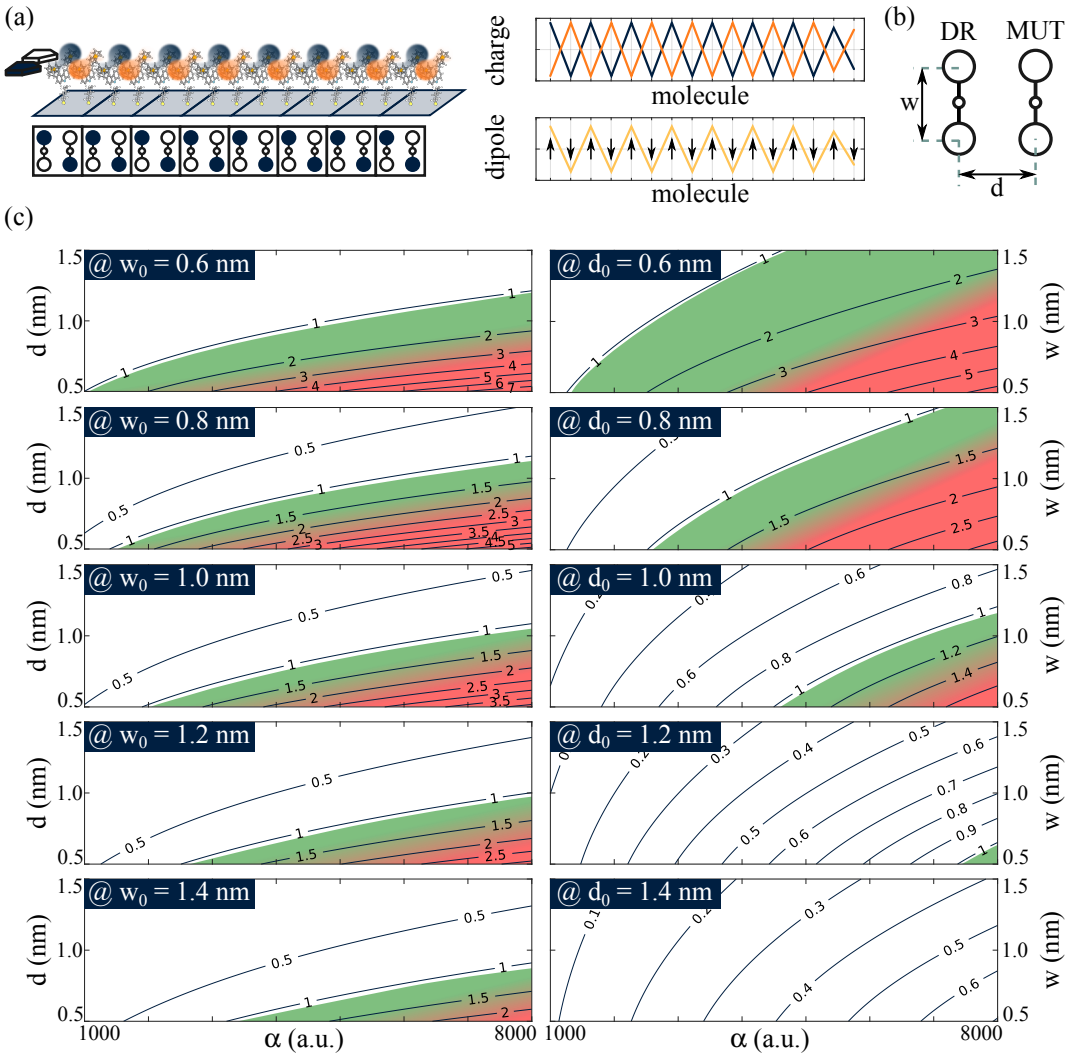

Fig. 2.1 Bistable propagation. (a) Charge and dipole along a wire in the case of bistable propagation. (b) System composed by the driver molecule and the molecule under test for calculating BF_0. (c) Bistable factor varying the polarizability α, the molecular width w, and the intermolecular distance d.

2.2.2 Molecules in space

Using the bisferrocene molecule, Fig. 2.2a defines the geometrical reference used throughout this document. Specifically, information propagates along the z-axis, the molecule stands along the x-axis, and the electric fields associated with the logic information are along the y-axis.

The geometrical structure of molecules affects the global electrostatic behavior and the physical occupation. Both aspects are crucial since the technology is based

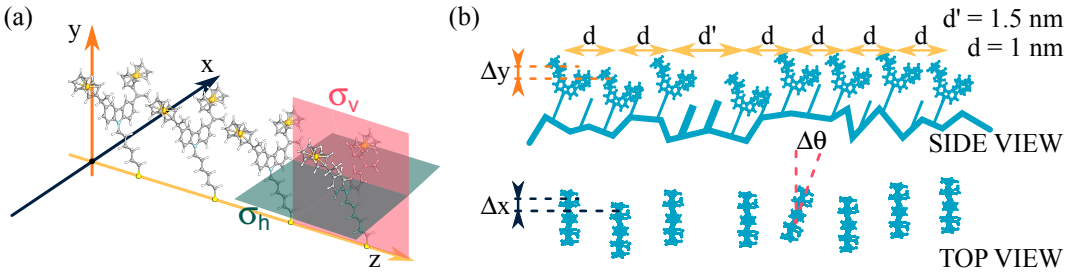

Fig. 2.2 Space organization of molecules. (a) Geometrical reference system and orientation of the molecule symmetry planes in space. (b) Possible process defects in a molFCN wire.

on electrostatic field coupling, and the logic devices are obtained through particular dispositions of the molecules.

Generally, along the x-axis, the molecule should be small enough to guarantee bistability, and the molecule should have a null net dipole so as not to unbalance the dipole moment linked to the information. Ideally, the molecule geometry should be Y-shaped or V-shaped, meaning that the molecule has a vertical symmetry σ_v and no horizontal symmetry σ_h. Fig. 2.2a shows the symmetry planes on the bisferrocene in the reference system. It should be imagined that the molecule aggregates its charge distribution on the three points of the 'Y' shape. In this way, the clock field can affect the charge distribution and provide the information reset ('NULL' state). Finally, the molecule should be synthesizable to implement an actual circuit.

Since molFCN is a technology based on the relative position of molecules and the electrostatics is crucial for the correct functioning, being able to build a device precisely helps the validation of a prototype. Molecules in a device must follow a specific pattern and orientation, and Fig. 2.2b shows that in an actual structure, we must consider process defects [97, 61]. Also, the molecule should not lose the electrostatic properties when deposited on the substrate. Besides, the substrate itself may be exploited to satisfy the requested properties, for example, obtaining charge localization using localized point defects [98].

Aiming to lighten the constraints on the nanometric layouts, which pose a significant challenge in molFCN technology, one solution is to workaround the necessity for nanometric patterning of molecular devices by exploiting molecules that organize in uniform Self-Assembled Monolayers (SAM) structures. Specifically, SAM can be considered a matrix of uniform blocks composed of several molecules capable of independently storing information and being activated [99]. Activating these

blocks in a controlled sequence enables the configuration of the SAM for mapping fundamental logic gates (such as majority voters and inverters) and routing elements.

2.3 Molecules from the literature

Researchers explored various organic and inorganic compounds to identify promising candidates for molFCN implementation. The choice of molecules is intricately linked to the desired functionalities of the device, such as logic operations and information storage. The goal is to harness the principles of quantum mechanics to create robust and scalable molecular systems. Several candidates have been proposed for both cases over the past 20 years. The geometry of all the following atoms is reported in Appendix A.

Among the proposed molecules to implement half cell, the $(NH_3)_5Ru(pyrazine)Ru(NH_3)_5$ has been deeply studied and is typically called Creutz-Taube ion [100]. Fig. 2.3a shows the geometry of the Creutz-Taube ion, studied in several works by Lieberman and Bernstein between 2000 and 2010, with an experimental goal [101–103] for both deposition and nanopatterning in molFCN. The Creutz-Taube ion has been used as a starting point to obtain mixed-valence complexes with different properties by changing the bridge between the two $(NH_3)_5Ru$ groups [104, 95].

Another interesting idea regards the possibility of exploiting the largely-studied fullerenes [105]. Fig. 2.3b shows a double-cage fluorinated fullerenes that form ordered arrays on Ag(100) surfaces [106, 107]. Even single fullerenes encapsulating single atoms or diatomic molecules show a sensitivity to an externally applied field, simplifying the global structure of the system [108].

These molecules model only two dots of the cell, and the effect of the clock field is not considered. So more recent studies investigate molecules that present three functional groups to encode also the 'null' state. One example is the $7-Fc^{+}-8-Fc-7,8-nido-[C_2B_9H_{10}]$, called diferrocenyl carborane, and shown in Fig. 2.3c [65]. The molecule has been synthesized to incorporate several features useful for a switching molecule for molFCN, in particular, the presence of the nido-carborane employed as an internal counterion. Authors in [109] investigate encoding and transmission using the diferrocenyl carborane embedded within the channels of

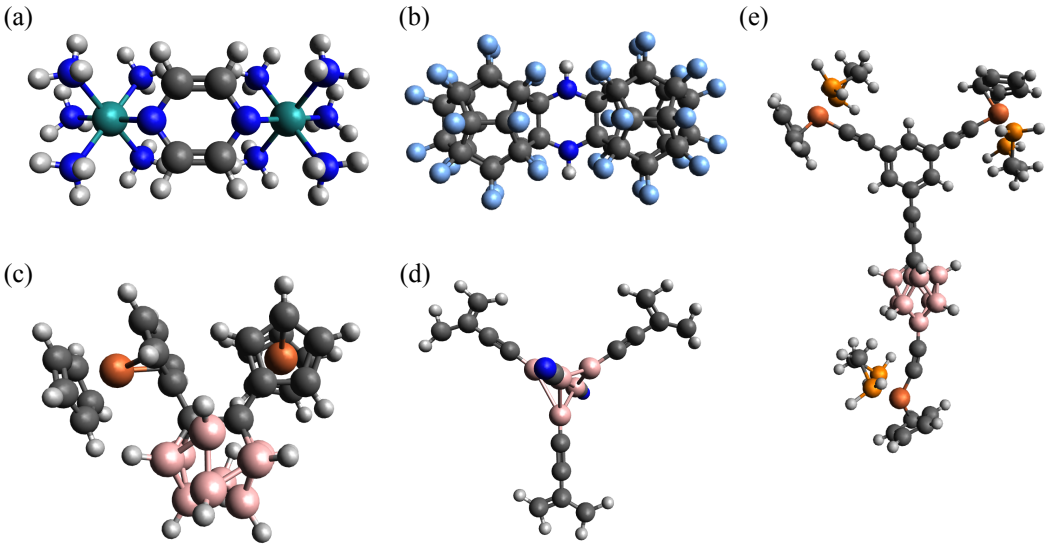

Fig. 2.3 Geometry of some molecules proposed in the literature for molFCN shown in a ball-and-stick diagram. (a) Creutz-Taube ion. (b) Double-cage fluorinated fullerenes. (c) Diferrocenyl carborane. (d) Zwitterionic three-dot molecule with di-anionic pentaborate counterion. (e) Three-dot 'Y'-shaped functionalized zwitterionic neutral closo-carborane. Atoms in figure are colored as follows: H = white, C = charcoal, N = blue, B = pink, Fe = orange, Ru = teal, F = sky blue, P = tangerine.

a microporous matrix. This approach allows molecules to self-assemble into a row inside the material's pores, forming an encased wire that benefits from the stability and protection provided by the crystalline environment.

Other works proposed molecules with boron cages as internal counterions. The three-dot 'Y'-shaped functionalized zwitterionic neutral closo-carborane model shown in Fig.2.3e uses a carborane core attached to three iron centers hosting the positive charge in the logic states [66]. Similarly, Fig. 2.3d shows the zwitterionic three-dot molecule with di-anionic pentaborate counterion where the functionalized cage is connected to simpler allyl groups for the three logic states [110].

Molecules presented so far have 2 or 3 dots, meaning they implement only half a cell. Researchers also proposed molecules implementing a whole molFCN cell with the four logic dots. Many of them use iron and cobalt atoms as the principal actors of the functional groups, inside metallocene structures [111–113] or not [114–116].

Besides the several proposals, there is still a lack of homogeneity among the studies, and only a few of them calculate the charge distribution using the ESP-derived partial charges more suitable for the molFCN application.

2.4 A case of study: Bis(trimethylsilyl) sulfide

From an application standpoint, the ultimate goal is to obtain a set of possible molecules with different properties that can be used in different contexts depending on the need. This section addresses this huge goal by analyzing a case-of-study of a molecule, where different parts of the molecule are substituted step-by-step to understand better how each functional group acts on the molecule transcharacteristic. All the following calculations are performed using the ORCA package [117, 118]. The coordinates of each molecule are reported in Appendix A.

The starting molecule is the bis(trimethylsilyl) sulfide, consisting of a central sulfur atom bonded to two silicon atoms. Each silicon atom is attached to three methyl groups CH_3, giving the molecule the chemical formula $((CH_3)_3Si)_2S$. Fig. 2.4a displays the geometry of the bis(trimethylsilyl) sulfide in a ball-and-stick diagram, obtained from the geometry optimization of the isolated molecule with the Unrestricted Kohn-Shann (UKS) method using CAM-B3LYP functional with def2-TZVP basis set [119]. Grimme D3 correction is applied [120, 121]. The charge distribution is analyzed by exploiting the ESP-derived CHELPG paradigm. The ORCA tool computes the electrostatic potential produced by the molecule and is shown in Fig. 2.4b, yielding a series of atom-centered charges through fitting [90]. Fig. 2.4c shows the ESP charges on each atom, presenting maximum values on the Si atoms and a minimum value on the S atom.

From the DFT simulation, we also extracted the polarizability tensor reported below in equation (2.6) in atomic units. The atomic unit for polarizability is expressed in terms of the atomic unit of length cubed per atomic unit of electric field squared, denoted as a_0^3/E_h, where a_0 is the Bohr radius ($\approx 0.5291 \times 10^{-10}$ m) and E_h is the Hartree energy ($\approx 4.3591 \times 10^{-18}$ J).

$$\alpha = \begin{pmatrix} 167.20344 & -0.32374 & 3.95419 \\ -0.32374 & 132.07003 & 0.66045 \\ 3.95419 & 0.66045 & 131.31831 \end{pmatrix} \tag{2.6}$$

The diagonalized tensor is expressed in equation (2.7), whereas the isotropic value is $\alpha_{iso} = 143.53059$ a.u..

$$\alpha_{diag} = \begin{bmatrix} 130.56878 & 132.38724 & 167.63575 \end{bmatrix} \tag{2.7}$$

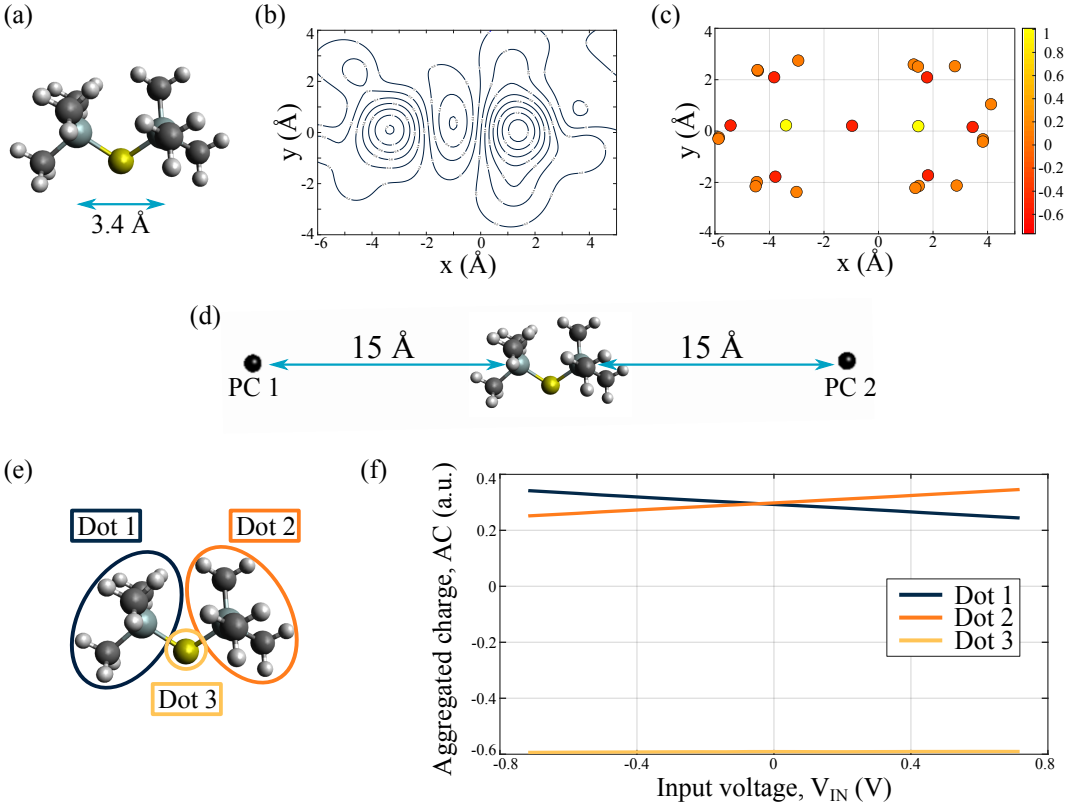

Fig. 2.4 Results of the DFT analysis on the bis(trimethylsilyl) sulfide molecule. (a) 3D geometry shown in a ball-and-stick diagram. (b) Molecular electrostatic potential evaluated with DFT calculation, the solid blue lines are isopotential curves. (c) ESP charges on each atom of the molecule. (d) 3D geometry of the molecule shown in a ball-and-stick diagram with the point charges used to generate the electric field represented as black dots. (e) Atom groups for the calculation of the aggregated charges. (f) V_{in}-AC transcharacteristic (VACT) of the bis(trimethylsilyl) sulfide. Atoms in figure are colored as follows: H = white, C = charcoal, S = yellow, Si = gray.

Once the relaxed structure is obtained, the goal is to study it in the presence of an external field to obtain the charge distribution so that we have the electrostatic model of the molecule when surrounded by other elements generating an electric field. The molecule is simulated in the presence of constant electric fields generated by positioning point charges in the space. Fig. 2.4d shows a 3D representation of the system composed of the bis(trimethylsilyl) sulfide and the position of the point charges used to start the simulations.

The generated electric field is calculated on the geometrical center ($x = -1.0192\,\text{Å}$, $y = 0.1898\,\text{Å}$, $z = 2 \times 10^{-7}\,\text{Å}$) of the molecule as the sum of the contri-

butions of all the point charges as expressed by the following equation:

$$E(x,y,z) = \sum_{i=1}^{N_{pc}} \frac{1}{4\pi\varepsilon_0} \frac{q \cdot pc_i}{r_i^2} \tag{2.8}$$

where N_{pc} is the total number of point charges, ε_0 is the vacuum permittivity, q is the electron charge, pc_i is the value of the i^{th} point charge, and r_i is the distance between the i^{th} point charge and the molecule geometrical center. Table 2.1 lists the electric field component along each axis for all the tested cases. The dominant values are along the x-axis, which is the direction of the switching field in a molFCN system.

Table 2.1 Values of the point charges and the relative electric field components for the simulation of the bis(trimethylsilyl) sulfide.

PC1 (a.u.)	**PC2** (a.u.)	E_x ($\mathrm{V\,nm^{-1}}$)	E_y ($\mathrm{V\,nm^{-1}}$)	E_z ($\mathrm{V\,nm^{-1}}$)
2.0	−2.0	2.0526	−0.0393	0.0572
1.8	−1.8	1.8473	−0.0354	0.0515
1.6	−1.6	1.6421	−0.0314	0.0458
1.4	−1.4	1.4368	−0.0275	0.0401
1.2	−1.2	1.2316	−0.0236	0.0343
1.0	−1.0	1.0263	−0.0197	0.0286
0.8	−0.8	0.8210	−0.0157	0.0229
0.6	−0.6	0.6158	−0.0118	0.0172
0.4	−0.4	0.4105	−0.0079	0.0114
0.2	−0.2	0.2053	−0.0039	0.0057
0	0	0	0	0
−0.2	0.2	−0.2053	0.0039	−0.0057
−0.4	0.4	−0.4105	0.0079	−0.0114
−0.6	0.6	−0.6158	0.0118	−0.0172
−0.8	0.8	−0.8210	0.0157	−0.0229
−1.0	1.0	−1.0263	0.0197	−0.0286
−1.2	1.2	−1.2316	0.0236	−0.0343
−1.4	1.4	−1.4368	0.0275	−0.0401
−1.6	1.6	−1.6421	0.0314	−0.0458
−1.8	1.8	−1.8473	0.0354	−0.0515
−2.0	2.0	−2.0526	0.0393	−0.0572

For each calculation, we extract the atomic charge by fitting the electrostatic potential. Subsequently, these atomic charges are aggregated into the groups shown in Fig. 2.4e to derive the Aggregated Charge (AC) distribution. From the electric field it is possible to obtain also the input voltage for each simulation, so Fig. 2.4f shows the VACT of the bis(trimethylsilyl) sulfide. The VACT points out a big charge separation between the negative sulfur and the positive trimethylsilane groups. Moreover, the application of a constant electric field does not impact the charge of the sulfur, since it only moves the charge from on Si to the other. The moving charge is small but still coherent with the molFCN information encoding.

We then study the oxidized molecule, aiming to obtain a bigger charge separation between logic dots. When a molecule undergoes oxidation, it loses electrons and becomes positively charged (a cation). This process can change the molecular structure and electronic properties, potentially leading to increased charge mobility and delocalization. We repeat the same analyses performed on the neutral molecule and Fig. 2.5a shows the ESP charges on each atom. Again, Si atoms show the maximum positive charge aggregation, but the charge on the sulfur atom is less negative in this case. The variation in the charge of the S atom is also reflected in the VACT shown in Fig. 2.5b. The aggregated charge on *Dot 3* (i.e., the sulfur atom) moved to -0.2 a.u.. The relative behavior between *Dot 1* and *Dot 2* did not change, except for the maximum charge separation, which is higher in this case.

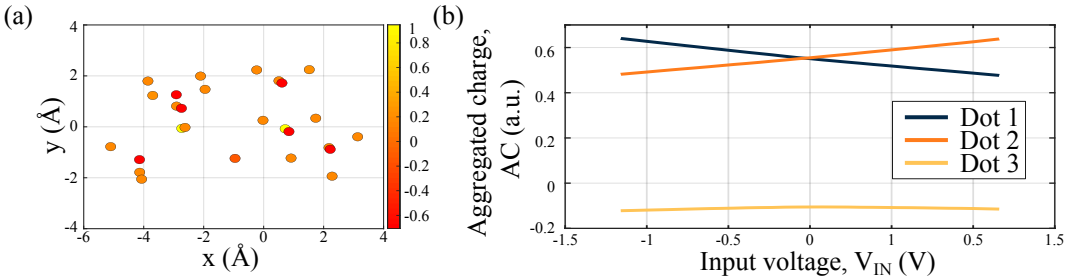

Fig. 2.5 Results of the DFT analysis on the oxidized bis(trimethylsilyl) sulfide molecule. (a) ESP charges on each atom of the molecule. (b) VACT of the bis(trimethylsilyl) sulfide.

The slightly increased charge separation is also reflected in the polarizability of the oxidized molecule, resulting in the following:

$$\alpha = \begin{pmatrix} 177.97479 & -2.99848 & 11.35569 \\ -2.99848 & 129.98007 & 0.44375 \\ 11.35569 & 0.44375 & 130.46194 \end{pmatrix} \tag{2.9}$$

The diagonalized tensor is expressed in equation (2.10), whereas the isotropic value is $\alpha_{iso} = 146.138\,93$ a.u..

$$\alpha_{diag} = \begin{bmatrix} 127.39440 & 130.31555 & 180.70685 \end{bmatrix} \tag{2.10}$$

2.4.1 Hexanedithiolbis(trimethylsilane)

The first modification increases the distance between the two trimethylsilane groups. By substituting the sulfur atom with the hexanedithiol, we obtain the molecule shown in Fig. 2.6a in a ball-and-stick diagram. The coordinates have been obtained from the geometry optimization of the isolated molecule with the UKS method using CAM-B3LYP functional with def2-TZVP basis set [119]. Grimme D3 correction is applied [120, 121]. The charge distribution is analyzed by exploiting the ESP-derived CHELPG paradigm. Following the same procedure as before, we use the ORCA tool to compute the electrostatic potential produced by the molecule, yielding a series of atom-centered charges through fitting [90]. Fig. 2.6b shows the ESP charges on each atom, again presenting maximum values on the Si atoms. This time, the connecting hexane does not hold any charge, whereas the S atoms hold a quite big negative charge. We then repeat the same analysis using the oxidized hexanedithiolbis(trimethylsilane). Oxidation removes an electron, making the molecule charge globally positive equal to 1 a.u.. Fig. 2.6(c) shows the ESP charges on each atom for the oxidized version of the molecule. Changes seem minimal, the biggest variation qualitatively observable is on the charge of both sulfur atoms becoming less negative.

The molecule polarizability is higher than the one obtained for the bis(trimethylsilyl) sulfide, resulting in the following:

$$\alpha = \begin{pmatrix} 307.57244 & 1.27015 & 3.76087 \\ 1.27015 & 206.68096 & 0.02147 \\ 3.76087 & 0.02147 & 195.49304 \end{pmatrix} \tag{2.11}$$

The diagonalized tensor is expressed in equation (2.12), whereas the isotropic value is $\alpha_{iso} = 236.582\,15$ a.u..

$$\alpha_{diag} = \begin{bmatrix} 195.36695 & 206.66503 & 307.71446 \end{bmatrix} \tag{2.12}$$

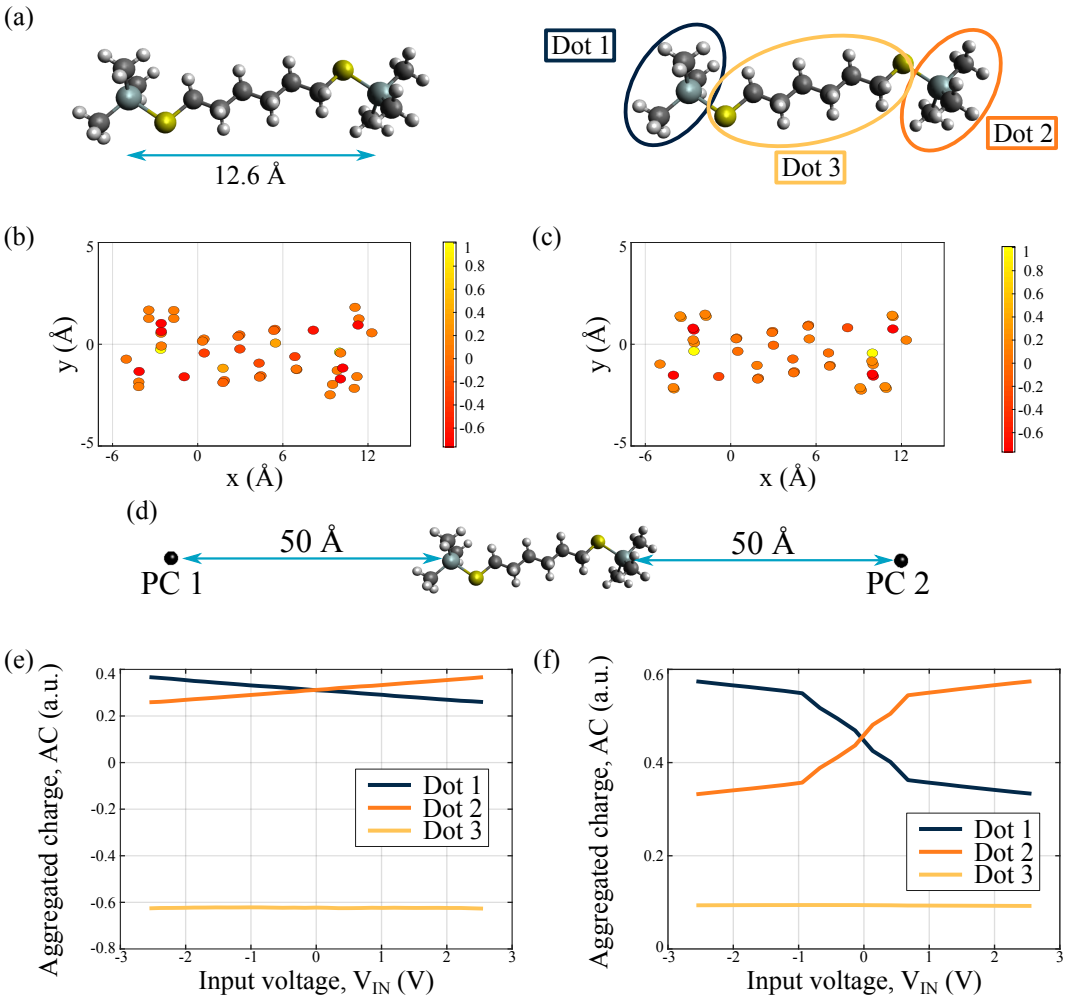

Fig. 2.6 Results of the DFT analysis on the hexanedithiolbis(trimethylsilane) molecule. (a) 3D geometry shown in a ball-and-stick diagram and the atom groups for the calculation of the aggregated charges. (b) ESP charges on each atom of the molecule. (c) ESP charges on each atom of the oxidized molecule. (d) 3D geometry of the molecule shown in a ball-and-stick diagram with the point charges used to generate the electric field represented as black dots. The scheme is not to scale. (e) VACT of the hexanedithiolbis(trimethylsilane). (f) VACT of the oxidized hexanedithiolbis(trimethylsilane). Atoms in figure are colored as follows: H = white, C = charcoal, S = yellow, Si = gray.

The molecule is then simulated in the presence of constant electric fields performed by positioning point charges in the space. Fig. 2.6d shows a 3D representation of the system composed of the hexanedithiolbis(trimethylsilane) and the position not to scale of the point charges used to start the simulations.

The generated electric field is calculated on the geometrical center ($x = 3.6846\,$Å, $y = -0.3861\,$Å, $z = -0.3126\,$Å) of the molecule using equation (2.8). We extract

the atomic charge for each electric field and aggregate them into the groups shown in Fig. 2.6a to derive the AC distribution. Fig. 2.6e shows the VACT of the molecule. The VACT confirms that the presence of the hexane does not influence the charge distribution on the molecule.

Fig. 2.6f shows the VACT of the oxidized molecule, pointing out the different behavior. The charge on *Dot 3* is now positive and almost equal to 0.1 a.u.. The two trimethylsilane groups still exchange charge, but the charge separation is, in this case, higher. For voltages bigger than $V_{IN} = 1\,\mathrm{V}$ in absolute value, the charge saturate to almost 0.3 a.u. and 0.6 a.u.. Since the charge separation is high, the information encoding for a molFCN system is stronger.

Oxidation, in this case profoundly, changed the characteristic of the molecule, and this is reflected in the polarizability tensor:

$$\alpha = \begin{pmatrix} 288.35743 & -756.33267 & -15.38033 \\ -756.33267 & 6892.61999 & 134.48621 \\ -15.38033 & 134.48621 & 192.29457 \end{pmatrix} \tag{2.13}$$

The biggest value is associated with the axis connecting the two silicon atoms. The diagonalized tensor is expressed in equation (2.14), whereas the isotropic value is $\alpha_{iso} = 2457.757\,33$ a.u..

$$\alpha_{diag} = \begin{bmatrix} 189.59316 & 202.85022 & 6980.82862 \end{bmatrix} \tag{2.14}$$

2.4.2 Dodecanedithiolbis(trimethylsilane)

Since the presence of the hexane as a linking bridge does not influence the charge distribution on the molecule, we substitute it with a dodecane chain, thus pulling the trimethylsilane further apart. Fig. 2.7a shows the resulting molecule in a ball-and-stick diagram, and the coordinates have been obtained from the geometry optimization of the isolated molecule with the UKS method using CAM-B3LYP functional with def2-TZVP basis set [119]. Grimme D3 correction is applied [120, 121]. The charge distribution is analyzed by exploiting the ESP-derived CHELPG paradigm, resulting in the ESP charges shown in Fig. 2.7b. Fig. 2.7c shows instead the ESP charges of the oxidized molecule dodecanedithiolbis(trimethylsilane). Considerations are very similar to the previous molecule. Hence, the silicon atoms present a

positive charge, whereas the sulfur and carbons in the methyl groups hold a negative charge. Again, the oxidation process impacts the most the charge on both S atoms and the dodecane chain.

Enlarging the distance between the two silicon atoms makes the polarizability grow, as expressed in the tensor:

$$\alpha = \begin{pmatrix} 408.80190 & 14.83344 & 10.31219 \\ 14.83344 & 269.17121 & 2.20230 \\ 10.31219 & 2.20230 & 253.03961 \end{pmatrix} \tag{2.15}$$

The diagonalized tensor is expressed in equation (2.16), whereas the isotropic value is $\alpha_{iso} = 310.337\,58$ a.u..

$$\alpha_{diag} = \begin{bmatrix} 252.26346 & 267.69308 & 411.05619 \end{bmatrix} \tag{2.16}$$

The molecule is then simulated in the presence of constant electric fields performed by positioning point charges in the space along the principal axis of the molecule, each at 50 Å from the Si atom on their side. The generated electric field is calculated on the geometrical center ($x = -0.4614$ Å, $y = -1.0219$ Å, $z = -0.3952$ Å) of the molecule using equation (2.8). We extract the atomic charge for each electric field and aggregate them into the groups shown in Fig. 2.7a to derive the AC distribution. Fig. 2.7d shows the VACT of the molecule. The VACT is almost identical to the one obtained for the hexanedithiolbis(trimethylsilane), demonstrating that the length of the connecting chain does not influence, acting as a neutral actor.

Fig. 2.7e shows the VACT of the oxidized molecule, pointing out the different behavior. The charge on *Dot 3* is now positive and almost equal to 0.1 a.u.. The two trimethylsilane groups still exchange charge, but the charge separation is, in this case, higher. The charge on *Dot 1* and *Dot 2* is not symmetrical to the INPUT voltage, as seen from the different V_{IN} values where the slope changes. For voltages bigger than $V_{IN} = 1.5$ V in absolute value, the charge saturates to almost 0.3 a.u. and 0.6 a.u., as in the case of the oxidized hexanedithiolbis(trimethylsilane).

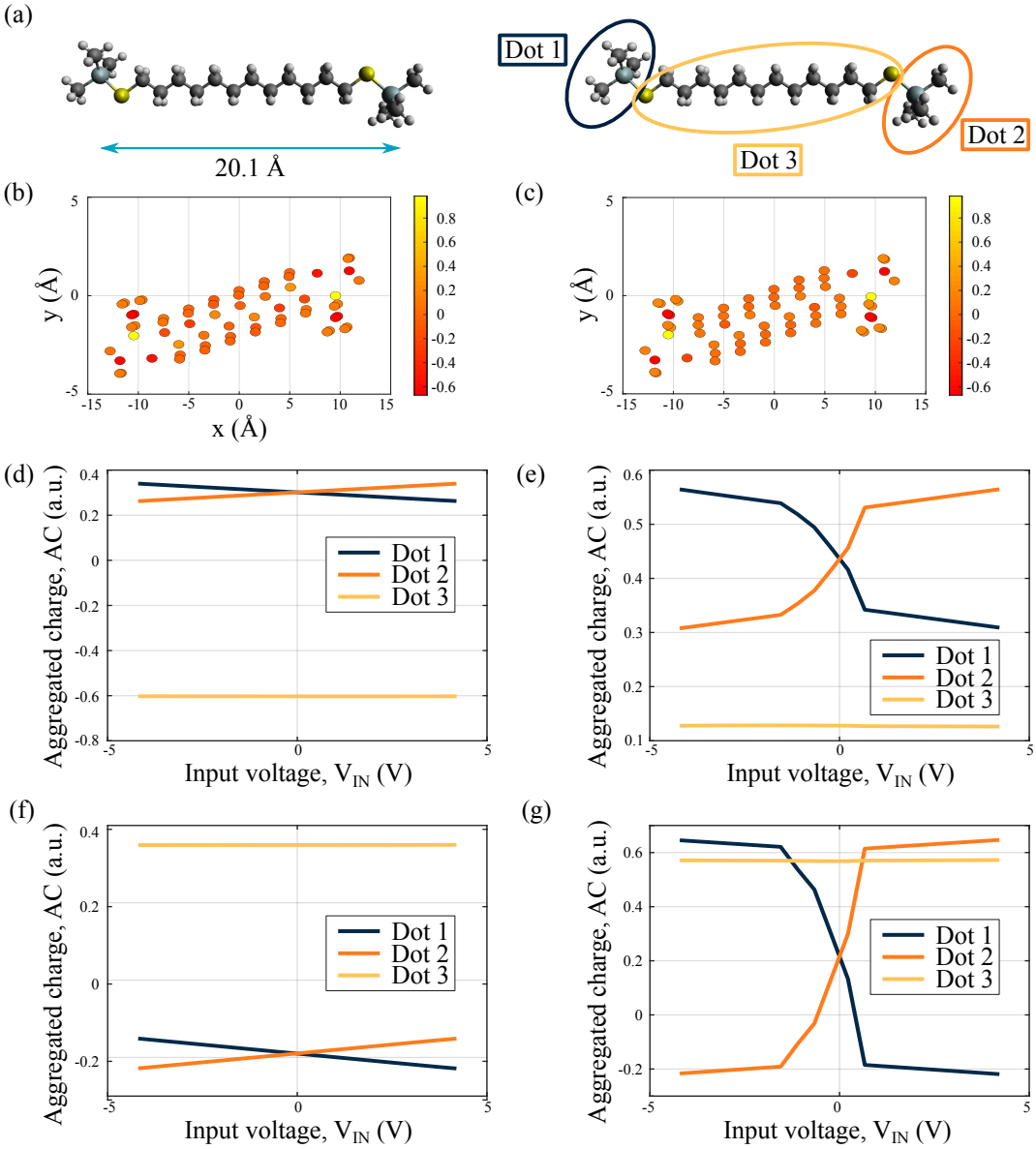

Fig. 2.7 Results of the DFT analysis on the dodecanedithiolbis(trimethylsilane) molecule. (a) 3D geometry shown in a ball-and-stick diagram and the atom groups for the calculation of the aggregated charges. (b) Molecular electrostatic potential evaluated with DFT calculation, the solid blue lines are isopotential curves. (c) ESP charges on each atom of the molecule. (d) VACT of the dodecanedithiolbis(trimethylsilane). (e) VACT of the oxidized dodecanedithiolbis(trimethylsilane). (f) VACT of the molecule with sulfur atoms belonging to *Dot 1* and *Dot 2*, instead of *Dot 3*. (g) VACT of the oxidized dodecanedithiolbis(trimethylsilane) with sulfur atoms belonging to *Dot 1* and *Dot 2*, instead of *Dot 3*. Atoms in figure are colored as follows: H = white, C = charcoal, S = yellow, Si = gray.

Even in case oxidation has a strong impact on the polarizability, indeed the tensor becomes:

$$\alpha = \begin{pmatrix} 14915.74840 & 2481.11846 & 879.81036 \\ 2481.11846 & 683.72260 & 150.26135 \\ 879.81036 & 150.26135 & 298.92055 \end{pmatrix} \tag{2.17}$$

The diagonalized tensor is expressed in equation (2.18), whereas the isotropic value is $\alpha_{iso} = 5299.463\,85$ a.u..

$$\alpha_{diag} = \begin{bmatrix} 246.03661 & 263.67372 & 15388.68122 \end{bmatrix} \tag{2.18}$$

Since from the charge values shown in Fig. 2.7b and Fig. 2.7c, the sulfur atoms emerge as key actors, we group them with *Dot 1* and *Dot 2*. So, in this case, *Dot 3* is just composed of the dodecane chain. Fig. 2.7f and Fig. 2.7g show the VACT obtained for the neutral and the oxidized molecules, respectively. The behavior of the aggregated charge strongly changes since, in both cases, the charge on *Dot 3* became positive. The charge exchange between the logic dots still occurs, but the values differ. This result demonstrates the importance of defining the molecule dots because even a few atoms can completely change the perspective of global behavior.

2.4.3 Tridecanedithiolbis(trimethylsilane)

The dodecane instead of the hexane does not change the aggregated charges behavior too much, but an asymmetry between *Dot 1* and *Dot 2* shows up in the oxidized molecule. To remove the asymmetry, we substitute the dodecane with a tridecane, leading to the structure shown in Fig. 2.8a. The coordinates have been obtained from the geometry optimization of the isolated molecule with the UKS method using CAM-B3LYP functional with def2-TZVP basis set [119]. Grimme D3 correction is applied [120, 121]. Since the VACT asymmetry is present only in the oxidized molecule, we analyzed only the difference in that case. Fig. 2.8b shows the ESP charges of the oxidized tridecanedithiolbis(trimethylsilane). Considerations are very similar to the previous molecules. Hence, the silicon atoms present a positive charge, whereas the sulfur atoms and the carbons in the methyl groups hold a negative charge.

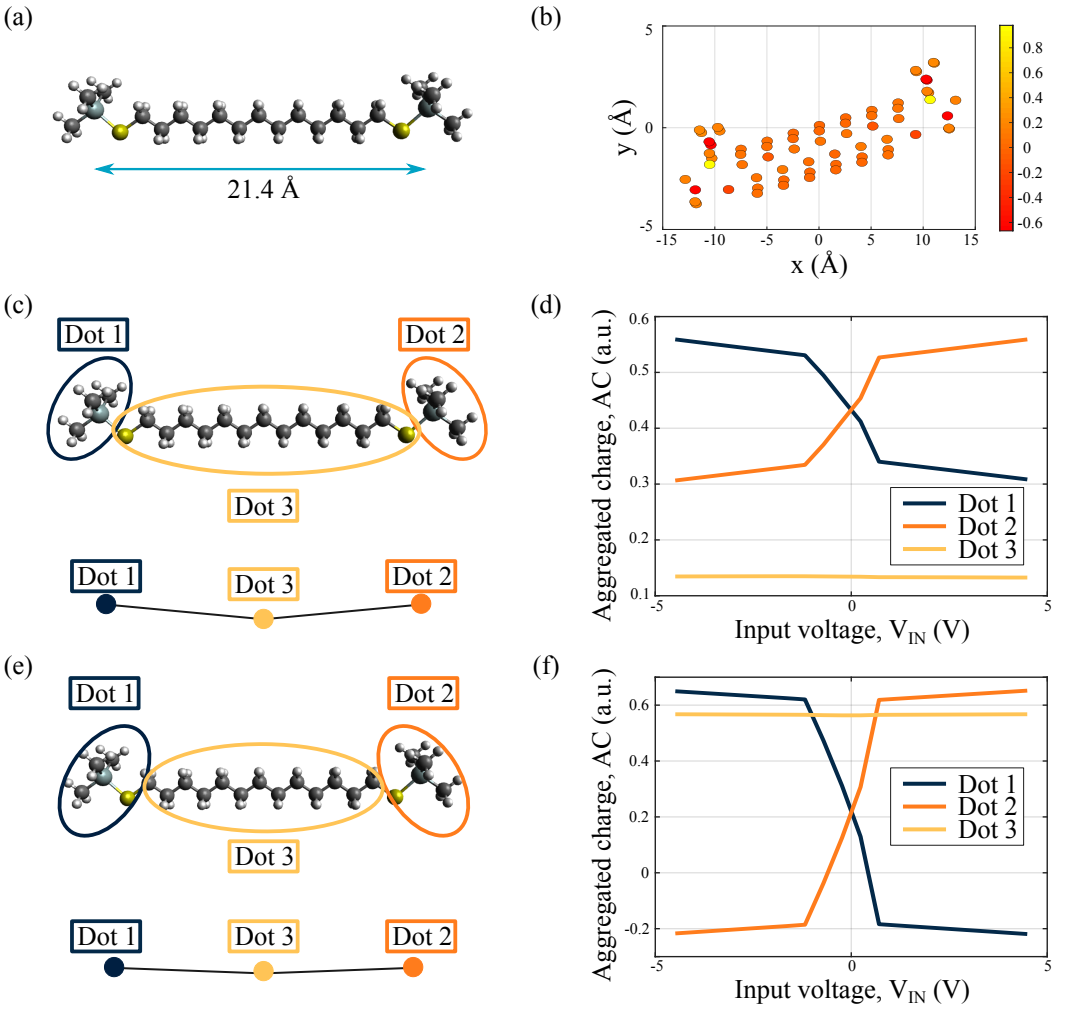

Fig. 2.8 Results of the DFT analysis on the tridecanedithiolbis(trimethylsilane) molecule. (a) 3D geometry shown in a ball-and-stick diagram. (b) ESP charges on each atom of the molecule. (c) Atom groups for the calculation of the aggregated charges and position of the point charges associated with the dots in the case in which S atoms belong to *Dot 3*. (d) VACT of the oxidized tridecanedithiolbis(trimethylsilane) with sulfur atoms belonging to *Dot 3*. (e) Atom groups for the calculation of the aggregated charges and position of the point charges associated with the dots in the case in which S atoms belong one to each logic dot. (f) VACT of the oxidized tridecanedithiolbis(trimethylsilane) with sulfur atoms belonging to *Dot 1* and *Dot 2*. Atoms in figure are colored as follows: H = white, C = charcoal, S = yellow, Si = gray.

Since the molecular width increases, also the polarizability increases, becoming

$$\alpha = \begin{pmatrix} 16851.23764 & 2496.05876 & 630.68429 \\ 2496.05876 & 649.99873 & 95.52290 \\ 630.68429 & 95.52290 & 279.48025 \end{pmatrix} \tag{2.19}$$

The diagonalized tensor is expressed in equation (2.20), whereas the isotropic value is $\alpha_{iso} = 5926.905\,54$ a.u..

$$\alpha_{diag} = \begin{bmatrix} 255.48929 & 274.17625 & 17251.05108 \end{bmatrix} \tag{2.20}$$

The molecule is then simulated in the presence of constant electric fields performed by positioning point charges in the space along the principal axis of the molecule, each at 50 Å from the Si atom on their side. The generated electric field is calculated on the geometrical center ($x = 0.1310$ Å, $y = -0.5863$ Å, $z = -0.4791$ Å) of the molecule using equation (2.8). By grouping the atoms as shown in Fig. 2.8c, that is, with the two sulfur atoms inside *Dot 3*, the resulting VACT is the one shown in Fig. 2.8d. The AC on *Dot 3* is still constant, and changing the field moves the charge between *Dot 1* and *Dot 2*. The curves for the logical dots are still not identical, but the global behavior improved its symmetry to V_{IN}, confirming that geometrical symmetry can imply electrostatic symmetry. Fig. 2.8c also shows the equivalent point charges system obtained by the group division that is eventually used in the Self-Consistent ElectRostatic Potential Algorithm (SCERPA) simulator. The position of the point charges associated with the dots is calculated considering both geometry and electrostatic influence, as described by the following equation

$$p_{Dot_j}(x,y,z) = \frac{\sum_{i=1}^{N_j} p_i(x,y,z) \cdot |q_i|}{\sum_{i=1}^{N_j} |q_i|} \tag{2.21}$$

where p_{Dot_j} indicates the position of the dot j, N_j is the number of atoms belonging to Dot_j, p_i is the position of the i^{th} atom inside Dot_j and q_i is its ESP charge.

Fig. 2.8e shows atoms grouping when the two S move from *Dot 3* to logic dot and the corresponding position of the point charges associated with the dots. The position changes minimally, *Dot 1* and *Dot 2* are slightly closer, and the angle formed with *Dot 3* is a bit smaller. Besides the minor changes in the geometrical definition of the dots, the electrostatic behavior of the dot changes significantly, as reported in Fig. 2.8f by the VACT. Compared to the previous situation, *Dot 3* loses half an electron, bringing the AC to almost 0.6 a.u.. Logic dots exchange charge between -0.2 a.u. and 0.6 a.u., so the maximum charge separation between logic dots is equal to 0.8 a.u., much higher than the 0.25 a.u. charge separation shown in Fig. 2.8d.

In both the analyzed cases, the actual behavior of the molecule is obviously the same, as the data are extracted from the same simulations. What changed was only the application of the aggregated charges model from MoSQuiTo. Indeed, each model comes with its own scope, and one must pay attention to the implications of applying a model. In this case, the choice of which atoms belong to each dot is crucial, and not only must we consider the electrostatic behavior but also the shape and extension of the molecule in order not to lose the actual behavior of the molecule and have a realistic model of the system we are considering.

2.4.4 1,3,5benzenetrithiol linked bis(hexanedithiol) bis(trimethylsilane)

All the molecules presented so far present a good charge separation and can be divided into three functional groups, paying attention to where to place atoms. In all the molecules seen so far, *Dot 3* does not influence the charge localization for information encoding and keeps a constant charge independently from the applied field. Also, all the molecules analyzed so far are mainly extended along a single axis, not presenting a 'V' or 'Y' shape, as we discuss in section 1.1.4. This shape may affect the ability to reset the molecule by applying an electric field orthogonal to the direction in which the molecule lays out. Given the importance of the clock and the ability to reset the molecule discussed in section 1.3, we include a functional group in the middle of *Dot 3*, serving as a sort of joint for an eventual third group for clock handling.

The first group that we use is 1,3,5benzenetrithiol composed of a benzene ring with three thiols linked to it. Fig. 2.9a shows how the thiols are used as linking points to hexanes, bringing to the two trimethylsilane, leaving a free thiol for the connection of an additional dot for the reset. The coordinates have been obtained from the geometry optimization of the isolated molecule with the UKS method using CAM-B3LYP functional with def2-TZVP basis set [119]. Grimme D3 correction is applied [120, 121]. Focusing on the oxidized version of the molecule, Fig. 2.9b shows the ESP charges, demonstrating that the introduction of the new group does not change drastically the equilibrium charge configuration. The most positive charge is still located on the silicon atoms, sulfur atoms hold a significant negative charge,

and the connecting chain comprising the ring seems balanced with all the atoms having a slightly positive charge.

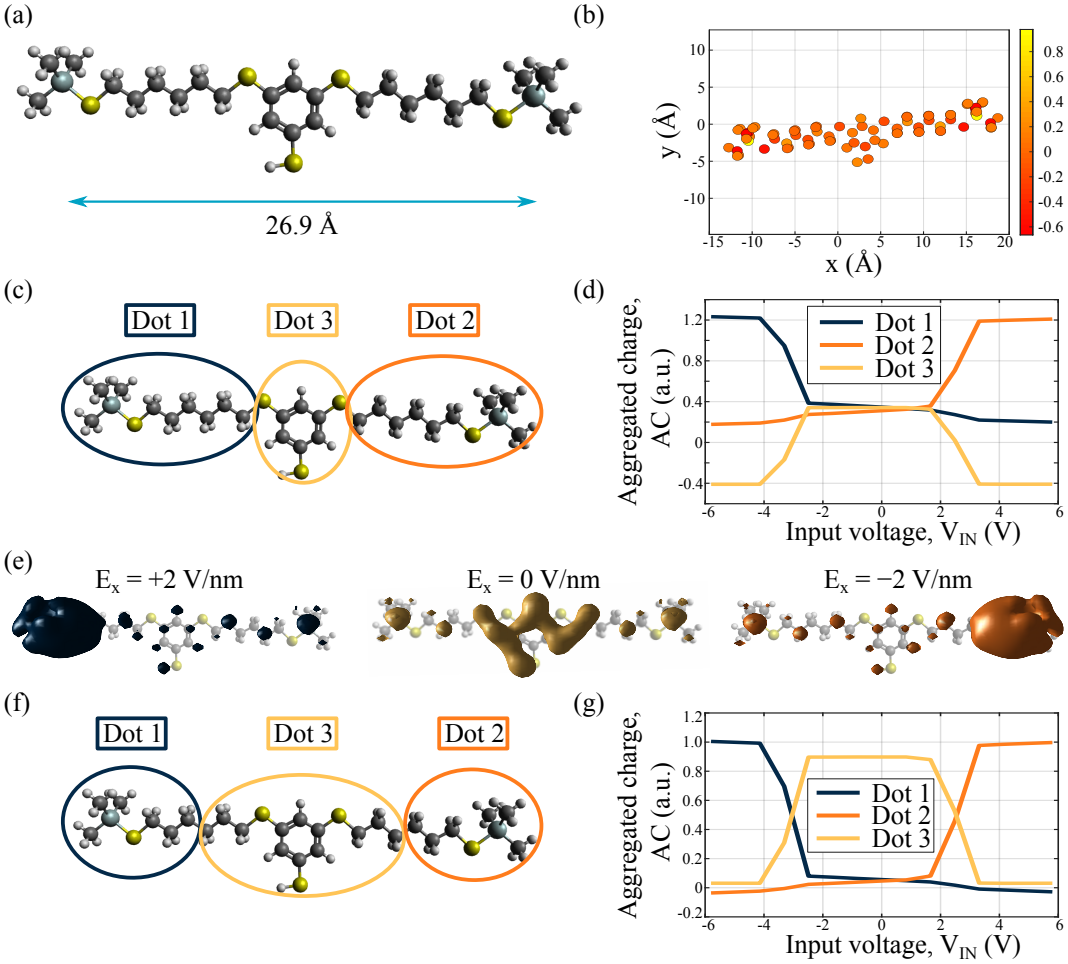

Fig. 2.9 Results of the DFT analysis on the oxidized 1,3,5benzenetrithiol linked bis(hexanedithiol) bis(trimethylsilane). (a) 3D geometry shown in a ball-and-stick diagram. (b) ESP charges on each atom of the molecule. (c) Atom groups for the calculation of the aggregated charges. (d) VACT of the molecule with only the 1,3,5benzenetrithiol belonging to *Dot 3*. (e) Isopotential surfaces for different electric field values showing where the charge localizes. (f) Atom groups for calculating the aggregated charges based on the analysis of the isopotential surfaces. (g) VACT of the molecule with dots chosen based on the actual charge localization on the molecule. Atoms in figure are colored as follows: H = white, C = charcoal, S = yellow, Si = gray.

The introduction of the benzene ring decreases the polarizability of the molecule, which is:

$$\alpha = \begin{pmatrix} 1086.18703 & 74.05931 & 20.51756 \\ 74.05931 & 498.60377 & 9.22278 \\ 20.51756 & 9.22278 & 306.30324 \end{pmatrix} \tag{2.22}$$

The diagonalized tensor is expressed in equation (2.23), whereas the isotropic value is $\alpha_{iso} = 630.36468\,\text{a.u.}$.

$$\alpha_{diag} = \begin{bmatrix} 305.47952 & 489.65150 & 1095.96303 \end{bmatrix} \tag{2.23}$$

By grouping atoms as shown in Fig. 2.9c, with *Dot 3* composed of only 1,3,5benzenetrithiol, and *Dot 1* and *Dot 2* are both equally composed with the trimethylsilane and the hexanedithiol. Fig. 2.9d shows the resulting VACT. The behavior observed in the presence of an electric field is different from the previous ones. For small fields, the charge is equally distributed on the three dots. For electric fields that generate voltages bigger than 2 V in absolute value, the charge moves from *Dot 3* to either *Dot 1* or *Dot 2*, depending on the sign of the electric field.

To check if the VACT describes the actual behavior accurately, we analyze the isopotential surfaces for different electric field values to see where the charge localizes. Fig. 2.9e shows the isopotential surface for $E_x = 2\,\text{V}\,\text{nm}^{-1}$, $E_x = 0\,\text{V}\,\text{nm}^{-1}$, and $E_x = -2\,\text{V}\,\text{nm}^{-1}$ corresponding to the VACT points where the voltage is respectively $V_{IN} = -6\,\text{V}$, $V_{IN} = 0\,\text{V}$, and $V_{IN} = 6\,\text{V}$. When the field is applied, the isopotential surface encloses the trimethylsilane and half of the hexanedithiol chain. On the contrary, when no or a small field is applied, the charge localizes on the central ring and the other halves of the hexanedithiol, leaving the external parts of the molecule with almost no charge.

Since the VACT of Fig. 2.9d does not point out this behavior, we modify the dot definition to match the actual functional group of the molecule, obtaining the configuration shown in Fig. 2.9f. With the new definition of the dots, we get a different VACT, shown in Fig. 2.9g. In this case, we see that for small fields, the charge is constant and mainly localized on *Dot 3*, whereas with a big applied field, *Dot 3* releases almost all the charge to either *Dot 1* or *Dot 2*, depending on the value of the electric field.

2.4.5 Trithiocyanuric acid linked bis(hexanedithiol) bis(trimethylsilane)

Besides the peculiar behavior obtained using the 1,3,5benzenetrithiol as a joining element, we also investigate a different one. Specifically, using the trithiocyanuric acid as a linking group, we obtain the molecule shown in Fig. 2.10a. The trithiocyanuric acid is a hexagonal ring composed of alternating carbon and nitrogen atoms, and the sulfurs to which we want to attach the hexanedithiol are bonded to the C atoms of the ring. The coordinates have been obtained from the geometry optimization of the isolated molecule with the UKS method using CAM-B3LYP functional with def2-TZVP basis set [119]. Grimme D3 correction is applied [120, 121].

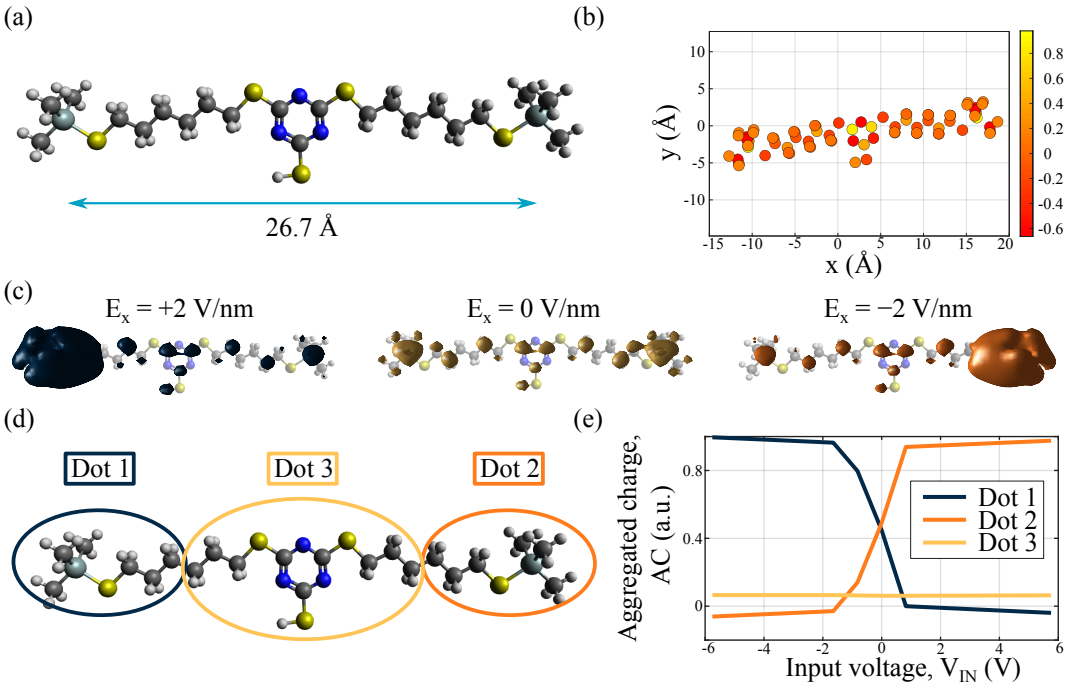

Fig. 2.10 Results of the DFT analysis on the oxidized trithiocyanuric acid linked bis(hexanedithiol) bis(trimethylsilane). (a) 3D geometry shown in a ball-and-stick diagram. (b) ESP charges on each atom of the molecule. (c) Isopotential surfaces for different electric field values showing where the charge localizes. (d) Atom groups for calculating the aggregated charges based on the analysis of the isopotential surfaces. (e) VACT of the molecule with dots chosen based on the actual charge localization on the molecule. Atoms in figure are colored as follows: H = white, C = charcoal, N = blue, S = yellow, Si = gray.

Even if the geometrical structure is similar to the previously analyzed case, the electrostatic behavior strongly changes. Fig. 2.10b shows the ESP charges of the

oxidized molecule at equilibrium. The Si atoms still keep a positive charge, and the two hexanedithiols hold a slightly positive charge. The trithiocyanuric acid charge alternates between a strong positive charge on the carbons and a strong negative charge on the nitrogen, especially on those linked to the two hexanedithiols through the S atoms.

The presence of the trithiocyanuric acid is also visible in the polarizability, which is much higher than the case in which the group is the benzenetrithiol

$$\alpha = \begin{pmatrix} 23550.06626 & 2978.05838 & 689.08133 \\ 2978.05838 & 742.56808 & 87.05502 \\ 689.08133 & 87.05502 & 295.61537 \end{pmatrix} \tag{2.24}$$

The diagonalized tensor is expressed in equation (2.25), whereas the isotropic value is $\alpha_{iso} = 8196.083\,24$ a.u..

$$\alpha_{diag} = \begin{bmatrix} 275.19988 & 360.14894 & 23952.90089 \end{bmatrix} \tag{2.25}$$

Fig. 2.10c shows the isopotential surface analyses for different electric field values. Similarly to the case with the 1,3,5benzenetrithiol, when an electric field is applied, the charge localizes on the trimethylsilane and half of the hexanedithiol on either left or right, depending on the sign of the electric field. When no field is present, a small positive charge is localized around both the silicon atoms and almost no charge is on the rest of the molecule.

Considering the charge localization described by the isopotential surface analysis, we group the atoms as shown in Fig. 2.10d. Fig. 2.10e shows the resulting VACT, confirming the constant slightly positive charge on *Dot 3*. With no applied field, the charge is balanced between *Dot 1* and *Dot 2*, which exchange charge in the presence of an electric field, reaching a maximum charge separation of almost 1 a.u..

2.4.6 Trithiocyanuric acid linked tris(hexanedithiol) bis(trimethylsilane)

The presence of the free thiol of the trithiocyanuric acid in the previous case allows for the connection of an additional hexanethiol to obtain a ‘T’ shape, theoretically helping the clock. The geometry of the resulting molecule is shown in Fig. 2.11a.

The choice of not attaching a third trimethylsilane group derives from the possibility of using the end of the hexanethiol to link the molecule to an eventual surface [122]. The coordinates have been obtained from the geometry optimization of the isolated molecule with the UKS method using CAM-B3LYP functional with def2-TZVP basis set [119]. Grimme D3 correction is applied [120, 121].

The introduction of the third hexanethiol slightly changes the polarizability, especially showing a reduced isotropic behavior:

$$\alpha = \begin{pmatrix} 25580.64594 & 5042.99662 & 670.19788 \\ 5042.99662 & 1518.71704 & 132.56929 \\ 670.19788 & 132.56929 & 377.85808 \end{pmatrix} \tag{2.26}$$

The diagonalized tensor is expressed in equation (2.27), whereas the isotropic value is $\alpha_{iso} = 9159.07369\,\text{a.u.}$.

$$\alpha_{diag} = \begin{bmatrix} 360.03482 & 504.56472 & 26612.62152 \end{bmatrix} \tag{2.27}$$

We group the atoms as in Fig. 2.11b and study the system with different applied electric fields. By using point charges, we generate an electric field in the clock direction equal to $E_y = 2\,\text{V}\,\text{nm}^{-1}$ to obtain the HOLD state and $E_y = -2\,\text{V}\,\text{nm}^{-1}$ to replicate the RESET state. For both situations, we superpose a switching field as in the previous cases along the axis connecting *Dot 1* and *Dot 2*.

Fig. 2.11c shows the isopotential surface when the clock field reproduces the HOLD state for the three switching fields $E_x = 2\,\text{V}\,\text{nm}^{-1}$, $E_x = 0\,\text{V}\,\text{nm}^{-1}$, and $E_x = -2\,\text{V}\,\text{nm}^{-1}$. The charge on *Dot 3* doesn't change with the switching field that moves the charge between the two regions with the silicon atoms. The introduction of the third hexanedithiol does not affect the global behavior of the charge, as emerges from the VACT shown in Fig. 2.11e. *Dot 3* holds a constant charge equal to -0.4 a.u. and logic dots are involved in the charge localization when E_x is different from zero.

Similarly, Fig. 2.11d shows the isopotential surfaces when the clock field reproduces the RESET state for the three switching fields $E_x = 2\,\text{V}\,\text{nm}^{-1}$, $E_x = 0\,\text{V}\,\text{nm}^{-1}$, and $E_x = -2\,\text{V}\,\text{nm}^{-1}$. The ideal situation would be to have the charge localized on *Dot 3*, independently from the applied E_x along the switching direction. As evinced by the isopotential surfaces, this is not the case since the charge localizes on the trimethylsilane when the switching field is different from zero. Fig. 2.11f shows the

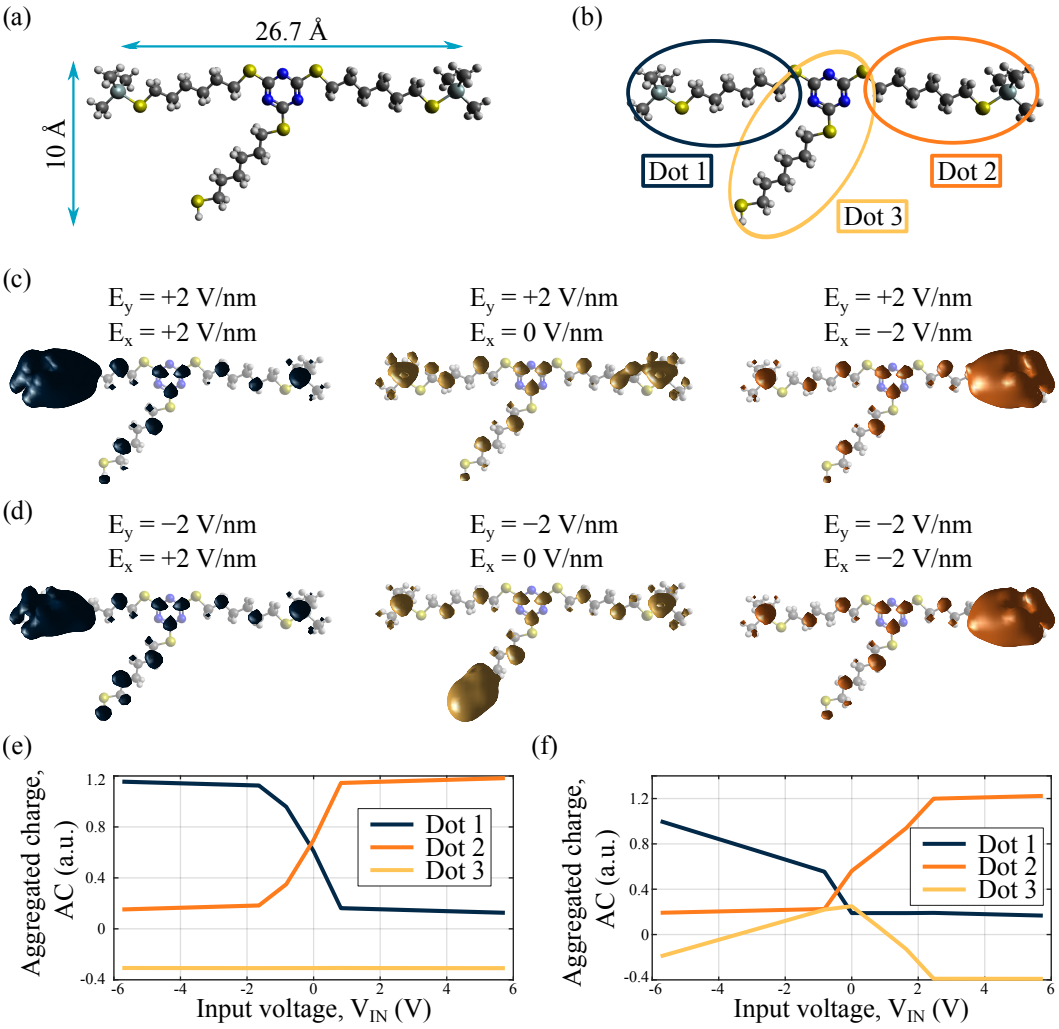

Fig. 2.11 Results of the DFT analysis on the oxidized trithiocyanuric acid linked tris(hexanedithiol) bis(trimethylsilane. (a) 3D geometry shown in a ball-and-stick diagram. (b) Atom groups for the calculation of the aggregated charges. (c) Isopotential surfaces when the clock field is $E_y = 2\,\mathrm{V\,nm^{-1}}$ for different electric field values in the switching direction, showing where the charge localizes. (d) Isopotential surfaces when the clock field is $E_y = -2\,\mathrm{V\,nm^{-1}}$ for different electric field values in the switching direction, showing where the charge localizes. (e) VACT of the molecule when the clock field is $E_y = 2\,\mathrm{V\,nm^{-1}}$, so in the HOLD state. (f) VACT of the molecule when the clock field is $E_y = -2\,\mathrm{V\,nm^{-1}}$, so in the RESET condition. Atoms in figure are colored as follows: H = white, C = charcoal, N = blue, S = yellow, Si = gray.

corresponding VACT, illustrating that the charge on *Dot 1* and *Dot 2* does switch, preventing the molecule from resetting the information. The differences observable between the case with positive and negative E_x derive from the lack of symmetry of

the molecule since the third hexanedithiol does not stand straight in the middle of the molecule.

The incremental theoretical results obtained on the presented case of study are promising for the electrostatic footprint shown and are an example of molecule engineering applied to molFCN. Further work, both theoretical and experimental, should address the method of providing a third dot able to hold the charge in the reset state while enabling surface attachment in ordered structures.

Chapter 3

Molecules electrostatics and environment

The analysis of the molecule in chapter 2 started to point out the centrality of intra-molecular interactions and the resulting electrostatic footprint in molecular Field-Coupled Nanocomputing (molFCN). The electrostatic footprint of molecules refers to the distribution and arrangement of electric charges within a molecular structure. Electrostatic interactions govern molecular behavior and thus play a pivotal role in determining how information propagates and can be manipulated.

Understanding how different charge distributions impact information treatment in molFCN is the first step to characterize intermolecular interactions between molecules. The ultimate goal is to reverse the process. Hence, starting from circuit requirements, design tailored molecules that accomplish the desired tasks [123].

Moreover, in this technology, circuits have traditionally utilized a single type of molecule, with logic functions achieved through tailored cell positioning. Integrating multiple types of molecules in the same layout augments circuit capabilities and introduces a fresh approach to conceptualizing molFCN. Specifically, by strategically incorporating different molecules with distinct electrostatic footprints into designated layout positions, it becomes feasible to emulate artificial neuron behavior using the Majority Voter (MV) layout [124].

The following sections consider three molecular species with different electrostatic behavior: neutral, oxidized, and zwitterionic. For each species, a reference geometry is fixed, and the electrostatic behavior is modeled by equation instead of

obtaining it by Density Functional Theory (DFT) simulations. The regularity of the molecular model enables the direct comparison of the effect of the pure electrostatic behavior in inter-molecular interactions. The fundamental cell-to-cell interactions are then analyzed, calculating the system energy for different charge configurations to obtain the energetically favored configurations. After that, we simulate a few elementary gates involving the fundamental interactions for all the considered molecular species. In this way, it is possible to detect the impact on logic computation of the electrostatic interaction of nearby molecules. The chapter continues with considering the electrostatic occupation of the whole device, which is a consequence of the crosstalk noise field. The last section discuss how it is possible to obtain a coplanar crossover interconnection exploiting a purely electrostatic solution.

3.1 Electrostatic molecular characteristics

Understanding the electrostatic characteristics of different molecular species is crucial for molFCN [125]. Researchers previously considered neutral, oxidized, and zwitterionic molecules as potential candidates.

Neutral molecules, lacking a net charge, constitute a significant portion of molecular species. Despite their lack of overall charge, neutral molecules exhibit intricate electrostatic characteristics arising from the distribution of electron densities within their structures.

Oxidized molecules are characterized by a positive charge resulting from the loss of electrons. The presence of a net positive charge imparts specific electrostatic behaviors to oxidized molecules, influencing their interaction with other molecules and their response to external stimuli. Oxidized molecules are the natural substitutes to realize a Quantum-dot Cellular Automata (QCA) cell. Indeed, a QCA cell is characterized by an excess of charge (electrons), as oxidized shows an excess of positive charge. Understanding the impact of the electrostatic profile of oxidized molecules in the fundamental interactions involved in molFCN is essential for understanding and designing circuits with tailored properties and functionalities.

It is known that circuits composed of oxidized molecules must be neutralized, for instance, with counterions or charged defects in the substrate, to prevent crosstalk effects [64]. Oxidized molecules with counterions behave similarly to zwitteri-

onic molecules regarding electrostatic properties, even if counterions disturb the electrostatic characteristics of intermolecular interactions [126, 127].

Zwitterionic molecules, featuring both positively and negatively charged functional groups within the same molecular structure, exhibit intriguing electrostatic characteristics. Despite the presence of localized charges, zwitterionic molecules maintain overall neutrality [128]. This unique electrostatic profile renders zwitterionic molecules versatile candidates, which have been intensely investigated in recent years [65, 66, 110, 126].

3.1.1 Reference structures and properties

To study the link between molecular electrostatics and information propagation or elaboration, we define a standard structure and conceptual characteristics for each molecule: neutral, oxidized, and zwitterionic. Working in terms of models allows for consistent observations with fewer geometry-dependent influences compared to using existent molecules.

Considering the typical dimensions of the proposed molecules, the conceptual molecule is 'V'-shaped, composed of three dots. Fig. 3.1a shows the relative position of the three dots. For the sake of simplicity, we placed *Dot 1* and *Dot 2* at 1 Å from each other. *Dot 3* is positioned 5 Å away from the plane containing logic dots and along the axis of their connecting segment. The quantitative analyses presented in the following sections rely on the specified geometry, although the conclusions drawn remain applicable even with potential variations in molecular size.

The curve describing the electrostatic behavior of neutral, oxidized, and zwitterionic molecules, is the VACT. VACTs describe the behavior of aggregated charges in the presence of an electric field and are typically obtained by analyzing DFT-derived ElectroStatic Potential (ESP) charges. Since we are referring to a conceptual molecule, we must assume a particular behavior for the three molecular species under investigation. Considering the analysis of other molecules from the literature ([62]) and those in chapter 2, we choose equation (3.1) as a reference curve shape for the Aggregated Charge (AC) on a dot in the hold state expressed in atomic units. Each AC is denoted as Q_i, where i represents the i*th* dot of the molecule. The value V_{in} is

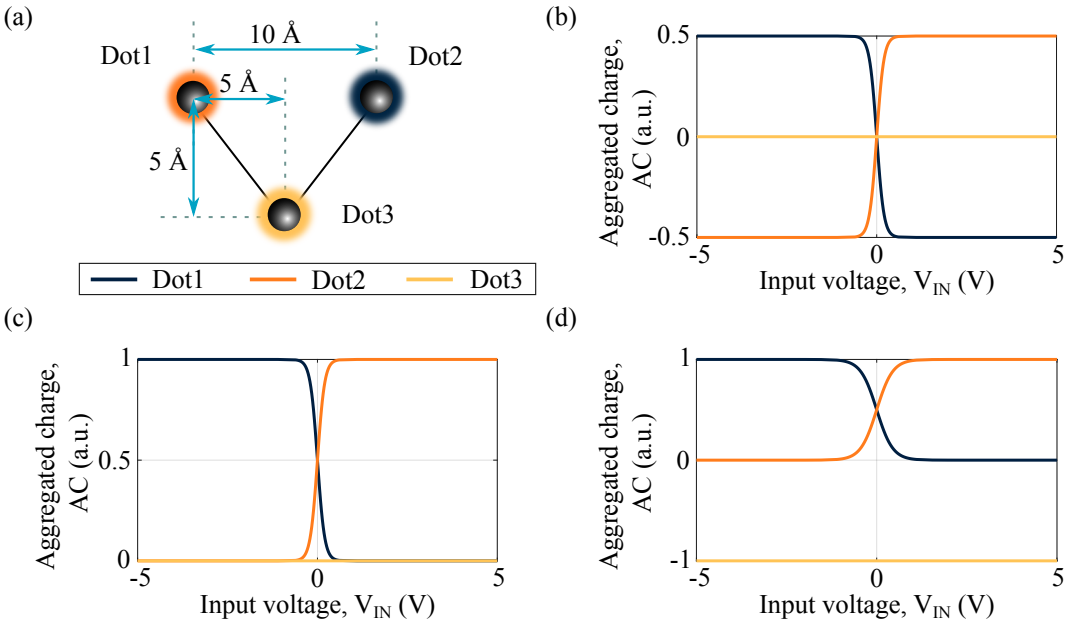

Fig. 3.1 Reference molecular structure and electrostatic properties of the conceptual molecules used to analyze the interactions. (a) Dot names and relative position. (b) V_{in}-AC transcharacteristic (VACT) defined for the neutral molecule in the hold state. (c) VACT defined for the oxidized molecule in the hold state. (d) VACT defined for the zwitterionic molecule in the hold state.

the input voltage expressed in volts.

$$Q_i = \frac{1}{1 + e^{10 \cdot V_{in}}} \tag{3.1}$$

Aiming to reduce the number of characters involved in the interactions, *Dot 3* always has a constant charge, and the value depends on the considered molecular species. Moreover, since we want to analyze the fundamental electrostatic interactions involved in propagation, we focus on the curves for the hold state, neglecting the reset condition.

Fig. 3.1b shows the VACT for the neutral molecule. The set of equations describing the AC is reported below in equation (3.2). The charge on *Dot 3* is chosen to be zero, so the charge on the logic dots is equal to the general curve shifted down by a

quantity equal to 0.5 a.u. to guarantee neutrality.

$$VACT_{ne} \rightarrow \begin{cases} Q_1 = \frac{1}{1+e^{10 \cdot V_{in}}} - 0.5 \\ Q_2 = \frac{1}{1+e^{-10 \cdot V_{in}}} - 0.5 \\ Q_3 = 0 \end{cases} \tag{3.2}$$

Fig. 3.1c shows the VACT for the oxidized molecule in the hold state. In this case, the total charge must be equal to 1 a.u. in all the points. Again, *Dot 3* does not hold any charge, and logic dots are the only ones involved in charge displacement. The equations describing the AC are reported below in equation (3.3).

$$VACT_{ox} \rightarrow \begin{cases} Q_1 = \frac{1}{1+e^{10 \cdot V_{in}}} \\ Q_2 = \frac{1}{1+e^{-10 \cdot V_{in}}} \\ Q_3 = 0 \end{cases} \tag{3.3}$$

Finally, Fig. 3.1d shows the VACT for the zwitterionic molecule in the hold state. As mentioned, they are neutral molecules presenting localized charge aggregation inside some functional groups. The behavior of zwitterionic molecules is thus in between those of neutral and oxidized species. We model its charge behavior as for oxidized molecules concerning the logic dots. However, this time *Dot 3* holds a negative charge equal to -1 a.u. to guarantee global charge neutrality and creates a vertical not-null dipole moment for $V_{in} = 0\,\mathrm{V}$.

$$VACT_{zw} \rightarrow \begin{cases} Q_1 = \frac{1}{1+e^{10 \cdot V_{in}}} \\ Q_2 = \frac{1}{1+e^{-10 \cdot V_{in}}} \\ Q_3 = -1 \end{cases} \tag{3.4}$$

Following the exploited model, the ideal oxidized molecules with an external counterion have the same electrostatic behavior as zwitterionic molecules.

The fundamental interactions between molecular cells in molFCN circuits are four and are represented in Fig. 3.2. The horizontal and vertical interactions are involved in information propagation and are the laying blocks of gates like the MV. Diagonal interactions are the central elements of inversion.

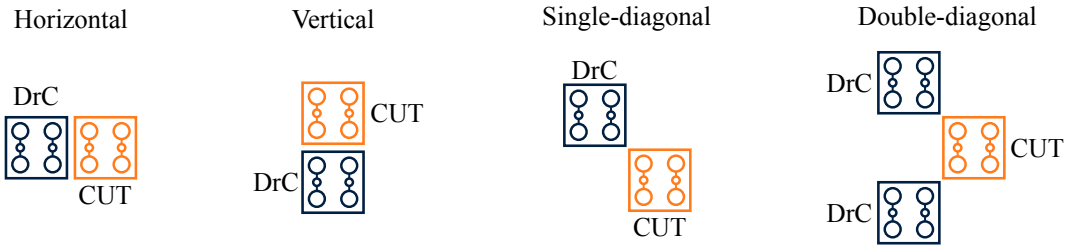

Fig. 3.2 Fundamental cell interaction involved in molFCN. The Driver Cell (DrC) is shown in blue, whereas the Cell Under Test (CUT) is shown in orange.

3.1.2 Molecule energy model

The electrostatic energy of a system of point charges refers to the potential energy associated with the arrangement of charged particles within the system. This energy arises from the electrostatic interactions between the charges, governed by Coulomb's law. Coulomb's law states that the force between two point charges is directly proportional to the product of their magnitudes and inversely proportional to the square of the distance between them. Mathematically, it is expressed as:

$$F = k \cdot \frac{q_1 q_2}{r^2} \tag{3.5}$$

where $k = 1/(4\pi\varepsilon_0)$ is the Coulomb's constant with ε_0 being the vacuum permittivity, q_1 and q_2 are the magnitudes of the charges, and r is the distance between the charges.

The electrostatic potential energy (U) of a system of point charges can be calculated from the work done to assemble the charges from infinity, where they exert no force on each other, to their final configuration. For a system of N point charges, the total electrostatic potential energy is the sum of the potential energies of all pairs of charges. Mathematically, it is expressed as

$$U = \sum_{i=1}^{N-1} \sum_{j=i+1}^{N} k \cdot \frac{q_i q_j}{r_{i,j}} \tag{3.6}$$

where k is the Coulomb's constant, q_i and q_j are the magnitudes of the charges, and $r_{i,j}$ is is the distance between the i^{th} and j^{th} charges

In the Molecular Simulator Quantum-dot cellular automata Torino (MoSQuiTo) methodology, molecules are properly replaced by a set of point charges with a charge equal to the AC. In a system composed of two molecules, like a molecular cell,

where the molecules are called *Mol a* and *Mol b*, the interaction energy is derived from equation (3.6), becoming:

$$W_{a,b} = \sum_{i \in a} \sum_{j \in b} k \cdot \frac{Q_i Q_j}{r_{i,j}} \tag{3.7}$$

where k is the Coulomb's constant, Q_i and Q_j are the values of the aggregated charges, and $r_{i,j}$ denotes the distance between the i^{th} of *Mol a* and the j^{th} of *Mol b* [129]. In a circuit composed of N molecules, the total energy is evaluated as:

$$W_{tot} = \sum_{i+1}^{N-1} \sum_{j=i+1}^{N} W_{i,j} \tag{3.8}$$

where $W_{i,j}$ is the interaction energy between the i^{th} and j^{th} molecules calculated as expressed in equation (3.7) [129].

Each molecule has a different set of AC and geometry, thus generating different interactions and energy. The analysis of the total energy of the system provides useful insight into the behavior the system has and can be used to predict the outcome.

In this section, we are interested in understanding the general implications of using different molecular species in the fundamental interactions depicted in Fig. 3.2. Except for the double-diagonal interaction system, the others are composed of two molecular cells (i.e., four molecules) named DrC and CUT. We can calculate their energy using equation (3.8), particularly when the cell encodes some logic values. Comparing the total energy of the system in different charge arrangements provides information regarding the minimum energy configurations that are expected to most likely appear.

We define W_{XY} as the total energy of the system when the DrC and the CUT encode logic values X and Y (i.e., '0' or '1'), respectively. Considering the cells as the unit elements, more in a QCA-like style, we need to remove the interaction between molecules of the same cells from the energy W_{XY}. In that case, the energy W_{XY} of the system becomes

$$W_{XY} = W_{tot} - W_{DrC}^{X} - W_{CUT}^{Y} \tag{3.9}$$

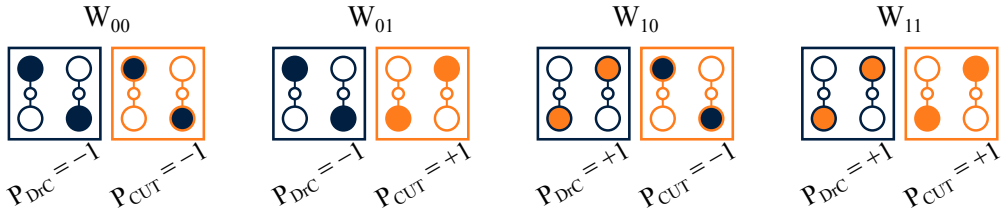

Fig. 3.3 Charge distribution in the cell for the four combinations of logic values in the horizontal interaction system.

where W_{tot} is the total energy of the whole DrC-CUT charge system, whereas W^X_{DrC} and W^Y_{CUT} are the electrostatic energies of the isolated DrC and CUT cells encoding logic values X and Y, respectively.

If we consider the cell as the unit element, thanks to the association between the logic value of a cell and its cell polarization defined in equation (1.3), we can refer W_{XY} to the DrC and CUT polarizations, P_{DrC} and P_{CUT}. Considering all the combinations of logic values for the two cells, we get:

- energy W_{00} when $P_{DrC} = -1$ and $P_{CUT} = -1$
- energy W_{01} when $P_{DrC} = -1$ and $P_{CUT} = +1$
- energy W_{10} when $P_{DrC} = +1$ and $P_{CUT} = -1$
- energy W_{11} when $P_{DrC} = +1$ and $P_{CUT} = +1$

Fig. 3.3 illustrates the charge distribution associated with the four cases in the system of DrC and CUT creating the horizontal interaction.

Another energy measurement value associated with the system energy is the so-called kink energy U_k [48]. Applied to the system of DrC and CUT we are considering, the kink energy measures the energy difference between the system with DrC and CUT encoding the same values (W_{00} or W_{11}) and the configuration encoding different logic values (W_{01} or W_{10}). The energy W_{XY} does not include the contribution of the interactions inside each single cell as expressed in equation (3.9), meaning that the U_k is a consequence of the interactions between separate cells only.

Referring the calculation to a specific DrC configuration, we obtain kink energies U_{k0} and U_{k1} according to the driver logic as:

$$U_{k0} = W_{00} - W_{01} \qquad U_{k1} = W_{11} - W_{10} \tag{3.10}$$

In the literature, the values U_{k0} and U_{k1} are always assumed to be equal, they are never distinguished. However, in a molecular system, a difference might exist between the two values in some cases, as shown in the following. It is possible to define also the kink error Δ as the difference between the kink energies for the two possible values of the DrC cell:

$$\Delta = U_{k0} - U_{k1} \tag{3.11}$$

The kink error is directly related to the functional behavior of the interaction, measuring the dependence of the interaction on the values encoded by the DrC. If the kink error is null, the interaction between DrC and CUT is identical for the logic states, so we have a symmetric interaction. Contrarily, a non-null value of Δ implies a non-symmetric interaction, so the DrC encoding a logic '0' or a logic '1' generates different outcomes.

The discussion until now has been carried out considering a system composed of two cells, the DrC and the CUT. All the considerations remain valid if we have two DrCs as in the double-diagonal interaction.

3.1.3 Energy analysis on the fundamental interactions

This section calculates the energy of the fundamental cell-to-cell interactions presented in Fig. 3.2 for the three molecular species we are discussing. The intermolecular distance d has been chosen to equal the molecular width $w = 1\,\text{nm}$.

Horizontal cell-to-cell interaction

Horizontal interaction is fundamental for propagation and elaboration. Two adjacent cells encode the same logic. Considering again the DrC and CUT system shown in Fig. 3.3, we expect that the minimum energy configurations are those with the CUT copying the information on DrC.

For all the molecular species, we evaluate the electrostatic energy of the system W_{XY} varying the value of the polarization of the two cells, spanning over the possible logic configurations W_{00}, W_{01}, W_{10}, and W_{11}. We expect the CUT to copy the information of the DrC. From an energy point of view, this is obtained if both the conditions expressed in equation (3.12) are satisfied. Table 3.1 lists the energy values

Table 3.1 Electrostatic energy values of the system obtained for the three molecular species in the case of horizontal cell-to-cell interaction.

Species	W_{00} eV	W_{01} eV	W_{10} eV	W_{11} eV	U_{k0} eV	U_{k1} eV	Δ
Neutral	−0.147	0.147	0.147	−0.147	−0.294	−0.294	0.000
Oxidized	2.913	3.208	3.208	2.913	−0.294	−0.294	0.000
Zwitterionic	0.099	0.394	0.394	0.099	−0.294	−0.294	0.000

obtained for the three species.

$$W_{11} < W_{10} \qquad W_{00} < W_{01} \tag{3.12}$$

If we use neutral molecules, the system energy is negative when both cells encode the same logic value, i.e., W_{00} and W_{11}. If cells have the wrong configuration, the energy of the system W_{XY} is positive, confirming that the minimum energy configurations exploit correct non-inverting propagation, as expressed in equation (3.12). Fig. 3.4a shows a map of the system energy evaluated for all the polarization values between −1 and 1, for both P_{DrC} and P_{CUT}. The two energy minima (black regions) are associated with the information being the same, whereas the inverting configurations correspond to the energy maxima (white regions).

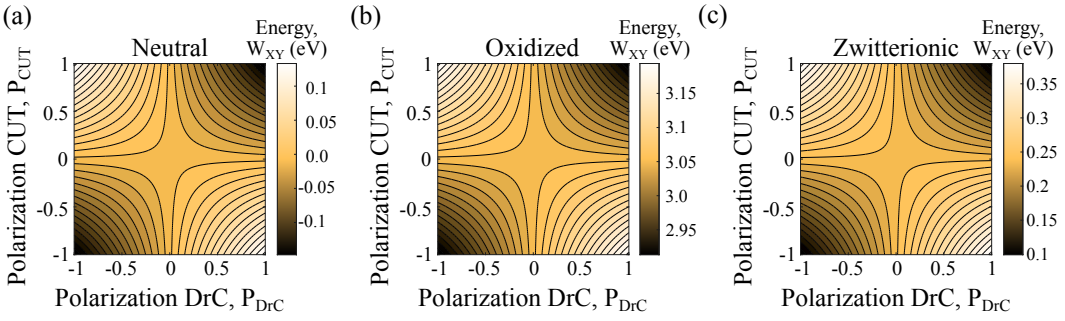

Fig. 3.4 Energy analysis for the horizontal cell-to-cell interaction for the different molecular species. (a) Energy of the two-cell system based on neutral molecules as a function of P_{DrC} and P_{CUT}. Each line represents a 0.01 eV energy increment. (b) Energy of the two-cell system based on oxidized molecules as a function of P_{DrC} and P_{CUT}. Each line represents a 0.01 eV energy increment. (c) Energy of the two-cell system based on zwitterionic molecules as a function of P_{DrC} and P_{CUT}. Each line represents a 0.01 eV energy increment.

The inequalities expressed in equation (3.12) also hold for oxidized and zwitterionic molecules. The positive charges in oxidized molecules induce purely repulsive interactions, resulting in positive energy values. In Fig. 3.4b, the energy map shows

for oxidized molecules the same trend obtained for neutral molecules, apart from the energy values, which are all positive. Conversely, Fig. 3.4c shows the energy map for the zwitterionic species, where values are again all positive. However, counterions mitigate the effects of oxidized molecules, leading to reduced energies.

Besides the different energy values, the behavior of the interaction is the same for all the species and independent from the logic encoded by the driver cell. We evaluate the kink energy according to equation (3.10) to confirm this observation. As reported in Table 3.1, the two kink energies are the same for the three species, leading to null kink errors Δ.

The logic encoded by the DrC does not affect the interaction for all molecular species. The adjacent horizontal cell-to-cell interaction is independent of the driver.

Vertical cell-to-cell interaction

Vertical interaction is fundamental for information propagation and is also present in gates such as the MV. In this case, the DrC and the CUT are vertically aligned, as Fig. 3.2 shows. Theoretically, in the QCA paradigm, there is no difference between this interaction and the horizontal adjacent one, given that the four logic dots are equally spaced and centered in the cell. For this reason, the energy analysis would give the same result obtained in the previous section.

However, two different situations happen by analyzing the field distribution in the horizontal and vertical interactions. Fig. 3.5 shows the two systems, highlighting the direction of the switching field on the CUT cell. If the DrC has only positive charges involved in the logic, as for oxidized molecules, then the generated radial field directly affects the adjacent CUT. As depicted in Fig. 3.5, the radial field is orthogonal to the switching field, which is unaffected, as the previous section demonstrated. Things change in the vertical interaction since, in this case, the two fields overlap, leading to possible unwanted charge configurations on the CUT. In the molecular implementation of QCA, the two molecules comprising the CUT are independent, contrarily to the general paradigm that permits only antipodal charge configurations. Hence, for a thorough interaction analysis, it is crucial to eliminate the assumption that the molecular cell only possesses diagonal charge distributions.

To highlight the difference with the horizontal interaction, we calculate the total energy of the two-cell system aligned vertically, with the DrC having a fixed logic

Fig. 3.5 Comparison between the direction of the switching field and the field generated by the DrC in adjacent horizontal and vertical cell-to-cell interaction.

value. Once the logic on the driver is fixed, we independently vary the charge distribution on the two molecules composing the CUT. Fig. 3.6a shows the case with $P_{DrC} = -1$ and the four limit configurations obtained by removing the constraint of having only antipodal charges. To identify the position of the charge in CUT, we use the normalized dipole moments $\widetilde{\mu_1}$ for molecule *Mol1* on the left of the cell and $\widetilde{\mu_2}$ for molecule *Mol2* on the right of the cell. Since vertical interaction should copy information from the DrC to the CUT, the minimum energy configuration must occur when $\widetilde{\mu_1} = +1$ and $\widetilde{\mu_2} = -1$ if $P_{DrC} = -1$.

At this point, we calculate the energy of the two-cell system linearly varying the dipole moment between -1 and 1. Fig. 3.6b shows the energy map for the system implemented with neutral molecules. From the map emerges a minimum value for $\widetilde{\mu_1} = +1$ and $\widetilde{\mu_2} = -1$, thus respecting the condition for correct propagation. The total energy in the four limit configurations is also reported in Table 3.2. In this case, since both positive and negative charge aggregation are involved, the DrC field does not affect the switching field as much as to prevent correct propagation.

Fig. 3.6c shows the energy map for the system realized with oxidized molecules. The global minimum occurs for the condition with $\widetilde{\mu_1} = \widetilde{\mu_2} = +1$. That configuration corresponds to the charge aggregations being as far as possible from the DrC. The cause is to be found in the globally positive charge of oxidized molecules, generating the maximum influence of the DrC field over CUT.

Fig. 3.6d shows the energy map obtained for zwitterionic molecules. The logic dot behavior of zwitterionic molecules is the same as oxidized molecules, but they possess a negative counterion balancing the total charge of the molecule. The neutralization due to the presence of the counterion mitigates the impact of the DrC field, bringing the system back to the correct functioning, as the energy minimum coincides with $\widetilde{\mu_1} = +1$ and $\widetilde{\mu_2} = -1$.

Table 3.2 Electrostatic energy values of the system obtained for the three molecular species in vertical cell-to-cell interaction with a fixed DrC polarization. The subscript numbers refer to the normalized dipole moment of the two molecules composing the CUT. The values in parentheses are the energy without considering the electrostatic contribution of charges within the same molecule.

	Species	$W_{-1,1}$ eV	$W_{1,1}$ eV	$W_{-1,-1}$ eV	$W_{1,-1}$ eV
$P_{DrC} = -1$	Neutral	-1.715	-1.440	-1.440	-2.009
	Oxidized	5.244	4.757	6.280	4.950
	Zwitterionic	-7.538	-7.435	-7.092	-7.833
$P_{DrC} = +1$	Neutral	-2.009	-1.440	-1.440	-1.715
	Oxidized	4.950	4.757	6.280	5.244
	Zwitterionic	-7.833	-7.435	-7.092	-7.538

By repeating the analysts fixing $P_{DrC} = +1$ as shown in Fig. 3.6e, the results are perfectly opposite since the only thing changing is a mirroring of the charge distribution of the DrC cell. Fig. 3.6f,g,h show the energy map obtained varying the normalized dipole moments for neutral, oxidized, and zwitterionic molecules.

As the energy analysis demonstrates, vertical interaction is sensitive to the specific molecular species used to implement the system, which must be considered in simulations.

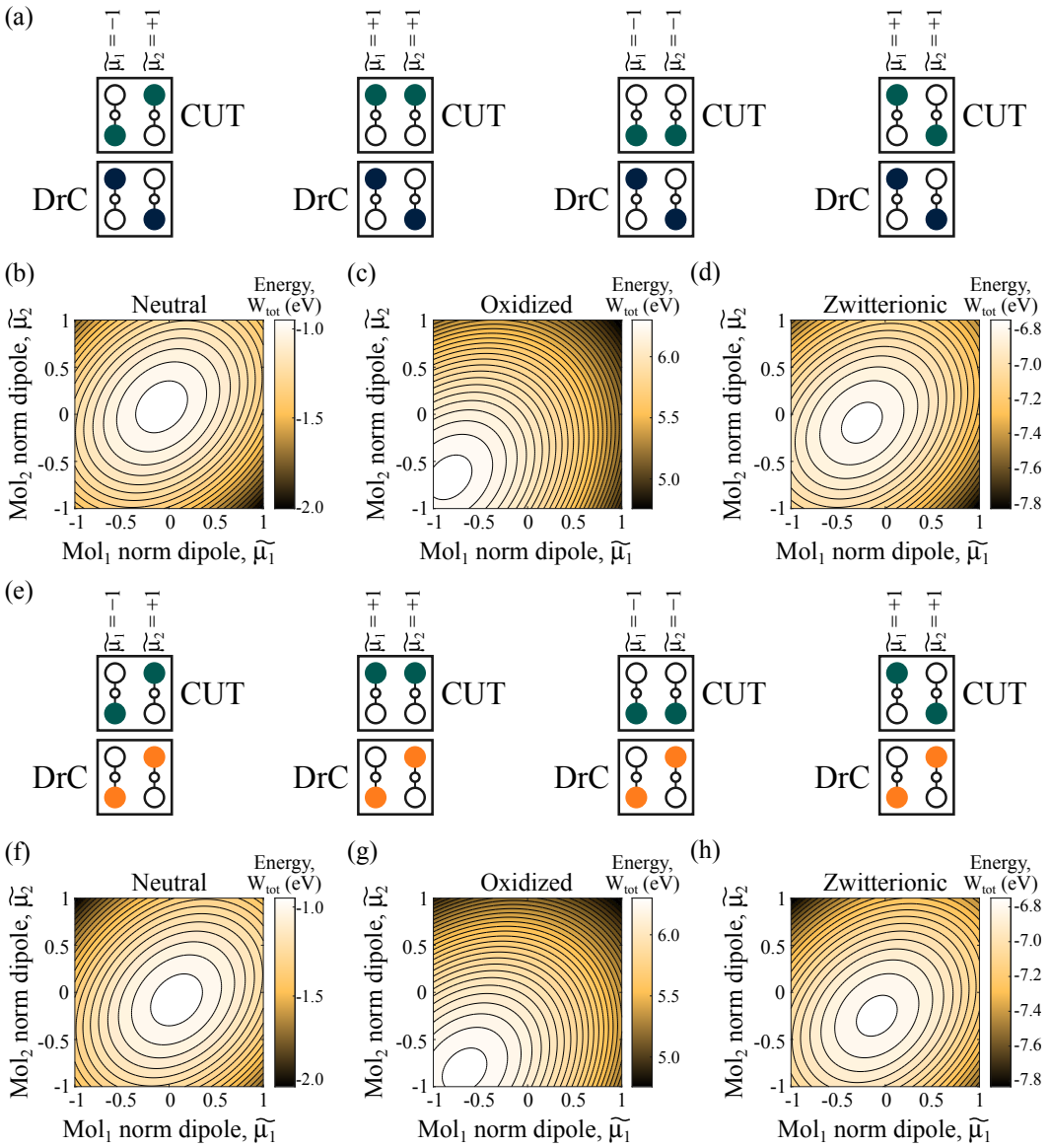

Fig. 3.6 Energy analysis for the vertical adjacent cell-to-cell interaction for the different molecular species. (a) The four limit configurations of the system when $P_{DrC} = -1$, showing the normalized dipole moments of the CUT molecules. (b) Energy of the two-cell system when $P_{DrC} = -1$ based on neutral molecules. Each line represents a 0.05 eV energy increment. (c) Energy of the two-cell system when $P_{DrC} = -1$ based on oxidized molecules. Each line represents a 0.05 eV energy increment. (d) Energy of the two-cell system when $P_{DrC} = -1$ based on zwitterionic molecules. Each line represents a 0.05 eV energy increment. (e) The four limit configurations of the system when $P_{DrC} == 1$, showing the normalized dipole moments of the CUT molecules. (f) Energy of the two-cell system when $P_{DrC} = +1$ based on neutral molecules. Each line represents a 0.05 eV energy increment. (g) Energy of the two-cell system when $P_{DrC} = +1$ based on oxidized molecules. Each line represents a 0.05 eV energy increment. (h) Energy of the two-cell system when $P_{DrC} = +1$ based on zwitterionic molecules. Each line represents a 0.05 eV energy increment.

Single-diagonal cell-to-cell interaction

Alongside adjacent interaction to copy information, diagonal interaction is fundamental for the inverting operation. Typical QCA layouts exploit only two cells arranged diagonally to invert information.

Fig. 3.7a illustrates the cell displacement and four limit charge configurations obtained by combining the two logic values. The theoretical expected behavior for the general QCA paradigm is that CUT encodes the opposite value of the DrC because of the interaction of the dots nearest to the touching angle. This behavior is obtained when both conditions expressed in equation (3.13) are satisfied.

$$W_{11} > W_{10} \qquad W_{00} > W_{01} \tag{3.13}$$

We calculate the total energy of the system W_{XY} linearly varying the DrC and CUT polarizations for all the considered species. Table 3.3 lists the energy values obtained for the three species for clarity. Using neutral molecules, the energy of the system is negative when both cells encode opposite logic values, i.e., W_{01} and W_{10}. If cells have the wrong configuration, the system energy W_{XY} is positive, confirming that the minimum energy configurations are those exploiting correct inverting propagation, as expressed in equation (3.13). Fig. 3.7b shows a map of the system energy evaluated for all the polarization values between -1 and 1, for both P_{DrC} and P_{CUT}. The two energy minima (black regions) are associated with opposite information, whereas the inverting configurations correspond to the energy maxima (white regions). From the values listed in Table 3.3 for neutral molecules, we notice that the system is symmetric from an electrostatic energy point of view ($W_{01} = W_{10} = -W_{11} = -W_{00}$). The symmetry of the values gives equal kink energies ($U_{k0} = U_{k1}$), meaning that the energy is independent of the input logic, which corresponds to a null kink error ($\Delta_n e = 0$). The diagonal interaction with neutral molecules is symmetric and makes possible the inversion operation with a single-branch inverter.

Fig. 3.7c shows the energy map calculated for the two-cell system implemented with oxidized molecules. The map shows only one global minimum, corresponding to the configuration in which $P_{DrC} = P_{CUT} = +1$. If the DrC encodes instead a logic zero ($P_{DrC} = -1$), the minimum energy configuration for CUT is again the one encoding a logic '1'. This behavior implies that the output of the device doesn't change by changing the input. From the values listed in Table 3.3 emerges an

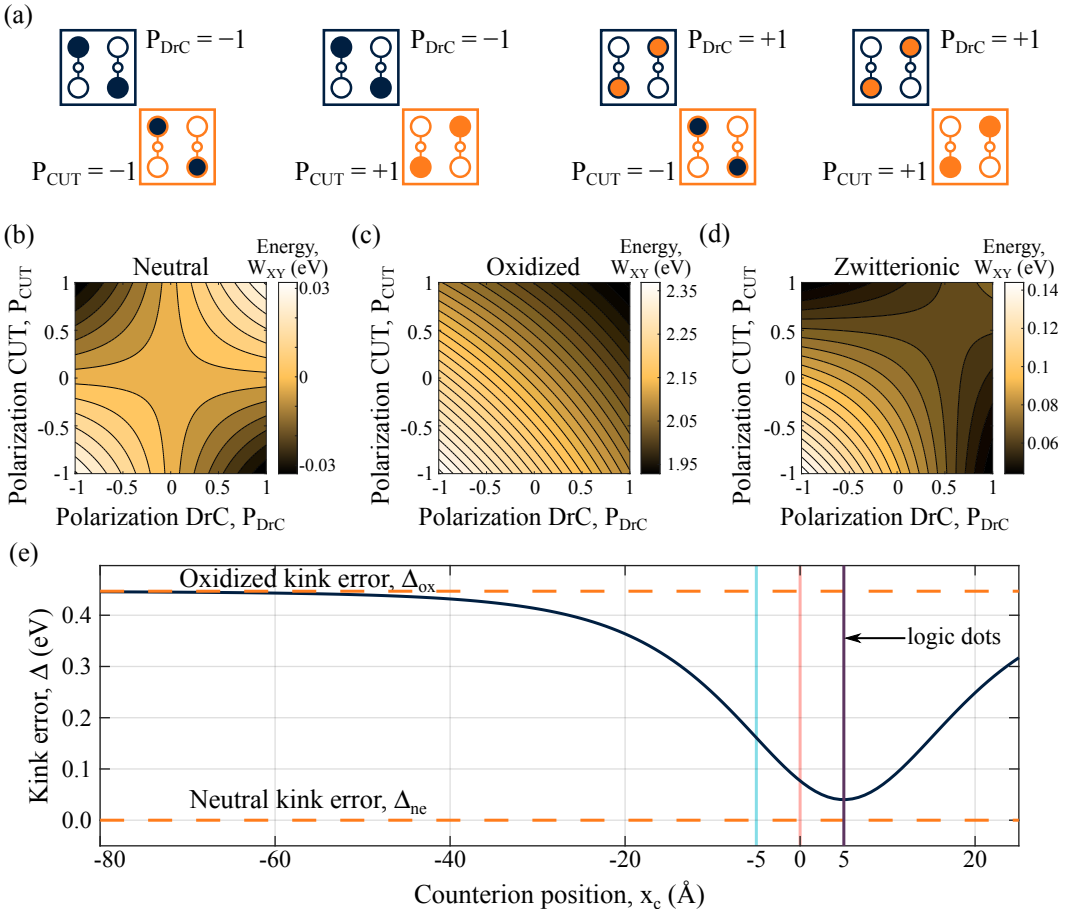

Fig. 3.7 Energy analysis for the single-diagonal cell-to-cell interaction for the different molecular species. (a) Charge distribution in the cell for the four combinations of logic values. (b) Energy of the two-cell system based on neutral molecules as a function of P_{DrC} and P_{CUT}. Each line represents a 0.005 eV energy increment. (c) Energy of the two-cell system based on oxidized molecules as a function of P_{DrC} and P_{CUT}. Each line represents a 0.015 eV energy increment. (d) Energy of the two-cell system based on zwitterionic molecules as a function of P_{DrC} and P_{CUT}. Each line represents a 0.005 eV energy increment. (e) Kink Error (Δ_{zw}) associated with the system composed of zwitterionic molecules as a function of the counterion distance from logic dots.

asymmetry of the electrostatic behavior, as $|W_{01}| \neq |W_{10}| \neq |W_{11}| \neq |W_{00}|$. In this case, the kink energies differ, and that's the reason why we must distinguish the kink energy for input encoding different logic values. When the system single-diagonal two-cell system is implemented with oxidized molecules, the interaction depends on the logic encoded by DrC, as confirmed by the non-null kink error $\Delta_{ox} = 0.477\,\text{eV}$.

As we already said, zwitterionic molecules have an electrostatic behavior between neutral and oxidized molecules. This statement is confirmed by the energy map

Table 3.3 Electrostatic energy values of the system obtained for the three molecular species in the case of single-diagonal cell-to-cell interaction.

Species	W_{00} eV	W_{01} eV	W_{10} eV	W_{11} eV	U_{k0} eV	U_{k1} eV	Δ
Neutral	0.033	−0.033	−0.033	0.033	0.066	0.066	0.000
Oxidized	2.376	2.087	2.087	1.929	0.289	−0.158	0.447
Zwitterionic	0.148	0.044	0.044	0.071	0.104	0.027	0.077

shown in Fig. 3.7d, where two equivalent minima for the inverting conditions, thus satisfying equation (3.13). The two correctly positioned minima indicate that the interaction correctly inverts the information. However, electrostatic asymmetry is still present for the maxima in the device, yet the counterion is mitigating the effect of the localized positive charges, indeed $\Delta_{zw} < \Delta_{ox}$. The counterion is the key element that balances the electrostatic behavior, making the single-diagonal interaction work with zwitterionic molecules. For this reason, we analyze the value of the kink error Δ_{zw} varying the position of the counterion in the molecule (x_c). Fig. 3.7e shows the obtained curve. For all the values of x_c, the kink error stays in between the constant kink errors obtained for neutral and oxidized molecules, confirming the assumption of intermediate behavior. In the referenced system used, logic dots lay on the plane $x = 5\,\text{Å}$, and in the simulation shown in Fig. 3.7d, the counterion position was $x_c = 0\,\text{Å}$. If the counterion is far from the logic dots plane, the Δ_{zw} increases since the neutralizing electric field generated by the counterion reduces with the distance. The minimum kink error is indeed obtained when the counterion is placed on the same plane of logic dots ($x_c = 5\,\text{Å}$), right in the middle of *Dot 1* and *Dot 2*. The analysis illustrates that single-diagonal inversion works only for well-engineered zwitterionic molecules, and again is fundamental to consider the specific electrostatic behavior to predict the outcome correctly.

Double-diagonal cell-to-cell interaction

The single-diagonal interaction is effective as logic inversion only for neutral and well-designed zwitterionic molecules. The interaction is non-symmetric for other species from an electrostatic point of view. The double-diagonal interaction helps to make the interaction electrostatically symmetric, favoring the success of the inversion and its stability.

Table 3.4 Electrostatic energy values of the system obtained for the three molecular species in the case of double-diagonal cell-to-cell interaction.

Species	W_{00} eV	W_{01} eV	W_{10} eV	W_{11} eV	U_{k0} eV	U_{k1} eV	Δ
Neutral	0.061	−0.070	−0.070	0.061	0.131	0.131	0.000
Oxidized	5.762	5.631	5.631	5.762	0.131	0.131	0.000
Zwitterionic	0.240	0.109	0.109	0.240	0.131	0.131	0.000

Fig. 3.8a shows the system in the four possible logic combinations. For the sake of simplicity, we force the polarization on the two DrCs to be the same. Then, by linearly varying P_{DrC} and P_{CUT} from '-1' to '+1', we calculate the system energy. Fig. 3.8b-d show the energy of the system when implemented with neutral, oxidized, and zwitterionic molecules, respectively. The three energy maps show the same profile, even if values are different for each species, that is, two minima located on the inverting values, satisfying the conditions expressed in equation (3.13). The energy values listed in Table 3.4 confirm that the system is symmetric from an energy standpoint for each species. The kink energy values U_{k0} and U_{k1} are equal, and the kink error is null for all the species, meaning that the behavior is independent of the input logic.

3.2 Electrostatics role in fundamental gates

The electrostatic analysis performed so far gives information regarding fundamental interactions and the behavior we can expect from devices that include those interactions. The simulation of circuits must consider the specific electrostatic footprint of the molecules used for the implementation since we demonstrated it impacts the final behavior of the system.

Currently, two tools are used to simulate molFCN circuits: Self-Consistent ElectRostatic Potential Algorithm (SCERPA) and QCADesigner. The SCERPA algorithm treats each molecule as an electronic device with its primary state variable being the aggregated charge Q_i, determined by the molecule's input voltage V_{in}. The input voltage for each molecule is determined by integrating the electric field produced by neighboring molecules along a path linking the two logic points. Consequently, the SCERPA algorithm iteratively assesses molecule input voltages and employs the

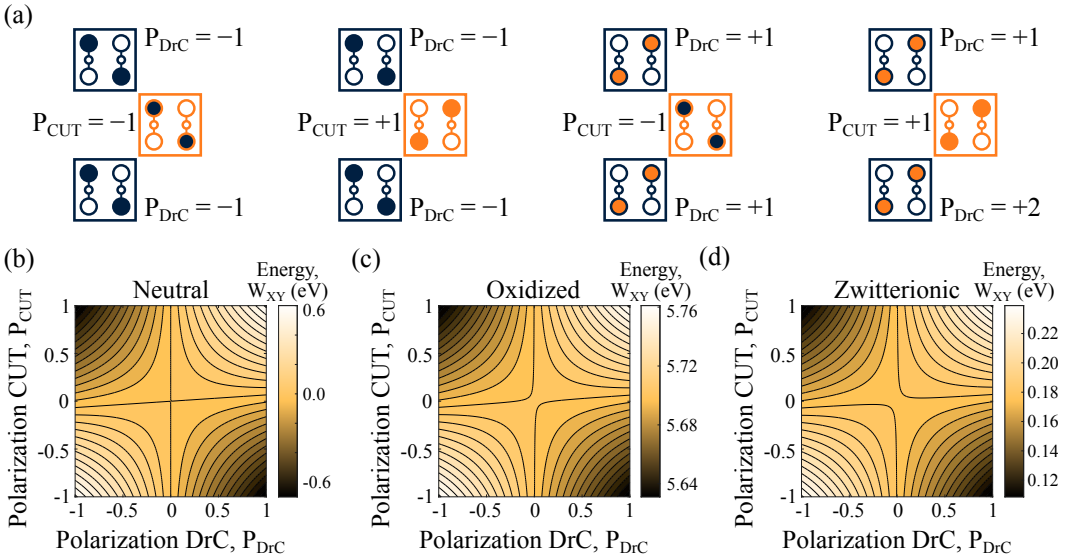

Fig. 3.8 Energy analysis for the double-diagonal cell-to-cell interaction for the different molecular species. (a) Charge distribution in the cell for the four combinations of logic values. (b) Energy of the system based on neutral molecules as a function of P_{DrC} and P_{CUT}. Each line represents a 0.005 eV energy increment. (c) Energy of the system based on oxidized molecules as a function of P_{DrC} and P_{CUT}. Each line represents a 0.005 eV energy increment. (d) Energy of the system based on zwitterionic molecules as a function of P_{DrC} and P_{CUT}. Each line represents a 0.005 eV energy increment.

VACT to compute the molecular charge [63, 64]. Since SCERPA uses the molecule VACT, it is implicit that it considers the electrostatics of the molecules.

QCADesigner is widely used in the literature to simulate QCA devices [59, 60]. This tool is intended for the general QCA paradigm and not specifically for molecular implementation. The QCADesigner tool mainly bases its calculations on kink energy, which is assumed to be input-independent. Thus it can correctly predict the behavior of circuits implemented with a few molecule types [125]. Since the energy analysis demonstrated that the kink energy, in some cases, depends on the encoded input, we perform the simulations using the SCERPA tool [130].[1]

The following sections examine the SCERPA simulations of a few elementary gates to relate the molecular physics underlying fundamental interaction to the logical behavior of a circuit. This procedure underscores the significance of incorporating the effective behavior of molecules in simulation tools.

[1]The tool is available online on GitHub at the following link https://github.com/vlsi-nanocomputing/SCERPA/tree/v4.0.1

All the circuits use an intermolecular distance of 1 nm and *Dot 3* of the zwitterionic molecule is fixed 5 Å far from the plane containing active dots, unless otherly specified.

3.2.1 Majority voter

The MV is a fundamental gate for designing logic since it provides AND and OR logic functions, as described in chapter 1. Fig. 3.9 shows the layout used for the electrostatic analysis, with the names of the three inputs and the output. All the cells belong to the same clock region. Since all the input branches have the same length, and the molecular with is equal to the intermolecular distance, the three input signals impact the output in the same way, so it does not need to be clocked independently to have a meaningful simulation.

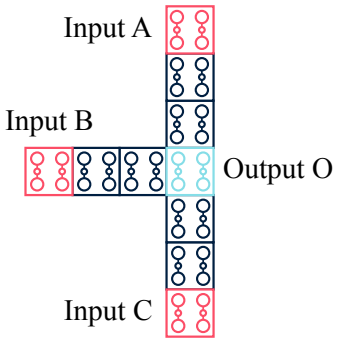

Fig. 3.9 Layout of the majority voter used for the electrostatic analysis and input/output definition. All the cells belong to the same clock region.

The MV exploits horizontal and vertical cell-to-cell interactions. The energy analyses on the two interactions suggest that the device should correctly work when implemented with neutral molecules. Fig. 3.10a shows, for the MV implemented with neutral molecules, the electrostatic potential evaluated with SCERPA on the plane 0.2 nm above the logic dot plane. White spots indicate aggregation of positive charges, whereas black dots are associated with negative charge aggregation. The figure shows all the possible eight input combinations, and the output is always correct, following the truth table commented in section 1.1.1.

Fig. 3.10b shows the results obtained with SCERPA for the gate implemented with oxidized molecules. The energy analysis shows that the vertical interaction is problematic since the charge on the CUT tends to maximize the distance from

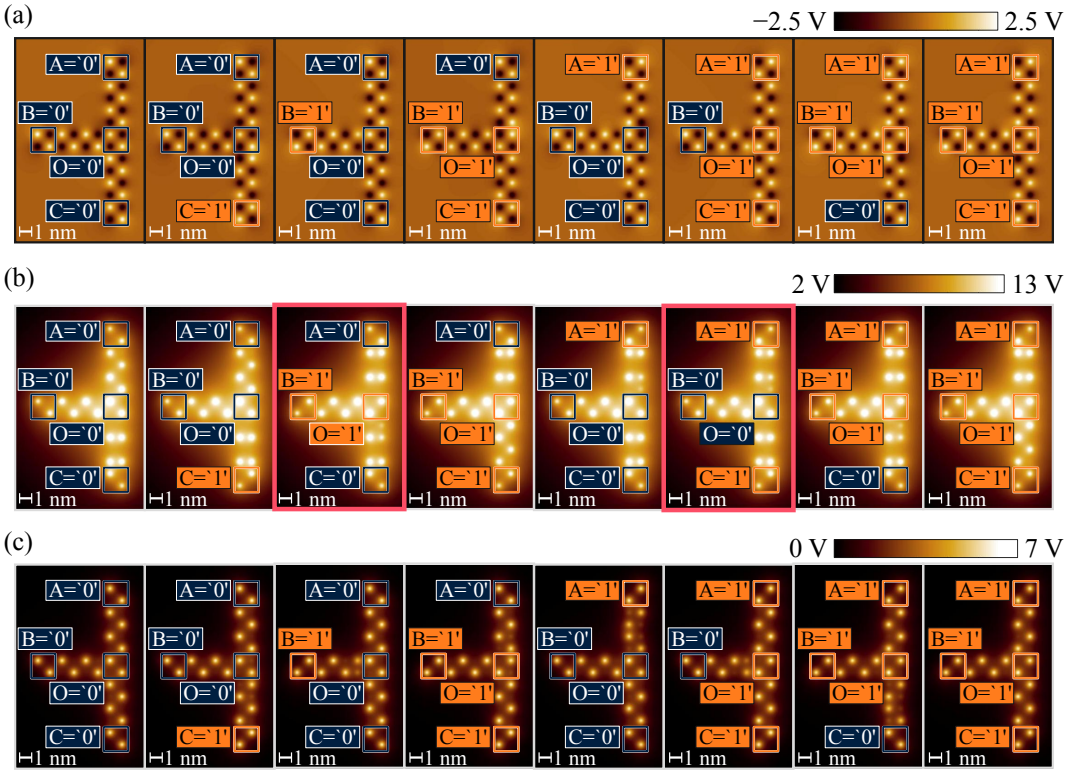

Fig. 3.10 Electrostatic potential obtained by the SCERPA simulation of a MV. The electrostatic potential is evaluated 0.2 nm above the logic dot plane, and the spots indicate the AC. (a) Simulation of the eight input combinations for a MV implemented with neutral molecules. (b) Simulation of the eight input combinations for a MV implemented with oxidized molecules. (c) Simulation of the eight input combinations for a MV implemented with zwitterionic molecules whose counterion position is $x_c = -5$ Å.

the DrC. As seen from the electrostatic potential distribution of the possible input combination, the same effect is found on the branches of *Input A* and *Input C*. In some cases, the incorrect information encoding on input branches does not affect the output correctness, like for the combinations $ABC =$ '000' and $ABC =$ '001'. However, the outcome is incorrect in the two cases in which the output should match the information encoded on both the top and bottom inputs. These two cases, corresponding to combinations $ABC =$ '010' and $ABC =$ '101', are bounded in red in Fig. 3.10b. In both situations, the branch of *Input B* dominates the output cell, forcing the incorrect value.

In the case of a MV implemented with zwitterionic molecules, the electrostatic potential of the eight input combinations is shown in Fig. 3.10c. The simulation is performed using zwitterionic molecules with the counterion placed at $x_c = -5$ Å,

that is, 10 Å away from the logic dot plane. In the previous section, we demonstrate that the behavior of the zwitterionic molecules is in between those of neutral and oxidized, depending on the position of the counterion. In the simulated case, the counterion is not very close to the logic dot plane, but still, the behavior is correct for all the input combinations. The only disturbing effect can be noted for the combinations $ABC = \text{`}010'$, $ABC = \text{`}100'$, $ABC = \text{`}101'$, and $ABC = \text{`}110'$, where the output cell polarization back-influence the input branch encoding the opposite information. This effect is typically known as *back-propagation*.

3.2.2 Single-branch inverter

The single-branch inverter, whose layout is shown in Fig. 3.11a, has been used in general QCA to invert information. The same layout is often used for molFCN, disregarding the effective functioning of the gate. Since the key interaction in this gate is single-diagonal, we can expect the device to work for neutral molecules and well-engineered zwitterionic molecules.

Fig. 3.11b shows the electrostatic potential evaluated 0.2 nm above the logic dot plane for the simulation of the device implemented with neutral molecules. With both input logic values, information is elaborated correctly, being helped by the fact that one logic dot has a positive charge and a negative charge on the other. The variation of the sign of the charge between logic dots favors, in the same way, the opposite value on the cells near the diagonal. Indeed, focusing on the two nearest dots to the diagonal, we have on the top line a positive (negative) charge aggregation corresponding to a white (black) spot, attracting a negative (positive) charge on the bottom line indicated with a black (white) spot.

Only repulsive forces are involved when the device is implemented with oxidized molecules, so the expected charge configuration is quite different. Fig. 3.11c shows the electrostatic potential evaluated from the SCERPA simulation. The two input combinations produce different situations. When the input is $A = \text{`}0'$, the polarization on the output cell is correct. Focusing on the molecules nearest to the diagonal, the molecule on the top branch should theoretically have a positive charge aggregation on *Dot 2*, pushing the cells to invert the charge configuration, producing a correct outcome. Nevertheless, the cells on the bottom line are positively charged, which back-influences the molecules on the top line. This interaction results in the charge

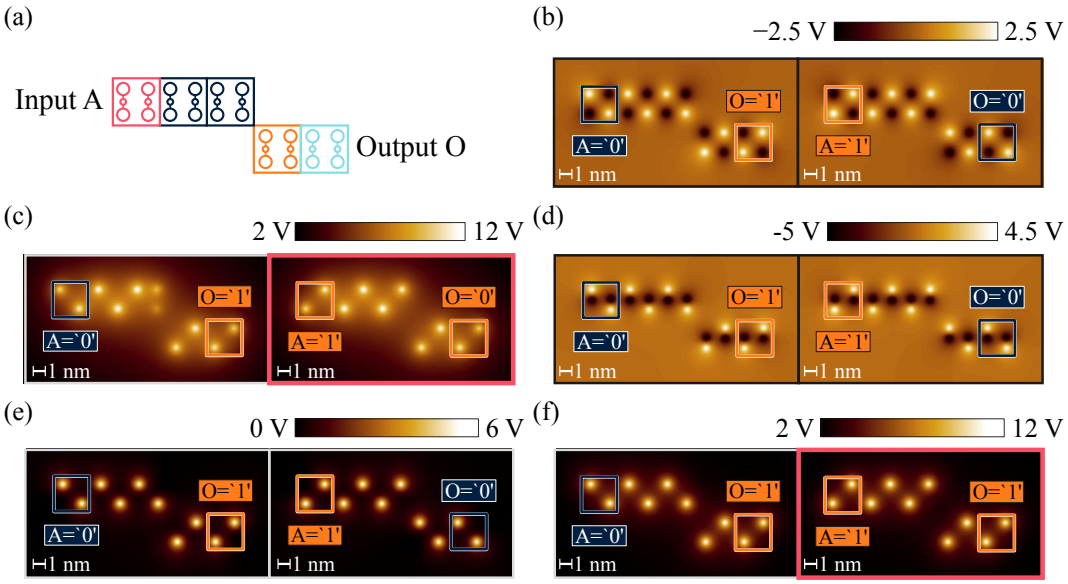

Fig. 3.11 Results obtained by the SCERPA simulation of a single-branch inverter. The electrostatic potential is evaluated 0.2 nm above the logic dot plane, and the spots indicate the AC. (a) Layout of the single-branch inverter used for the electrostatic analysis and input/output definition. The blue cells and input belong to the same clock region, whereas the orange cell and output belong to another. (b) Simulation of the two input combinations for the gate implemented with neutral molecules. (c) Simulation of the two input combinations for the gate implemented with oxidized molecules. (d) Simulation of the two input combinations for the gate implemented with zwitterionic molecules whose counterion position is $x_c = 5$ Å. (e) Simulation of the two input combinations for the gate implemented with zwitterionic molecules whose counterion position is $x_c = 0$ Å. (f) Simulation of the two input combinations for the gate implemented with zwitterionic molecules whose counterion position is $x_c = -5$ Å.

equally distributed on both dots for the last molecule of the top line. Contrarily, the only involved positive charges prevent the device from working when the input is $A =$ '1'. In this case, the output still encodes a logic zero because the output configuration globally maximizes the distance of the charges nearest to the diagonal.

Implementation with zwitterionic molecules behaves in the middle of neutral and oxidized versions, and the outcome strictly depends on the position of the counterion that neutralizes the molecules. For this reason, we simulated the single-branch inverter using three different counterion positions, that are $x_c = 5$ Å, $x_c = 0$ Å, and $x_c = -5$ Å. For the reference system that we are using, these positions correspond to a counterion/logic dots distance of 0 Å, 5 Å, and 1 nm, respectively. The three values give different kink error values for the single-diagonal interaction and are

highlighted with three different colored lines in Fig. 3.7e. The expectation is that the closer the counterion to logic dots, the stronger the neutralization effect that helps the correct inversion.

Fig. 3.11d shows the electrostatic potential obtained with SCERPA when $x_c = 5$ Å. The presence of the counterion is clearly visible as a black spot between the logic dots. With this implementation, the device works perfectly for both input values, as the negative counterion helps pull the positive charge on *Dot 1* of the first molecule of the bottom line. Fig. 3.11e shows the electrostatic potential obtained with SCERPA when $x_c = 0$ Å. In this situation, the counterion is no longer visible from the plane where the potential is calculated, but its effect is still visible since the information is correctly inverted. Finally, Fig. 3.11f shows the result obtained when the counterion is 1 nm far from logic dots. The increased distance is reflected in the increased potential values measured 0.2 nm above the logic dot plane, which resembles that obtained for oxidized molecules. In this case, the presence of the counterion is insufficient to balance the electrostatic force generated by the positively charged logic dots, so the output is always $O =$ '1', independently from the logic encoded on the input cell.

3.2.3 Double-branch inverter

The single-branch inverter derived by the general QCA paradigm does not always work for molecular implementation and depends on the specific electrostatic of the molecule used. The problem has been addressed in the literature introducing the double-branch inverter layout, reported in Fig. 3.12. The double-branch inverter exploits two branches for the inversion, so the laying interaction is double-diagonal, which the energy analysis proved independent from the molecular species.

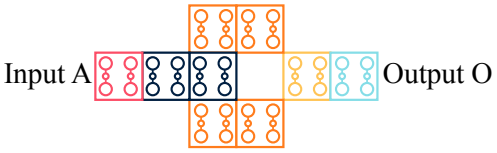

Fig. 3.12 Layout of the double-branch inverter used for the electrostatic analysis and input/output definition. Blue, orange, and yellow cells belong to different clock regions. Input and output cells belong to the same clock region of the nearest cell.

For a system made of neutral molecules, the single-branch inverter was enough to invert the information, so the outcome is correct even in the over-dimensioned double-branch inverter. Fig. 3.13a shows the electrostatic potential obtained with the SCERPA simulation for both input values.

According to the energy analysis, the system should work when the system is implemented with oxidized molecules. However, from the electrostatic potential map shown in Fig. 3.13b, we see that the gate is not inverting for both inputs. The cause is the repulsion that the molecules in the middle line induce on the top and bottom lines since the system is not globally neutral. Anyway, it is possible to simulate only the system of cells involved in the double-diagonal interaction to validate the principle. The system is analyzed in Fig. 3.8. In the simulation, the polarization of the two driver cells is fixed, so only the CUT can vary its polarization. Under this condition, Fig. 3.13c shows the electrostatic potential obtained with SCERPA for the three-cell system. Since the output cell is the only one that can vary, the simulation is coherent with the expectation derived from the energy analysis done in the previous section.

Finally, Fig. 3.13d shows the electrostatic potential for the system implemented with neutral molecules when $x_c = -5\,\text{Å}$, that is the case making the molecule sufficiently similar to oxidized species. With this counterion position, the single-

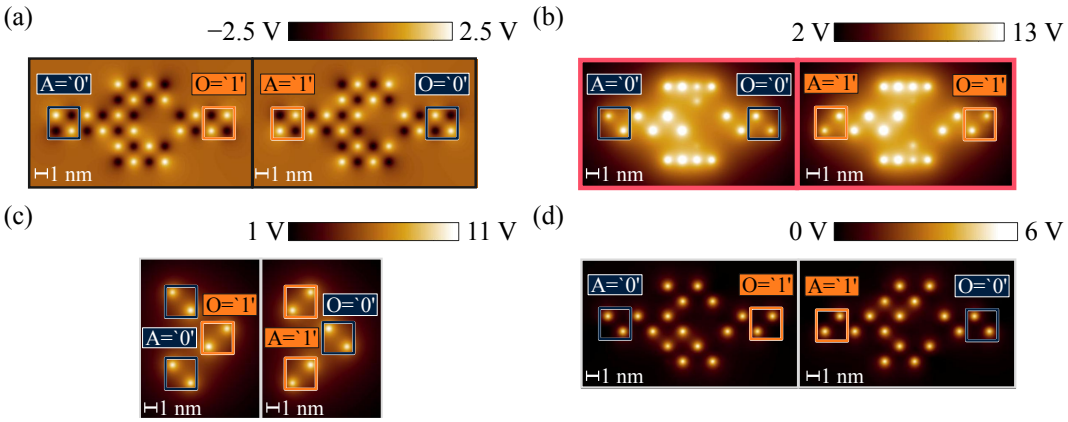

Fig. 3.13 Electrostatic potential obtained by the SCERPA simulation of a double-branch inverter. The electrostatic potential is evaluated 0.2 nm above the logic dot plane, and the spots indicate the AC. (a) Simulation of the two input combinations for the gate implemented with neutral molecules. (b) Simulation of the two input combinations for the gate implemented with oxidized molecules. (c) Simulation of the double-diagonal interaction implemented with oxidized molecules. (d) Simulation of the two input combinations for the gate implemented with zwitterionic molecules whose counterion position is $x_c = -5\,\text{Å}$.

branch inverter did not work correctly, but in this case, the symmetry given by the layout geometry is helping the system invert the information. As predicted by the energy analysis, the double-branch inverter is insensible to the molecular species used since the electrostatic symmetry is reached through the geometrical symmetry of the layout.

3.2.4 Three-way splitter (fanout circuit)

An interesting device to analyze involving only horizontal and vertical interactions is the three-way splitter, generally called *fanout circuit*, shown in Fig. 3.14. This device has a structure similar to the MV but has one input and three outputs, meaning that the liberty of the electrostatic interaction changes, especially on the top and bottom outputs.

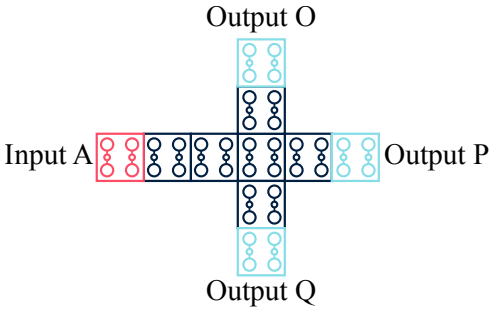

Fig. 3.14 Layout of the three-way splitter (also known as fanout circuit) used for the electrostatic analysis and input/output definition. All cells belong to the same clock region.

Even in this case, we simulated the device with SCERPA considering the various molecular species. Fig. 3.15a shows the electrostatic potential map for the device implemented with neutral molecules. For both inputs, the information is correctly replicated on the three outputs, as could have been expected from the energy analysis. On the other hand, when the device is implemented with oxidized molecules, only the central output P propagates. Fig. 3.15b shows the electrostatic potential evaluated 0.2 nm above the logic dots plane, and the behavior is analogous to the one of the MV and the double-branch inverter. Indeed, the charge of the molecules of the line corresponding to outputs O and Q maximizes the distance from the center, producing an undefined logic value, having the two molecules with concordant dipole moments.

For zwitterionic molecules, we again expect a behavior between the two just presented, depending on the position of the counterion. Fig. 3.15c shows the case

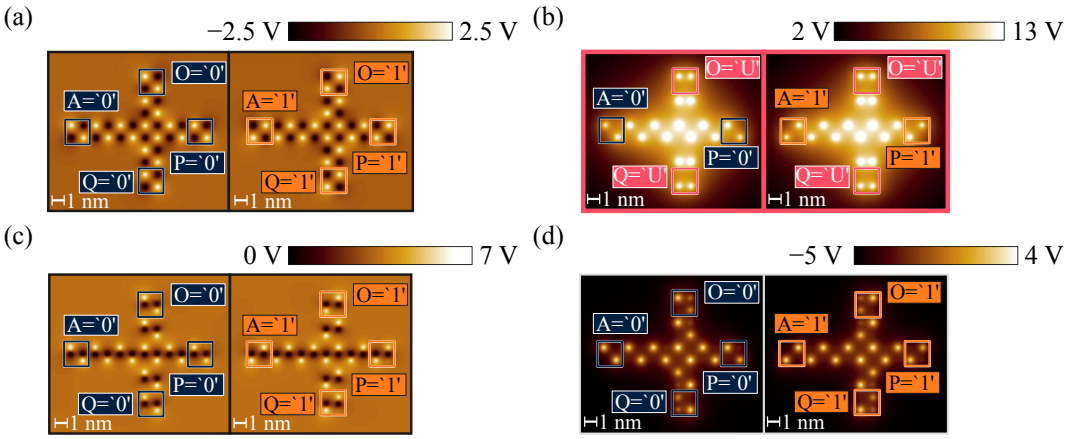

Fig. 3.15 Electrostatic potential obtained by the SCERPA simulation of a three-way splitter. The electrostatic potential is evaluated 0.2 nm above the logic dot plane, and the spots indicate the AC. (a) Simulation of the two input combinations for the gate implemented with neutral molecules. (b) Simulation of the two input combinations for the gate implemented with oxidized molecules. (c) Simulation of the two input combinations for the gate implemented with zwitterionic molecules whose counterion position is $x_c = 5\,\text{Å}$. (d) Simulation of the two input combinations for the gate implemented with zwitterionic molecules whose counterion position is $x_c = -5\,\text{Å}$.

more similar to neutral molecules with the counterion in the same plane of logic dots ($x_c = 5\,\text{Å}$). As for neutral molecules, the polarization of all the cells on the output lines encodes the correct information independently of the logic input. The situation with the fanout circuit implemented with zwitterionic molecules with $x_c = -5\,\text{Å}$ shown in Fig. 3.15d is different. The behavior in this case resembles more the one of oxidized molecules that, for instance, prevent the correct functioning of the single-branch inverter. In this case, the circuit works, but the disturbance of the central line is still visible. The information encoded on outputs O and Q is far from a perfect diagonal ideal configuration. The analysis reveals that the output cells display a notable charge distribution across three out of the four logic dots within the molecular cell. This observation suggests that one of the molecules may not be fully polarized. Furthermore, these border effects vary depending on the input logic value and directly result from the vertical interactions exerted within the system.

3.3 Crosstalk effect

The situation occurring with oxidized molecules in the devices shown before is the consequence of the so-called *crosstalk field*, which affects the device internally [64]. The crosstalk field can influence undesired parts of the considered circuit or nearby devices. As demonstrated in the previous section, in the context of intra-device crosstalk, the electrostatic properties of individual molecules play a pivotal role.

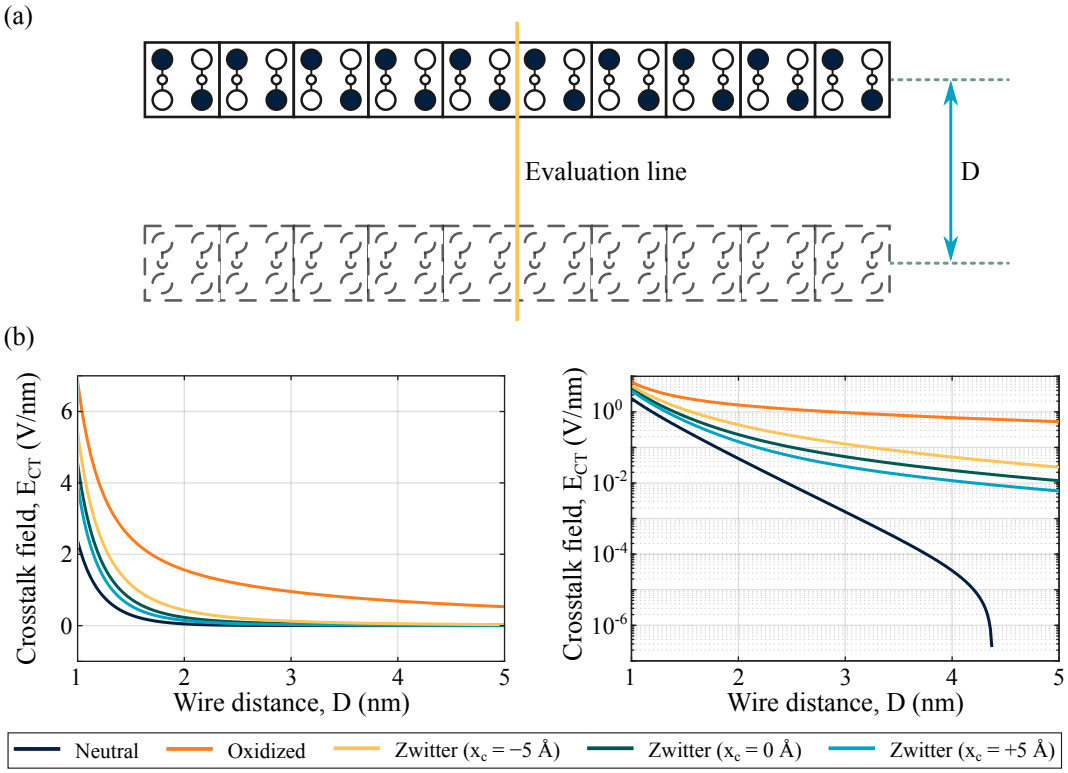

Fig. 3.16 Analysis of crosstalk field E_{CT}. (a) The setup employed for crosstalk analysis highlighting the evaluation line orthogonal to a fully-polarized molecular wire on which E_{CT} is computed. The position of a hypothetical molecular wire is at a distance D measured center-to-center. (b) A comparison of the generated crosstalk field based on the distance D, utilizing various molecular species. The graphs on the right represent the same quantities on a logarithmic scale to appreciate the different behaviors.

This section delves into assessing the impact of the crosstalk field between devices using a fully polarized molecular wire. Fig. 3.16a introduces the setup used to evaluate this field, which occurs at the midpoint of a 20-molecule wire (evaluation line) at the logic dots plane. Subsequently, this calculated field interacts with a hypothetical wire positioned at a distance D, potentially influencing the polarization

of the wire molecules. Fig. 3.16b illustrates the electric field E_{CT} generated by a molecular wire along the orthogonal axis for the various molecular species.

As Fig. 3.16b depicts, oxidized molecules yield a higher crosstalk field E_{CT}, which aligns with expectations considering that an oxidized molecule wire lacks neutrality. Consequently, adhering to Gauss's law, it generates a non-zero field that diminishes with distance. For instance, considering the double-branch inverter described before, the center-to-center distance between the top and bottom lines is $D = 2\,\text{nm}$. According to Fig. 3.16b, the crosstalk field generated by the polarized wire implemented with oxidized molecules is $E_{CT} = 1.562\,\text{V}\,\text{nm}^{-1}$, that generates a noise input voltage comparable to those typically found in molFCN devices, thus justifying the incorrect behavior.

On the contrary, when it comes to neutral species, the absence of a positive/negative net charge significantly reduces the electric field generated by the wire, rendering neutral molecules the optimal choice for mitigating crosstalk.

In the case of zwitterionic molecules, the positioning of the counterion assumes paramount importance. While zwitterionic species maintain overall neutrality, the field E_{CT} is notably reduced compared to the oxidized case. Fig. 3.16b further illustrates the crosstalk field generated by zwitterionic species across three possible counterion positions. Notably, when the counterion is aligned with the logic-dot level ($x_c = 5\,\text{Å}$), the proximity between the positive charge of the logic dots and the counterion's negative charge minimizes the generated net electric field. Conversely, altering the distance between the logical dots and the counterion, as seen in cases $x_c = 0\,\text{Å}$ and $x_c = -5\,\text{Å}$, amplifies the net electric field at the logic dots level, thereby resembling the behavior observed in oxidized species.

As molecule dimensions define the molecular safe-operating area and intermolecular distance defines the technological safe-operating area, the electrostatic occupation of molecules and devices defines the Device Safe-Operating Area (DSOA). The DSOA measures the electrostatic occupation of a gate, delimiting the region where it is not safe to place another device. The main factor influencing it is the crosstalk field, and we have already seen that not respecting it induces an error in the device and nearby gates.

3.4 Design of a coplanar cross-wire interconnection

Unlike other Field-Coupled Nanocomputing (FCN) implementations, up to now, a prototype or a clear technological direction for fabrication is missing, as discussed in Chapter 1. Considering the few current fabrication concepts, molFCN is considered an in-plane technology. Hence, it is impossible to exploit the vertical direction for signal routing or 3D-stacked systems. This comes with the consequence that signal routing must be performed in the same plane as logic functions. If we imagine a realistic system made of several interconnected gates, it is reasonable to expect that routing would require significant space on the circuit.

The QCA paradigm has proposed two solutions for coplanar signal crossing. The first solution involves one of the two lines having 45°-rotated cells [131]. Fig. 3.17a illustrates the charge distribution for the four possible input combinations. However, this solution has proven to be delicate due to the assumption that horizontal and vertical wires do not interact strongly. From an electrostatic standpoint, this holds true within a minimal range and a slight asymmetry in the system can favor one line over the other [131]. The second issue with this solution is associated with the technological requirement of precisely rotating a few molecules. This necessitates the ability to control the lattice orientation within a small region of a few nanometers so that molecules can self-assemble at different angles.

The second solution proposed for general QCA exploits the diagonal interaction [132]. The system is represented in Fig. 3.17b for the four possible combinations. We must distinguish two situations to understand the behavior. First, if the inputs encode the same logic values, then the central computing cell and the output will all copy the same logic value. If the two inputs encode opposite logic values, the central computing cell is subjected to equal and opposite fields. In an ideal system, the opposite influence leads the central cell not to assume any logic value. Hence, the charge is equally distributed among the four logic dots. If the central computing cell does not assume a logic polarization, the dominating interactions are the two single-diagonals composed of the input and the nearest output cells. Hence, information crossing is performed through a couple of contemporary single-branch inverters in this case.

The second solution is based on two assumptions. First, the system must be perfectly symmetric from an electrostatic point of view rather than geometrically.

Secondly, the single-branch inverter must work correctly. The analysis performed in chapter 3 on the fundamental interactions demonstrated that the two assumptions are guaranteed for neutral molecules and well-engineered zwitterionic molecules.

The following sections discuss various implementations of the coplanar crossover, considering the precise physics of molecules to forecast the functionality of the interconnection [133]. Moreover, we modify the electrostatic characteristics of the involved molecules to assess the resilience of the cross-wire against static electrostatic variations, thereby offering valuable insights for the tailored synthesis of molecules for molFCN applications.

3.4.1 Coplanar crossover simulation

The device behavior depends on the molecule used to implement it, so we analyze it using neutral and zwitterionic molecules, considering the same VACT used in chapter 3 and reported in equation (3.2) and equation (3.4).

We first consider neutral molecules, and the reference structure of the analyzed crosswise is shown in Fig. 3.18. By simulating it with SCERPA, we obtain a correct

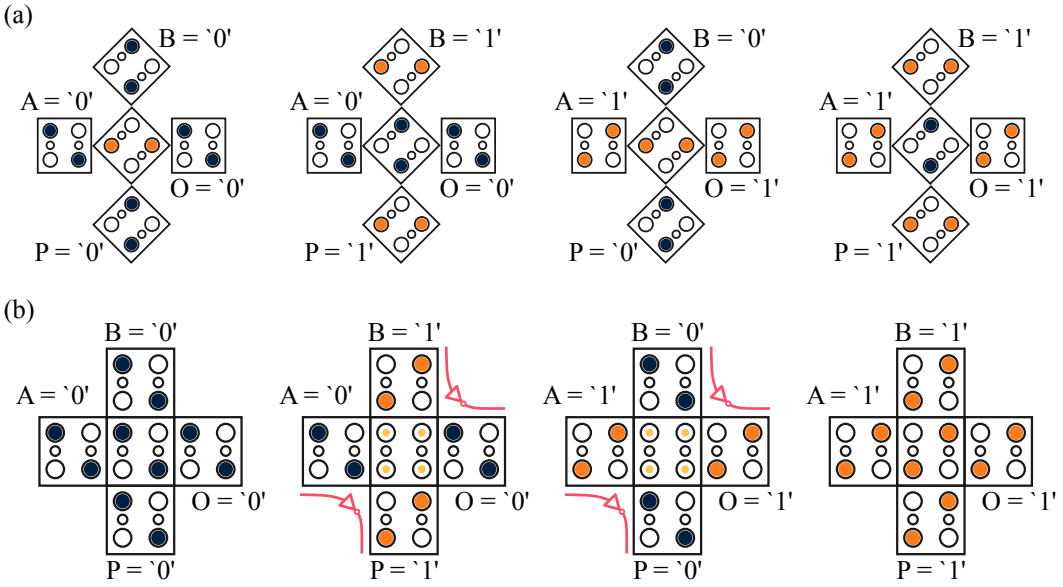

Fig. 3.17 Solutions for coplanar information crossing in the QCA paradigm. (a) Charge configuration for the four possible input combinations in the crossover implemented with rotated cells. (b) Charge configuration for the four possible input combinations in the crossover exploiting diagonal interaction.

propagation of the two logic inputs only if the output wires are in the same clock region of the intersecting computing cell. In Fig. 3.18, the clock zones are identified with different cell colors, so the cells on the input lines are blue-colored. In contrast, the intersecting cell and the cells propagating toward the outputs are orange-colored. For the described layout, Fig. 3.19 shows the electrostatic potential evaluated 0.2 Å above the logic dot plane in the final step of the four input combinations. From the simulations emerges that information is correctly cross-propagated in all cases.

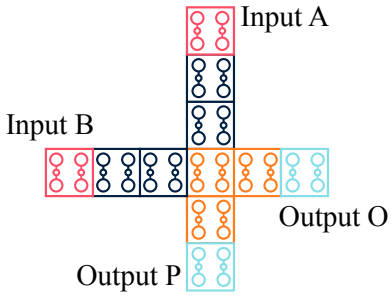

Fig. 3.18 Layout of the coplanar crossover used for the simulation in SCERPA. Blue and orange cells belong to different clock regions. Input and output cells belong to the same clock region of the nearest cell.

From the theoretical behavior, we expect the central cell not to encode any logic value if $A \neq B$. However, from the simulation of those two cases, it is noticeable that the central shared cell retains a particular logic value despite achieving the correct final configurations. This phenomenon remains consistent with the anticipated behavior. Initially, as the clock field initiates the switching process in the output cells, the central cell remains void of encoded information. Consequently, the output branches adhere to the inverting interaction originating from the diagonals. However, towards the end of the propagation, the input voltages on the central molecules cease to be null, resulting in the central cell adopting a logic value as well.

If we want to understand how sensitive the device functioning is to electrostatic variations, we have to modify the VACT. Electrostatic variations can map different molecules themselves or eventual noise affecting the electrostatic behavior of a molecule. Indeed, if some random noise affects the charge distribution on a molecule, we would have a different charge profile for the same input voltage, which is like having a different VACT. Changing the VACT of all the molecules in the circuit is a simplification since noise should be random on the molecules rather than constant. Still, the analysis provides valuable information regarding the device resilience to minor static electrostatic variations.

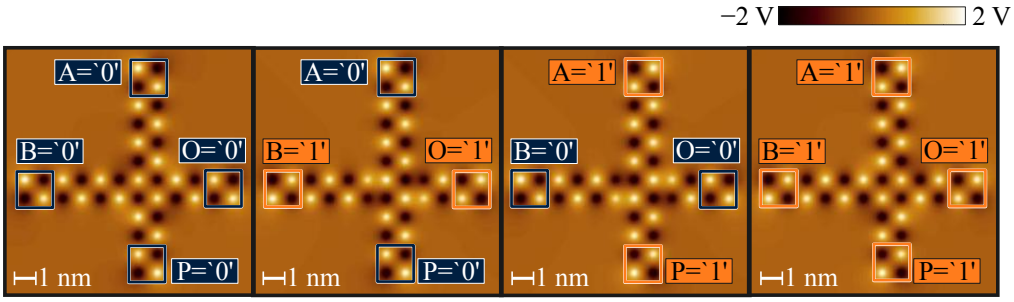

Fig. 3.19 Simulation using SCERPA of a crosswire interconnection utilizing neutral molecules: the four images depict the electrostatic potential for the four input combinations at the final propagation step, evaluated 0.2 nm above the logic dot plane.

The variations we apply are rigid horizontal shifts of the neutral VACT and variations of the steepness. To implement those modifications, we can rewrite the starting equation (3.1) for the charge and write it in a general form, that is:

$$Q_i = \frac{1}{1 + e^{w \cdot (V_{in} + s)}} \tag{3.14}$$

where w acts on the curve steepness and s acts on the rigid shift of the crossing point between AC_{Dot1} and AC_{Dot2}.

Varying the values of w and s, we can obtain the working range for the implementation using neutral molecules. Fixing the value of the weight $w + 10\,\mathrm{V}^{-1}$, the range of allowed shifts to continue having a working interconnection is

$$-30\,\mathrm{mV} \leq s \leq 30\,\mathrm{mV} \tag{3.15}$$

Fig. 3.20a illustrates the shift range on the VACT acceptable to maintain a functional interconnection. If the rigid shift exceeds $|\pm 30\,\mathrm{mV}|$, at least one configuration propagates an incorrect logic value. This result implies that the charge difference at equilibrium ($V_{in} = 0\,\mathrm{V}$) between *Dot 1* and *Dot 2* must be less than $\Delta AC_{MAX} = 0.15\,\mathrm{a.u.}$ when $w = 10\,\mathrm{V}^{-1}$.

Similarly, we can fix the shift $s = 0\,\mathrm{V}$ and vary the steepness of the slope, which is described by w. The working range for the crossover implemented with neutral molecules is $w \in [9; 12]\,\mathrm{V}^{-1}$. Fig. 3.20b illustrates the VACT obtained for the two boundary values $w = 9\,\mathrm{V}^{-1}$ and $w = 12\,\mathrm{V}^{-1}$. Besides the neutral molecule being the best-behaving and the device correctly working, small electrostatic variations could generate errors in the propagation.

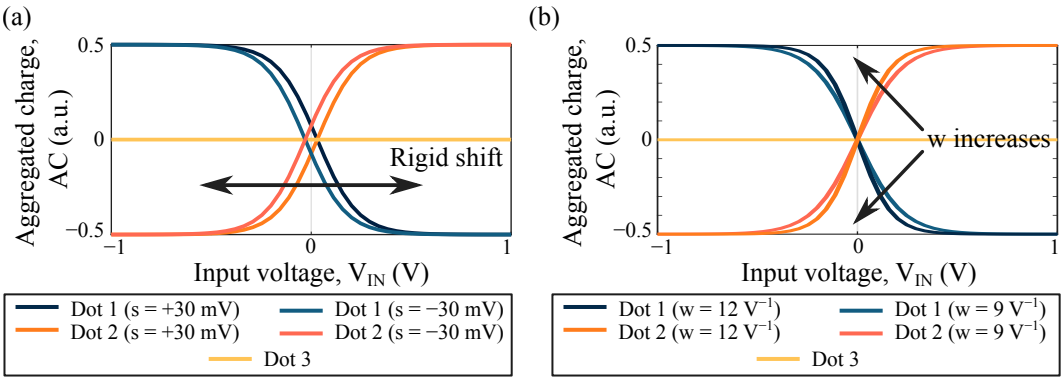

Fig. 3.20 Ranges of VACT variations to maintain functionality in the crosswire interconnection implemented with neutral molecules. (a) Application of rigid shifts to the VACT, with maximum allowable shifts of ±30 mV. (b) Alteration of the slope of the VACT, where w in equation (3.2) can vary within the interval $[9; 12]\,V^{-1}$.

Recently, the literature has demonstrated how single-line devices can be susceptible to weak charge separation in some cases [64]. For instance, the device is susceptible if the molecule used has a bistable factor near one. Hence, information is hardly bistable when there are no other molecules after the output.

Multi-line devices have been proposed to address this problem and strengthen information stability. In the case of a crossover implemented using diagonal interaction, one assumption is null charge separation on the molecule composing the intersecting cell. The need for a weak charge separation for the crosswire could contrast with the need to strengthen the information elsewhere by employing two-line devices. Consequently, we investigate the behavior of a crossover device implemented following the multi-line approach. Fig. 3.21 depict the proposed layout.

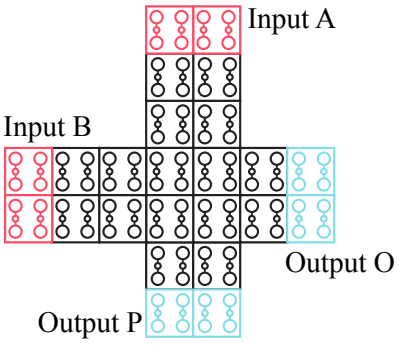

Fig. 3.21 Layout of the multi-line coplanar crossover used for the simulation in SCERPA.

It comes up that the crossing mechanism fails to operate effectively for the multi-line layout implemented with neutral molecules, with any clock distribution. Specifically, in scenarios where A and B differ, the presence of multiple molecules in the central region leads to mutual influence among them. Consequently, these molecules encode distinct logic values, thereby hindering the proper functioning of the interconnection. This underscores the complexity introduced by the collective behavior of molecules in this system, posing challenges to its smooth operation across varied conditions.

In previous sections, zwitterionic molecules showed various behaviors, more or less similar to neutral or oxidized molecules, depending on the counterion position. In this case, the single-line crossover does not work with the considered VACT, independently from the clock field distribution or the counterion position. Fig. 3.22 shows the result of the SCERPA simulation when the crosswire is implemented with zwitterionic molecules whose third dot is on the same plane of logic dots ($x_c = 5\,\text{Å}$). Even if we demonstrated that this configuration is the most similar to neutral molecules, the information does not correctly cross when inputs encode opposite logic values.

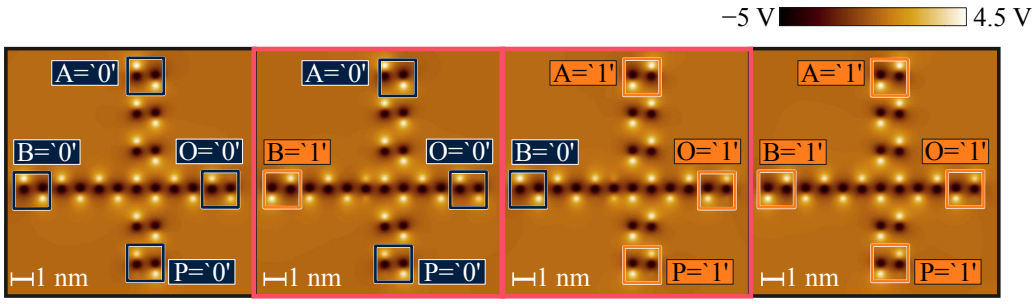

Fig. 3.22 Simulation using SCERPA of a crosswire interconnection utilizing zwitterionic molecules with $x_c = 5\,\text{Å}$: the four images depict the electrostatic potential for the four input combinations at the final propagation step, evaluated 0.2 nm above the logic dot plane.

While the single-diagonal interaction might manage to invert the logic signal under certain conditions, it's worth noting that the adjacent interaction holds greater energetic favorability, as discussed in previous sections. In this scenario, altering the slope of the VACT or introducing a shift proves ineffective in aiding the propagation. Additionally, simply adjusting the geometrical position of *Dot 3* to favor the diagonal interaction does not affect this setup, unlike the case of the single-branch inverter illustrated in section 3.2.2.

3.4.2 Multi-molecule coplanar crossover

Having valid alternatives for crossing information is crucial for the development of the technology. Without the possibility to perform this operation, it's basically impossible to obtain circuits larger than a few elementary gates.

One possibility is to use tailored molecules behaving in a particular way, enabling the attainment of the target functionality required. The combination of multiple types of molecules has been utilized to achieve the behavior of a three-input neuron using the majority voter layout [124]. In that example, different molecular characteristics serve to implement weights and the activation function in the neuron.

In this case, to determine how molecules should behave, we should start by analyzing the expected functioning of the cells in the crosswire. The crucial behavior is dictated by the interconnecting cell in the middle of the two branches. The central cell must assume two distinct configurations depending on the input signals.

When both inputs are equal, the charge on the logic dots must be well localized and coherent with the logic inputs. Since the two inputs encode the same logic, the global electrostatic influence on the central region favors the charge to stay either on *Dot 1* or *Dot 2*, depending on the logic value. Considering typical VACTs, including those depicted in Fig. 3.1 and used throughout this chapter, when the charge is localized on only one logic dot, we are in the saturation region.

In the case where the two inputs are opposite, theoretically, the electrostatic influence of one input is counterbalanced by the influence of the other input. The two contributions ideally cancel each other out, giving a total null input voltage on the molecules composing the central cell. However, the system composed of the input cells and the central interconnecting cell is not geometrically symmetric, or electrostatically symmetric if we use zwitterionic molecules. This asymmetry leads to small non-null input voltages on the central cell, and is the reason behind the fact that practically the crossover doesn't work for zwitterionic molecules or multi-line devices.

Since the problem lies in the behavior for small voltages, we can anticipate the system to function if the involved molecules exhibit a sort of indecision region. That is, for small voltages, the charge remains constant on logic dots, preventing the molecule from polarizing. This behavior is observed in molecules such as 1,5,9-decatriene cation [62, 51] or in the 1,3,5benzenetrithiol linked bis(hexanedithiol)

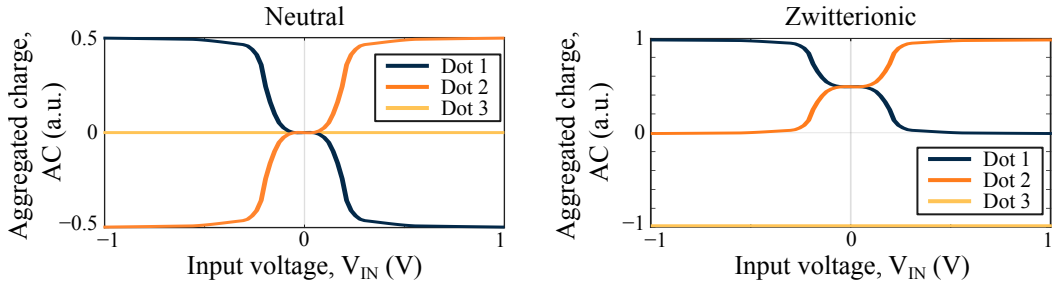

Fig. 3.23 VACT of the neutral and zwitterionic molecules used to favor the crossing mechanism, synthesized inspired by the behavior of the 1,5,9-decatriene cation and the 1,3,5benzenetrithiol linked bis(hexanedithiol) bis(trimethylsilane).

bis(trimethylsilane) presented in section 2.4.4. In both cases, small voltage variations do not affect the equilibrium charge distribution, meaning that the charge is equally distributed among all logic dots, and the molecular cell does not assume a specific logic value.

For the sake of coherence of the work presented here, rather than directly utilizing the VACT of the mentioned molecules, we synthesize the desired behavior on an artificial reference molecule. Fig. 3.23 illustrates the VACT designed for neutral and zwitterionic molecules to reinforce the expected behavior for the crosswire. The geometrical reference system for these molecules is the same as used throughout this chapter and reported in Fig. 3.1a. Since the discussed behavior is expected only from the central cell, the modified molecules should be assigned only to the central cell, creating a device composed of multiple molecular cell types [124].

Single-line multi-molecule coplanar crosswire

The presence of the *ad hoc* designed molecules alters the behavior of the crossover. Fig. 3.24 illustrates the layout used in this case. Unlike the solution that utilized a single molecule type, here the system functions even with the central cell clocked independently, a symptom of the increased robustness of the multi-molecule device. In this layout, the central interconnecting cell is composed of two molecules with a VACT inspired by decatriene, featuring a central plateau. The remaining cells, as well as driver cells, are composed of molecules with the classical VACT used for neutral molecules and reported in equation (3.2).

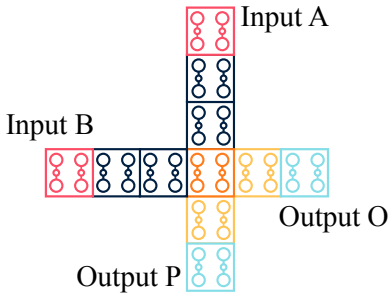

Fig. 3.24 Layout of the coplanar crossover used for the simulation in SCERPA. Blue, orange, and yellow cells belong to different clock regions. Input and output cells belong to the same clock region as the nearest cell.

Fig. 3.25 shows the electrostatic potential calculated with SCERPA for the implementation based on neutral molecules. Since the device is now divided into three clock regions, a single simulation step where both input and output branches are active is missing. While output cells are switching to the *hold* phase, the input cells are transitioning to the *reset* phase. For this reason, to follow information propagation, we need to observe two subsequent clock steps. In Fig. 3.25, the first clock step s is represented on the top line for the four possible input combinations, and the following clock step $s+1$ is reported in the bottom part of the image.

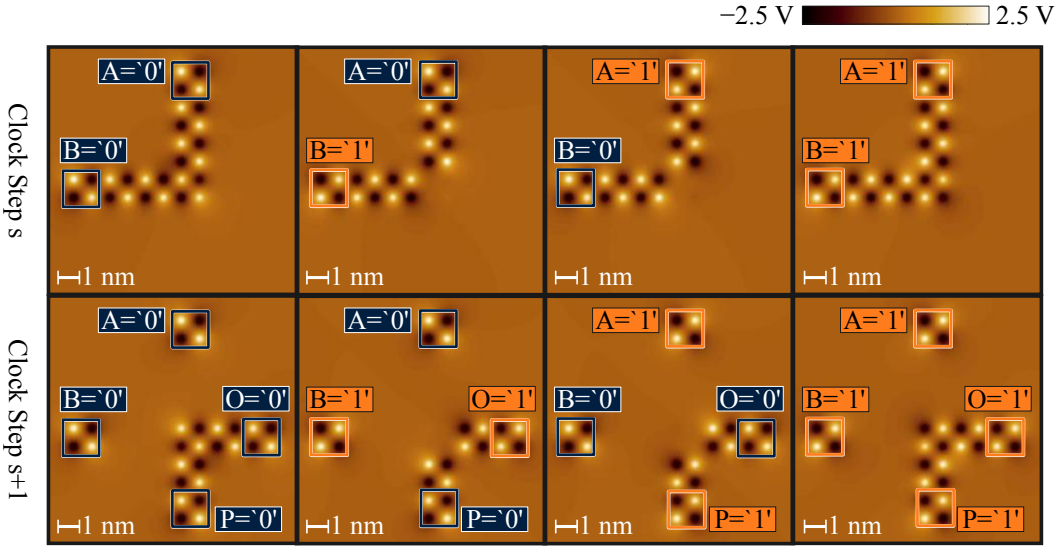

Fig. 3.25 Simulation using SCERPA of a single-line multi-molecule crosswire interconnection based on neutral molecules: the images depict the electrostatic potential for the four input combinations evaluated 0.2 nm above the logic dot plane. The top and bottom lines of the images represent subsequent clock steps.

From the electrostatic potential map, we can observe that when $A = B$, the interconnecting cell encodes the same logic value as them, as for the single-molecule implementation. The most significant difference occurs when $A \neq B$. In that situation, the effects of the two input branches cancel out, resulting in the central cell proposing an equal charge distribution on the four logic dots. Since the charge is almost zero on the logic dots of the interconnecting cell, their presence cannot be discerned from the potential map.

More interestingly, we consider the implementation with zwitterionic molecules. We start from the simplest case from an electrostatic point of view, using the layout shown in Fig. 3.24 implemented with the zwitterionic molecules having *Dot 3* on the same plane as the logic dots on both input and output branches. The interconnecting cell is composed of molecules with the *ad hoc* synthesized VACT presented in Fig. 3.23. For the decatriene-inspired molecules, the position of *Dot 3* is fixed at $x_c = 0\,\text{Å}$, which is 5 Å away from the logic dots.

Fig. 3.26a shows the electrostatic potential calculated with SCERPA. The considerations regarding the clock steps are the same as those made previously for the neutral multi-molecule implementation. The electrostatic potential map highlights the correct behavior for all input combinations and the behavior of the interconnecting cell. Again, when inputs are equal, the central cell clearly polarizes according to the logic value encoded by the drivers. Besides the proper behavior, when $AB = \text{`}11'$, the central cell presents a slight internal crosstalk phenomenon, evidenced by the distribution on three out of four logic dots, similar to the case of the fanout circuit (Section 3.2.4). When inputs encode opposite logic values, the electrostatic profile clearly highlights the evenly distributed charge among the four logic dots of the interconnecting cell. The evenly distributed charge lets the diagonal interaction dominate on the output branch, ensuring that the correct value is propagated on both outputs O and P.

The situation remains very similar if we move *Dot 3* to $x_c = 0\,\text{Å}$, even for the molecules on the input and output branches. Fig. 3.26b shows the electrostatic potential calculated with SCERPA. When $A = B$, the considerations are the same as before: the central cell polarizes according to the input values, and a slight presence of crosstalk is evident when $AB = \text{`}11'$. The reason for the presence of crosstalk only for that configuration is the asymmetry of the system with branches connected as an 'L' or a 'Γ'. Since with zwitterionic molecules the charge on logic dots is positive, it

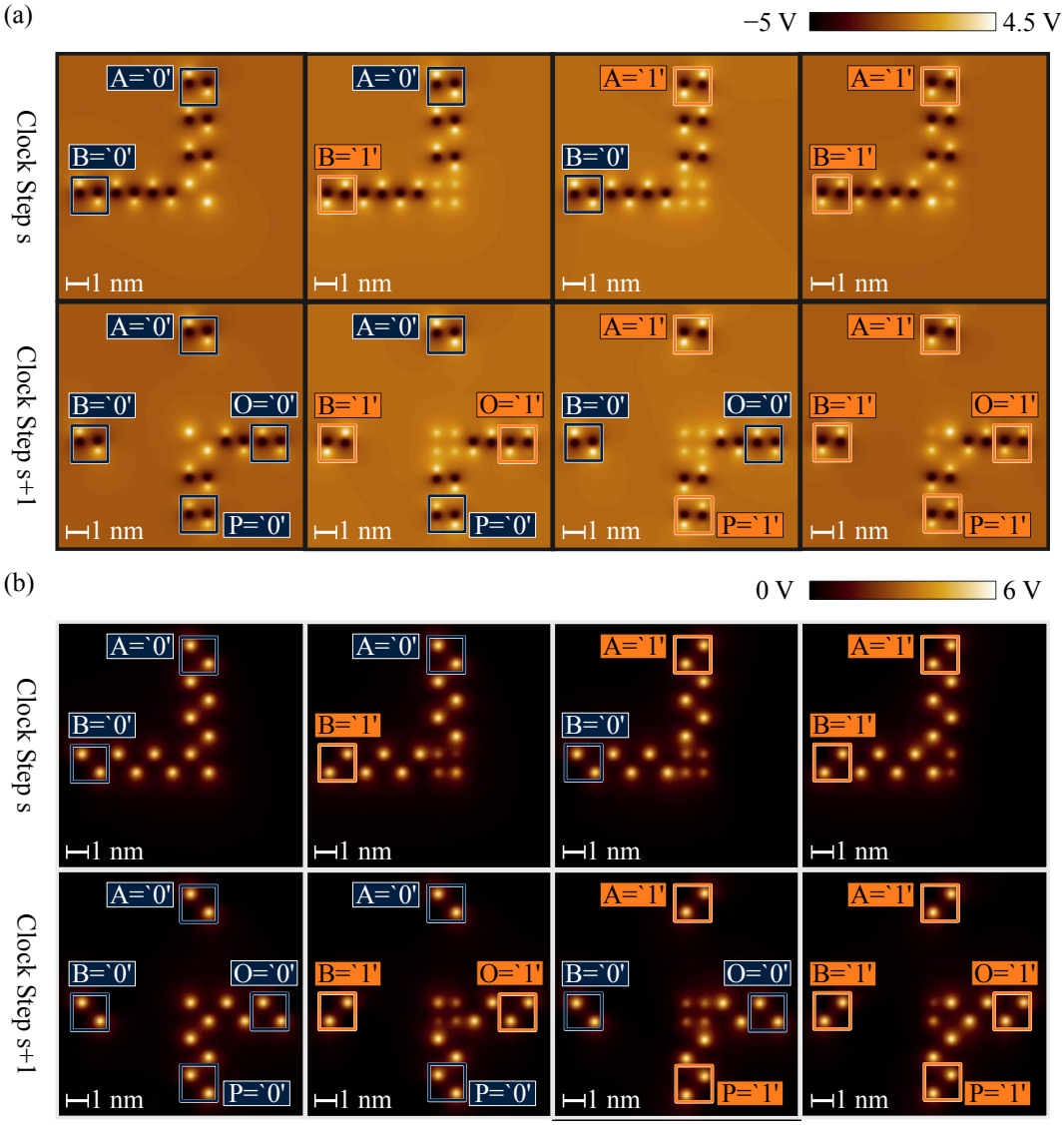

Fig. 3.26 Simulation using SCERPA of a single-line multi-molecule crosswire interconnection based on zwitterionic molecules: the images depict the electrostatic potential for the four input combinations evaluated 0.2 nm above the logic dot plane. The top and bottom lines of the images represent subsequent clock steps. (a) *Dot 3* is on the same plane as logic dots ($x_c = 5$ Å). (b) The postion of *Dot 3* is $x_c = 0$ Å.

tends to maximize the distance by occupying *Dot 2* of the right molecule in the first clock step, and *Dot 1* of the left molecule in the second clock step, which are the farthest positions for the charge. For configurations with $A \neq B$, the charge is evenly distributed, favoring diagonal interactions.

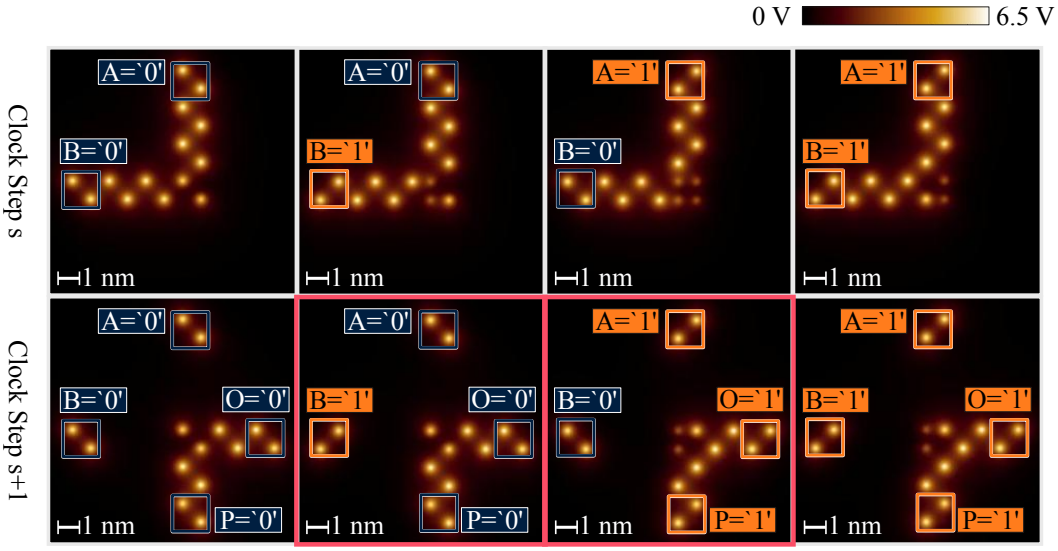

Fig. 3.27 Simulation using SCERPA of a single-line multi-molecule crosswire interconnection based on zwitterionic molecules with $x_c = -5\,\text{Å}$: the images depict the electrostatic potential for the four input combinations evaluated 0.2 nm above the logic dot plane. The top and bottom lines of images represent subsequent clock steps.

Having moved *Dot 3* far away from the logic dot plane highlights a small crosstalk effect when $AB =$ '01'. Even if a small crosstalk effect is present, the solution is resilient against electrostatic variations, demonstrated by the wide working range, i.e., $w \in [6;13]\,\text{V}^{-1}$ referring to equation (3.14).

The multi-molecule crossover implementation increases the set of working devices, including also zwitterionic molecules with various electrostatic footprints. However, we must remember that the working principle is a single-branch inversion, which is dependent on the implementation. Indeed, if we simulate the crossover implemented with zwitterionic molecules having $x_c = -5\,\text{Å}$, the situation changes drastically, even with the decatriene-inspired molecules in the center. Fig. 3.27 shows the electrostatic potential obtained from the SCERPA simulation. In this implementation, when A and B encode the same logic, information propagates correctly, with just a slight crossover effect. However, when $A \neq B$, both outputs encode the same logic value as input A, demonstrating that a correct single-branch inversion is the essence of the functioning.

Multi-line multi-molecule coplanar crosswire

Multi-line devices are of particular interest for strengthening the information flow in a circuit, as border effects and information decay are strongly reduced. The parallel lines composing the circuits replicate the same information, enhancing the relative influence and allowing the molecular charge to be well localized on one of the two logic dots.

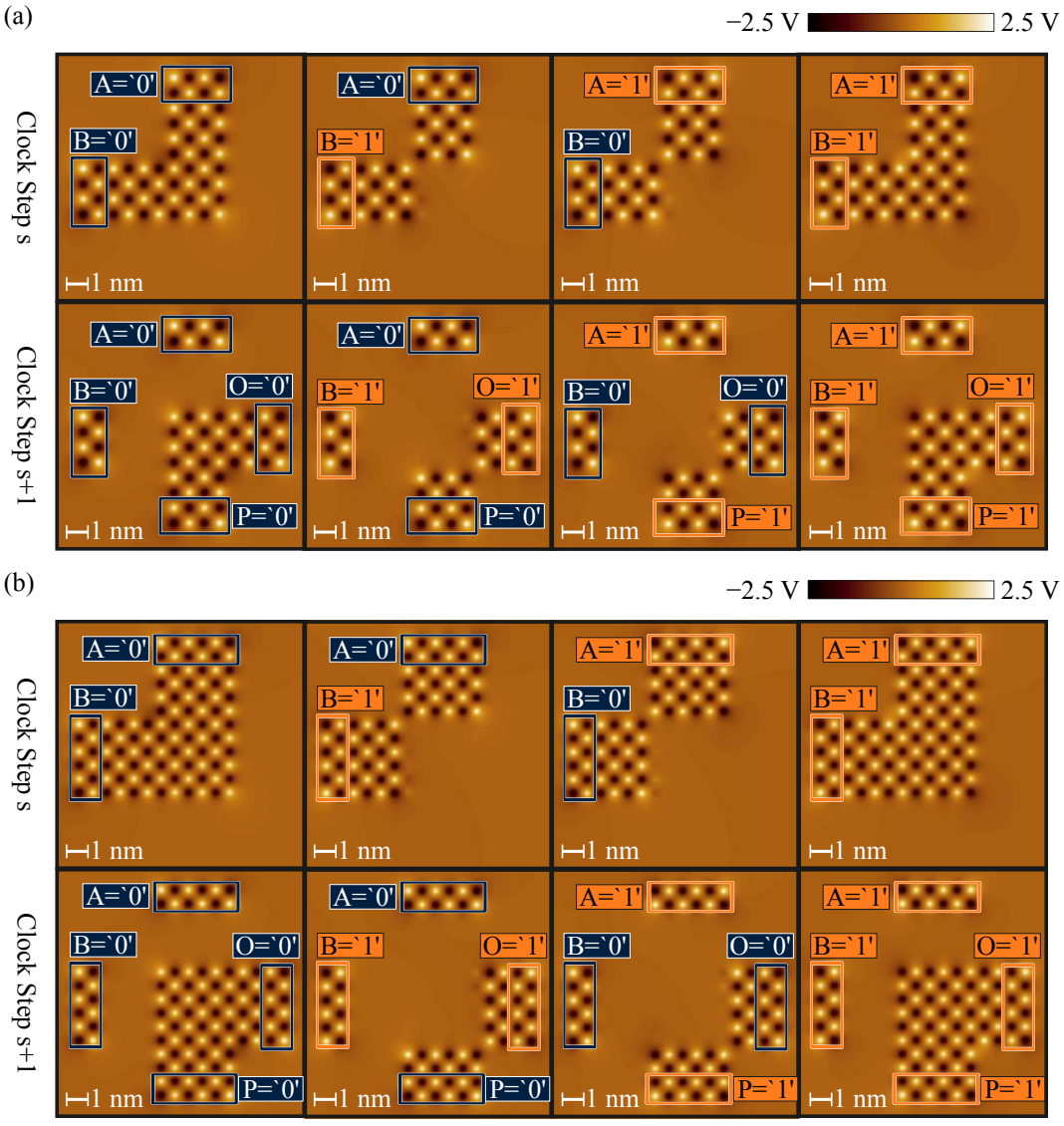

Fig. 3.28 Simulation using SCERPA of a multi-line multi-molecule crosswire interconnection based on neutral molecules: the images depict the electrostatic potential for the four input combinations evaluated 0.2 nm above the logic dot plane. The top and bottom lines of images represent subsequent clock steps. (a) Two-line layout. (b) Three-line layout.

One of the two fundamental assumptions for the crosswire to function properly is that the superposition of the effects of the input branches cancels out in the central region when inputs differ. We have seen that asymmetries, both geometrical and electrostatic, complicate the balancing of the generated electric field in the interconnecting region, leading to unwanted polarization. Indeed, in single-molecule implementations, information crossovers do not work correctly.

Multi-molecule devices that utilize the decatriene-inspired molecules in the center are supposed to mitigate the polarization of the central region. We verify the behavior of multi-line crossover interconnections implemented with neutral molecules using SCERPA. Fig. 3.28a shows the electrostatic potential for the four input combinations in a two-line crosswire. In this case, the central region where the decatriene-inspired molecules are present is composed of four cells. The behavior is exactly as expected based on theoretical principles: when inputs are equal, cells in the central region polarize according to the encoded logic, whereas when inputs differ, the central region is not visible since the charge is nearly zero on logic dots.

To verify the robustness of the implementation with neutral molecules, we also simulate a three-line crosswire, which can be useful in the case of computation on Self-Assembled Monolayers (SAM)[99]. Fig.3.28b shows the electrostatic potential obtained from the SCERPA simulation. Even the increased distance between some cells in the central region from input branches does not affect the behavior of the system, which remains correct in all four input combinations.

Until now, we have observed that implementations with neutral molecules tend to be more straightforward than implementations with zwitterionic molecules. The two-line multi-molecule crossover based on zwitterionic molecules works in a limited set of cases.

We focus on the implementation with *Dot 3* placed 5 Å away from the logic dots ($x_c = 0\,\text{Å}$), since it is borderline for functioning. In this condition, the crossover provides correct propagation only when $w = 6\,\text{V}^{-1}$ or $w = 7\,\text{V}^{-1}$, referring to equation (3.14). Fig. 3.29 shows the electrostatic potential obtained with SCERPA in the case with $w = 7\,\text{V}^{-1}$. For higher values of w, the electrostatics are sufficiently strong to polarize the central cells when $A \neq B$. On the contrary, for smaller values of w, the electrostatics are not strong enough to induce inversion when $A \neq B$.

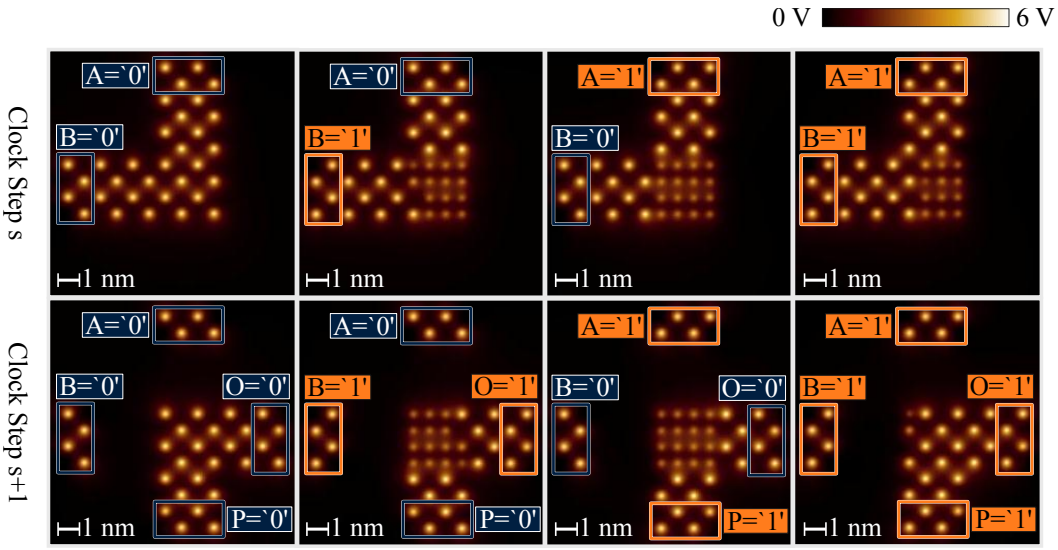

Fig. 3.29 Simulation using SCERPA of a two-line multi-molecule crosswire interconnection based on zwitterionic molecules with $x_c = 0$ Å: the images depict the electrostatic potential for the four input combinations evaluated 0.2 nm above the logic dot plane. The top and bottom lines of images represent subsequent clock steps.

Chapter 4

Device modeling

Performing experiments in molecular-based technologies such as molecular Field-Coupled Nanocomputing (molFCN) poses significant challenges and expenses. Consequently, adopting a prudent approach by anticipating potential outcomes beforehand is advisable. In contemporary times, simulation tools exhibit increasing accuracy, and the availability of computational power facilitates the exploration of larger systems.

In the case of molFCN, as discussed in Chapter 2, *ab initio* simulation and Density Functional Theory (DFT) enable the precise study of molecules with dozens of atoms. However, comprehensive optimization and calculation for each V_{in}-AC transcharacteristic (VACT) can take up to a week or more, depending on the molecule. Moreover, the time required does not increase linearly with the complexity of the analyzed system but exponentially.

This necessity led to the development of an electrostatic model specific to molFCN, simplifying the treatment while remaining linked to the physical behavior of the molecule. The Molecular Simulator Quantum-dot cellular automata Torino (MoSQuiTo) methodology and the Self-Consistent ElectRostatic Potential Algorithm (SCERPA) tool allow the simulation of small devices, as those presented in Chapter 3, in short times, often less than a minute. Additionally, SCERPA enables simulations with different types of molecules, corroborating the predictions of energy calculations, which make it physically accurate.

However, SCERPA also has its limits. It can simulate devices with a few hundred molecules in a few hours. Such times are prohibitive if one aims to accurately simulate even a simple arithmetic unit composed of thousands of molecules.

This chapter delves into enhancing the level of abstraction to develop physically accurate models of entire devices. This approach allows us to treat them as black boxes whose behavior is delineated by a specific number of variables and tables.

The methodology we employ consists of several key steps. First, we establish clear rules to describe the behavior of gates in terms of their input and output interactions. This step helps us understand how each gate functions within a circuit. Next, we automate the characterization process for elementary gates, which essentially means we analyze their behavior systematically. This analysis helps us build a comprehensive library of devices, where each device is characterized by its unique input/output behavior.

Once we have this library in place, we can move on to evaluating the behavior of more complex circuits. By utilizing the predefined characteristics of the elementary gates, we can predict how these gates will interact with each other in larger circuit configurations.

To ensure the reliability of our methodology, we rigorously validate the accuracy of the gate models. We do this by simulating designs that incorporate these models and comparing the results with SCERPA simulations that we demonstrate to be accurate. This validation step is crucial as it ensures that our models accurately represent the actual behavior of the gates.

4.1 Device figures of merit

Imagine a molFCN circuit, such as the XOR gate, comprising various elementary gates like ANDs, ORs, and inverters [64]. Our methodology suggests simulating each of these elementary gates individually once and then storing the simulation results in a Look-Up Table (LUT). This LUT serves as a reference for obtaining information about any circuit or architecture containing these gates without the need to simulate the elementary blocks again. Essentially, each circuit can be viewed as a collection of black boxes, where the behavior of each box is cataloged in library files that link input and output signals.

This approach remains effective even for more complex systems. For example, we can describe a ripple-carry adder as an interconnection of XORs and ANDs, using the simulative data we already have to predict the final result. In practice, we replace each elementary gate with a black box featuring input and output ports. The behavior of each block is described by a LUT that relates input to output, possibly including other parameters.

In molFCN, information travels through electric field coupling, a long-range field. This implies that breaking a circuit into smaller blocks and simulating these blocks in isolation may not accurately represent the global behavior of the original circuit. Additionally, changes in the molecule or the extension of the clock region can produce different behavioral results, highlighting the significance of physics at this scale, as we demonstrated in Chapter 3. Therefore, simulating the elementary gates used to construct the library files must consider the physics of the interaction within and between devices to accurately describe the expected outcome. This section proposes a framework for a comprehensive and precise description of a generic device, incorporating the underlying physics to model its behavior accurately.

4.1.1 Input and output signals

To begin, it's essential to establish how signals represent the inputs and outputs of the device. This ensures that they accurately capture the charge state of molecules. By storing the input values, we can uniquely identify a particular physical state, enabling us to predict the correct output under similar conditions.

In previous chapters, two main approaches have been used to describe the charge state of a molecule or a molecular cell. The first method involves considering the molecule input voltage V_{IN} and its VACT, describing the charge configuration on dots for each value of V_{IN}. The second approach involves cell polarization, a measure of the charge distribution within the molecular cell as used for the energy analysis in Chapter 3. Between the two options, we opt for input voltages, as the SCERPA simulator operates with the transcharacteristics of molecules.

Then, we know that information propagates through the sequential activation of clock regions. This kind of propagation is similar to having information packages moving along the circuit, so information at the output is meaningful only if sampled in the correct time step. We are interested in sampling the information on the output

when the clock signal is in the hold state. The intermediate states are not of any influence in the input/output model of a device, so there is no need to store them. This means that for each information package sent into the device input, we will store in the LUT only the output values during the hold phase. If we know the molecule used and the clock field value, then the molecule input voltage is sufficient to describe the molecular charge state thoroughly and uniquely.

After deciding that the molecular input voltage is the signal of interest for inputs and outputs, we must decide on which cells we have to read that information on order to obtain a meaningful input/output description of the Device Under Test (DUT). Specifically, we must ensure that the model aligns with the actual circuit implementation. This means that even spatially we have to remember that inputs and outputs correspond to actual molecular cells.

For instance, consider the situation shown in Fig. 4.1a with two single-line wires, *Wire A* and *Wire B*, each composed of 6 molecular cells, receiving an input

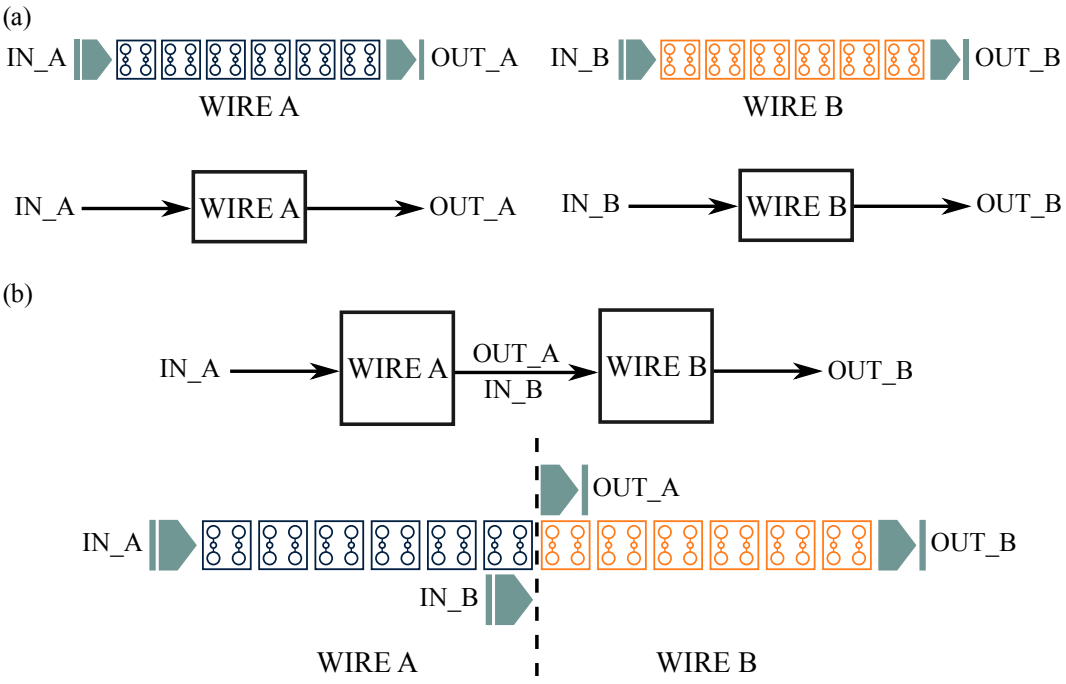

Fig. 4.1 Choice of the input and output signals of a device on an example system. (a) Scheme of the two wires *A* and *B* used for the example, with input and output pins highlighted. At the bottom is shown an input/output schematic representation. (b) Connection between *Wire A* and *Wire B*. The schematic view of the signals is on top, whereas at the bottom, the corresponding physical circuit shows the overlapping of the cells and pins at the joint, giving two possible choices for signal compliance.

signal from the driver pin and generating an output state on the output pin. In an input/output model, the 6-cell wires can both be substituted by a generic box, which receives an input signal and produces an output signal.

When we connect *Wire B* to *Wire A*, we expect a 12-cell single-line wire, with the output of *Wire A* (OUT_A) corresponding to the input signal of *Wire B* (IN_B). Fig. 4.1b shows that we cannot use both the output pin of *Wire A* and the driver pin of *Wire B*, otherwise the real implementation would not correspond to a 12-cell wire.

Two equivalent cases show up for signal compliance: either we use the first cell of *Wire B* and the output pin of *Wire A*, or we use the driver pin of *Wire B* and the last cell of *Wire A*. We select the latter option, ensuring that the input refers to the driver pin and the output to the last cell of the device under test.

Taking into account the decisions made thus far, we assign distinct names to the molecules of interest to designate the device's input and output signals and their positions. In Fig. 4.2a, we illustrate the example of a Majority Voter (MV) with multiple inputs (IN1, IN2, IN3) and a single output (OUT). Input signals must be taken on driver pins, which are thus substituted with controllable molecular cells. On these cells, we are interested in the molecule voltage (V), and because it is for identifying the device input, we attach the label IN. The branch related to input IN1 is associated with the identifier UP, since it comes from upward. Similarly, the branch related to input IN3 is associated with the label DW, as the signal comes from downward. The signal associated with input IN3 does not have any additional identifying label. The voltages related to the device output signal are identified with the label OUT. Regarding molecule labeling, the first and second molecules in a cell are denoted by the letters A and B, respectively.

The title entry of the MV LUT will look like Table 4.1 for the single-line MV shown in Fig. 4.2a.

Table 4.1 Title entry of the LUT describing the input/output behavior of a single-line MV.

$V_{IN\_UP\_A}$	$V_{IN\_UP\_B}$	V_{IN_A}	V_{IN_B}	$V_{IN\_DW\_A}$	$V_{IN\_DW\_B}$	V_{OUT_A}	V_{OUT_B}
...	...	...	...	...	...	...	...

Fig. 4.2b shows the example of a fanout circuit with a single input (IN) and three outputs (OUT 1, OUT 2, OUT 3). As described before, V_{IN} is associated with device input signals, and V_{OUT} describes the device's output. The branch related to

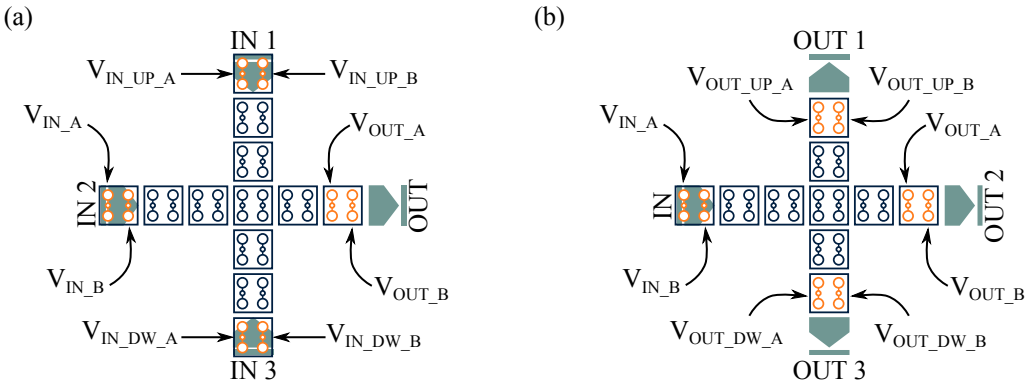

Fig. 4.2 Rules for naming device's input and output signals before being stored in the LUT. The molecules of interest are orange-colored. (a) Example on the MV layout with three inputs and one output. (b) Example on the fanout circuit layout with one input and three outputs.

output OUT 1 is associated with the identifier *UP*, as it goes upward. Similarly, the branch related to output OUT 3 is associated with the label *DW*, as the signal goes downward. The signal associated with input OUT 3 does not have any additional identifying label. Additionally, letters *A* and *B* identify the molecules on the left and right of the cell, respectively. Table 4.2 reports the title entry for the input/output signals of a single-line three-way splitter.

Table 4.2 Title entry of the LUT describing the input/output behavior of a single-line fanout circuit.

V_{IN_A}	V_{IN_B}	$V_{OUT\_UP\_A}$	$V_{OUT\_UP\_B}$	V_{OUT_A}	V_{OUT_B}	$V_{OUT\_DW\_A}$	$V_{OUT\_DW\_B}$
...	...	...	...	...	...	...	...

For multi-line devices, which present duplicated transmission lines, we must store the voltages of both the cells constituting the input and output signals. To distinguish them, we add the labels *H* and *L*. On horizontal lines, *H* is associated with the higher line, and *L* with the one on the bottom. In vertical lines, *H* is associated with the line on the left, whereas *L* identifies the line on the right.

4.1.2 Information stability

After selecting the input and output signals, we must also consider the simulation conditions, particularly regarding the output. Devices may exhibit vanishing information

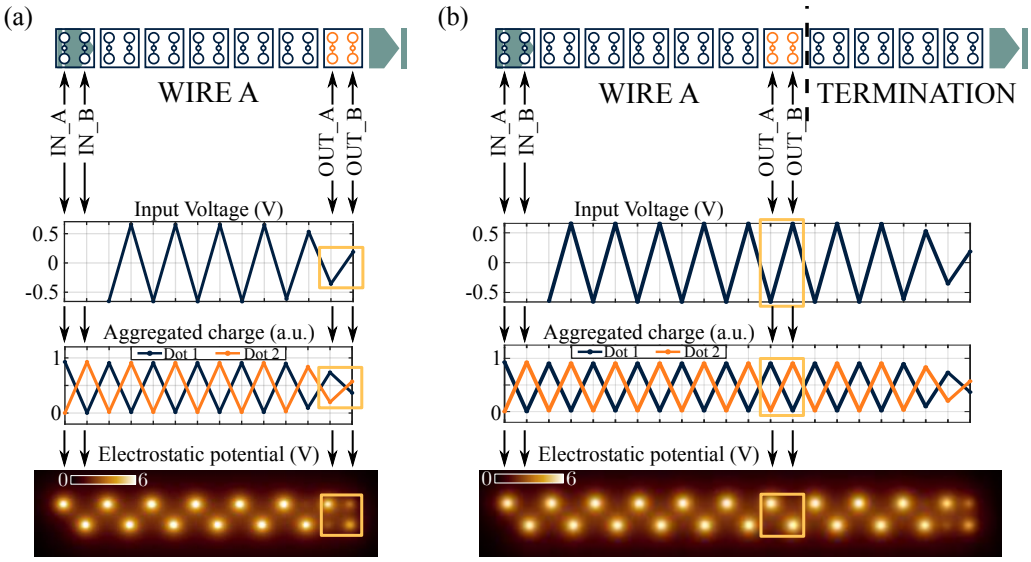

Fig. 4.3 Border effect on information propagation. (a) Propagation in a single-line wire simulated with SCERPA, showing the vanishing data at the end of the wire, corresponding to output molecules A and B. The three graphs represent the input voltage, the aggregated charge value, and the electrostatic potential on each molecule of *Wire A*. (b) Propagation in a single-line wire connected to a termination block composed of 4 cells simulated with SCERPA, showing the restored data on the output of *Wire A*. The three graphs represent the input voltage, the aggregated charge value, and the electrostatic potential on each molecule of the system composed with the wire and the termination.

at their terminus, even in cases of bistable propagation [64]. In an isolated device, no molecules reinforce the information beyond the output, leading to less pronounced charge separation between the dots of the final molecules. Fig. 4.3a showcases the SCERPA results of the same *Wire A* mentioned previously and implemented with bisferrocene molecules.

Fig. 4.3a illustrates that if *Wire A* is simulated in isolation, the wire output voltages (V_{OUT_A} and V_{OUT_B}) are lower than the voltage on other molecules because of the information decay. However, when we connect a second device at the end of *Wire A*, the diminishing information on *Wire A* output is restored by the presence of the attached device. Fig. 4.3b presents the results obtained from SCERPA of *Wire A* with a 4-cell termination wire connected at its end. The simulation demonstrates that information on the original output cell of *Wire A*, boxed in yellow in Fig. 4.3, is restored. The termination wire acts as a stub at the end of the DUT helping to restore information.

When conducting simulations to assess the input/output behavior of a device, with the intention of incorporating it as a connected module within a larger design, it's crucial to account for the phenomenon just described. Thus, as we isolate and simulate each gate for characterization, we need to anticipate its connection to other circuits during actual operation. Even if we simulate our DUT isolated, we must remember that in the steady-state functioning, the DUT is supposed to be connected to other gates that will act as the termination wire in the example of Fig. 4.3b. To consider this, we enhance the device model by simulating it in conjunction with a termination circuit, mimicking the presence of a cascaded device. This ensures that the stored output voltages align with the behavior expected in the context of a cascade setup, maintaining precision to the underlying physical system.

Termination circuits can take various forms, and in this chapter, we utilize a short wire to reinforce information retention at the output cell, without introducing excessive complexity that may slow down simulations. Specifically, our termination wire consists of four cells, and in the case of multi-line setups, it is replicated across both lines.

4.1.3 Additional information for the model

When explaining the functionality of a device, it's crucial to account for various factors, including the distribution of the clock signal, the voltages at input and output nodes, and the incorporation of a termination circuit. The division of the device into phases significantly impacts signal synchronization and is intimately tied to latency considerations, which are pivotal in circuit design as they dictate path balancing. By ensuring that a device terminates with the maximum available clock phase, we can characterize latency and synchronization using two key parameters: the maximum number of phases (*maxPhases*) and the number of repetitions of those phases (*phaseRepetition*). For instance, in the XOR gate illustrated in Fig. 4.4a [64], with a maximum of four phases ($maxPhases = 4$) repeated three times ($phaseRepetition = 3$), the latency amounts to 12.

Additional critical parameters relate to the physical and electrostatic footprint of the device. Physical occupation can be quantified in nanometers (absolute area) or in terms of unit cells within a grid system (relative area). On the other hand, electrostatic occupancy primarily considers crosstalk effects within the device, as

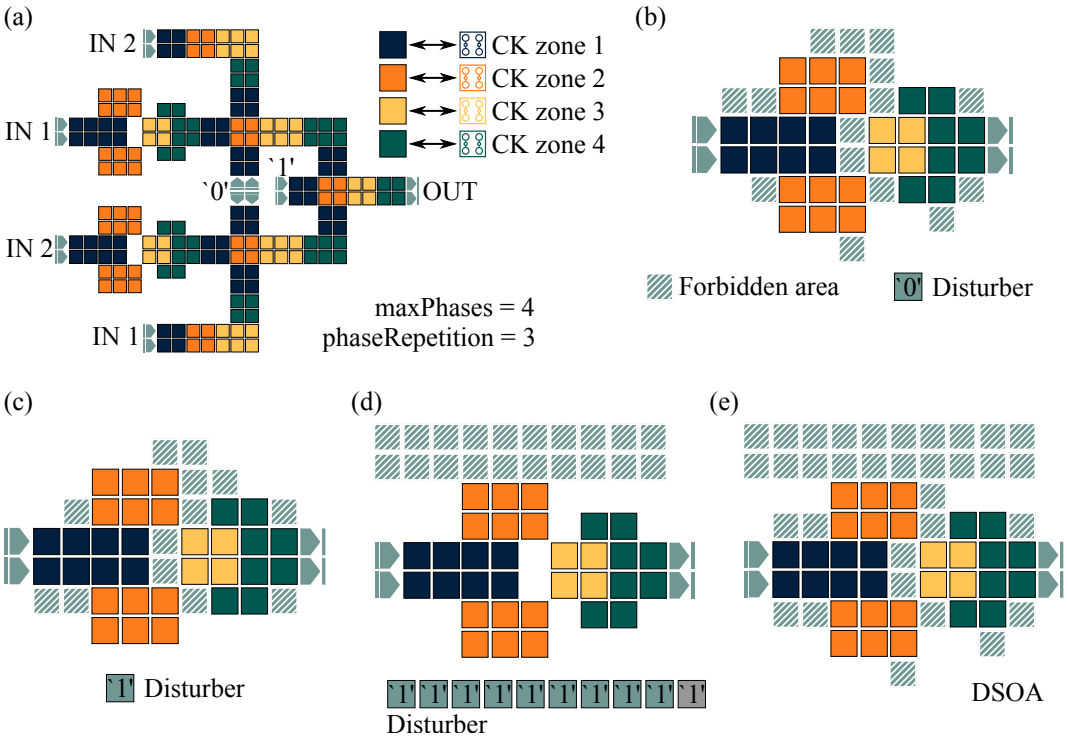

Fig. 4.4 Additional information needed for a complete description of a device. (a) Layout of a XOR gate highlighting clock zones for synchronization and their repetition for latency. (b) Forbidden area for a multi-line double-branch NOT gate when the disturber is a single driver cell encoding a logic '0'. (c) Forbidden area for a multi-line double-branch NOT gate when the disturber is a single driver cell encoding a logic '1'. (d) Forbidden area for a multi-line double-branch NOT gate when the disturber is a whole polarized wire encoding a logic '1'. (e) Device safe operating area of the multi-line double-branch NOT gate.

described in section 3.3. To determine the Device Safe-Operating Area (DSOA) and prevent errors, we must conduct multiple simulations of the DUT under various conditions, incorporating different types of disturbers in its vicinity. These disturbers are modeled by fixed-logic driver cells or wires. For instance, in the case of the multi-line double-branched NOT gate, Fig. 4.4b illustrates the forbidden area obtained using a single-cell disturber encoding a logic '0', while Fig. 4.4c depicts the forbidden area derived using a single-cell disturber encoding a logic '1'. Disturber can be whole polarized wires, as in the case of Fig. 4.4d, showing the forbidden area using a disturber wire encoding a logic '1'. By aggregating all the forbidden regions, we delineate the DSOA of the gate, as shown in Fig. 4.4e.

The library files must encapsulate all the parameters discussed in this section to adequately describe the DUT behavior. To streamline this process, we've developed

a program that automatically evaluates the requisite parameters and generates the library files for each device. However, manual intervention is still required for DSOA analysis, as automating the design process for composite circuits remains a work in progress. Standardizing this process may entail numerous simulations tailored to the specific device. Nonetheless, the designer expertise is sufficient to build small circuits that adhere to the gate's DSOA.

4.2 Automated algorithm for device characterization

The previous section highlighted the key elements that must be accounted for when simulating a device. The general idea is to obtain a set of files for each gate, containing all the relevant information, starting from the input/output behavior, the latency, and the area occupation. Then, once we have all these files for each gate, we should be able to simulate larger designs that are a collection of these gates interconnected in some way.

Aiming to standardize the process and simplify the treatment for a general user, we developed an automatic tool that handles the simulation of the DUT and the creation of the relative files in the library. The Block-Based characterization (BBchar) tool automatically simulates devices and extracts the needed properties.[1]

The following sections describe the principal elements of BBchar to create a complete set of library files and the written code. The program applies to molFCN circuits designed in MagCAD [134, 135], which produces a file describing the layout of a circuit, including input and output pins. The BBchar tool is able to:

- automatically generate input files for the simulation of the circuit in SCERPA;
- automatically characterize the circuit to provide a LUT with the input/output description plus some additional information regarding timing and area;
- provide the output of a circuit in the library given a generic combination of the inputs.

The expected workflow for each DUT is to simulate it multiple times with SCERPA until we obtain a correct behavior. Then we have to attach the termination

[1]The tool and all the files presented in this chapter are available online at https://github.com/vlsi-nanocomputing/BBchar.

before launching the complete simulation that we use to extract the data for the library files. Finally, we can extract the information we need from the simulation data and store them in the library files related to the DUT. All the steps are handled automatically by the BBchar tool.

4.2.1 Drivers and clocks

The focal point of the entire process lies in conducting a comprehensive simulation, allowing us to gather a sufficiently extensive dataset to extract and generate valuable library files. Indeed, the richness of data in these files directly impacts the precision of output predictions for any given input. Consequently, meticulous attention must be given to configuring the clock signal for each clock region and determining driver voltages.

Initially, it's necessary to establish the structure of a single clock cycle. Common clock signals typically exhibit trapezoidal waveforms as described in chapter 1, exemplified in Fig. 4.5a. The clock signal is divided into four stages (*num_stages*): switch, hold, release, and reset. Each of these stages is divided into a specific number of steps that can be set by the user with the variable $clock\_step$. The variables *clock_low* and *clock_high* define the lower and upper voltage levels for the clock signal. Once we know these three variables, we can obtain the clock voltage for each simulation step. For instance, if $clock\_step = 5$, $clock\_low = -2\,\mathrm{V}$, and $clock\_high = 2\,\mathrm{V}$, we obtain the following clock signal sequence for the various phases:

$$\begin{aligned} pSwitch &\rightarrow -2 \quad -1 \quad 0 \quad +1 \quad +2 \\ pHold &\rightarrow +2 \quad +2 \quad +2 \quad +2 \quad +2 \\ pRelease &\rightarrow +2 \quad +1 \quad 0 \quad -1 \quad -2 \\ pReset &\rightarrow -2 \quad -2 \quad -2 \quad -2 \quad -2 \end{aligned}$$

The complete unit cycle ($pCycle$) is defined as the union of the four stages just described and is replicated as needed.

Circuits are divided into clock regions, typically four regions are sufficient to correctly propagate the information by sequentially activating each region. Each

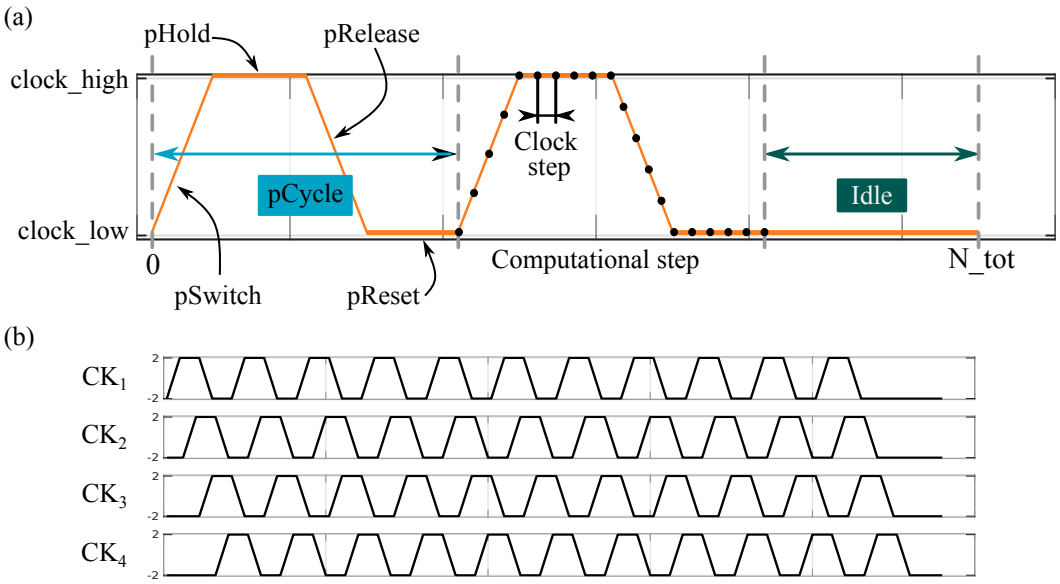

Fig. 4.5 Clock signal for DUT simulations. (a) Definition of the terminology for a trapezoidal clock signal. (b) Example of a complete set of clock signal for a device having four clock regions, with 11 periods plus the idle phase.

clock region receives a waveform as the one described before, just out of phase of one stage. Fig. 4.5b shows the clock waveform for a circuit having four regions. For the steps added to comply with the waveform shift, we can associate the clock value of the reset, i.e., *clock_low*. The length of this *idle* period is the same as the period *pCycle* for each region and divided between the beginning and end of the simulation according to the specific region. So, for instance, for region1, the idle phase is fully at the end, for region3 it is divided between the beginning and end, and for region 4 it is all at the beginning.

In addition to the voltage values and the shape of the period for the clock cycle, we need to define how many periods we need to propagate the set of inputs we are interested in simulating. The total number of periods is linked to how many times the four clock regions are repeated between the input and the output, that is the latency of the DUT. In the case of a single input value to be propagated from the input to the output, the total number of computational steps is

$$N\_tot = clock\_step * num\_stages * latency + idle \tag{4.1}$$

Together with the clock signal, the signals associated with the inputs are fundamental for performing a complete simulation of the DUT under different conditions.

First, we need to determine how many different inputs are present in the design and how they are identified in the MagCAD layout file, so that we can locate their positions. Even if inputs are replicated, as in the example of the XOR gate shown in Fig. 4.4a, they are considered as a single input, and thus, they receive the same signal.

As discussed earlier, input signals are represented by voltages on molecules. Therefore, we need to determine the maximum voltage to be applied ($V_{in_{MAX}}$). This value depends on the specific molecule used for the DUT implementation. For instance, for bisferrocene molecules, an input voltage range of ± 1 V is sufficient to saturate the charge on one logic dot rather than the other. Testing the DUT only for the maximum voltages could lead to a limited set of simulation data from which to extrapolate entries for the LUT. To address this, in addition to permitting the simulation of constant '0' and '1' (associated with $\pm V_{in_{MAX}}$), we allow for more signals: a positive and a negative ramp between the maximum allowable voltages. The positive ramp corresponds to a sweep from the voltage associated with '0' to the voltage associated with '1', while the negative ramp sweeps from the voltage associated with '1' to the voltage associated with '0'. These ramps can be linearly or logarithmically divided into N_driver_step, depending on the user's requirements. The ability to simulate the DUT for voltages that do not saturate the molecular charge helps in predicting all simulation cases, including non-ideal scenarios, thereby improving confidence in the data stored in the LUT. A higher value of N_driver_step results in more entries in the input/output LUT that describe the circuit behavior, enhancing the predictive capability when the library file is used.

The preceding section highlighted that for each physical input, we require two signals, one for each molecule composing the cell. Typically, since charge in a cell localizes on antipodal dots, the two molecules composing the cell exhibit opposite voltages. Moreover, in multi-line devices, inputs are composed of multiple cells. For instance, considering the multi-line NOT gate shown in Fig. 4.4b, we will have four distinct input signals. Fig. 4.6 illustrates a set of possible inputs for the multi-line NOT gate, where we request a positive ramp divided into $N\_driver\_step = 10$. From the waveforms, we observe that the two molecules in the cell (A and B) exhibit opposite ramps, while the upper line (H) and the lower line (L) show the same behavior. The ramp is executed in small steps, and each value is held constant for a period. This choice is rooted in the physical system. Information propagates in

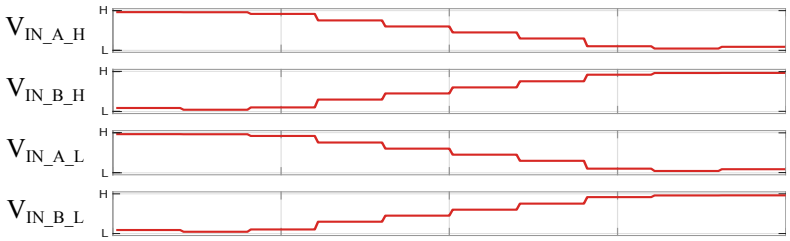

Fig. 4.6 Example of input signals for the simulation of a two-line NOT gate.

the form of packages, and inputs must remain stable for an entire *pCycle* to avoid generating conflicts.

Finally, to formulate a comprehensive algorithm, we must also account for specifying multiple contiguous input combinations (*N_comb*) for a single simulation.

Considering all constraints, the number of clock cycles necessary to propagate all the input values is given by:

$$N\_cycles = N\_driver\_step * N\_comb + \\ (phasesRepetition - 1) + idle\_phase \quad (4.2)$$

The first row of equation (4.2) is related to the number of provided inputs. The second row determines the cycles required to propagate the last input to the output, effectively clearing the pipeline.

4.2.2 Termination

Section 4.1.2 emphasized the importance of adding a termination to the DUT to adequately characterize it in case a second device is attached. We have already mentioned that the termination circuit can be of any type. In BBchar, the default termination is a 4-cells-long wire, single-line, or multi-line depending on the DUT, and is added automatically.

A termination is added to each physical output in the following clock phase, ensuring that a new clock region is not added. Therefore, for instance, in a circuit with four clock regions, if the output is in clock region 4, the termination will be added in region 1. Similarly, if the output is in region 3, the termination will be added in clock region 4. Once the termination is added, the driver and clock matrices must

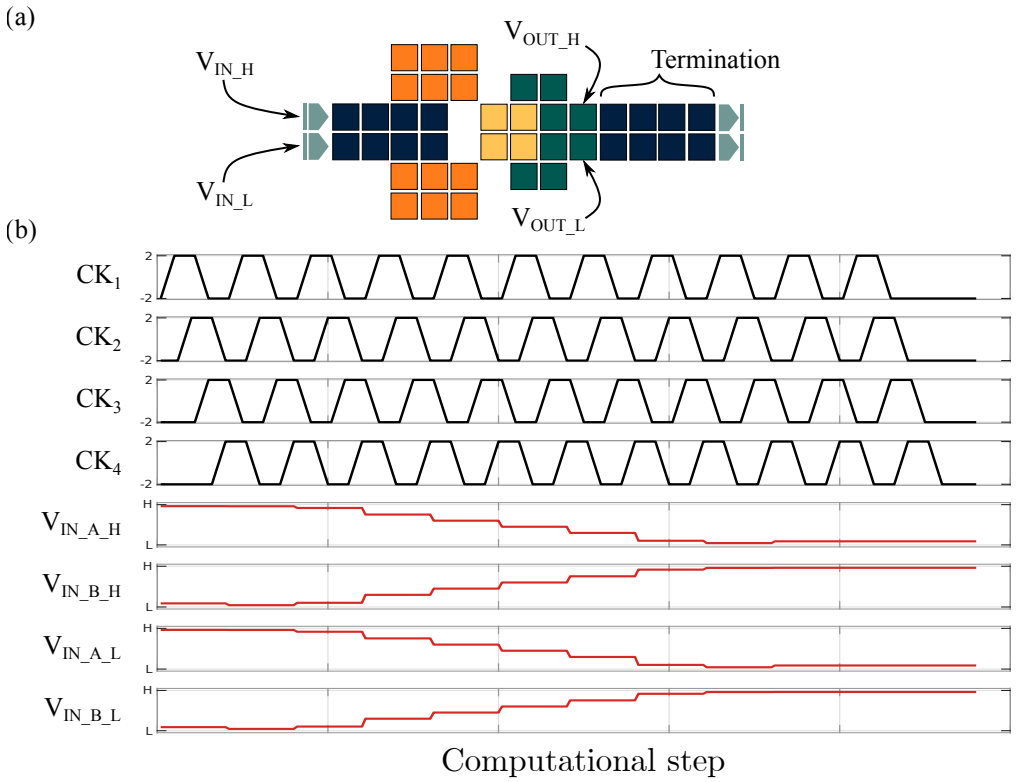

Fig. 4.7 Example of the simulation of a two-line NOT gate with a termination attached to the end. (a) Layout of the gate highlighting the termination and the cells on which input and output signals are considered. (b) Clock and input signals for the simulation of a two-line NOT gate with a termination attached to the end.

be updated to include the new region: a clock cycle is added to the phase matrix, and the last driver value is replicated for its length.

Consider again the example of a two-line NOT gate divided into four clock regions. The termination circuit will be in clock region 1, as shown in Fig. 4.7a. Input signal refers to the driver pins. Output signals will be read on the two cells right before the termination, and because of it, information is not vanishing. For the simulation, we fix $N\_driver\_step = 10$ and $N\_comb = 1$ since we want to simulate a single positive sweep. The original circuit has four clock regions repeated a single time $phasesRepetition = 1$. According to equation (4.2), we obtain $N\_cycles = 10 + idle\_phase$. However, because of the presence of the termination, we need an additional cycle, as correctly represented in Fig. 4.7b, where 11 cycles are visible.

4.2.3 Library files creation

The generation of library files serves the crucial function of ultimately predicting the logic value at the output of a circuit. Therefore, their generation is fundamental to obtaining high accuracy in output prediction.

The primary focus lies in the voltage values of both the input and output molecular cells. We must ensure meticulous sampling of signals during the appropriate hold clock phase, considering the delay between input and output due to latency. Moreover, we should obtain a sufficiently large set of input/output pairs to increase the number of entries in the Look-Up Table (LUT). The more entries we have, the more input/output associations we have when using the LUT.

Understanding the waveforms utilized for simulation alongside the circuit's clock phase repetitions simplifies the identification of simulation steps aligning with the correct sampling intervals. Each input voltage employed for simulation is logged in the LUT, recording the corresponding voltage values on the output molecules during the hold state of the clock region to which the output belongs and after the correct number of repetitions.

In molFCN technology, the functionality of a device is directly related to its geometrical occupancy. In addition, interconnections between gates are not time-independent and are subject to all the behavioral rules of a gate. This means that the library not only should encompass several gates, with multiple versions, but also interconnections. Fig. 4.8 illustrates the layout of the interconnections used in the following section for the validation of the device modeling methodology with their identification names. We simulate them using SCERPA, using $N\_clock\_step = 5$, $N\_driver\_step = 10$, and $V_{in_{MAX}} = 1\,\mathrm{V}$. Table 4.3 lists the SCERPA simulation time for the various layouts and the number of cells composing each interconnection. Once we have performed the simulations, we have all the data to extract and calculate the parameters for the library files that we previously described. The last column of Table 4.3 reports the overhead time needed to generate and store the library files. As can be seen from the table, the time for the generation of library files is negligible for interconnections comprising 20 or 30 molecular cells.

The two fundamental gates used to build other functions are the MV and the NOT gate. Even in this case, we need more than one version of this gate, which can be connected in different ways in a layout that uses them. Fig. 4.9 depicts

the layout that we use in the next section for the validation of the methodology, together with their identification names. The NOT gate is identified with 'inv'. The gate called 'invDr' is an inverter gate that also provides the output equal to the input, serving as a generic driver gate. For the 'MVlong' gate, we simulate three different output configurations. The SCERPA simulations are performed using the same parameters as before, namely $N\_clock\_step = 5$, $N\_driver\_step = 10$, and $V_{in_{MAX}} = 1\,\text{V}$. Table 4.4 reports the simulation time obtained with those parameters

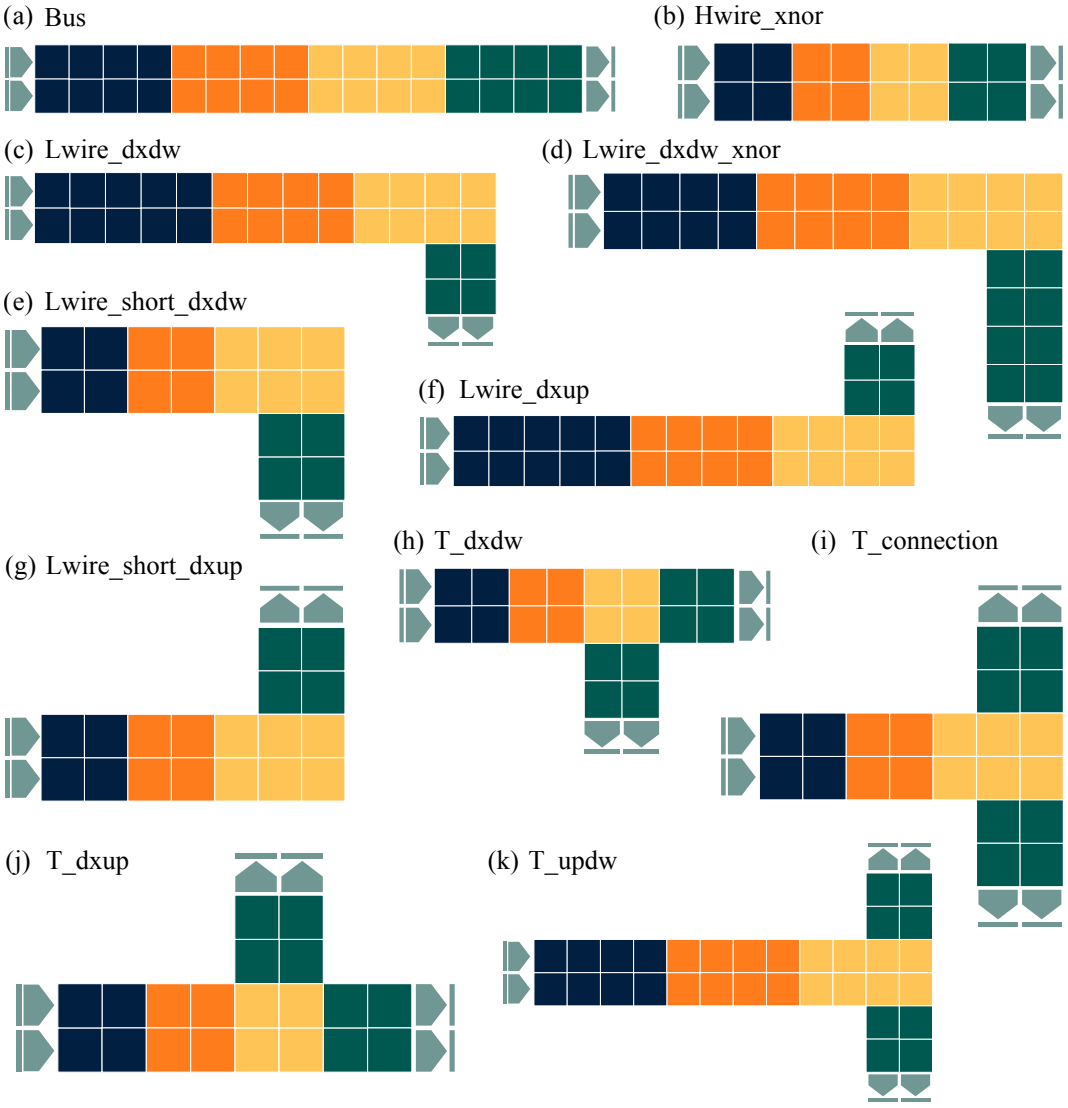

Fig. 4.8 Layout of the interconnections used in this chapter and characterized for the library. (a) Bus. (b) Hwire_xnor. (c) Lwire_dxdw. (d) Lwire_dxdw_xnor. (e) Lwire_short_dxdw. (f) Lwire_dxup. (g) Lwire_short_dxup. (h) T_dxdw. (i) T_connection. (j) T_dxup. (k) T_updw.

Table 4.3 Simulation time for a complete characterization performed with $N\_clock\_step = 5$, $N\_driver\_step = 10$, and $V_{in_{MAX}} = 1\,\mathrm{V}$, number of cells, and overhead time for generating the library files of some interconnections.

Name	Sim. time (min:sec)	# cells (-)	Lib. gen. time (s)
bus	05:14	32	0.1242
Hwire_xnor	02:24	16	0.0762
Lwire_dxdw	06:28	30	0.0904
Lwire_dxdw_xnor	07:31	32	0.0958
Lwire_dxup	07:34	30	0.0341
Lwire_short_dxdw	03:52	18	0.1068
Lwire_short_dxup	04:52	18	0.0928
T_connection	09:20	22	0.1234
T_dxdw	07:18	20	0.0786
T_dxup	09:26	20	0.1380
T_updw	12:30	32	0.1372

and the cell count. Intuitively, the time needed for the SCERPA simulation depends on the cell count: the more cells, the longer the simulation time. However, simulation time is also proportional to the number of sequential input combinations, as in the case of the MV, which, besides the limited number of cells, requires the simulation of 8 input combinations. The last factor influencing the simulation time is the number of interacting molecules, depending on clock regions distribution and number of cells per region. The last column of Table 4.4 lists the time needed for the extraction of the interesting data and the creation of the library files. Conversely to simulation time, the library files generation time demonstrates minimal variance and is negligible when compared to the simulation time.

4.2.4 Input file analysis and algorithm description

The BBchar tool is a MATLAB program for characterizing and simulating the behavior of a molFCN circuit layout designed in MagCAD. Summing up all the focal points previously described, Fig. 4.10 illustrates a flowchart of the characterization of a device.

At the beginning, we must provide several settings and parameters. The launching script begins by defining various file paths for data storage and retrieval. The main fields are:

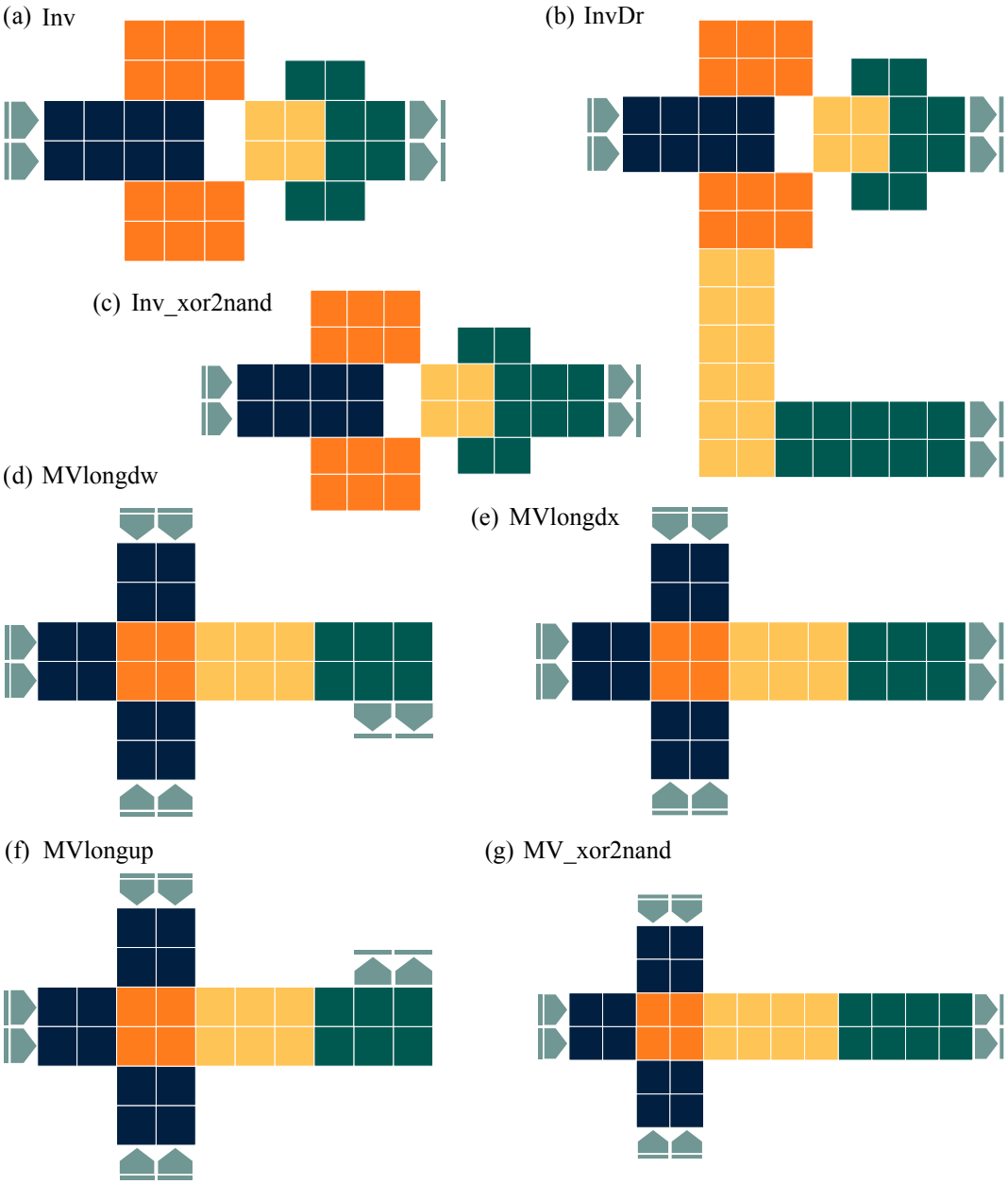

Fig. 4.9 Layout of the gates used in this chapter and characterized for the library. (a) Inv. (b) InvDr. (c) Inv_xor2nand. (d) MVlongdw. (e) MVlongdx. (f) MVlongup. (g) MV_xor2nand.

- **myDataPath**: The root path to data storage.
- **BBcharPath**: Path to BBchar program in the file systems
- **BBcharCodePath**: Path to BBchar code files.

Table 4.4 Simulation time for a complete characterization performed with $N\_clock\_step = 5$, $N\_driver\_step = 10$, and $V_{in_{MAX}} = 1\,\mathrm{V}$, cell counts, and overhead time for generating the library files of the interconnections used in this work.

Name	Sim. time (min:sec)	# cells (-)	Lib. gen. time (s)
inv	09:46	32	0.1116
invDr	29:58	54	0.1126
inv_xor2nand	09:52	34	0.1480
MV_xor2nand	33:20	32	0.1867
MVlongdw	31:33	28	0.3592
MVlongdx	29:22	28	0.2868
MVlongup	36:00	28	0.1699

- **thisPath**: Current working directory.
- **scerpaPath**: Path to SCERPA program.
- **libraryPath**: Path to the device library.
- **outputPath**: Path for storing SCERPA simulation output.
- **file**: Name of the MagCAD layout file of the DUT.

After that, we must define the parameters for the design of the input signals for drivers and clock waveforms. The main fields are:

- **clock_low** and **clock_high**: Low and high voltage levels for the clock signal.
- **clock_step**: Number of steps for each clock phase.
- **pSwitch**, **pHold**, **pRelease**, and **pReset**: Clock signal profiles for different phases.
- **pCycle**: Combined clock signal for a full simulation cycle.
- **Ninputs**: Number of physical inputs. If a driver is repeated several times in the circuit (repeated input, constant input, bus layout, etc.), it still counts as 1.
- **driverNames**: Names of the drivers as they are in the .qll layout file.
- **maxVoltage**: Maximum voltage value in volts for the drivers.

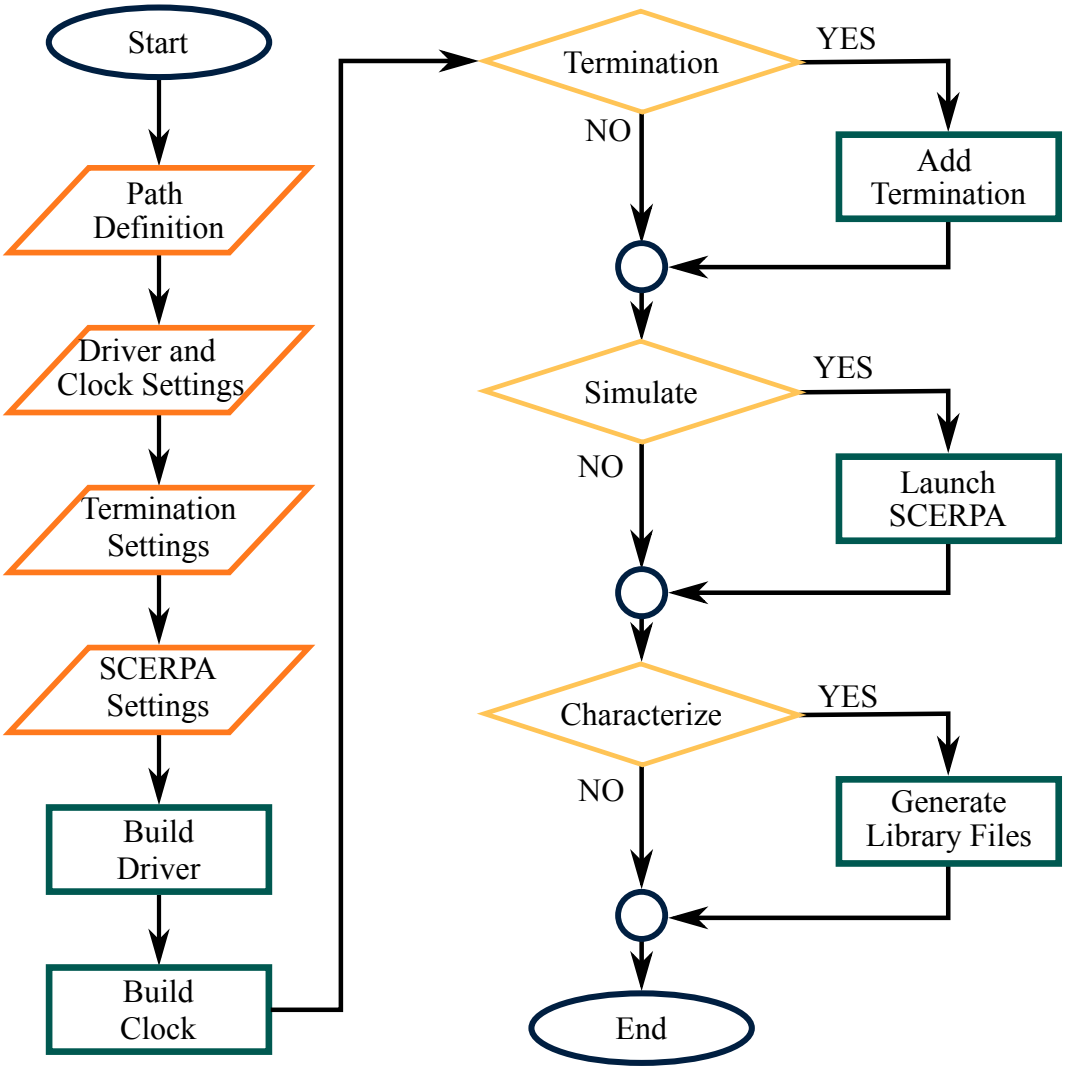

Fig. 4.10 Flowchart of the BBchar program to simulate and characterize the DUT.

- **driverModes**: Values assumed by the drivers in the simulations, can be more than 1 value at a time. The possible values are:
  - *sweep*: variation vector between '0' and '1' (voltage variation between $-maxVoltage$ and $maxVoltage$)
  - *not_sweep*: variation vector between '1' and '0' (voltage variation between $maxVoltage$ and $-maxVoltage$)
  - *0*: constant value equal to logic '0'
  - *1*: constant value equal to logic '1'

- **sweepType**: Type of sweep for driver simulation. It can be *lin* for linear variations or *log* for logarithmic variations.
- **NsweepSteps**: Number of steps in the sweep, if the driver modes specify a constant value, than it is repeated.
- **cycleLength**: Length of a complete clock cycle.
- **NclockRegions**: Number of clock regions.
- **phasesRepetition**: Number of times clock regions repeat.

Finally, we have to provide information regarding the termination circuit. The main fields are:

- **enableTermination**: Flag for enabling termination addition.
- **customLength**: Custom number of cells for termination.
- **busLayout**: Flag for bus or single line layouts.

Once we have defined the parameters for the simulations, we call the function that builds the driver and clock signal matrix for the SCERPA simulation, for which we already specified the parameters. If the user wants to simulate the device with the termination attached to its outputs, then we call the routine to generate the new layout file including the terminations and to adjust the driver and clock matrices.

Finally, if we want to simulate the DUT, we call SCERPA; otherwise, we call the characterization function. The characterization function analyzes the output files produced by SCERPA and extracts the significant data. It creates a new folder in the device library where it copies the layout used for the modeling, the generated input/output table, and a text file containing the additional information discussed previously.

The MATLAB code of the main functions is reported in Appendix B. There's an example of a launching script, the functions to build drivers and clocks, the routine to attach the termination, and the characterization function.

4.3 Validation of the block-based simulation

Once we have a populated device library, the idea is that we do not need to simulate those devices again, and we can instead use the stored values themselves. For example, if we have a NAND gate and we want to test an input combination, instead of simulating it, we interrogate the library files of the MV for the input combination we're interested in and read the output values. Those outputs become the inputs of an inverter, so we interrogate the library again. The output of the inverter coincides with the output of the NAND gate we had at the beginning.

Therefore, the main operation to perform on the library is to read from the LUT the proper value for a generic input set. If the set of input voltages is present as an entry of the LUT, then we just read the corresponding output voltages from the same entry. If the input voltages are not present in the table, then we extract the row that minimizes the distance, quantified using the Euclidean norm. Appendix B reports the code of the evaluation function, providing the output of a specified device for the required input combination.

Also, by scrutinizing the LUTs of various devices, it emerges a remarkable similarity for input combinations yielding the same logic. As an example, Table 4.5 reports the LUT of the *Inv* gate. The uniformity of the output values is a direct consequence of the termination attachment making information bistable. For this reason, the number of entries of the LUT can be reduced without losing precision on the predicted output.

Table 4.5 LUT describing the input/output behavior of a two-line inverter (*Inv*). All the values are expressed in volts.

$V_{IN\_1A\_H}$	$V_{IN\_1B\_H}$	$V_{IN\_1A\_L}$	$V_{IN\_1B\_L}$	$V_{OUT\_1A\_H}$	$V_{OUT\_1B\_H}$	$V_{OUT\_1A\_L}$	$V_{OUT\_1B\_L}$
-1.0000	+1.0000	-1.0000	+1.0000	+0.3453	-0.7601	+0.8578	-0.3568
-0.7777	+0.7777	-0.7777	+0.7777	+0.3453	-0.7601	+0.8578	-0.3568
-0.5555	+0.5555	-0.5555	+0.5555	+0.3453	-0.7601	+0.8578	-0.3568
-0.3333	+0.3333	-0.3333	+0.3333	+0.3453	-0.7601	+0.8577	-0.3568
-0.1111	+0.1111	-0.1111	+0.1111	+0.3454	-0.7600	+0.8581	-0.3566
+0.1111	-0.1111	+0.1111	-0.1111	-0.8212	+0.3628	-0.3297	+0.8222
+0.3333	-0.3333	+0.3333	-0.3333	-0.8212	+0.3628	-0.3297	+0.8222
+0.5555	-0.5555	+0.5555	-0.5555	-0.8211	+0.3628	-0.3297	+0.8222
+0.7777	-0.7777	+0.7777	-0.7777	-0.8212	+0.3628	-0.3297	+0.8222
+1.0000	-1.0000	+1.0000	-1.0000	-0.8212	+0.3628	-0.3297	+0.8222

In order to validate the characterization procedure, we tested it on some simple devices built with interconnections of MV and inverters that we characterized in the previous section. Specifically, we used the NAND/NOR, the XOR, the XNOR, and the MUX21 gates.

Fig. 4.11 shows the layout of a NAND/NOR gate, which is composed of an MV followed by an inverter. As for the MV, by fixing one of the majority voter inputs we obtain either a NAND gate (fixing a '0') or a NOR gate (fixing a '1'). The global truth table is reported in Table 4.6.

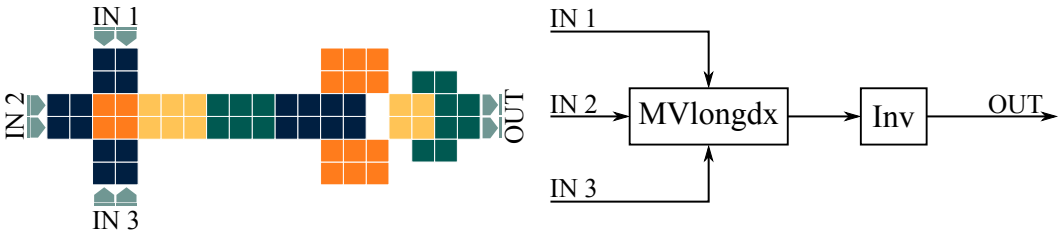

Fig. 4.11 Layout of the NAND/NOR gate with a schematic representation of the fundamental devices composing it.

First, we simulated the device in SCERPA for all the input combinations to have a reference. The simulation is performed with $N\_clock\_step = 5$ and $V_{in_{MAX}} = 1$ V as for fundamental gates and interconnections. However, in this case, we are interested solely in the functional behavior, not in the complete characterization, so we simulate only one voltage value for each combination, setting $N\_driver\_step = 1$. This situation corresponds to testing just one voltage value for each combination to obtain a basic logic correctness check of the truth table. The SCERPA simulation for the

Table 4.6 Truth table of the NAND/NOR gate, if IN 1 is fixed to '0' than we have the NAND behavior (top half), if IN 1 is fixed to '1' than we obtain a NOR gate (bottom half).

IN 1	IN 2	IN 3	OUT
0	0	0	1
0	0	1	1
0	1	0	1
0	1	1	0
1	0	0	1
1	0	1	0
1	1	0	0
1	1	1	0

eight combinations required 24 min and 8 s. For completeness, we generate the library files based on this simulation, which will present a large granularity between inputs. The time required for the library files generation is comparable to the one seen for the fundamental gates and interconnections, being 0.0838 s. The characterization time is still comparable, demonstrating that the overhead needed to create the library files is negligible.

We then compare the results provided by SCERPA for the whole device with the result obtained using the library. Starting from the input values we want to test, we access the library for the first time to read the corresponding output of the *MVlongdx* gate. Then, we use the output provided by the first access to the library to interrogate it again for the *Inv* gate, which gives us the final output voltage set. Since the device is multi-line, the output is composed of four voltages. As an example, equation (4.3) reports the output voltages of the four involved molecules obtained from SCERPA, and equation (4.4) reports the output from the library, for the input combination with all zeros considered with maximum voltage ($V_{in_{MAX}} = \pm 1\,\mathrm{V}$).

$$OUT_{SCERPA} = \begin{pmatrix} 0.3453408 & -0.7601388 \\ 0.8577583 & -0.3568273 \end{pmatrix} \mathrm{V} \tag{4.3}$$

$$OUT_{Lib} = \begin{pmatrix} 0.3453358 & 0.7601387 \\ 0.8577604 & 0.3568268 \end{pmatrix} \mathrm{V} \tag{4.4}$$

In order to validate the accuracy of the BBchar procedure, we evaluate the minimum, maximum, and average values of the difference between OUT_{SCERPA} and OUT_{Lib} for each input combination. Table 4.7 lists the obtained values for the errors, and Fig. 4.12 provides a graphical representation of the same values.

The maximum error observed across all input combinations is on the order of 100 µV. Considering that typical voltage values on molecules align closely with those presented in equations (4.3) and (4.4), mean errors fall within the range of 0.001 %. This remarkably low value underscores the extreme accuracy of the methodology proposed for device modeling and the reliable functioning of the BBchar tool. Moreover, achieving such precision comes with minimal time overhead. The time required for the library evaluation of all input combinations amounts to a few tens of milliseconds, rendering it negligible compared to the characterization time and the simulation of the entire device.

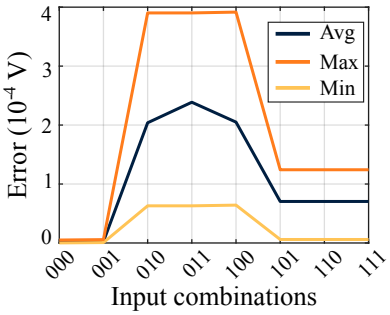

Fig. 4.12 Average, minimum, and maximum errors for the NAND/NOR gate between the output voltages calculated directly with SCERPA and using the library files.

The same procedure has been applied to the other tested devices, namely the XOR, XNOT, and MUX21 devices. Fig. 4.13 shows their layout with the subdivision into smaller blocks taken from the library.

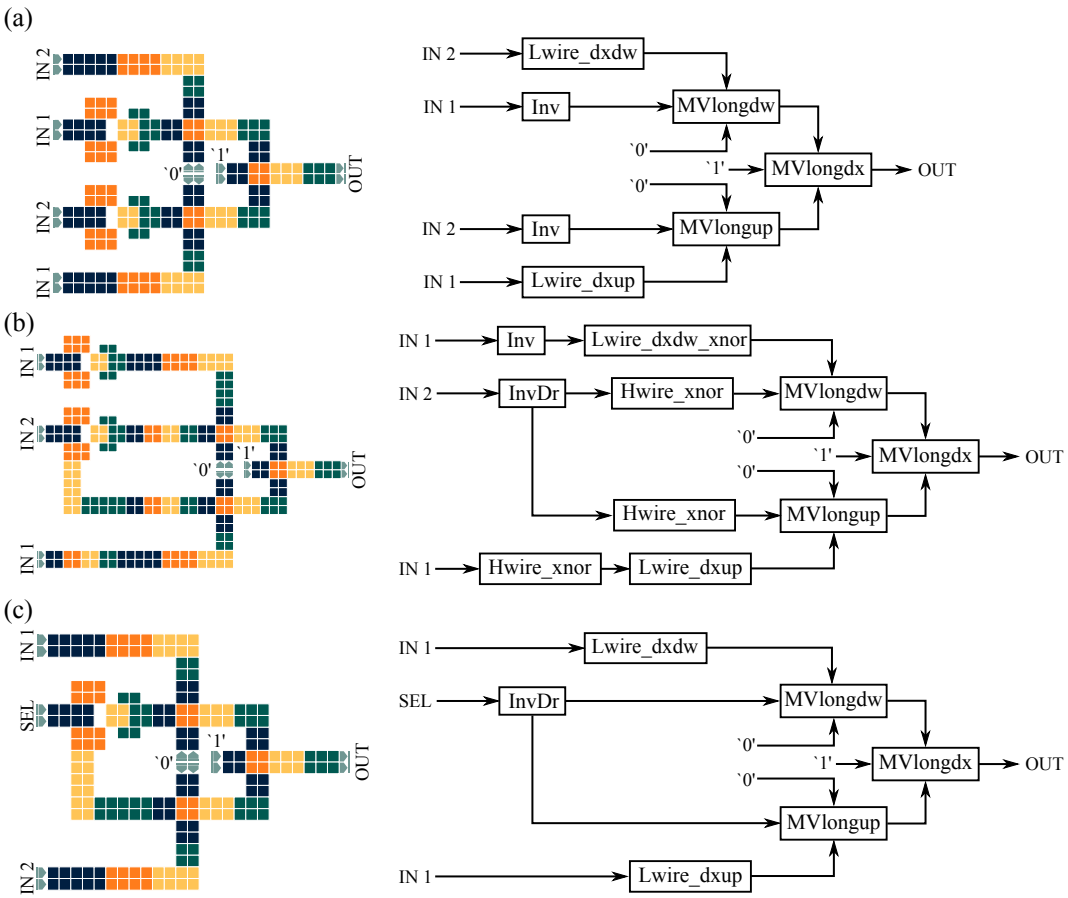

Fig. 4.13 Layout of the tested gates with a schematic representation of the fundamental device composing them. (a) XOR gate. (b) XNOR gate. (c) MUX21 gate.

Table 4.7 Average, minimum, and maximum errors for each input combination, evaluated on the molecules composing the output of the tested devices.

Gate	error	Input combinations			
		000	001	010	011
NAND	avg	1.9×10^{-6}	2.4×10^{-6}	2.0×10^{-4}	2.4×10^{-4}
	min	1.0×10^{-7}	7.0×10^{-7}	6.3×10^{-5}	6.3×10^{-5}
	max	5.0×10^{-6}	5.7×10^{-6}	3.9×10^{-4}	3.9×10^{-4}
		100	101	110	111
NOR	avg	2.0×10^{-4}	7.0×10^{-5}	7.0×10^{-5}	7.0×10^{-5}
	min	6.4×10^{-5}	5.9×10^{-6}	5.9×10^{-6}	5.9×10^{-6}
	max	3.9×10^{-4}	1.2×10^{-4}	1.2×10^{-4}	1.2×10^{-4}
		000	001	010	011
MUX21 ($s = 0$)	avg	4.3×10^{-5}	4.6×10^{-5}	1.2×10^{-4}	1.2×10^{-4}
	min	1.4×10^{-6}	2.6×10^{-5}	2.7×10^{-5}	3×10^{-6}
	max	1.5×10^{-4}	1.6×10^{-4}	2.2×10^{-4}	4.0×10^{-4}
		100	101	110	111
MUX21 ($s = 0$)	avg	6.9×10^{-5}	9.5×10^{-5}	4.5×10^{-5}	9.4×10^{-5}
	min	1.7×10^{-5}	1.2×10^{-5}	1.2×10^{-5}	1.3×10^{-5}
	max	1.1×10^{-4}	3.1×10^{-4}	7.6×10^{-5}	2.4×10^{-4}
		00	01	10	11
XOR	avg	1.3×10^{-4}	1.2×10^{-4}	6.3×10^{-5}	4.5×10^{-5}
	min	2.9×10^{-5}	4.1×10^{-6}	1.6×10^{-5}	8.0×10^{-7}
	max	2.4×10^{-4}	3.9×10^{-4}	1.0×10^{-4}	1.6×10^{-4}
		00	01	10	11
XNOR	avg	6.6×10^{-5}	4.2×10^{-5}	1.1×10^{-4}	9.4×10^{-5}
	min	1.7×10^{-5}	1.8×10^{-6}	2.5×10^{-5}	1.3×10^{-5}
	max	1.1×10^{-4}	1.5×10^{-4}	2.0×10^{-4}	2.4×10^{-4}
		00	01	10	11
XOR_2	avg	2.2×10^{-2}	1.3×10^{-2}	1.3×10^{-2}	2.2×10^{-2}
	min	6.2×10^{-3}	4.0×10^{-3}	3.9×10^{-3}	6.0×10^{-3}
	max	5.6×10^{-2}	2.6×10^{-2}	2.6×10^{-2}	5.6×10^{-2}

We compared the output voltages obtained from the SCERPA simulation of the entire device and the values obtained by the interconnection of smaller gates using the library files. Even in this case, the simulation of the whole device in SCERPA has been performed setting $N\_clock\_step = 5$, $V_{in_{MAX}} = 1\,\mathrm{V}$, and $N\_driver\_step = 1$, meaning that we only test the logic functionality of these devices.

Table 4.8 Simulation time to validate the truth table of the gate used for testing the BBchar methodology, their cell counts, and the respective overhead time for creating the library files. Simulation are performed with $N\_clock\_step = 5$, $N\_driver\_step = 1$ and $V_{in_{MAX}} = 1\,\mathrm{V}$.

Gate	Sim. time	# cells (-)	Lib. gen. time (s)
NAND/NOR	24 min 8 s	60	0.0838
MUX21	6 h 40 min 8 s	198	0.1286
XOR	4 h 19 min 59 s	208	0.1375
XNOR	9 h 5 min 9 s	280	0.1716

Starting with the same combination tested in SCERPA for the whole device, we follow the signal through the intermediate gates and use the library files to predict the values of the cascade layouts. The simulations for testing each combination using the library files last just a few milliseconds for all the devices, confirming the substantial enhancement of the simulation time using the proposed methodology. The improvement is substantial, as the simulation in SCERPA only for logic functionality last hours for each of the three devices. Table 4.8 lists the SCERPA simulation time and the cell counts, which also substantially increases with respect to the cell count of the NAND/NOR gate. For the sake of completeness, we perform the characterization of these devices to have their library files, and the last column of Table 4.8 reports the negligible time required.

Even in this case, we calculate the voltage error on output molecules to verify the precision of the simulation using the proposed device model. The obtained values for each combination are listed in Table 4.7 and graphically shown in Fig. 4.14. The errors are of the same order of magnitude as the NAND/NOR gate, confirming the accuracy of 0.001 %.

As a final validation, we implemented an XOR gate made with NAND gates, named XOR_2 hereafter and shown in Fig. 4.15 with the schematic representation of the fundamental device composing it. The NAND gate composing it is a bit longer than the one presented before, due to signal synchronization, and is here called NAND_XOR2, built up with the interconnection of an MV_xor2nand and an Inv_xor2nand. The time required for a complete characterization of the NAND_XOR2 with $N\_driver\_step = 10$, as we did for elementary gates and interconnections, becomes prohibitive. We want to test the accuracy of the procedure when one of the internal gates has a less granular LUT. The LUT of the

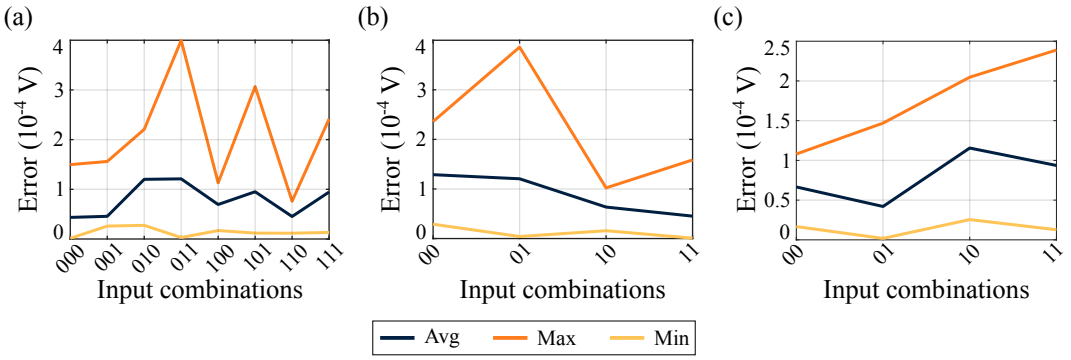

Fig. 4.14 Average, minimum, and maximum errors for the tested devices between the output voltages calculated directly with SCERPA and using the library files. (a) MUX21. (b) XOR. (c) XNOR.

NAND_XOR2 only comprises the eight entries for the input combinations obtained with the maximum voltage ($V_{in_{MAX}} = 1\,\text{V}$).

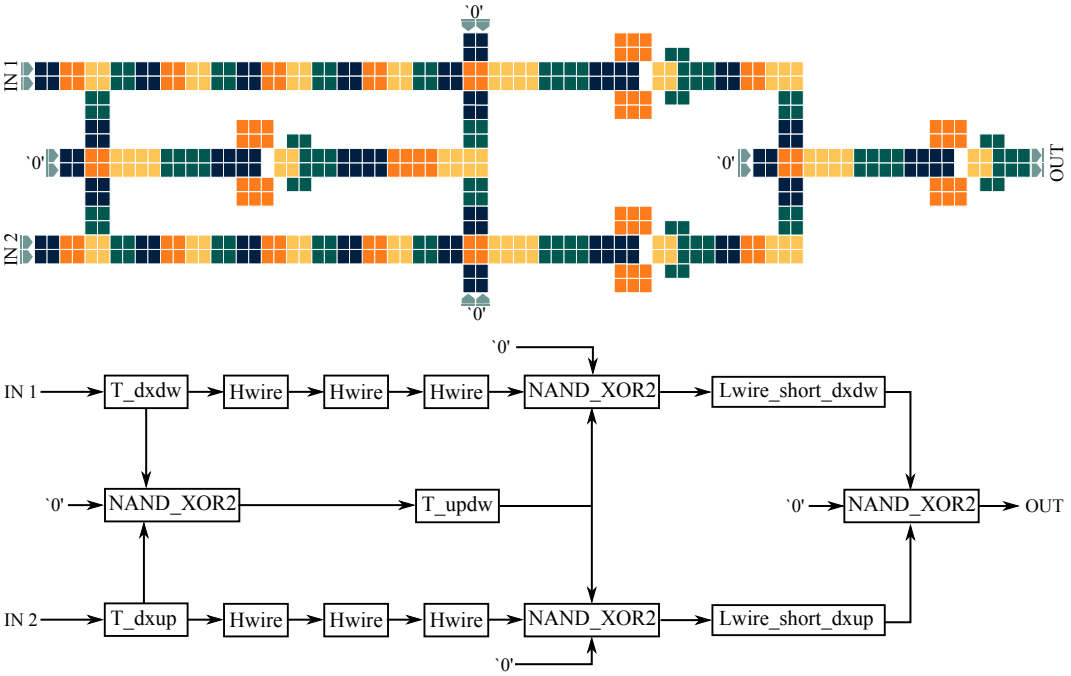

Fig. 4.15 Layout of the XOR_2 gate with a schematic representation of the fundamental device composing it.

The XOR_2 gate is made with 468 cells, and the time required for the SCERPA simulation of the four input combinations calculated with the maximum voltage required 1 d16 h43 min34 s. Even with this large design, the time required to generate the library files is comparable to others (0.2724 s). The time needed to calculate the

output using the library files is a few tens of milliseconds, demonstrating once again the huge improvement in terms of simulation time.

We test the accuracy of the library-based simulation by calculating the error with respect to the SCERPA simulation. Fig. 4.16 depicts the obtained result and the exact values are reported in Table 4.7.

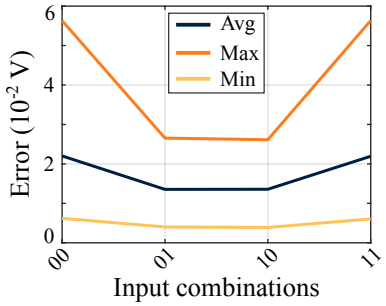

Fig. 4.16 Average, minimum, and maximum errors for the XOR_2 gate between the output voltages calculated directly with SCERPA and using the library files.

The device shows errors two orders of magnitude higher than other devices. The origin of that has to be found in the poor characterization of the NAND_XOR2 device since we only stored its output voltages for the maximum input voltages. Nevertheless, the mean error in the prediction of the XOR_2 gate is around 1 %, which is still acceptable, demonstrating the robustness of the proposed methodology to poor characterizations. The case of the XOR_2 gate also demonstrates that it is unnecessary to divide larger designs into the smallest possible gates with a fine characterization. Indeed, errors are negligible even if we do not use densely populated library files, simplifying the future design process and simulation of architectures.

Chapter 5

Interface with the external world

Previous chapters deeply investigate with a simulative approach what we can expect from a molecular Field-Coupled Nanocomputing (molFCN) device, for example depending on the molecule used, and describe the effective model at different abstraction levels that let us make such predictions. The first level is related to the single molecule study and modeling to validate and simplify the molecular behavior (Chapter 2). The second abstraction level deals with the electrostatic interaction of a bunch of molecules, and uses Self-Consistent ElectRostatic Potential Algorithm (SCERPA) to validate the expectation from the the energetic analysis (Chapter 3). SCERPA proves physically accurate and provides a set of various functionalities that address possible process variations [136]. The highest abstraction level describes how to effectively model entire devices and reuse simulation data in larger designs including them (Chapter 4). The simulations performed with Block-Based characterization (BBchar) demonstrate the combination of high accuracy with the prediction made by SCERPA, while strongly cutting simulation time.

All this work helps delineate the safe working space, excluding non-interacting molecules, or non-propagating layouts, simplifying the experimental investigation on the molFCN technology. It is established that experimental validations of the technology are hard to obtain, as introduced in Chapter 1 because of the combination of several challenging aspects. One major hurdle is the difficulty in accurately measuring molecule charges for validation purposes, which is the core procedure of experimental validation.

This chapter proposes a novel modified implementation of the molFCN paradigm, that builds upon the strengths of molFCN while addressing the challenges of reading the stored information onto a molecule [137]. The approach is named bend-boosted molFCN and exploits the spatial arrangement of fluctuating molecules to enhance information encoding capabilities. Through Density Functional Theory (DFT) simulations using 6-(ferrocenyl)hexanethiol cations, this chapter demonstrates the feasibility of this paradigm and its potential for practical implementation.

This chapter also discusses the compatibility with the existing molFCN paradigm, that here we call charge-based to differentiate it. By exploiting a molecular junction built with a 6-(ferrocenyl)hexanethiol cation, and thanks to the successful integration with charge-based molFCN, the proposed system establishes a pathway for the realization of a read-out system. This read-out mechanism not only enables experimental validation of molFCN principles but also contributes to the integration of molFCN with CMOS technology.

5.1 A new paradigm for molecular FCN

Despite its potential advantages, the practical realization of a functional prototype of molFCN faces several challenges. The obstacles include aspects from different areas of expertise. First of all, the synthesis of tailored molecules is difficult, and up to today is still missing a set of working molecules presenting the minimum requirements. Another strong challenge is related to the difficulty of precisely fabricating nanoppaterned electrodes or trenches to host the molecules, and depositing molecules onto these nanopatterned structures increases even more the task difficulty even more. Finally, it's challenging to read the charge-encoded logic information, because of the non-idealities of the possible sample and because we want the measure to not back influence the sample.

All these aspects are of great interest to researchers, and some innovative approaches have been proposed to address the challenges. Novel molecules are frequently proposed, as discussed in 2. To avoid the need for nanopatterned structures, we previously proposed to directly use uniform self-assembled monolayers for computing porpuses [99]. Additionally, advancements in scanning-probe techniques are promising for in-lab measurement of the information stored in the molecule charge distribution [81, 80]. Another solution could be the use of Raman scattering to detect

the state of the molecule at the laboratory level [138]. Regarding in-circuit reading, authors in [139] proposed to use asymmetric mixed-valence molecules to detect information. Besides the promising and interesting results over different aspects, remains challenging to put things together and have a solution that inglobates several of these aspects.

The following sections discuss a novel molFCN implementation, named bend-boosted molFCN, aimed at simplifying in-circuit and in-lab read-out operations. The laying idea is to associate the information with different molecule orientations. Different orientations mean different spatial occupations depending on the information. This association could simplify in-lab read-out, as it is established that is possible to perform atomic-precise topographic measurements [140–142]. Additionally, the proposed principle can be integrated with a molecular junction, serving as a single-molecule sensor [143].

5.1.1 Conceptual vision of the new paradigm

Starting again from the information encoding in molFCN, we associate a logic value to the charge localization in a molecule. By applying an electric field, the charge moves to different regions of the molecule, but the molecule stays ideally fixed in the same position, as reported in Fig. 5.1a with bisferrocene molecule. In the bend-boosted paradigm, the molecule is no more fixed, but able to move as a sort of inverted pendulum, with the pivot placed on a substrate.

As an example, we here use the 6-(ferrocenyl)hexanethiol cation (Fc^+C_6S) as a reference molecule, shown in Fig. 5.1b. Fc^+C_6S is a molecule known for its unique ability to form uniform Self-Assembled Monolayers (SAM)s on various substrates [144]. This compound consists of a ferrocene unit attached to a hexanethiol chain, enabling it to form robust and well-ordered monolayers through chemisorption on metal surfaces such as gold and silver. The ferrocene moiety provides stability and control over the monolayer structure, while the hexanethiol chain facilitates the attachment to the substrate, ensuring uniform coverage.

Fig. 5.1c depicts how the application of an external electric field affects the molecule if we imagine it anchored to a substrate. Being the molecule positively charged, the presence of a uniform field aligns the molecule with the field lines, but since the molecule is anchored, the resulting movement is bending. The sensibility

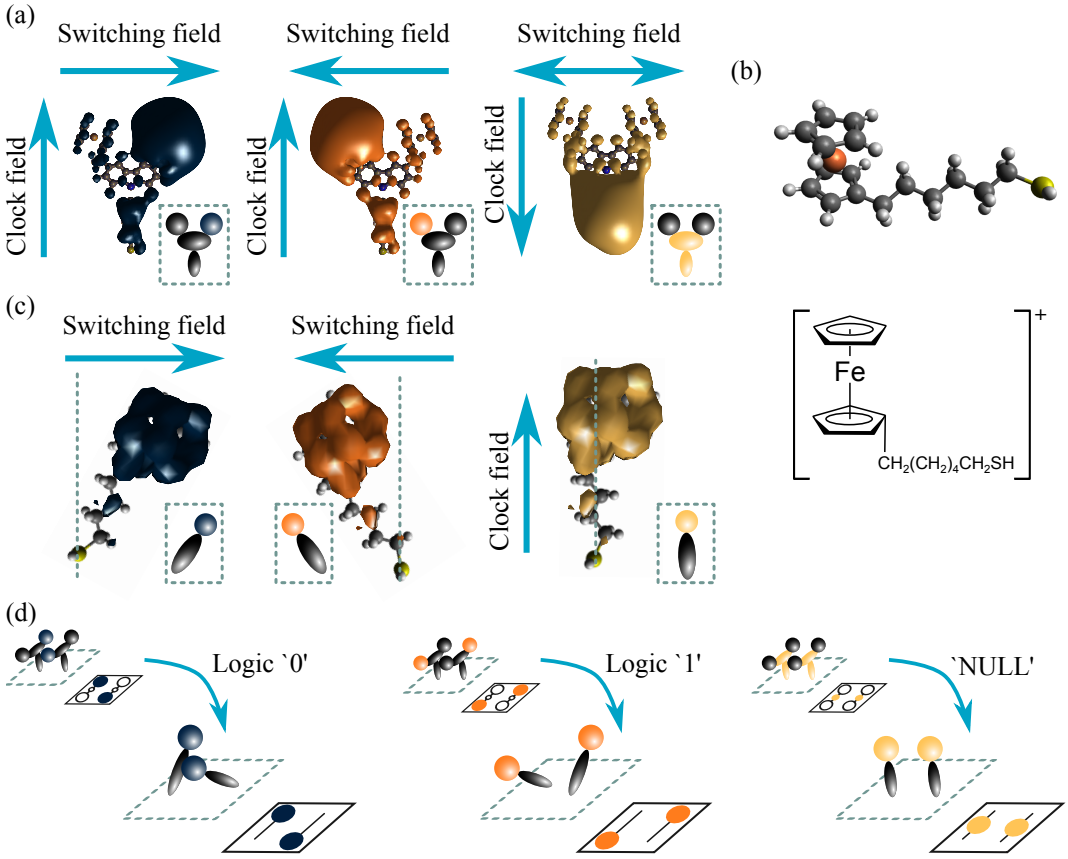

Fig. 5.1 Representation of the conceptual behavior of the bend-boosted molFCN. (a) Charge localization on the bisferrocene molecule varying the applied fields. (b) 3D geometry shown in a ball-and-stick diagram and chemical structure of the $Fc^{+}C_6S$ cation. (c) Charge localization and bending of the $Fc^{+}C_6S$ cation varying the applied fields. (d) Unit cell in the three logic states, compared to the charge-based unit cell to show the equivalence from a conceptual point of view. Atoms in figure are colored as follows: H = white, C = charcoal, N = blue, S = yellow, Fe = orange.

of the molecule to an external field guarantees the write-in operation, fundamental for driving circuits.

When we place two of these molecules next to each other, the presence of the oxidation charge will make them repel, so they'll bend in opposite directions, as shown in Fig. 5.1d. Assuming that the oxidation charge localizes on the ferrocene groups of the two $Fc^{+}C_6S$, we obtain a charge configuration equivalent to a Quantum-dot Cellular Automata (QCA) cell. The similarity of the charge behavior leads to the same logic encoding as the charge-based molFCN, so from a logical point of view, we can assume a similar gate design.

To validate the conceptual working, the next two sections analyze the isolated $Fc^{+}C_6S$ as a case of study. The results aim to validate the working principle and the encoding capabilities, proving the ground base for the development of the bend-boosted molFCN paradigm.

5.1.2 Theoretical background

The bend-boosted molFCN paradigm is based on molecular movements, meaning that we need to extend the simulation of a single molecule to the time domain. We exploit two computational techniques: Ab Initio Molecular Dynamics (AIMD) and classical Molecular Dynamics (MD).

AIMD is a computational technique used to simulate the dynamic behavior of atoms and molecules from first principles, without the need for empirical force fields [145].

In AIMD simulations, the positions and velocities of atoms are propagated forward in time using Newton's equations of motion, while the electronic structure is updated at each time step based on the instantaneous atomic configurations. These simulations are also known as Born-Oppenheimer molecular dynamics simulations. This is because they approximately solve the time-independent Schrödinger equation to calculate gradients, which are then used to guide the movement of the atoms [146].

However, AIMD also comes with computational challenges. The computational cost scales with the system size, limiting its applicability to small systems.

Unlike AIMD, classical MD simulations rely on the principle of Newtonian mechanics, where the forces acting on each atom are determined based on their interactions with neighboring atoms [147]. These interactions are typically described using interatomic potentials, which can be derived from empirical observations or calculated from quantum mechanical principles. Common types of interatomic potentials include pairwise potentials, such as Lennard-Jones or Coulombic potentials, as well as more sophisticated potentials like the reactive force field [148].

MD simulations are more computationally favorable with respect to AIMD methods, with the accuracy dependent on the accuracy of the interatomic potentials used.

In this context, we first simulate the behavior of the Fc^+C_6S with AIMD to validate the conceptual behavior. Subsequently, we compare the obtained result with a more simplistic MD simulation to verify the coherence of the results. The possibility of using MD for technological validation would release some of the computational complexity typically needed for molecular simulations.

5.1.3 Single-molecule simulation with *ab-initio* techniques

As already mentioned, we use the Fc^+C_6S cation as a reference molecule to validate the working principle. The molecule is shown in Fig. 5.2a in a ball-and-stick diagram, highlighting the two functional groups *Dot 1* and *Dot 2* associated with the ferrocene and the hexanethiol, respectively. The coordinates have been obtained from the geometry optimization of the isolated molecule with the Unrestricted Kohn-Shann (UKS) method using B3LYP functional with def2-TZVP basis set [119]. Grimme D3 correction is applied [120, 121].

The charge distribution is analyzed by exploiting the ESP-derived CHarges from ELectrostatic Potentials using a Grid (CHELPG) paradigm. Following the same procedure as in Chapter 2, we use the ORCA tool to compute the electrostatic potential produced by the molecule and shown in Fig. 5.2b, which is radial because we are analyzing the oxidized molecule. The maximum is located on the ferrocene group, suggesting where the oxidation charge localize. Fig. 5.2c shows the ESP charges on each atom, presenting maximum values on the carbon atom of the

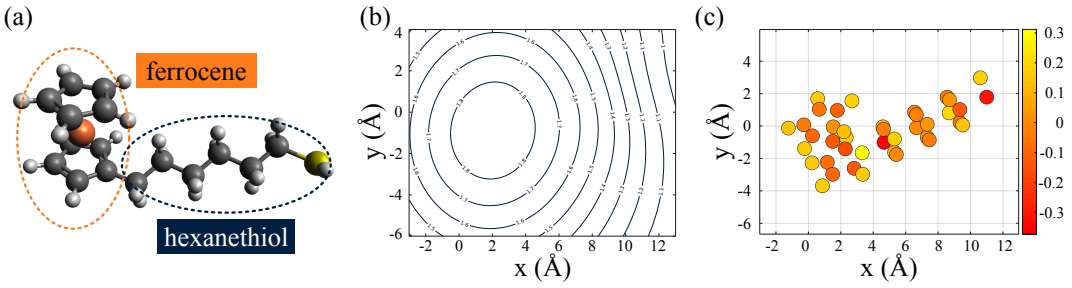

Fig. 5.2 Analysis of the isolated Fc^+C_6S cation at equilibrium through DFT simulation. (a) 3D geometry shown in a ball-and-stick diagram of the relaxed molecule highlighting the atom groups for the calculation of the aggregated charges. (b) Molecular electrostatic potential evaluated with DFT calculation, the solid blue lines are isopotential curves. (c) ElectroStatic Potential (ESP) charges on each atom of the molecule. Atoms in figure are colored as follows: H = white, C = charcoal, S = yellow, Fe = orange.

pentacene connecting to the hexane. On the contrary, the most negative charge appears on the sulfur atom of the thiol group. The confirmation of the positive charge aggregation is given also by the charge distribution shown in Fig. 5.1c, where we show the conceptual working principle of the bend-boosted molFCN paradigm.

By calculating the Aggregated Charge (AC) value on the ferrocene and the hexanethiol we obtain the following values

$$\begin{cases} Q_{Fc} = 0.9595\,\text{a.u.} \\ Q_{C6S} = 0.0405\,\text{a.u.} \end{cases} \tag{5.1}$$

confirming the positive charge aggregation on the ferrocene and the electrostatic neutrality of the hexanethiol, as already demonstrate in Chapter 2.

Because of the charge distribution, when the molecule is subjected to an electric field and acnhored to a substrate through the thiol, we can expect that the movement is dictated by the ferrocene. The hexane, being neutral, would behave as a bar holding the ferrocene.

To study the dynamic behavior of the isolated Fc^+C_6S cation we exploit AIMD and we apply an electric field in time to the molecule. The simulation of the molecule in the presence of constant electric fields is crucial to validate the working principle. As already mentioned in Chapter 2, electric fields are applied in ORCA by positioning point charges in space. Fig. 5.3 shows a 3D representation of the system consisting of the Fc^+C_6S cation and the point charges used for initiating the AIMD simulations.

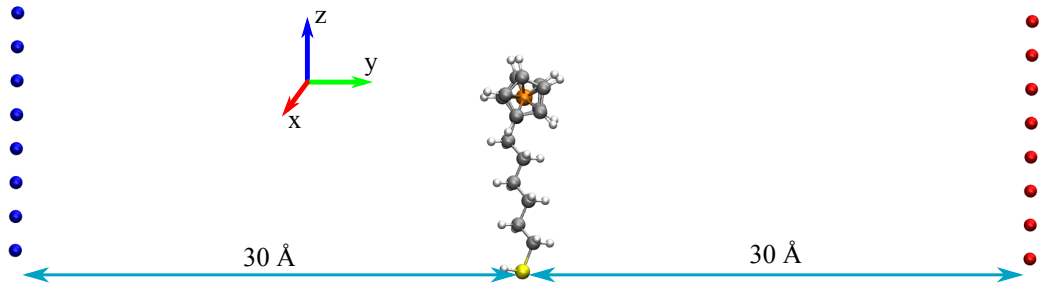

Fig. 5.3 The Fc^+C_6S cation alongside the point charges employed for generating the electric field in AIMD simulations. Negative point charges are denoted by blue dots, while positive ones are indicated by red dots. This configuration yields a positive uniform electric field aligned along the y-axis. The molecule has the sulfur atom placed in the origin of the axis. Atoms in figure are colored as follows: H = white, C = charcoal, S = yellow, Fe = orange.

Table 5.1 Values and coordinates of the point charges used to generate a uniform electric field along the positive y-axis equal to 4.9451 V nm^{-1}.

Value (a.u.)	**x** (Å)	**y** (Å)	**z** (Å)
+2	0.0	+30.0	1.0
+2	0.0	+30.0	3.0
+2	0.0	+30.0	5.0
+2	0.0	+30.0	7.0
+2	0.0	+30.0	9.0
+2	0.0	+30.0	11.0
+2	0.0	+30.0	13.0
+2	0.0	+30.0	15.0
-2	0.0	-30.0	1.0
-2	0.0	-30.0	3.0
-2	0.0	-30.0	5.0
-2	0.0	-30.0	7.0
-2	0.0	-30.0	9.0
-2	0.0	-30.0	11.0
-2	0.0	-30.0	13.0
-2	0.0	-30.0	15.0

Referring to the initial position of the molecule as identified in Fig. 5.3 with the S atom placed in the origin, Table 5.1 lists the values and positions of the point charges used to generate a uniform electric field along the positive y-axis.

The value of the electric field generated is calculated at the geometrical center ($x = 0.3145$ Å, $y = 0.0549$ Å, $z = 7.3003$ Å) of the molecule. It is computed as the sum of contributions from all point charges, as expressed by equation (5.2), where N_{pc} is the total number of point charges, ε_0 is the vacuum permittivity, q is the electron charge, pc_i is the value of the i-th point charge, and r_i is the distance between the i-th point charge and the molecule geometrical center.

$$E(x,y,z) = \sum_{i=1}^{N_{pc}} \frac{1}{4\pi\varepsilon_0} \frac{q \cdot pc_i}{r_i^2} \tag{5.2}$$

Using the charge configuration specified in Table 5.1, we obtain $E_x = 0.0003\,\mathrm{V\,nm^{-1}}$, $E_y = -4.9451\,\mathrm{V\,nm^{-1}}$, and $E_z = -0.0006\,\mathrm{V\,nm^{-1}}$. Consequently, the dominant field is along the y-axis, and the other components can be neglected. By

following the same procedure but changing the sign of the point charges, a positive uniform electric field equal to $E_y = 4.9451\,\mathrm{V\,nm^{-1}}$ can be obtained.

We thus perform two AIMD simulations, applying an electric field equal to $\pm 4.9451\,\mathrm{V\,nm^{-1}}$, respectively. The value of the electric field is high with respect to typical fields we used in DFT simulation in Chapter 2. The choice helps limiting the computational time required by the simulation of the complete molecule bending. The next section will verify the paradigm under reduced electric fields and extended durations using classical molecular dynamics simulations.

In Fig. 5.4 is represented the molecule behavior obtained from the AIMD simulations for both the positive and negative field. The blue dot are the atoms in the initial position, corresponding with the 'NULL' state. The simulation reproduces the case in which the clock field is instantaneously released and the molecule can thus bend on one side or another depending on the surrounfing electric field. During the simulation, the thiol group is fixed to the same coordinates, emulating the anchoring to a substrate placed on the plane $z = 0$. After 3 ps, the molecule reaches the position represented with the orange dot configuration, and the iron atom of the ferrocene follows the dotted light blue line.

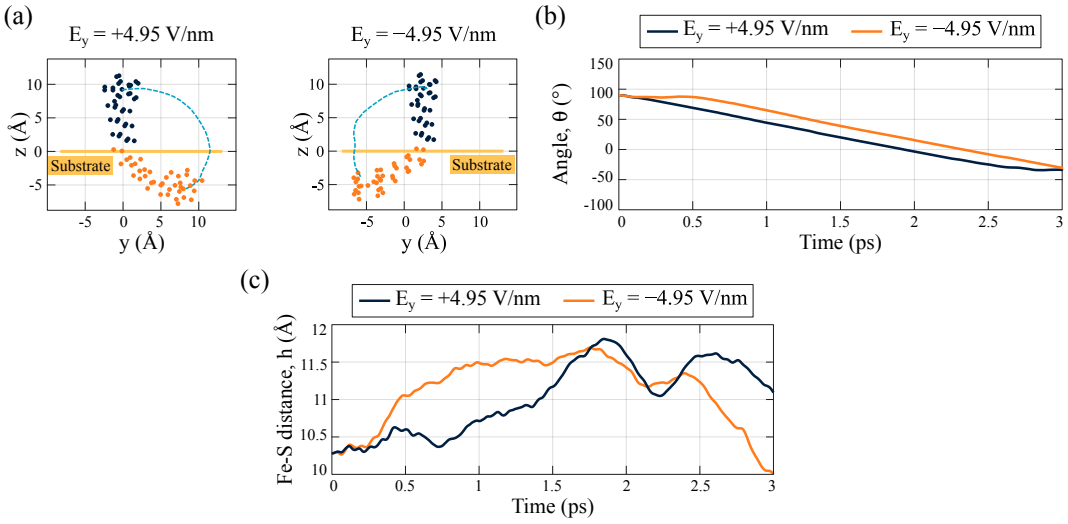

Fig. 5.4 Results of the AIMD simulation of the $Fc^{+}C_6S$ cation. (a) Simulation with a costant electric field ($E_y = \pm 4.95\,\mathrm{V\,nm^{-1}}$). The light blue dotted line represents the trajectory followed by the Fe atom from the starting position (blue dots) and after 3 ps (orange dots). The molecule rotates around the thiol group $-$SH, fixed on the fictitious substrate line. (b) Temporal evolution of the angle (θ) between the Fe$-$S segment and the plane $z = 0$ where the molecule is anchored. (c) Temporal evolution of the Fe$-$S distance (h) during the AIMD calculation.

When the applied field is positive, the molecule bends clockwise, whereas the negative field bends the molecule counterclockwise around the anchoring point. Since the simulation are performed with the isolated molecule, the molecule can overcome the plane $z = 0$, as the absence of the substrate is reflected in a missing repulsive force that blocks the molecule. The molecule behaves similarly for both fields and the angular rotation has the same amplitude, demonstrating encoding capability and equivalent movements.

Fig. 5.4b illustrates the progression of the angle (θ) between the Fe−S segment and the substrate line ($z = 0$) over the course of the simulation. The angle measurements are referenced to the positive y-axis for clockwise rotation and the negative y-axis for counterclockwise rotation to ensure comparability. At its maximum value ($\theta = 90°$), the molecule is in the 'NULL' state, perpendicular to the substrate. The graph in Fig. 5.4b showcases a linear bending dynamic, where the molecule undergoes controlled rotation. The rotational speed is almost identical between different electric field directions, measuring approximately $0.0528\,\mathrm{deg/fs}$ for the negative field value and $0.0522\,\mathrm{deg/fs}$ for the positive one. The curve for the angle also show a small plateau at the begging or at the end of the simulations, modeling a sort of inertia of the molecule to variation from the equilibrium position. The difference in the plateau can be a consequence of the asymmetry of the anchoring point, as the molecule show resistance to bend on the side where there is the hydrogen atom of the thiol, i.e., toward negative y-axis.

Fig. 5.4c provides insights into the Fe−S distance (h) during the simulation. The average strains recorded for the two electric fields are $1.1131\,\text{Å}$ and $1.1026\,\text{Å}$, respectively. Comparatively, the equilibrium value is $h = 1.0283\,\mathrm{nm}$, indicating relative strains of 10.8% and 10.7%, respectively. These results suggest that the molecule experiences minimal strain during the rotational movement, underscoring its rigid-bar behavior. This observation is significant as it emphasizes the structural stability of the hexanethiol under the influence of external electric fields, which is crucial for its functional integrity The results also confirms the expectations of the hexanethiol behaving as a rigid-bar connecting the ferrocene to the substrate.

For the paradigm definition, the encoding dynamic range is delineated by the angles $\theta = 90°$ and $\theta = 0°$. We adapt to the traditional definition of rising (falling) time as defined for CMOS technology, i.e., the time required for a transition between 10% and 90% (90% and 10%) of the full dynamic. Thus, we define the encoding time

(τ_e) as the time required to transition from $\theta = 81^\circ$ to $\theta = 9^\circ$, representing 90% and 10% of the total encoding dynamic, respectively. For the performed simulations, the encoding time is $\tau_{e,cw} = 1381.4180\,\text{fs}$ for the positive field (clockwise rotation) and $\tau_{e,ccw} = 1421.6907\,\text{fs}$ for the negative field (counterclockwise rotation). On average, the molecule switches in $\overline{\tau_e} = 1401.5544\,\text{fs}$.

To estimate the maximum switching frequency, we consider driving the molecule from the 'NULL' state ($\theta = 90^\circ$) to encode a specific logic value and then resetting it to replicate an entire switching operation. For instance, we imagine the molecule tilting to $\theta = 0^\circ$ with a clockwise rotation and subsequently returning to the standing configuration with a counterclockwise rotation.

To complete the switching dynamic, we should simulate also the reset condition, where the molecule is initially laying on the substrate ($\theta = 0^\circ$) and we apply the clock field to make the molecule standing up again. For consistency, from that simulation we could extract the reset time (τ_r) as the time required to transition the molecule from 9° to 81°. However, from the simulation described previously, we obtained very similar encoding times for both rotations, where differences are due to constraints on the thiol group. Given the similarity between the encoding time, we can approximate the reset time to be equivalent to the switching time corresponding to the same rotation. In simpler terms, if the encoding time is $\tau_{e,cw}$, the reset time is approximately $\tau_{e,ccw}$, and vice versa. This approximation allows us to have a first-order approximation of the expected frequency at which the molecule can switch states, crucial for assessing the operational limits and performance of molecular-scale information processing systems.

Considering the previous assumptions, the complete switching operation is performed in a time equal to $\tau_{e,cw} + \tau_{e,ccw}$, giving a switching frequency (f_{sw}) for $E_y = \pm 4.9451\,\text{V nm}^{-1}$ of:

$$f_{sw} \approx \frac{1}{\tau_{e,cw} + \tau_{e,ccw}} = 356.75\,\text{GHz} \tag{5.3}$$

The obtained value provides an initial estimation of the achievable switching frequency. In addition to approximating the reset time as the encoding time with the same rotation, it's essential to note that the simulations are conducted without a substrate, which could potentially attract or repulse the molecule, thus impacting the effective dynamics by either accelerating or slowing down the process. Furthermore,

the encoding time calculation does not incorporate potential delays in the first and last femtoseconds, such as the time required for the molecule to move out of equilibrium commented before. Conversely, it's conceivable to achieve encoding with lower angles, allowing for a reduction in the switching time. This acknowledgment underscores the need for further refinement and consideration of various factors to provide a more accurate assessment of the switching frequency achievable in practical applications.

5.1.4 Single-molecule simulation using molecular mechanics

The results obtained with the AIMD calculations suggest the feasibility of utilizing electric fields to encode information through the bending of $Fc^{+}C_6S$. However, the simulations are done with quite high electric field values to reduce the computational time as already stated. Indeed, we can expect that the intensity of the applied electric field is directly related to the velocity of the molecule to cross the substrate line. Reducing the electric field would thus reduce the maximum obtainable switching frequency, although offering the potential for reducing associated power dissipation.

To explore this further while mitigating computational costs, we employ classical MD simulations, initially validating the approach with the same field values used in the AIMD simulations. Thus, starting from the same initial configuration, we conduct dynamic simulations over a period of 3 ps, applying electric fields of $E_y = 4.9451\,\mathrm{V\,nm^{-1}}$ and $E_y = -4.9451\,\mathrm{V\,nm^{-1}}$. Considering the results from the AIMD simulations, where the molecule exhibited rigidity during bending, we treat the molecule as a rigid system in the MD simulations. In these simulations, the only permitted movements are stretches of the S-molecule bond and rotations around the sulfur anchoring point, simulating its interaction with an imaginary substrate. This approach allows for a more detailed exploration of the dynamics of the system under lower electric field intensities, yet is an approximation of the actual complexity of the system.

Fig. 5.5a displays the overlay of the final configurations of the molecule obtained through both AIMD and MD simulations after 3 ps, along with the trajectory traced by the iron atom. Notably, the last configurations exhibit remarkable similarities between the two approaches, with minor variations attributed to the differences in molecular rigidity observed in MD simulations. Particularly, significant differences

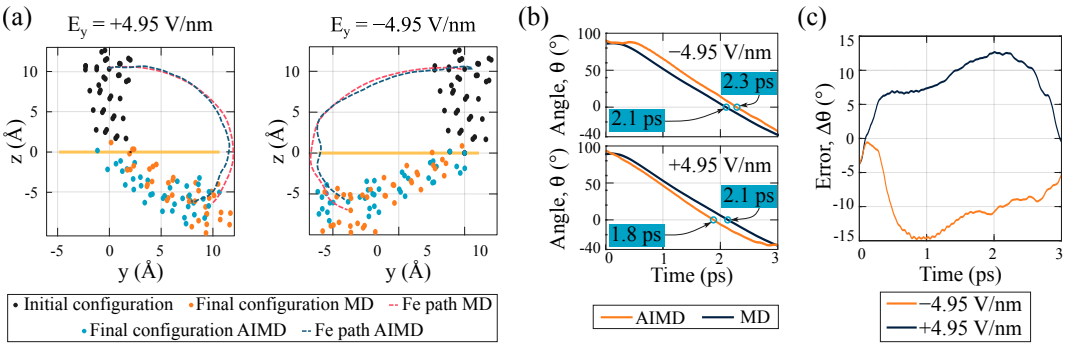

Fig. 5.5 Results of the MD simulation of the Fc^+C_6S cation compared to the results obtained with AIMD. (a) Comparison of AIMD and MD trajectories of the Fc^+C_6S cation when subjected to positive and negative electric fields. The blue/red dotted line represents the movement of the Fe atom in the AIMD/MD simulation from the starting position (black circles) and after 3 ps (light blue/orange circles). (b) Comparison of the angle created by the Fc^+C_6S cation along the evolution of AIMD and MD simulations, with both a positive and a negative electric field. The points highlighted identify the time value where the angle θ equals 0°. (c) Absolute error between MD and AIMD in the angle created by the Fc^+C_6S with the substrate for both positive and negative driving electric fields.

emerge when the molecule aligns with the y-axis, experiencing the maximum impact of the applied electric field, leading to slight deformations. In MD simulations, these deformations manifest primarily as elongations in the bond between S and the hexane, owing to the rigid nature of the rest of the system. Despite the simplified model utilized in MD, the trajectory closely mirrors the more detailed AIMD calculation, demonstrating the reliability of the results obtained from both simulation methods.

Fig. 5.5b provides further insights into the comparison by depicting the angle between the molecule and the $z = 0$ plane during both AIMD and MD simulations, with emphasis on the points where $\theta = 0°$. Remarkably, the MD curves exhibit almost identical behavior for both positive and negative fields due to the rigid nature of the system. Additionally, the steepness of the curves appears comparable in AIMD and MD for both field orientations. In the case of the two MD simulations, the encoding times are determined to be $\tau_{e,cw} = 1495.4204\,\text{fs}$ for the positive field (clockwise rotation) and $\tau_{e,ccw} = 1488.5061\,\text{fs}$ for the negative field (counterclockwise rotation), resulting in a lower switching frequency compared to AIMD. The switching frequency equals $f_{sw} \approx 335.129\,\text{GHz}$, evaluated using equation (5.3).

The primary difference between AIMD and MD emerges in the initial femtoseconds, affecting the calculated switching time values. Specifically, in AIMD simulations, the initial resistance of the molecule to movement varies depending

on the direction of the applied field. Conversely, this initial resistance is absent in MD simulations due to the simplification of the model. This variation in the initial instants leads to discrepancies in the angle measurements. Fig. 5.5c illustrates the differences in the angle between AIMD and MD simulations for both positive and negative electric fields. Notably, during the transient phase, the error may be significant (approximately $\sim 15^{\circ}$), primarily attributed to the assumption of a rigid molecule model in MD. However, the trajectory followed by both AIMD and MD converges toward the end of the simulation, indicating the feasibility of employing MD to estimate the behavior of the paradigm with minimal loss in precision.

Since both AIMD and MD simulations yield consistent results, yet with MD simulations offering faster computation times, we leverage the latter to validate the behavior across various applied electric fields and assess the switching time. Fig. 5.6a collect the temporal variation of the angles formed by the molecule with the $z = 0$ plane for the tested field values. It is observed that reducing the field intensity decelerates the bending of the molecule and amplifies the discrepancies between opposite signs of the same field, while still preserving the fundamental principle of the paradigm. Notably, for smaller fields, the angle requires more time to traverse the $z = 0$ plane, where the hypothetical substrate is located.

The switching time, depicted in Fig. 5.6b, exhibits variation with the driving electric field as a consequence of the variation in the bending velocity. The dashed line represents the average encoding time $\tau_{e,\mu} = 2.1\,\text{ps}$. It is evident that reducing the applied field intensity prolongs the switching time. For instance, with a field of $E_y = -0.4945\,\text{V nm}^{-1}$, the switching frequency is approximately $f_{sw} \approx 186.440\,\text{GHz}$, as calculated using equation (5.3), indicating that halving the applied field decreases the frequency by half. Furthermore, beyond a certain threshold, increasing the driving field results in a disproportionate increase in power consumption without yielding significant improvements in frequency performance. For instance, with $E_y = -7.4177\,\text{V nm}^{-1}$, the frequency is approximately $f_{sw} \approx 349.075\,\text{GHz}$, signifying that a 33% increase in the field only yields a roughly 4% increase in frequency.

To further explore the behavior of the molecule over an extended duration, we exploit MD to perform a simulation that surpasses the typical timeframes utilized in previous analyses. By applying an electric field along the y-axis, we expect the $Fc^{+}C_6S$ molecule to align with the substrate plane $z = 0$. Fig. 5.6c depicts the angle oscillations around the y-axis when the driving electric field is set to $2.48\,\text{V nm}^{-1}$.

The dashed lines delineate the region where oscillations settle below 9°, representing 10% of the encoding dynamic. This simulation corroborates the alignment of the molecule with the applied field. Furthermore, the angle exhibits characteristics indicative of an underdamped second-order system, with two complex conjugate roots, as it approaches the regime value.

Introducing a substrate is expected to impact the molecule's behavior significantly. Specifically, the attraction and repulsion exerted by the substrate may either speed up or decelerate the bending of the molecule, thereby altering the settling angle. Subsequent research endeavors should explore the electrostatic influence exerted by the substrate and the potential for charge exchange between the two entities. Additionally, exploring the effects of different substrate materials must be investigated in future research.

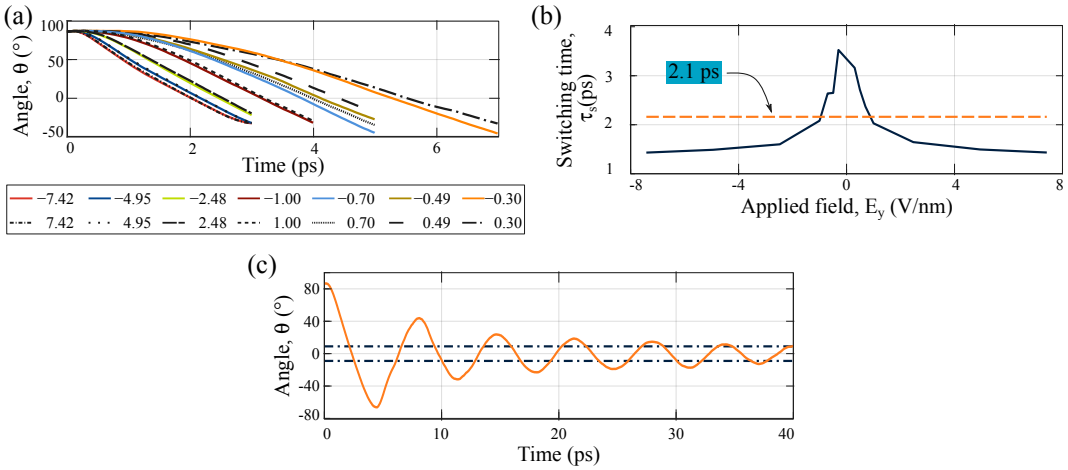

Fig. 5.6 Results of the MD simulation of the Fc^+C_6S cation for various applied electric field. (a) Angle θ ceated by the Fc^+C_6S with the substrate plane ($z = 0$) calculated with MD for different electric fields. The smaller the applied field, the slower the molecule to reach the substrate. (b) Switching time evaluated as the difference between the time needed to move from an angle of 81° to 9° (i.e., 90% and 10% of the total dynamic, respectively) varying the intensity of the electric field. (c) Angle θ created by the Fc^+C_6S with the plane $z = 0$ calculated with a long MD simulation when the driving field equals $2.48\,\mathrm{V\,nm^{-1}}$. The angle oscillated around 0°, which is the expected regime value. The black dotted line identifies the range between −9° and 9° (i.e., ±10% of the switching dynamic).

5.2 Read-out architecture

The comprehensive analyses presented in the previous section demonstrate the potential of utilizing an electric field to encode binary information into the bending of the molecule. It is noteworthy that various cations possess the capacity to generate an electric field, which could drive neighboring molecules, thereby facilitating the propagation of information. However, successful information propagation depends on overcoming steric hindrance during the molecular rearrangement process. While a detailed examination of logic propagation and elaboration is deferred to subsequent studies, it is imperative to highlight the promising readout capabilities offered by the bend-boosted molFCN mechanism. This mechanism enables the detection of encoded information at the laboratory level by measuring the orientation of the molecule through scanning probe microscopy [142]. Such advancements hold significant implications for the future development and practical application of molFCN.

The bend-boosted molFCN concept offers the possibility of integration with the charge-based paradigm, presenting exciting prospects for enhanced functionality and experimental validation. Notably, prior research has highlighted that the bis-ferrocene cation can generate switching fields within the range of $[-0.4; 0.4]\,\mathrm{V\,nm^{-1}}$ [62], which align with the requirements for driving the bending mechanism as elucidated in the previous section. Consequently, the electric field produced by the bis-ferrocene molecule, serving as a representative example, holds the potential to serve as a driving signal for the $Fc^{+}C_6S$ molecule.

By integrating bend-boosted molFCN with the charge-based paradigm, it becomes feasible to conduct in-lab measurements of charge-based molFCN logic using scanning probe microscopy. This integration offers significant advantages, facilitating the assessment and validation of charge-based molFCN technology under controlled laboratory conditions. Such synergistic integration holds promise for advancing our understanding of molecular field-coupled nanocomputing and unlocking its full potential for future technological applications.

In the following sections, we illustrate the modulation of current in a molecular junction, which is facilitated by the encoded information stored within the molFCN system. This capability enables real-time readout directly within the circuit, providing a means for evaluating the performance and feasibility of molFCN technology.

Furthermore, this in-circuit readout capability opens possibilities for exploring the integration of molFCN with CMOS technology. By integrating molFCN functionality into existing CMOS architectures, we can exploit the benefits of both technologies, paving the way for novel computing paradigms and enhanced device functionalities.

5.2.1 Theory of electronic transport

The molecular junction used for the readout system is analyzed by exploiting the Non-Equilibrium Green's Functions (NEGF) formalism. The NEGF formalism is a theoretical framework used to study quantum transport phenomena in nanoscale electronic devices [149]. It provides a rigorous mathematical description of electron transport in systems where quantum effects dominate. NEGF is particularly well-suited for modeling devices operating far from thermal equilibrium, where traditional transport theories based on equilibrium assumptions fall short.

The NEGF formalism provides a rigorous treatment of electronic conduction through molecular systems by accounting for contact self-energies and broadening functions, which reflect the influence of molecular contacts on conduction. These factors allow for a comprehensive description of the system's response to external stimuli.

Moreover, the transmission coefficient derived from NEGF facilitates the calculation of current flow through the system, enabling researchers to evaluate electronic transport properties with greater precision. Landauer's equation, integrated within the NEGF framework, offers insights into ballistic transport phenomena, while the flexibility of NEGF allows for the modeling of incoherent scattering effects, further enhancing its applicability to real-world scenarios.

The simulations described in the following section are performed using QuantumATK [150, 151]. The geometry relaxation process is carried out utilizing employing DFT calculations at the generalized gradient approximation (GGA) level within the Perdew, Burke, and Ernzerhof (PBE) framework. A double-ζ plus polarization (DZP) basis set is employed for all elements except gold, for which a single-ζ plus polarization (SZP) basis set is utilized.

To simulate the transport process, Dirichlet Boundary Conditions (DBC) are applied in the transport direction, while Periodic Boundary Conditions (PBC) are implemented in the transverse directions. The limited memory quasi-Newton method

for large-scale optimization (LBFGS) optimization algorithm is employed, with a force tolerance set to $0.05\,\mathrm{eV/Å}$ and a maximum step size of $0.02\,\mathrm{Å}$. These computational techniques ensure efficient and accurate relaxation of the molecular configurations, enabling reliable predictions of transport properties in the $Fc^{+}C_6S$-gold junction system.

The electronic structure properties of the $Au{-}FcC_6S$ junction are thoroughly investigated using QuantumATK, employing DFT calculations with GGA-PBE exchange-correlation functional. To accurately capture the electronic interactions, Hubbard (on-site - shell) corrections are incorporated for exchange-correlation terms.

For the atomic basis sets, a SZP basis set is employed for gold (Au), while a DZP basis set is utilized for the other elements involved. The Brillouin zone integration is carried out using a Monkhorst-Pack grid with (3,1,135) k-points.

To accurately describe the electronic structure in both equilibrium and non-equilibrium situations, a sparse recursion method for self-energy calculation is employed. Additionally, an additional continuum spatial region is introduced within the simulation boundary cell. This region allows for the consideration of the vanishing electrostatic potential, mimicking the behavior in a dielectric substrate. By incorporating this continuum spatial region, abrupt potential decay to zero at the simulation cell boundary is avoided, ensuring more accurate and physically realistic simulations of the $Au{-}FcC_6S$ junction.

5.2.2 Charge sensing

This section illustrates how bend-boosted molFCN facilitates the integration of molFCN with standard current-based technologies, and ultimately with CMOS technology. As depicted in Fig. 5.7a, the setup for information readout involves a single $Fc^{+}C_6S$ cation anchored to a nanowire (NW) positioned within a metallic nanogap, adjacent to a charge-based molFCN wire. The metallic nanogap comprises electrodes labeled as E0 and E1, allowing for a tunneling current between either E1 or E0 and the NW via the molecule.

The encoded information alters the orientation of the $Fc^{+}C_6S$ molecule, consequently affecting its distance from the electrodes. For instance, when the molecule encodes a logic ‘1’, the ferrocene group moves closer to E1, enhancing the tunneling current through the E1 electrode while significantly reducing the current through

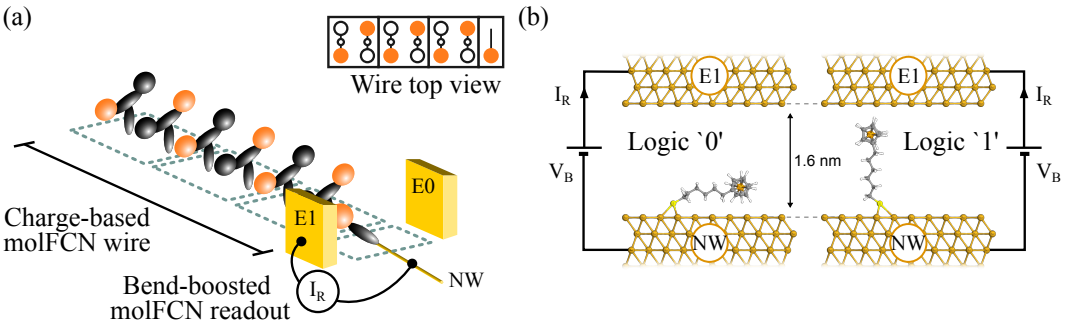

Fig. 5.7 Architecture of the readout system based on bend-boosted molFCN. (a) Charge-based molFCN wire propagating a logic '1' terminated with a Fc^+C_6S cation placed between two electrodes (E0, E1) for the conductive measurement. Molecules are supposed anchored to an ideal nanowire (NW). The schematic amperometer measures the readout current (I_R). (b) Geometries used to study the conduction between the electrode E1 and the nanowire NW with DFT. In the left figure, the cation encodes a logic '0' (far from the E1 electrode), whereas in the right figure the cation encodes a logic '1' (close to the E1 electrode). A bias voltage (V_B) is applied between E1 and NW.

E0. Conversely, when encoding a logic '0', the ferrocene group shifts towards E0, enabling the conversion of the information into a current.

This operational principle is demonstrated through modeling a Fc^+C_6S single-molecule junction, showcasing two distinct configurations as depicted in Fig. 5.7b. These configurations arise from a geometric relaxation of the pre-optimized Fc^+C_6S structure, representing logic '0' (Fc positioned away from E1) and logic '1' (Fc situated near E1), respectively. In this model, the cation is anchored onto a face-centered-cubic (111) gold substrate, specifically a 10x4 atoms slab. The distance between E1 and the NW is set to 1.6 nm, with both E1 and NW contacts fabricated from gold.

The configurations utilized for the transport measurements are generated by initially specifying a tilting angle as the initial guess for the Fc^+C_6S molecule anchored to the gold substrate, with a Au−S distance set to 2.39 Å according to literature values [152]. Subsequently, these configurations undergo relaxation using DFT simulations, wherein the Fc^+C_6S molecule is relaxed together with the first layer of gold atoms while keeping the remaining gold atoms fixed.

To verify the functionality of the readout structure, we assess the electronic transport properties of the junction using both DFT and NEGF methodologies. The transport equations are solved self-consistently with the system electrostatics, calculated by solving Poisson equation with the parallel conjugate gradient method

with DBC in the transport direction and PBC in the transverse ones. The readout current I_R is computed through a Landauer-like formula for current [153]:

$$I_R = \frac{2q}{h} \int_{-\infty}^{+\infty} T(E, V_B) \left[f_{NW}(E) - f_{E1}(E) \right] dE \tag{5.4}$$

where h is the Planck constant, E is the electron energy, V_B is the bias voltage, and f_{NW} and f_{E1} are the electrode Fermi-Dirac distributions. $T(E, V_B)$ is the transmission function representing the NW-to-E1 electron transmission probability of the device. Six bias points are considered from $V_B = 0\,\mathrm{V}$ to $V_B = 1\,\mathrm{V}$. In each of them, the $T(E)$ function and its integral (5.4) in the following are calculated considering an energy array from -1 eV to 1 eV with 201 values; transverse k-point (Monkhorst grid) (7,3); Krylov method for self-energy calculation.

In Fig. 5.8a, we present the resulting readout current I_R as a function of the applied bias voltage (V_B) between electrodes E1 and NW for both configurations. In the logic '1' configuration, a notable current I_R is observed. For instance, at a bias voltage of $V_B = 0.4\,\mathrm{V}$, the readout current is measured at $I_R = 32.53\,\mathrm{nA}$. Conversely, in the logic '0' configuration, the current is zero, indicating a clear distinction between the two logic states. This confirms the efficacy of the readout structure in accurately detecting and distinguishing between different logic states based on the molecular orientation.

By analyzing the transmission spectrum $T(E)$, we aim to elucidate the underlying cause of the current discrepancy. In Fig. 5.8b, $T(E)$ is depicted as a function of the energy shift (E) with $V_B = 0.4\,\mathrm{V}$ held constant. Here, $E = 0\,\mathrm{eV}$ represents the equilibrium Fermi level of the system. The inset in Fig. X provides a closer look at $T(E)$ within the range $[-0.4, 0]$ eV. Notably, a discernible peak in electron transmission probability emerges in the logic '1' configuration, with a peak value of $T(E) = 0.682$ observed at $E = -0.15\,\mathrm{eV}$. These peaks in transmittivity predominantly occur at negative energy levels, corresponding to occupied $Fc^{+}C_6S$ molecular orbitals. Specifically, the conduction is primarily governed by the Highest Occupied Molecular Orbital (HOMO). Conversely, in the logic '0' configuration, electron transmission probability remains negligible across all considered energy values, resulting in negligible I_R.

Moreover, by examining the NW-to-E1 Transmission Pathways (TP) at a bias voltage of $V_B = 0.4\,\mathrm{V}$ and an energy level of $E = -0.15\,\mathrm{eV}$, we discern the underlying

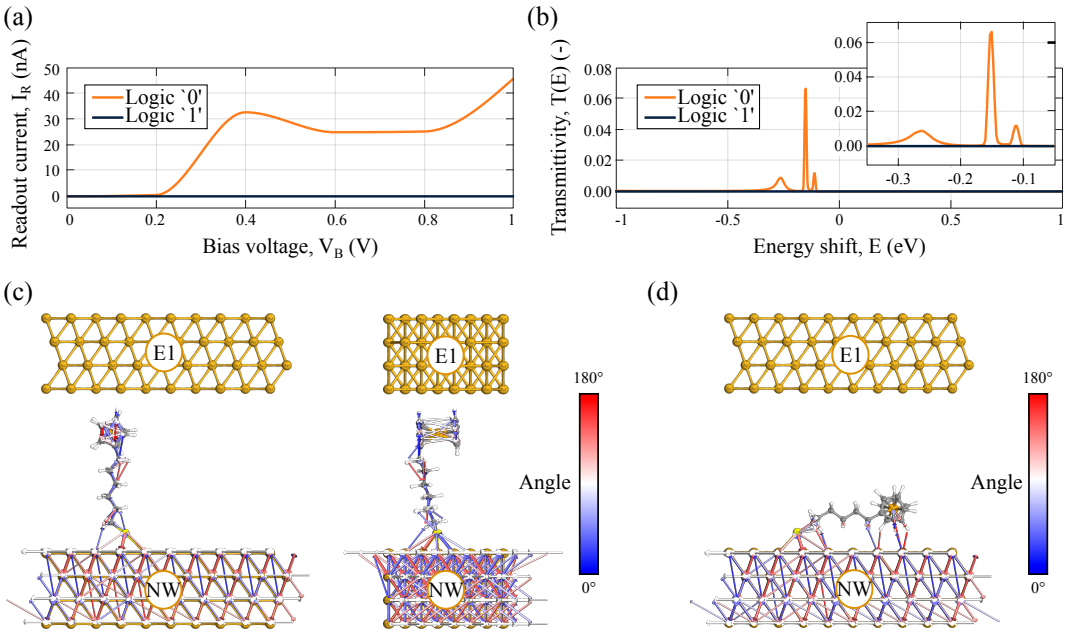

Fig. 5.8 Results of the DFT analysis of the molecular junction representing the charge-sensing readout system. (a) Readout current (I_R) calculated with DFT between E1 and NW when the Fc^+C_6S encodes the two logic values. (b) Transmission spectrum ($T(E)$) calculated with DFT when the Fc^+C_6S encodes the two logic values. The inset shows an enlargement of the transmittivity where is non-zero. (c) Transmission pathways for the electrons transmitted from the NW to E1 electrode when the cation encodes a logic '1'. (d) Transmission pathways for the electrons transmitted from the NW to E1 electrode when the cation encodes a logic '0'.

factors contributing to the disparities in $T(E)$ between the logic '0' and logic '1' scenarios. The TP analysis, as detailed in [154], elucidates the local influences on $T(E)$, with arrow direction indicating the direction of propagation and arrow size denoting transmission probability.

Fig. 5.8c illustrates the TPs for the logic '1' configuration, providing both frontal and lateral perspectives. Notably, transmission is highly probable from the NW to the sulfur atom, as indicated by the presence of large arrows, whereas transmission through the saturated chain is less likely, depicted by smaller arrows. No arrows connect the ferrocene to E1, indicating a significant tunneling barrier. Arrows become discernible when a lower transmission probability is portrayed, suggesting the presence of a finite $T(E)$.

These findings align with expectations: the anchoring sulfur atom contributes well-delocalized states due to its covalent bond with gold, while the saturated hex-

anethiol exhibits localized orbitals with minimal transmission probability along the carbon atoms. Conversely, the ferrocene displays good delocalization, attributed to the presence of Fe and cyclopentadiene π-type orbitals, resulting in numerous and relatively large arrows. The primary bottleneck to transmission is the tunneling barrier between Fc^+C_6S and E1. In the logic '1' configuration, the Fc^+C_6S molecule acts as a molecular bridge between NW and E1, yet with a small tunneling barrier.

In contrast, in the logic '0' configuration, depicted in Fig. 5.8d, the role of Fc^+C_6S as a molecular bridge is prevented. Despite notable electron transmission between NW and sulfur, the rotational freedom of the molecule results in minimal transmission along the hexane chain. The TP analysis reveals sparse and diminutive arrows, primarily directed toward the NW, thereby forming limited connections between NW and Fc. Consequently, electrons originating from NW encounter a tunneling barrier approximately equivalent to the NW-E1 distance, rendering $T(E)$ negligible.

The distinct separation observed in I_R between the two logic states underlines the efficacy of the readout system. However, the reliability of the readout process could be susceptible to external influences. For instance, an external electric field generated by nearby electrodes might perturb the positioning of the molecule. Hence, future investigations should consider such external factors to validate the robustness of the readout mechanism.

The discussion and the results presented so far represent a conceptual idea for one possible alternative way of solving a specific issue typically related to charge-based molFCN: the conversion of charge into readable information. To bring this theoretical investigation to reality, there are several feasibility aspects to consider.

One of the key challenges lies in fabricating electrodes at the nanoscale with the requisite precision and alignment. Current techniques such as Electron Beam Lithography (EBL) and Focused Ion-Beam (FIB) offer the high resolutions needed for such work. Nevertheless, these methods also come with challenges related to complexity, time consumption, and cost. Achieving consistent reproducibility at this scale is critical for ensuring reliable device performance, making this an area ripe for innovation. Advances in these nanofabrication techniques could significantly enhance the feasibility of the device, paving the way for more consistent and cost-effective production methods. Further study should address the impact of process variations and include them in the model.

Material selection is another vital aspect to consider. The materials used for electrodes and nanowires must combine excellent electrical conductivity with mechanical stability and compatibility with nanofabrication processes. At such small scales, even slight changes in physical and chemical properties can have a pronounced impact on device performance. Research into new materials or improved processing methods could help overcome these challenges, leading to more robust and reliable devices.

The presence of counterions, necessary for stabilizing the ferrocenium state, introduces additional complexity but also opportunities for innovation. These counterions can shield the charge, potentially reducing the switching efficiency. However, understanding and controlling the Debye screening effect at this scale can lead to new ways to mitigate this issue. By carefully managing the distribution and concentration of counterions, it may be possible to minimize their impact on the intended electronic response. Addressing the impacts of unwanted scattering sites on transport involves developing strategies to control or limit the mobility of counterions, thereby preserving the electrical conductivity and mobility essential for devices. Innovations in materials and device design could help mitigate these effects, leading to improved performance and stability.

Moreover, the current choice of using a cation has been made to address the problem gradually, but in future works, it can be substituted with polar or engineered zwitterionic molecules, preventing the need for counterions in the substrate for charge balance.

Environmental factors such as temperature play a significant role in device performance. Nanoscale devices are highly sensitive to these conditions, which can influence the behavior of both nanostructures and counterions. Developing devices that are less sensitive to environmental variations or incorporating protective measures could enhance their robustness and reliability in real-world applications.

Chapter 6

Conclusion and future perspective

The research presented in this thesis explores the use of molecular Field-Coupled Nanocomputing (molFCN) as a promising paradigm for future electronics. The ultimate goal of this technology is to facilitate the realization of a prototype to validate the paradigm and its working principles. Achieving this goal necessitates vast knowledge in various research areas, such as the synthesis of molecules and their deposition, as well as the fabrication of nanoelectrodes for the clock system and nanostructures patterned following the desired logic. The driving force behind investments in these directions lies in the potential for obtaining significant performance improvements in specific target areas, such as compute-in-memory, neural computing, or arithmetic acceleration. With the increased precision and computational power of simulation frameworks, performance validation can be conducted before the development of a working prototype.

In this context, the present work focuses on analyzing the relationship between variations at the physical level and their impact on circuit behavior, thereby expanding the current simulation framework for molFCN technology. The exploration is structured across multiple abstraction levels, each starting from a modelistic simplification of the previous layers. This approach enables the decomposition of the overall goal into smaller, addressable tasks.

The first level of analysis regards molecules, the elemental units of the technology. This work collects and discusses a set of properties that molecules should possess to behave suitably for the molFCN application. Other than constraints on dimensions or symmetries, the key features are related to the electrostatic behavior,

such as polarizability. Subsequently, the work presents a case study: starting from bis(trimethylsilyl) sulfide, we evaluate, through Density Functional Theory (DFT), the impact of modifications to subparts of the molecules on their electrostatic characteristics (mainly the charge distribution and the V_{in}-AC transcharacteristic (VACT)). This process aims to identify suitable chemical composites or specific molecular compositions for the ultimate definition of a set of candidate molecules for different purposes within a circuit.

Since electrostatic interactions among a set of molecules are at the core of the technology, we proceed with their analysis at the following level. Having defined a suitable electric model for molecules, we can study their interactions without the need for heavy DFT calculations. Focusing on three molecular species, namely neutral, oxidized, and zwitterionic, to target a complete set of behaviors, this work analyzes the system energy of fundamental interactions. The analysis relates molecular behavior to the logical behavior expected from various cell layouts found in fundamental gates, defining more molecular properties for successful information processing. The energy analysis is then compared with the results of SCERPA simulations of fundamental gates to demonstrate the coherence of the predictions. The final step advances this process by defining a set of feasible VACTs for the correct realization of in-plane information crossing.

The confident simulations of elementary gates using SCERPA are the starting point for the design of more elaborate circuits. Due to its tight integration with single-molecule behavior, the complexity of the simulation and thus its execution time increases exponentially with the number of cells. In order to advance the analysis of potential use-cases for the molFCN technology, there is a need to add an abstraction layer. This work proposes a precise and comprehensive method to model molFCN gates, making it possible to consider them as whole entities rather than collections of molecules. We develop a tool to automatically handle the characterization and treatment of the library of created devices, enabling the speeding up of circuit simulations from days to milliseconds while maintaining an accuracy higher than 99%.

Finally, the last step of this work aims to simplify the possibility of experimentally measuring the outcome of a molFCN circuit. This work proposes a modification of the current charge-based molFCN to include molecule bending in the information encoding. The addition of physical movement simplifies the measurement in a

laboratory and is compatible with the charge-based paradigm. Moreover, by integrating the new bend-boosted paradigm with a molecular junction, the conversion of the information stored in the charge into a current provides a way for in-circuit information readout and integration with standard current-based technologies.

With regard to the ultimate goal of developing molFCN technology, this work has taken a small yet significant step forward in providing the tools and knowledge for future technology assessment. The research has yielded several significant outcomes aimed at establishing clear parameters and insightful predictions of expected behaviors. These efforts are crucial for facilitating future experimental validations and the development of functional prototypes.

One key achievement is the establishment of precise characteristics required for molecules to exhibit suitable behaviors for molFCN. Additionally, validating the impact of their electrostatic footprint on circuit-level simulations has resulted in the formulation of specific guidelines for identifying suitable molecules.

Moreover, the development and publication of tools capable of generating valuable predictions in a short period have been instrumental. These tools not only expedite research progress but also encourage contributions from other researchers, fostering collaborative advancements in the field.

Furthermore, a noteworthy contribution involves proposing a modified version of the paradigm. This modified paradigm retains the inherent advantages of molFCN while simplifying information measurement in laboratory settings and facilitating integration with conventional current-based devices.

The research activity pursued during the development of the present work has been characterized by a miscellaneous and interdisciplinary context. This necessitated addressing various topics, including single-molecule simulations, understanding technological limitations and possibilities, abstracting physical behavior to develop manageable models, and creating algorithms and tools to predict the digital behavior of circuits effectively. Single-molecule simulations have been particularly demanding computationally, often taking weeks to complete or sometimes not being feasible due to limited computational resources. Additionally, the ability to develop robust models has been hindered by a lack of experimental data in the literature on the molecules or structures of interest. These two factors have constrained the scope of exploration within a three-year program.

Collectively, the results obtained can converge into a comprehensive roadmap outlining fundamental next steps essential for the experimental validation of the technology. This roadmap serves as a guiding framework for future research endeavors in the field. The first key element to be analyzed is the molecular design process, delineating the requisite criteria that molecules must meet to ensure their efficacy and reliability in operation. Although this task has been partially addressed in this work, the sky is the limit for its completion. With some of the constraints delineated, chemists are empowered to embark on the synthesis of molecules that conform to the prescribed requirements, thus ensuring optimal performance within the designated operational parameters. This iterative process of theoretical analysis, simulation, and synthesis constitutes a crucial step toward the advancement and refinement of molFCN technology, facilitating the development of robust and reliable molecular circuits for diverse applications.

The second aspect that must be part of the roadmap for the future development of molFCN is the exploration of the intricate physical and structural prerequisites necessary for the fabrication of sub-nanometric molecular patterns, crucial for achieving desired functionalities. The meticulous design of sub-nanometric molecular patterns stands as a pivotal determinant in ensuring the operation of molFCN circuits. As such, the achievement of a functional molFCN prototype depends on the precise control of atomic deposition processes. Future works should explore contemporary nanofabrication methodologies. The outcomes of these analyses furnish crucial insights that can be incorporated within the SCERPA framework to assess propagation characteristics and discern feasible fabrication pathways.

Lastly, future research should further investigate the intricate terrain of hybrid integration between molFCN and CMOS, paving the way for seamless convergence between molecular and semiconductor technologies. The distinguishing feature of molFCN technology lies in its unique characteristic of information propagation and processing without the flow of current. While this attribute affords minimal power consumption, it poses challenges in interfacing with established technologies reliant on current conduction. Consequently, the transduction of information encoded within the charge distribution assumes crucial importance in validating a prototype and facilitating its hybrid integration with other technologies. This work offers one possible solution to be further investigated. Future research should perform a comprehensive exploration of the mechanisms underlying the transduction of charge-encoded logic information into an electrical quantity. The potential of single-

molecule junction sensors in facilitating the integration of molFCN technology with existing electronic architectures must follow rigorous theoretical analyses and experimental validation.

In conclusion, this thesis has presented a comprehensive exploration of molFCN technology. Through rigorous investigation and analysis, significant contributions have been made to understanding the relationship between underlying physics and the logic behavior of devices. The findings of this research not only advance the theoretical understanding of molFCN technology but also hold practical implications for the future realization of a working prototype. By addressing key research questions and objectives, this study has laid the groundwork for future research endeavors in the technological realization of a prototype. Moreover, the methodologies and approaches developed herein provide valuable insights and tools for researchers and the engineering community. As we look to the future, the findings of this thesis serve as a springboard for further exploration and innovation, with the ultimate goal of driving positive change and progress in future electronics.

References

[1] Aaron D. Franklin, Mark C. Hersam, and H.-S. Philip Wong. Carbon nanotube transistors: Making electronics from molecules. *Science*, 378(6621):726–732, 2022.

[2] Gage Hills, Christian Lau, Andrew Wright, Samuel Fuller, Mindy D. Bishop, Tathagata Srimani, Pritpal Kanhaiya, Rebecca Ho, Aya Amer, Yosi Stein, Denis Murphy, Arvind, Anantha Chandrakasan, and Max M. Shulaker. Modern microprocessor built from complementary carbon nanotube transistors. *Nature*, 572(7771):595–602, 04 2019.

[3] Abu Sebastian, Manuel Le Gallo, Riduan Khaddam-Aljameh, and Evangelos Eleftheriou. Memory devices and applications for in-memory computing. *Nature Nanotechnology*, 15(7):529–544, 2020.

[4] Vivienne Sze, Yu-Hsin Chen, Tien-Ju Yang, and Joel S. Emer. Efficient processing of deep neural networks: A tutorial and survey. *Proceedings of the IEEE*, 105(12):2295–2329, 2017.

[5] IRDS Technical Community. The international roadmap for devices and systems (irds), 2022.

[6] Gordon E. Moore. Cramming more components onto integrated circuits. *Electronics*, 38(8), 04 1965.

[7] Gourab Chatterjee, Neil Dalchau, Richard A. Muscat, Andrew Phillips, and Georg Seelig. A spatially localized architecture for fast and modular dna computing. *Nature Nanotechnology*, 12(9):920–927, 2017.

[8] Satoshi Sugahara and Junsaku Nitta. Spin-transistor electronics: An overview and outlook. *Proceedings of the IEEE*, 98(12):2124–2154, 2010.

[9] Bhavin J. Shastri, Alexander N. Tait, T. Ferreira de Lima, Wolfram H. P. Pernice, Harish Bhaskaran, C. D. Wright, and Paul R. Prucnal. Photonics for artificial intelligence and neuromorphic computing. *Nature Photonics*, 15(2):102–114, 2021.

[10] Neal G. Anderson and Sanjukta Bhanja. *Field-Coupled Nanocomputing*. Springer Berlin, Heidelberg, 2014.

[11] C. S. Lent, P. D. Tougaw, W. Porod, and G. H. Bernstein. Quantum cellular automata. *Nanotechnology*, 4(1):49–57, 1993.

[12] W. Porod, C. S. Lent, G. H. Bernstein, A. O. Orlov, I Hamlani, G. L. Snider, and J. L. Merz. Quantum-dot cellular automata: computing with coupled quantum dots. *International Journal of Electronics*, 86(5):549–590, 1999.

[13] P. Douglas Tougaw and Craig S. Lent. Logical devices implemented using quantum cellular automata. *Journal of Applied Physics*, 75(3):1818–1825, 1994.

[14] Islamshah Amlani, Alexei O. Orlov, Geza Toth, Gary H. Bernstein, Craig S. Lent, and Gregory L. Snider. Digital logic gate using quantum-dot cellular automata. *Science*, 284(5412):289–291, 1999.

[15] W. Porod, C. S. Lent, G. H. Bernstein, A. O. Orlov, I. Hamlani, G. L. Snider, and J. L. Merz. Quantum-dot cellular automata: computing with coupled quantum dots. *International Journal of Electronics*, 86(5):549–590, 1999.

[16] Géza Tóth and Craig S. Lent. Quasiadiabatic switching for metal-island quantum-dot cellular automata. *Journal of Applied Physics*, 85(5):2977–2984, 03 1999.

[17] Eric S. Mandell and Mahfuza Khatun. Quasi-adiabatic clocking of quantum-dot cellular automata. *Journal of Applied Physics*, 94(6):4116–4121, 08 2003.

[18] C. S. Lent, G. L. Snider, G. Bernstein, W. Porod, A. Orlov, M. Lieberman, T. Fehlner, M. Niemier, and P. Kogge. *Quantum-Dot Cellular Automata*, pages 397–431. Springer US, Boston, MA, 2003.

[19] Vamsi Vankamamidi, Marco Ottavi, and Fabrizio Lombardi. Two-dimensional schemes for clocking/timing of qca circuits. *IEEE Transactions on Computer-Aided Design of Integrated Circuits and Systems*, 27(1):34–44, 2008.

[20] M.B. Tahoori, Jing Huang, M. Momenzadeh, and F. Lombardi. Testing of quantum cellular automata. *IEEE Transactions on Nanotechnology*, 3(4):432–442, 2004.

[21] G. L. Snider, A. O. Orlov, I. Amlani, X. Zuo, G. H. Bernstein, C. S. Lent, J. L. Merz, and W. Porod. Quantum-dot cellular automata: Review and recent experiments (invited). *Journal of Applied Physics*, 85(8):4283–4285, 04 1999.

[22] Alexei O. Orlov, Islamshah Amlani, Ravi K. Kummamuru, Rajagopal Ramasubramaniam, Geza Toth, Craig S. Lent, Gary H. Bernstein, and Gregory L. Snider. Experimental demonstration of clocked single-electron switching in quantum-dot cellular automata. *Applied Physics Letters*, 77(2):295–297, 07 2000.

[23] Islamshah Amlani, Alexei O. Orlov, Gregory L. Snider, Craig S. Lent, and Gary H. Bernstein. Demonstration of a six-dot quantum cellular automata system. *Applied Physics Letters*, 72(17):2179–2181, 04 1998.

[24] Gary H. Bernstein. Quantum-dot cellular automata: Computing by field polarization. In *Proceedings of the 40th Annual Design Automation Conference*, DAC '03, page 268–273, New York, NY, USA, 2003. Association for Computing Machinery.

[25] Mo Liu and C.S. Lent. High-speed metallic quantum-dot cellular automata. In *2003 Third IEEE Conference on Nanotechnology, 2003. IEEE-NANO 2003.*, volume 2, pages 465–468 vol. 2, 2003.

[26] F. Perez-Martinez, I. Farrer, D. Anderson, G. A. C. Jones, D. A. Ritchie, S. J. Chorley, and C. G. Smith. Demonstration of a quantum cellular automata cell in a gaas/algaas heterostructure. *Applied Physics Letters*, 91(3):032102, 07 2007.

[27] M. Mitic, M. C. Cassidy, K. D. Petersson, R. P. Starrett, E. Gauja, R. Brenner, R. G. Clark, A. S. Dzurak, C. Yang, and D. N. Jamieson. Demonstration of a silicon-based quantum cellular automata cell. *Applied Physics Letters*, 89(1):013503, 07 2006.

[28] S. R. Schofield, P. Studer, C. F. Hirjibehedin, N. J. Curson, G. Aeppli, and D. R. Bowler. Quantum engineering at the silicon surface using dangling bonds. *Nature Communications*, 4(1):1649, 2013.

[29] Robert A. Wolkow, Lucian Livadaru, Jason Pitters, Marco Taucer, Paul Piva, Mark Salomons, Martin Cloutier, and Bruno V. C. Martins. *Silicon Atomic Quantum Dots Enable Beyond-CMOS Electronics*, pages 33–58. Springer Berlin Heidelberg, Berlin, Heidelberg, 2014.

[30] Taleana Huff, Hatem Labidi, Mohammad Rashidi, Lucian Livadaru, Thomas Dienel, Roshan Achal, Wyatt Vine, Jason Pitters, and Robert A. Wolkow. Binary atomic silicon logic. *Nature Electronics*, 1(12):636–643, 2013.

[31] Taleana R. Huff, Thomas Dienel, Mohammad Rashidi, Roshan Achal, Lucian Livadaru, Jeremiah Croshaw, and Robert A. Wolkow. Electrostatic landscape of a hydrogen-terminated silicon surface probed by a moveable quantum dot. *ACS Nano*, 13(9):10566–10575, 2019.

[32] Marcel Walter, Samuel Sze Hang Ng, Konrad Walus, and Robert Wille. Hexagons are the bestagons: Design automation for silicon dangling bond logic. In *Proceedings of the 59th ACM/IEEE Design Automation Conference*, DAC '22, page 739–744, New York, NY, USA, 2022. Association for Computing Machinery.

[33] Samuel Sze Hang Ng, Jacob Retallick, Hsi Nien Chiu, Robert Lupoiu, Lucian Livadaru, Taleana Huff, Mohammad Rashidi, Wyatt Vine, Thomas Dienel, Robert A. Wolkow, and Konrad Walus. Siqad: A design and simulation tool for

atomic silicon quantum dot circuits. *IEEE Transactions on Nanotechnology*, 19:137–146, 2020.

[34] Hsi Nien Chiu, Samuel S. H. Ng, Jacob Retallick, and Konrad Walus. Poissolver: a tool for modelling silicon dangling bond clocking networks. In *2020 IEEE 20th International Conference on Nanotechnology (IEEE-NANO)*, pages 134–139, 2020.

[35] Samuel Sze Hang Ng, Jacob Retallick, Hsi Nien Chiu, Robert Lupoiu, Lucian Livadaru, Taleana Huff, Mohammad Rashidi, Wyatt Vine, Thomas Dienel, Robert A. Wolkow, and Konrad Walus. Siqad: A design and simulation tool for atomic silicon quantum dot circuits. *IEEE Transactions on Nanotechnology*, 19:137–146, 2020.

[36] Marcel Walter, Robert Wille, Frank Sill Torres, Daniel Große, and Rolf Drechsler. fiction: An Open Source Framework for the Design of Field-coupled Nanocomputing Circuits, May 2019. arXiv:1905.02477.

[37] RP Cowburn and ME Welland. Room temperature magnetic quantum cellular automata. *Science*, 287(5457):1466–1468, 2000.

[38] MT Niemier, Gary H Bernstein, G Csaba, A Dingler, XS Hu, S Kurtz, S Liu, J Nahas, W Porod, M Siddiq, et al. Nanomagnet logic: progress toward system-level integration. *Journal of Physics: Condensed Matter*, 23(49):493202, 2011.

[39] G. Csaba, A. Imre, G.H. Bernstein, W. Porod, and V. Metlushko. Nanocomputing by field-coupled nanomagnets. *IEEE Transactions on Nanotechnology*, 1(4):209–213, 2002.

[40] Marco Vacca, Mariagrazia Graziano, Luca Di Crescenzo, Alessandro Chiolerio, Andrea Lamberti, Davide Balma, Giancarlo Canavese, Federica Celegato, Emanuele Enrico, Paola Tiberto, Luca Boarino, and Maurizio Zamboni. Magnetoelastic clock system for nanomagnet logic. *IEEE Transactions on Nanotechnology*, 13(5):963–973, 2014.

[41] Mariagrazia Graziano, Marco Vacca, Alessandro Chiolerio, and Maurizio Zamboni. An ncl-hdl snake-clock-based magnetic qca architecture. *IEEE Transactions on Nanotechnology*, 10(5):1141–1149, 2011.

[42] György Csaba and Wolfgang Porod. Behavior of nanomagnet logic in the presence of thermal noise. In *2010 14th International Workshop on Computational Electronics*, pages 1–4, 2010.

[43] Marco Vacca, Mariagrazia Graziano, and Maurizio Zamboni. Majority voter full characterization for nanomagnet logic circuits. *IEEE Transactions on Nanotechnology*, 11(5):940–947, 2012.

[44] György Csaba, Markus Becherer, and Wolfgang Porod. Development of cad tools for nanomagnetic logic devices. *International Journal of Circuit Theory and Applications*, 41(6):634–645, 2013.

[45] Michael Joseph Donahue and Donald G Porter. Oommf user's guide, version 1.0, 1999.

[46] Arne Vansteenkiste, Jonathan Leliaert, Mykola Dvornik, Mathias Helsen, Felipe Garcia-Sanchez, and Bartel Van Waeyenberge. The design and verification of mumax3. *AIP advances*, 4(10), 2014.

[47] Fabrizio Riente, Giovanna Turvani, Marco Vacca, Massimo Ruo Roch, Maurizio Zamboni, and Mariagrazia Graziano. Topolinano: A cad tool for nano magnetic logic. *IEEE Transactions on Computer-Aided Design of Integrated Circuits and Systems*, 36(7):1061–1074, 2017.

[48] Craig S. Lent, Beth Isaksen, and Marya Lieberman. Molecular quantum-dot cellular automata. *Journal of the American Chemical Society*, 125(4):1056–1063, 2003.

[49] Valentina Arima, Matteo Iurlo, Luca Zoli, Susmit Kumar, Manuel Piacenza, Fabio Della Sala, Francesca Matino, Giuseppe Maruccio, Ross Rinaldi, Francesco Paolucci, Massimo Marcaccio, Pier Giorgio Cozzi, and Alessandro Paolo Bramanti. Toward quantum-dot cellular automata units: thiolated-carbazole linked bisferrocenes. *Nanoscale*, 4:813–823, 2012.

[50] C.S. Lent and B. Isaksen. Clocked molecular quantum-dot cellular automata. *IEEE Transactions on Electron Devices*, 50(9):1890–1896, 2003.

[51] Yuhui Lu and Craig S Lent. A metric for characterizing the bistability of molecular quantum-dot cellular automata. *Nanotechnology*, 19(15):155703, mar 2008.

[52] John Timler and Craig S. Lent. Power gain and dissipation in quantum-dot cellular automata. *Journal of Applied Physics*, 91(2):823–831, 01 2002.

[53] Saket Srivastava, Sudeep Sarkar, and Sanjukta Bhanja. Estimation of upper bound of power dissipation in qca circuits. *IEEE transactions on nanotechnology*, 8(1):116–127, 2008.

[54] Bruce Hoeneisen and Carver A Mead. Fundamental limitations in microelectronics—i. mos technology. *Solid-State Electronics*, 15(7):819–829, 1972.

[55] Yuhui Lu and Craig S. Lent. Theoretical Study of Molecular Quantum-Dot Cellular Automata. *Journal of Computational Electronics*, 4(1):115–118, 2005.

[56] Yuri Ardesi, Alessandro Gaeta, Giuliana Beretta, Gianluca Piccinini, and Mariagrazia Graziano. Ab initio molecular dynamics simulations of field-coupled nanocomputing molecules. *Journal of Integrated Circuits and Systems*, 16(1):1–8, 2021.

[57] John Timler and Craig S. Lent. Maxwell's demon and quantum-dot cellular automata. *Journal of Applied Physics*, 94(2):1050–1060, 06 2003.

[58] Yuhui Lu, Mo Liu, and Craig Lent. Molecular quantum-dot cellular automata: From molecular structure to circuit dynamics. *Journal of Applied Physics*, 102(3):034311, 08 2007.

[59] K. Walus, T.J. Dysart, G.A. Jullien, and R.A. Budiman. Qcadesigner: a rapid design and simulation tool for quantum-dot cellular automata. *IEEE Transactions on Nanotechnology*, 3(1):26–31, 2004.

[60] Frank Sill Torres, Robert Wille, Philipp Niemann, and Rolf Drechsler. An energy-aware model for the logic synthesis of quantum-dot cellular automata. *IEEE Transactions on Computer-Aided Design of Integrated Circuits and Systems*, 37(12):3031–3041, 2018.

[61] Azzurra Pulimeno, Mariagrazia Graziano, Aleandro Antidormi, Ruiyu Wang, Ali Zahir, and Gianluca Piccinini. Understanding a bisferrocene molecular qca wire. *Field-Coupled Nanocomputing: Paradigms, Progress, and Perspectives*, pages 307–338, 2014.

[62] Yuri Ardesi, Azzurra Pulimeno, Mariagrazia Graziano, Fabrizio Riente, and Gianluca Piccinini. Effectiveness of molecules for quantum cellular automata as computing devices. *Journal of Low Power Electronics and Applications*, 8(3):24, 2018.

[63] Yuri Ardesi, Ruiyu Wang, Giovanna Turvani, Gianluca Piccinini, and Mariagrazia Graziano. Scerpa: A self-consistent algorithm for the evaluation of the information propagation in molecular field-coupled nanocomputing. *IEEE Transactions on Computer-Aided Design of Integrated Circuits and Systems*, 39(10):2749–2760, 2019.

[64] Yuri Ardesi, Giovanna Turvani, Mariagrazia Graziano, and Gianluca Piccinini. Scerpa simulation of clocked molecular field-coupling nanocomputing. *IEEE Transactions on very large scale integration (VLSI) systems*, 29(3):558–567, 2021.

[65] John A. Christie, Ryan P. Forrest, Steven A. Corcelli, Natalie A. Wasio, Rebecca C. Quardokus, Ryan Brown, S. Alex Kandel, Yuhui Lu, Craig S. Lent, and Kenneth W. Henderson. Synthesis of a neutral mixed-valence diferrocenyl carborane for molecular quantum-dot cellular automata applications. *Angewandte Chemie International Edition*, 54(51):15448–15451, 2015.

[66] Thomas Groizard, Samia Kahlal, and Jean-François Halet. Zwitterionic mixed-valence species for the design of neutral clocked molecular quantum-dot cellular automata. *Inorganic Chemistry*, 59(21):15772–15779, 2020.

[67] Azzurra Pulimeno, Mariagrazia Graziano, Danilo Demarchi, and Gianluca Piccinini. Towards a molecular qca wire: Simulation of write-in and read-out systems. *Solid-State Electronics*, 77:101–107, 2012.

[68] Enrique P Blair. Quantum-dot cellular automata: A clocked architecture for high-speed, energy-efficient molecular computing. In *Unconventional Computation and Natural Computation: 16th International Conference, UCNC 2017, Fayetteville, AR, USA, June 5-9, 2017, Proceedings 16*, pages 56–68. Springer, 2017.

[69] Wenchuang Hu, K. Sarveswaran, M. Lieberman, and G.H. Bernstein. High-resolution electron beam lithography and dna nano-patterning for molecular qca. *IEEE Transactions on Nanotechnology*, 4(3):312–316, 2005.

[70] Lander Verstraete, Pawel Szabelski, Ana M Bragança, Brandon E Hirsch, and Steven De Feyter. Adaptive self-assembly in 2d nanoconfined spaces: dealing with geometric frustration. *Chemistry of Materials*, 31(17):6779–6786, 2019.

[71] J Christopher Love, Lara A Estroff, Jennah K Kriebel, Ralph G Nuzzo, and George M Whitesides. Self-assembled monolayers of thiolates on metals as a form of nanotechnology. *Chemical reviews*, 105(4):1103–1170, 2005.

[72] Susan M Barlow and Rasmita Raval. Complex organic molecules at metal surfaces: bonding, organisation and chirality. *Surface Science Reports*, 50(6-8):201–341, 2003.

[73] Federico Ravera, Yuri Ardesi, Gianluca Piccinini, and Mariagrazia Graziano. Technology-aware simulation for prototyping molecular field-coupled nanocomputing. *IEEE Transactions on Nanotechnology*, 23:521–528, 2024.

[74] Jan Drewniok, Marcel Walter, and Robert Wille. Temperature behavior of silicon dangling bond logic. In *2023 IEEE 23rd International Conference on Nanotechnology (NANO)*, pages 925–930, 2023.

[75] Mohammad Salehi Fashami, Kamaram Munira, Supriyo Bandyopadhyay, Avik W. Ghosh, and Jayasimha Atulasimha. Switching of dipole coupled multiferroic nanomagnets in the presence of thermal noise: Reliability of nanomagnetic logic. *IEEE Transactions on Nanotechnology*, 12(6):1206–1212, 2013.

[76] Alejandro Santana-Bonilla, Leonardo Medrano Sandonas, Rafael Gutierrez, and Gianaurelio Cuniberti. Exploring the write-in process in molecular quantum cellular automata: a combined modeling and first-principle approach. *Journal of Physics: Condensed Matter*, 31(40):405502, jul 2019.

[77] Shmuel Zilberg. Design of light-induced molecular switcher for the driver of the quantum cellular automata (qca) based on the transition through the intramolecular charge transfer (ict) structure. *Israel Journal of Chemistry*, 60(5-6):570–576, 2020.

[78] Konrad Walus, Faizal Karim, and André Ivanov. Architecture for an external input into a molecular qca circuit. *Journal of Computational Electronics*, 8(1):35–42, 2009.

[79] Islamshah Amlani, Alexei O. Orlov, Gregory L. Snider, and Gary H. Bernstein. Differential charge detection for quantum-dot cellular automata. *Journal of Vacuum Science & Technology B: Microelectronics and Nanometer Structures Processing, Measurement, and Phenomena*, 15(6):2832–2835, 11 1997.

[80] Leo Gross, Fabian Mohn, Peter Liljeroth, Jascha Repp, Franz J. Giessibl, and Gerhard Meyer. Measuring the charge state of an adatom with noncontact atomic force microscopy. *Science*, 324(5933):1428–1431, 2009.

[81] B Mallada, M Ondráček, M Lamanec, A Gallardo, A Jiménez-Martín, B de la Torre, P Hobza, and P Jelínek. Visualization of π-hole in molecules by means of kelvin probe force microscopy. *Nat. Commun.*, 14(1):4954, August 2023.

[82] Errol G. Lewars. *Ab initio Calculations*, pages 175–390. Springer Netherlands, Dordrecht, 2011.

[83] W. Kohn and L. J. Sham. Self-consistent equations including exchange and correlation effects. *Phys. Rev.*, 140:A1133–A1138, Nov 1965.

[84] P.W. Atkins, J. De Paula, and J. Keeler. *Atkins' Physical Chemistry*. Oxford University Press, 2017.

[85] R. S. Mulliken. Electronic population analysis on lcao–mo molecular wave functions. i. *The Journal of chemical physics*, 23:1833–1840, Oct 1955.

[86] R. S. Mulliken. Criteria for the construction of good self-consistent-field molecular orbital wave functions, and the significance of lcao-mo population analysis. *The Journal of chemical physics*, 36:3428–3439, Jun 1962.

[87] Tapas Kar and A.B. Sannigrahi. Effect of basis set on mulliken and löwdin atomic charges, bond orders and valencies of some polar molecules. *Journal of Molecular Structure: THEOCHEM*, 165(1):47–54, 1988.

[88] Per-Olov Löwdin. On the nonorthogonality problem. volume 5 of *Advances in Quantum Chemistry*, pages 185–199. Academic Press, 1970.

[89] C. J. Cramer. *Essentials of computational chemistry*. Wiley, Chichester, UK, 2004.

[90] Curt M. Breneman and Kenneth B. Wiberg. Determining atom-centered monopoles from molecular electrostatic potentials. the need for high sampling density in formamide conformational analysis. *Journal of Computational Chemistry*, 11(3):361–373, 1990.

[91] F. Martin and H. Zipse. Charge distribution in the water molecule—a comparison of methods. *Journal of Computational Chemistry*, 26(1):97–105, 2005.

[92] AD McLean and M Yoshimine. Theory of molecular polarizabilities. *The Journal of Chemical Physics*, 47(6):1927–1935, 1967.

[93] Kenneth J Miller. Calculation of the molecular polarizability tensor. *Journal of the American Chemical Society*, 112(23):8543–8551, 1990.

[94] Roberto Listo, Federico Ravera, Giuliana Beretta, Yuri Ardesi, Gianluca Piccinini, and Mariagrazia Graziano. Unveiling charge dynamics in molecular field-coupled nanocomputing. In *2024 IEEE 24th International Conference on Nanotechnology (NANO)*, 2024.

[95] Sonja B Braun-Sand and Olaf Wiest. Biasing mixed-valence transition metal complexes in search of bistable complexes for molecular computing. *The Journal of Physical Chemistry B*, 107(36):9624–9628, 2003.

[96] Yuri Ardesi, Luca Gnoli, Mariagrazia Graziano, and Gianluca Piccinini. Bistable propagation of monostable molecules in molecular field-coupled nanocomputing. In *2019 15th Conference on Ph.D Research in Microelectronics and Electronics (PRIME)*, pages 225–228, 2019.

[97] Azzurra Pulimeno, Mariagrazia Graziano, Alessandro Sanginario, Valentina Cauda, Danilo Demarchi, and Gianluca Piccinini. Bis-ferrocene molecular qca wire: Ab initio simulations of fabrication driven fault tolerance. *IEEE Transactions on Nanotechnology*, 12(4):498–507, 2013.

[98] Bruno Schuler, Jun-Ho Lee, Christoph Kastl, Katherine A. Cochrane, Christopher T. Chen, Sivan Refaely-Abramson, Shengjun Yuan, Edo van Veen, Rafael Roldán, Nicholas J. Borys, Roland J. Koch, Shaul Aloni, Adam M. Schwartzberg, D. Frank Ogletree, Jeffrey B. Neaton, and Alexander Weber-Bargioni. How substitutional point defects in two-dimensional ws2 induce charge localization, spin–orbit splitting, and strain. *ACS Nano*, 13(9):10520–10534, 2019.

[99] Yuri Ardesi, Giuliana Beretta, Christian Fabiano, Mariagrazia Graziano, and Gianluca Piccinini. A reconfigurable field-coupled nanocomputing paradigm on uniform molecular monolayers. In *2021 International Conference on Rebooting Computing (ICRC)*, pages 124–128, 2021.

[100] Carol Creutz and H Taube. Binuclear complexes of ruthenium ammines. *Journal of the American Chemical Society*, 95(4):1086–1094, 1973.

[101] Qingling Hang, Yuliang Wang, Marya Lieberman, and Gary H Bernstein. Molecular patterning through high-resolution polymethylmethacrylate masks. *Applied Physics Letters*, 80(22):4220–4222, 2002.

[102] Wenchuang Hu, Koshala Sarveswaran, Marya Lieberman, and Gary H Bernstein. High-resolution electron beam lithography and dna nano-patterning for molecular qca. *IEEE Transactions on Nanotechnology*, 4(3):312–316, 2005.

[103] Yuliang Wang, Marya Lieberman, Qingling Hang, and Gary Bernstein. Selective binding, self-assembly and nanopatterning of the creutz-taube ion on surfaces. *International Journal of Molecular Sciences*, 10(2):533–558, 2009.

[104] Sonja B Braun-Sand and Olaf Wiest. Theoretical studies of mixed-valence transition metal complexes for molecular computing. *The Journal of Physical Chemistry A*, 107(2):285–291, 2003.

[105] Klaus D. Sattler. *Handbook of Nanophysics*. CRC Press, 2010.

[106] Xingyong Wang and Jing Ma. Electron switch in the double-cage fluorinated fullerene anions, e-@ c 20 f 18 (xh) 2 c 20 f 18 (x= n, b): new candidates for molecular quantum-dot cellular automata. *Physical Chemistry Chemical Physics*, 13(36):16134–16137, 2011.

[107] Xingyong Wang, Shuang Chen, Jin Wen, and Jing Ma. Exploring the possibility of noncovalently surface bound molecular quantum-dot cellular automata: Theoretical simulations of deposition of double-cage fluorinated fullerenes on ag(100) surface. *The Journal of Physical Chemistry C*, 117(3):1308–1314, 2013.

[108] Grygoriy A Dolgonos and Gilles H Peslherbe. Encapsulation of diatomic molecules in fullerene c 60: implications for their main properties. *Physical Chemistry Chemical Physics*, 16(47):26294–26305, 2014.

[109] Alberto M. Pintus, Andrea Gabrieli, Federico G. Pazzona, Giovanni Pireddu, and Pierfranco Demontis. Molecular qca embedding in microporous materials. *Phys. Chem. Chem. Phys.*, 21:7879–7884, 2019.

[110] Nishattasnim Liza, Yuhui Lu, and Enrique P Blair. Designing boron-cluster-centered zwitterionic y-shaped clocked qca molecules. *IOP Nanotechnology*, 33(46):5201, 2022.

[111] Jieying Jiao, Gary J Long, Fernande Grandjean, Alicia M Beatty, and Thomas P Fehlner. Building blocks for the molecular expression of quantum cellular automata. isolation and characterization of a covalently bonded square array of two ferrocenium and two ferrocene complexes. *Journal of the American Chemical Society*, 125(25):7522–7523, 2003.

[112] Yuhui Lu and Craig S Lent. Theoretical study of molecular quantum-dot cellular automata. *Journal of Computational Electronics*, 4:115–118, 2005.

[113] Nathan R Erickson, Cole D Holstrom, Hannah M Rhoda, Gregory T Rohde, Yuriy V Zatsikha, Pierluca Galloni, and Victor N Nemykin. Tuning electron-transfer properties in 5, 10, 15, 20-tetra (1'-hexanoylferrocenyl) porphyrins as prospective systems for quantum cellular automata and platforms for four-bit information storage. *Inorganic chemistry*, 56(8):4716–4727, 2017.

[114] Yonggang Zhao, Dong Guo, Yang Liu, Cheng He, and Chunying Duan. A mixed-valence (fe ii) 2 (fe iii) 2 square for molecular expression of quantum cellular automata. *Chemical Communications*, (44):5725–5727, 2008.

[115] Benjamin Schneider, Serhiy Demeshko, Sven Neudeck, Sebastian Dechert, and Franc Meyer. Mixed-spin [2x2] fe4 grid complex optimized for quantum cellular automata. *Inorganic Chemistry*, 52(22):13230–13237, 2013.

[116] Thomas Groizard, Samia Kahlal, and Jean-Francois Halet. Theoretical studies of mixed-valence organometallic species for potential utilization as quantum cellular automata. *Journal of Organometallic Chemistry*, 844:35–42, 2017.

[117] Frank Neese. The orca program system. *Wiley Interdisciplinary Reviews: Computational Molecular Science*, 2(1):73–78, 2012.

[118] Frank Neese. Software update: the orca program system, version 4.0. *Wiley Interdisciplinary Reviews: Computational Molecular Science*, 8(1):e1327, 2018.

[119] Florian Weigend and Reinhart Ahlrichs. Balanced basis sets of split valence, triple zeta valence and quadruple zeta valence quality for h to rn: Design and assessment of accuracy. *Physical Chemistry Chemical Physics*, 7(18):3297, 2005.

[120] Stefan Grimme, Jens Antony, Stephan Ehrlich, and Helge Krieg. A consistent and accurate ab initio parametrization of density functional dispersion correction (dft-d) for the 94 elements h-pu. *The Journal of Chemical Physics*, 132(15):154104, 2010.

[121] Stefan Grimme, Stephan Ehrlich, and Lars Goerigk. Effect of the damping function in dispersion corrected density functional theory. *Journal of Computational Chemistry*, 32(7):1456–1465, 2011.

[122] J. Christopher Love, Lara A. Estroff, Jennah K. Kriebel, Ralph G. Nuzzo, and George M. Whitesides. Self-assembled monolayers of thiolates on metals as a form of nanotechnology. *Chemical Reviews*, 105(4):1103–1170, 2005.

[123] F. Karim, K. Walus, and A. Ivanov. Analysis of field-driven clocking for molecular quantum-dot cellular automata based circuits. *Journal of Computational Electronics*, 9(1):16–30, 2010.

[124] Giuliana Beretta, Yuri Ardesi, Mariagrazia Graziano, and Gianluca Piccinini. Multi-molecule field-coupled nanocomputing for the implementation of a neuron. *IEEE Transactions on Nanotechnology*, 21:52–59, 2022.

[125] Yuri Ardesi, Giuliana Beretta, Marco Vacca, Gianluca Piccinini, and Mariagrazia Graziano. Impact of molecular electrostatics on field-coupled nanocomputing and quantum-dot cellular automata circuits. *Electronics*, 11(2), 2022.

[126] Nishattasnim Liza, Daniel J. Coe, Yuhui Lu, and Enrique P. Blair. Ab initio studies of counterion effects in molecular quantum-dot cellular automata. *Journal of Computational Chemistry*, 45(7):392–404, 2024.

[127] Hua Qi, Sharad Sharma, Zhaohui Li, Gregory L. Snider, Alexei O. Orlov, Craig S. Lent, and Thomas P. Fehlner. Molecular quantum cellular automata cells. electric field driven switching of a silicon surface bound array of vertically oriented two-dot molecular quantum cellular automata. *Journal of the American Chemical Society*, 125(49):15250–15259, 2003.

[128] Yuhui Lu and Craig Lent. Self-doping of molecular quantum-dot cellular automata: mixed valence zwitterions. *Phys. Chem. Chem. Phys.*, 13:14928–14936, 2011.

[129] Yuri Ardesi, Mariagrazia Graziano, and Gianluca Piccinini. A model for the evaluation of monostable molecule signal energy in molecular field-coupled nanocomputing. *Journal of Low Power Electronics and Applications*, 12(1), 2022.

[130] Giuliana Beretta, Yuri Ardesi, Gianluca Piccinini, and Mariagrazia Graziano. vlsi-nanocomputing/scerpa: Scerpa v4.0.1, December 2022.

[131] K. Walus and G.A. Jullien. Design tools for an emerging soc technology: Quantum-dot cellular automata. *Proceedings of the IEEE*, 94(6):1225–1244, 2006.

[132] Ali Majeed and Esam Alkaldy. A new approach to bypass wire crossing problem in qca nano technology. *Circuit World - Emerald Publishing Limited*, 49(2):145–152, 2023.

[133] Giuliana Beretta, Yuri Ardesi, Gianluca Piccinini, and Mariagrazia Graziano. Robustness of the in-plane data crossing for molecular field-coupled nanocomputing. In *2023 IEEE 23rd International Conference on Nanotechnology (NANO)*, pages 732–736, 2023.

[134] Fabrizio Riente, Umberto Garlando, Giovanna Turvani, Marco Vacca, Massimo Ruo Roch, and Mariagrazia Graziano. Magcad: Tool for the design of 3-d magnetic circuits. *IEEE Journal on Exploratory Solid-State Computational Devices and Circuits*, 3:65–73, 2017.

[135] Umberto Garlando, Fabrizio Riente, and Mariagrazia Graziano. Funcode: Effective device-to-system analysis of field-coupled nanocomputing circuit designs. *IEEE Transactions on Computer-Aided Design of Integrated Circuits and Systems*, 40(3):467–478, 2020.

[136] Yuri Ardesi, Umberto Garlando, Fabrizio Riente, Giuliana Beretta, Gianluca Piccinini, and Mariagrazia Graziano. Taming molecular field-coupling for nanocomputing design. *J. Emerg. Technol. Comput. Syst.*, 19(1), dec 2022.

[137] Yuri Ardesi, Giuliana Beretta, Fabrizio Mo, Chiara Elfi Spano, Gianluca Piccinini, and Mariagrazia Graziano. Unveiling field-coupled nanocomputing: leaning molecules to shape readable bits. *Nano Research*, 2024.

[138] Yi Cao and Mengtao Sun. Tip-enhanced raman spectroscopy. *Reviews in Physics*, 8:100067, 2022.

[139] N. Liza, D. Murphey, P. Cong, D. W. Beggs, Y. Lu, and E. P. Blair. Asymmetric, mixed-valence molecules for spectroscopic readout of quantum-dot cellular automata. *Nanotechnology*, 33(11), December 2021.

[140] Jinbo Peng, Sophia Sokolov, Daniel Hernangómez-Pérez, Ferdinand Evers, Leo Gross, John M. Lupton, and Jascha Repp. Atomically resolved single-molecule triplet quenching. *Science*, 373(6553):452–456, 2021.

[141] Shantanu Mishra, Shadi Fatayer, Saleta Fernández, Katharina Kaiser, Diego Peña, and Leo Gross. Nonbenzenoid high-spin polycyclic hydrocarbons generated by atom manipulation. *ACS Nano*, 16(2):3264–3271, 2022.

[142] Jeremy Hieulle, Silvia Castro, Niklas Friedrich, Alessio Vegliante, Francisco Romero Lara, Sofía Sanz, Dulce Rey, Martina Corso, Thomas Frederiksen, Jose Ignacio Pascual, and Diego Peña. On-surface synthesis and collective spin excitations of a triangulene-based nanostar. *Angewandte Chemie International Edition*, 60(48):25224–25229, 2021.

[143] Fabrizio Mo, Yuri Ardesi, Massimo Ruo Roch, Mariagrazia Graziano, and Gianluca Piccinini. Investigation of amperometric sensing mechanism in gold–c60–gold molecular dot. *IEEE Sensors Journal*, 22(20):19152–19161, 2022.

[144] Stephen E. Creager and Gary K. Rowe. Competitive self-assembly and electrochemistry of some ferrocenyl-n-alkanethiol derivatives on gold. *Journal of Electroanalytical Chemistry*, 370(1):203–211, 1994.

[145] John S. Tse. Ab initio molecular dynamics with density functional theory. *Annual Review of Physical Chemistry*, 53(Volume 53, 2002):249–290, 2002.

[146] Martin Brehm. Orca 5.0 molecular dynamics module. https://brehm-research.de/files/orca_md_manual_5.0.pdf, 2021.

[147] Daan Frenkel and Berend Smit. *Understanding molecular simulation: from algorithms to applications*. Elsevier, 2023.

[148] Thomas P Senftle, Sungwook Hong, Md Mahbubul Islam, Sudhir B Kylasa, Yuanxia Zheng, Yun Kyung Shin, Chad Junkermeier, Roman Engel-Herbert, Michael J Janik, Hasan Metin Aktulga, et al. The reaxff reactive force-field: development, applications and future directions. *npj Computational Materials*, 2(1):1–14, 2016.

[149] Mads Brandbyge, José-Luis Mozos, Pablo Ordejón, Jeremy Taylor, and Kurt Stokbro. Density-functional method for nonequilibrium electron transport. *Physical Review B*, 2002.

[150] Søren Smidstrup, Troels Markussen, Pieter Vancraeyveld, Jess Wellendorff, Julian Schneider, Tue Gunst, Brecht Verstichel, Daniele Stradi, Petr A Khomyakov, Ulrik G Vej-Hansen, et al. Quantumatk: An integrated platform of electronic and atomic-scale modelling tools. *J. Phys: Condens. Matter*, 32:015901, 2020.

[151] Søren Smidstrup, Daniele Stradi, Jess Wellendorff, Petr A Khomyakov, Ulrik G Vej-Hansen, Maeng-Eun Lee, Tushar Ghosh, Elvar Jónsson, Hannes Jónsson, and Kurt Stokbro. First-principles green's-function method for surface calculations: A pseudopotential localized basis set approach. *Physical Review B*, 96(19):195309, 2017.

[152] José A. Rodriguez, Joseph Dvorak, Tomas Jirsak, Gang Liu, Jan Hrbek, Yosslen Aray, and Carlos González. Coverage effects and the nature of the metal-sulfur bond in s/au(111): High-resolution photoemission and density-functional studies. *Journal of the American Chemical Society*, 125(1):276–285, 2003.

[153] Supriyo Datta. *Quantum Transport: Atom to Transistor*. Cambridge University Press, 2005. doi: 10.1017/CBO9781139164313.

[154] Gemma C. Solomon, Carmen Herrmann, Thorsten Hansen, Vladimiro Mujica, and Mark A. Ratner. Exploring local currents in molecular junctions. *Nature Chemistry*, 2(3):223–228, Mar 2010.

Appendix A

Molecules geometry

Appendix A reports the coordinates of all the molecules shown in this work in order of appearance.

A.1 Thiolated-carbazole linked bisferrocenes

Table A.1 reports the coordinates of the optimized geometry of the isolated thiolated-carbazole linked bisferrocenes with the Unrestricted Kohn-Shann (UKS) method using Becke3 Lee–Yang–Parr (B3LYP) functional with LANL2DZ basis set[1]. The geometry optimization is performed using the ORCA package [117, 118].

Table A.1 Coordinates of the optimized geometry of the thiolated-carbazole linked bisferrocenes.

Atom	**x (Å)**	**y (Å)**	**z (Å)**
C	−4.918827 0000	−6.503 165 0000	−0.858 753 0000
C	−3.579 317 0000	−6.985 817 0000	−0.896 848 0000
C	−3.081 190 0000	−7.006 256 0000	0.436 876 0000
C	−4.112 678 0000	−6.535 603 0000	1.299 485 0000
C	−5.248 466 0000	−6.225 703 0000	0.498 685 0000
Fe	−3.621 776 0000	−5.061 555 0000	−0.093 920 0000
C	−3.050 836 0000	−3.321 389 0000	0.899 548 0000
C	−1.962 576 0000	−3.796 463 0000	0.105 018 0000
C	−2.416 639 0000	−3.822 346 0000	−1.249 553 0000
C	−3.763 476 0000	−3.365 730 0000	−1.289 245 0000
C	−4.158 567 0000	−3.058 639 0000	0.042 877 0000
C	−0.558 257 0000	−4.131 058 0000	0.553 616 0000
C	−0.465 246 0000	−4.439 280 0000	2.058 170 0000
C	0.444 124 0000	−3.044 541 0000	0.163 909 0000
C	0.139 553 0000	−1.691 654 0000	0.283 352 0000
C	1.096 090 0000	−0.729 637 0000	−0.041 332 0000
C	2.373 864 0000	−1.140 125 0000	−0.491 853 0000
C	2.696 541 0000	−2.486 842 0000	−0.619 626 0000
C	1.721 577 0000	−3.418 903 0000	−0.288 960 0000
C	1.100 825 0000	0.719 432 0000	−0.041 284 0000
C	2.381 274 0000	1.121 592 0000	−0.491 743 0000
N	3.133 515 0000	−0.011 731 0000	−0.755 438 0000

[1] [H - Ne]: T. H. Dunning Jr. and P. J. Hay, Methods El. Str. Th. Vol. 2, PLENUM PRESS (1977). [Na - Hg]: P. J. Hay and W. R. Wadt, J. Chem. Phys. 82, 270 (1985) // P. J. Hay and W. R. Wadt, J. Chem. Phys. 82, 284 (1985) // P. J. Hay and W. R. Wadt, J. Chem. Phys. 82, 299 (1985)

C	0.1506340000	1.6876640000	0.2835270000
C	0.4640790000	3.0385460000	0.1642530000
C	1.7439360000	3.4045770000	−0.2886090000
C	2.7127700000	2.4661720000	−0.6193800000
C	−0.5311710000	4.1315020000	0.5541900000
C	−0.4363400000	4.4386040000	2.0588550000
C	−1.9376210000	3.8062770000	0.1053370000
C	−2.3913780000	3.8354980000	−1.2492670000
C	−3.7412770000	3.3880170000	−1.2891560000
C	−4.1385450000	3.0833300000	0.0428750000
C	−3.0291350000	3.3384160000	0.8996890000
Fe	−3.5882010000	5.0825740000	−0.0935380000
C	−5.2072030000	6.2577310000	0.4984930000
C	−4.8753910000	6.5326720000	−0.8589280000
C	−3.5326750000	7.0063390000	−0.8968080000
C	−3.0347280000	7.0237190000	0.4370340000
C	−4.0695530000	6.5601770000	1.2994980000
H	−0.2590570000	−5.0363310000	0.0166720000
H	−1.1460800000	−5.2457240000	2.3369930000
H	0.5509870000	−4.7382870000	2.3199200000
H	−0.7105020000	−3.5592170000	2.6561410000
H	−1.1118790000	5.2494350000	2.3378330000
H	−0.6874840000	3.5599870000	2.6565090000
H	0.5818070000	4.7308230000	2.3208380000
H	−5.5209280000	6.3894550000	−1.7106570000
H	−2.9833760000	7.2839840000	−1.7823070000
H	−2.0437840000	7.3235600000	0.7394440000
H	−3.9993490000	6.4438930000	2.3692920000
H	−6.1479530000	5.8692480000	0.8547970000
H	−1.8033050000	4.1508180000	−2.0971830000
H	−3.0272300000	3.2211060000	1.9713650000
H	−5.1126950000	2.7403010000	0.3534950000
H	−4.3615770000	3.3192620000	−2.1686130000
H	−1.8307520000	−4.1414420000	−2.0975700000
H	−4.3833560000	−3.2926400000	−2.1686480000

H	−5.1303610000	−2.7091200000	0.3536370000
H	−3.0480810000	−3.2043100000	1.9712480000
H	−5.5636110000	−6.3558540000	−1.7103550000
H	−6.1865260000	−5.8309030000	0.8551380000
H	−4.0414210000	−6.4195020000	2.3692290000
H	−2.0921750000	−7.3125600000	0.7391150000
H	−3.0321230000	−7.2673380000	−1.7824260000
H	−0.8459960000	−1.3865790000	0.6138220000
H	1.9530010000	−4.4739140000	−0.3875970000
H	3.6706100000	−2.8049730000	−0.9719930000
H	3.6889010000	2.7779530000	−0.9717200000
H	1.9822740000	4.4580580000	−0.3871300000
H	−0.8368880000	1.3890330000	0.6140000000
H	−0.2259770000	5.0349770000	0.0175930000
C	5.0775300000	−0.0180640000	−1.4665380000
C	5.9729190000	−0.0238510000	−0.3644280000
H	5.2476050000	0.8561080000	−2.0596640000
H	5.2406300000	−0.8911760000	−2.0631730000
H	5.8098200000	0.8492620000	0.2322060000
H	5.8028450000	−0.8980230000	0.2286980000
C	7.3104610000	−0.0282330000	−0.8412520000
H	7.4735580000	−0.9013430000	−1.4378910000
H	7.4805370000	0.8459430000	−1.4343720000
C	8.2058500000	−0.0340200000	0.2608580000
C	9.5433800000	−0.0410050000	−0.2159690000
H	8.0344630000	−0.9072070000	0.8550560000
H	8.0440740000	0.8400680000	0.8564230000
H	9.7147690000	0.8321860000	−0.8101620000
H	9.7051540000	−0.9150900000	−0.8115400000
C	10.4387680000	−0.0467920000	0.8861400000
H	10.2769940000	0.8272980000	1.4817040000
H	10.2673800000	−0.9199780000	1.4803390000
S	11.7762980000	−0.0537770000	0.4093130000
H	11.7125470000	0.9439170000	0.0279430000

A.2 Creutz-Taube ion

Table A.2 reports the coordinates of the optimized geometry of the isolated Creutz-Taube ion with the UKS method using CAM-B3LYP functional with def2-TZVP basis set [119]. Grimme D3 correction is applied [120, 121]. The geometry optimization is performed using the ORCA package [117, 118].

Table A.2 Coordinates of the optimized geometry of the Creutz-Taube ion.

Atom	**x (Å)**	**y (Å)**	**z (Å)**
N	−1.479 889 467 967 56	−0.052 852 054 571 58	1.274 984 480 717 20
C	−0.670 772 419 744 49	1.092 927 169 632 93	1.351 499 175 975 68
C	0.671 609 702 214 53	1.092 497 185 891 77	1.350 976 211 460 75
H	−1.185 959 713 952 40	2.036 726 585 011 47	1.510 166 663 252 16
N	1.479 768 049 618 15	−0.053 911 810 221 50	1.274 520 632 247 58
H	1.187 442 487 770 38	2.036 072 781 418 05	1.508 713 948 945 85
Ru	3.096 438 853 302 20	−0.009 675 687 414 06	−0.085 327 311 926 98
C	0.671 261 672 519 13	−1.200 614 226 909 20	1.277 464 992 799 27
C	−0.672 273 056 065 69	−1.200 132 570 578 35	1.277 314 322 706 35
Ru	−3.096 293 296 378 08	−0.006 086 266 168 05	−0.085 112 905 115 56
H	1.183 990 768 034 82	−2.154 230 638 986 05	1.380 918 067 571 77
H	−1.185 580 924 673 58	−2.153 499 573 844 86	1.379 892 365 420 18
H	1.286 899 129 370 46	1.765 668 083 461 04	−0.876 306 534 431 78
N	2.200 816 366 453 52	1.531 781 651 982 14	−1.267 911 627 336 66
H	5.602 072 107 691 73	−0.544 576 535 462 32	−1.044 139 638 179 74
N	2.180 934 579 676 15	−1.491 994 056 462 46	−1.338 675 835 714 80
H	1.270 647 147 636 17	−1.727 937 758 771 95	−0.939 775 109 401 89
N	−4.842 461 197 408 89	0.060 152 638 614 48	−1.384 405 527 876 30
N	−2.206 910 019 831 19	1.547 208 329 181 51	−1.257 182 009 736 36
N	−3.925 845 929 637 64	−1.519 672 550 337 29	1.184 350 135 775 77
N	−3.959 707 819 054 86	1.429 465 649 969 08	1.238 338 410 811 72
N	−2.173 464 088 609 36	−1.476 193 797 655 41	−1.347 513 203 897 88
H	4.650 168 448 731 75	−0.228 180 173 499 62	−2.351 246 179 827 49
N	3.929 163 856 479 76	−1.511 003 227 508 42	1.196 582 453 307 11
H	5.220 837 154 884 00	1.007 402 101 840 25	−1.427 884 805 116 39
H	2.076 692 247 153 64	1.269 333 926 269 52	−2.244 939 286 391 98

H	2.770 977 384 183 81	2.378 181 012 945 87	−1.279 395 736 676 79
N	4.842 703 754 178 42	0.054 295 153 099 54	−1.384 581 282 882 86
H	2.730 832 389 395 39	−2.346 355 967 629 69	−1.408 628 481 857 35
H	2.040 750 892 658 52	−1.170 438 789 027 53	−2.295 137 622 863 67
N	3.955 135 904 128 87	1.438 817 981 395 78	1.227 356 377 633 19
H	4.907 233 239 523 43	−1.339 224 676 273 33	1.420 577 947 729 40
H	3.876 228 260 229 95	−2.469 763 148 421 96	0.860 827 264 476 09
H	3.376 919 225 445 17	−1.436 911 068 255 87	2.050 964 377 850 74
H	4.935 018 984 752 52	1.240 252 267 019 94	1.422 302 855 307 81
H	3.429 211 180 061 69	1.394 926 309 568 40	2.099 900 964 430 82
H	3.927 528 777 909 84	2.396 342 741 988 53	0.879 284 658 153 31
H	−3.377 566 539 385 18	−1.450 333 253 256 53	2.041 529 082 052 82
H	−3.868 169 162 261 01	−2.475 722 289 227 58	0.841 616 945 818 87
H	−4.905 387 060 021 03	−1.353 250 355 580 85	1.405 980 026 831 70
H	−1.264 605 318 020 86	−1.714 101 579 943 43	−0.946 331 051 588 35
H	−2.029 363 641 967 97	−1.146 729 240 135 30	−2.300 714 363 760 09
H	−2.722 012 011 889 31	−2.330 573 506 773 14	−1.426 802 376 204 39
H	−5.599 570 293 470 15	−0.543 789 507 715 31	−1.047 813 922 164 71
H	−4.648 863 105 308 59	−0.215 573 200 945 77	−2.352 782 541 185 30
H	−5.224 290 018 819 35	1.012 030 694 024 61	−1.421 520 058 041 21
H	−1.292 358 460 197 42	1.780 204 149 383 77	−0.866 347 597 549 82
H	−2.779 075 295 635 20	2.392 278 892 878 84	−1.260 195 949 684 67
H	−2.085 079 327 867 73	1.292 872 292 278 44	−2.236 654 534 963 41
H	−3.430 721 470 142 24	1.381 610 920 756 32	2.108 861 909 632 94
H	−4.938 025 320 472 00	1.224 694 319 339 07	1.434 710 110 491 03
H	−3.937 811 605 222 20	2.389 543 673 626 04	0.897 013 112 976 34

A.3 Double-cage fluorinated fullerenes

Table A.3 reports the coordinates of the optimized geometry of the isolated double-cage fluorinated fullerenes with the UKS method using B3LYP functional with TZVP basis set and Grimme D3 correction [120, 121]. The geometry optimization is performed using the ORCA package [117, 118].

Table A.3 Coordinates of the optimized geometry of the double-cage fluorinated fullerenes.

Atom	**x (Å)**	**y (Å)**	**z (Å)**
C	1.815 391 582 160 88	−0.745 948 890 269 84	−1.396 069 263 065 69
C	2.041 262 911 650 57	0.713 161 816 633 75	−0.895 500 667 931 58
C	0.589 645 655 722 61	−0.742 639 806 631 03	−2.362 266 603 007 15
C	0.056 662 304 771 52	0.720 524 219 320 33	−2.457 272 595 229 41
C	0.953 792 079 282 82	1.618 967 198 642 14	−1.549 339 920 325 02
C	−0.529 787 752 326 01	−1.621 697 954 318 06	−1.722 605 464 504 94
C	−1.754 354 680 675 18	−0.704 437 434 760 46	−1.424 084 342 487 23
C	−1.391 359 923 799 99	0.743 179 823 436 12	−1.875 936 675 904 15
C	0.003 785 770 536 14	−2.160 915 855 722 54	−0.360 664 843 472 32
C	−0.891 454 662 966 37	−1.584 422 991 755 37	0.773 895 337 722 76
C	−1.973 664 983 415 61	−0.684 201 088 836 79	0.122 533 384 937 82
C	1.448 595 015 795 87	−1.621 152 225 656 08	−0.159 515 454 837 34
C	1.454 599 528 227 16	−0.708 167 654 826 09	1.100 813 074 246 31
C	−0.000 347 698 403 41	−0.689 902 785 294 34	1.737 460 774 875 20
C	1.816 793 170 523 32	0.731 467 572 030 71	0.649 808 142 671 85
C	0.597 713 823 738 14	1.642 793 066 048 25	0.948 613 563 276 90
C	−0.531 822 021 742 31	0.768 903 311 917 82	1.642 974 789 916 30
C	−1.748 018 802 398 71	0.766 832 261 906 23	0.621 612 250 635 27
C	−1.384 391 876 445 02	1.649 291 880 328 09	−0.607 266 874 559 03
C	0.060 442 310 095 16	2.188 668 133 474 19	−0.406 057 023 019 86
F	2.919 440 085 001 52	−1.222 550 095 134 40	−2.017 195 144 296 58
F	3.284 586 946 425 25	1.145 602 516 614 33	−1.209 739 974 573 16
F	0.935 333 970 161 45	−1.211 475 277 188 04	−3.583 798 289 161 08
F	0.071 100 922 482 49	1.158 617 762 686 52	−3.737 836 282 829 42
F	1.520 627 984 047 62	2.617 674 474 874 44	−2.265 718 038 657 27
F	−0.874 746 039 598 10	−2.639 901 399 806 77	−2.545 237 687 215 07
F	−2.861 080 902 457 79	−1.149 091 724 206 06	−2.063 656 065 856 81
F	−2.274 579 002 679 78	1.201 144 865 569 82	−2.793 751 890 714 92
F	−0.005 816 951 955 62	−3.516 898 364 281 72	−0.342 853 197 888 36
F	−1.473 833 359 487 89	−2.603 723 504 567 59	1.455 073 978 990 91
F	−3.218 962 034 593 51	−1.117 143 070 519 47	0.436 475 569 524 85
F	2.325 411 997 845 74	−2.645 961 988 163 61	−0.018 569 425 712 90

F	2.369 457 042 996 09	−1.169 332 381 012 48	1.989 866 186 059 16
N	0.001 698 904 282 61	−1.225 591 397 257 23	3.049 358 148 582 03
F	2.924 837 794 845 43	1.177 055 271 411 80	1.290 970 641 061 55
F	0.965 491 240 509 88	2.680 445 370 356 98	1.740 883 778 765 21
N	−0.927 136 757 872 88	1.325 434 377 538 83	2.884 994 905 176 72
F	−2.875 703 224 835 90	1.246 269 095 278 37	1.205 926 534 192 05
F	−2.262 466 435 668 61	2.673 692 371 908 54	−0.743 459 528 831 54
F	0.068 516 826 733 49	3.544 743 472 579 72	−0.418 894 663 596 84
C	0.892 493 541 566 03	−0.641 591 871 029 52	5.295 602 959 830 04
C	1.127 014 745 542 84	0.812 776 106 896 20	5.781 583 203 000 01
C	−0.343 100 528 732 27	−0.650 624 494 833 38	4.297 604 127 328 07
C	−0.876 192 397 612 60	0.807 876 064 707 28	4.202 942 074 604 20
C	0.033 341 154 860 10	1.708 802 642 263 95	5.143 762 022 358 27
C	−1.458 871 973 494 15	−1.519 040 145 428 60	5.019 506 854 653 32
C	−2.672 559 603 989 07	−0.606 078 326 212 34	5.333 545 340 504 35
C	−2.318 516 404 049 02	0.830 252 337 408 45	4.866 808 109 839 97
C	−0.896 320 110 841 81	−2.056 014 714 513 30	6.367 336 477 670 87
C	−1.768 704 952 312 65	−1.478 442 327 411 07	7.522 830 854 331 54
C	−2.868 142 738 674 07	−0.577 085 395 446 88	6.883 085 823 200 62
C	0.551 876 054 021 87	−1.515 342 810 009 12	6.537 525 400 498 72
C	0.582 280 804 968 90	−0.600 834 613 434 08	7.799 855 667 676 38
C	−0.854 952 725 727 42	−0.574 091 870 527 58	8.407 688 214 426 61
C	0.936 722 561 895 43	0.843 590 971 153 55	7.331 725 572 112 09
C	−0.282 371 508 336 43	1.763 045 750 360 22	7.646 525 091 453 00
C	−1.389 699 262 208 63	0.888 437 244 459 68	8.312 611 334 306 82
C	−2.633 007 719 082 01	0.885 200 038 256 09	7.369 274 476 770 68
C	−2.289 147 717 659 67	1.752 094 771 574 62	6.120 459 162 216 83
C	−0.840 722 595 577 26	2.292 892 979 121 05	6.290 910 740 140 41
F	2.007 793 269 861 74	−1.124 935 301 659 51	4.693 988 440 920 96
F	2.366 344 900 163 01	1.243 426 668 551 75	5.441 371 124 630 20
F	0.601 676 963 204 81	2.722 344 974 778 00	4.444 944 819 753 84
F	−3.792 206 621 161 43	−1.056 400 470 868 33	4.716 736 188 994 68
F	−0.904 946 285 715 87	−3.412 088 449 579 15	6.388 927 908 290 61
F	−2.322 238 299 610 80	−2.472 430 209 752 18	8.256 054 580 693 38
F	−4.105 520 390 028 80	−1.007 442 065 297 58	7.222 750 676 585 03

F	1.431 768 760 589 48	−2.539 348 976 924 65	6.664 639 306 121 87
F	1.481 790 304 204 37	−1.053 100 989 049 44	8.704 567 273 649 89
F	−0.846 126 789 162 98	−1.003 501 299 578 39	9.691 267 295 533 65
F	2.054 812 066 967 42	1.292 952 511 401 02	7.947 854 384 180 88
F	0.077 144 671 580 49	2.786 741 673 485 35	8.456 062 449 026 39
F	−1.713 276 514 813 05	1.365 251 522 098 03	9.537 100 707 510 09
F	−3.725 651 213 535 95	1.365 990 201 940 70	8.007 387 547 986 05
F	−3.168 841 053 448 98	2.775 589 036 984 42	5.988 093 399 075 91
F	−0.832 401 218 248 24	3.648 801 680 385 38	6.263 840 813 502 84
F	−1.842 207 096 851 23	−2.563 364 612 839 19	4.241 087 139 573 59
F	−3.251 293 495 844 66	1.285 560 896 085 32	3.991 484 764 266 79
H	0.284 477 139 414 42	−2.190 906 721 758 73	3.101 532 666 998 95
H	−1.330 225 702 634 86	2.245 987 721 892 95	2.817 335 862 823 89

A.4 Diferrocenyl carborane

Table A.4 reports the coordinates of the mean geometry of the diferrocenyl carborane obtained from the optimization of the isolated molecule with the UKS method using B3LYP functional with TZVP basis set and Grimme D3 correction [120, 121]. The geometry optimization is performed using the ORCA package [117, 118].

Table A.4 Coordinates of the mean geometry of the diferrocenyl carborane.

Atom	**x (Å)**	**y (Å)**	**z (Å)**
C	1.415 708	0.262 184	−0.819 146
C	1.182 495	−0.980 907	−0.745 066
C	2.039 432	−1.764 391	−1.452 743
C	2.830 782	−1.022 917	−1.956 793
C	2.458 709	0.212 152	−1.554 627
C	4.793 123	−1.597 985	0.238 682
C	4.066 247	−2.388 661	0.700 172
C	3.190 470	−1.683 018	1.396 297
C	3.376 987	−0.465 480	1.370 291
C	4.362 661	−0.407 320	0.654 408

Fe	2.977211	−0.978202	−0.228484
H	5.523789	−1.855540	−0.330375
H	4.146251	−3.347343	0.533744
H	2.482883	−1.999708	1.833422
H	2.826928	0.297343	1.776322
H	4.698499	0.403369	0.443879
H	2.878737	0.993040	−1.758348
H	0.490735	−1.269883	−0.228468
H	2.098794	−2.746543	−1.569916
H	3.598181	−1.338821	−2.521591
C	−4.362661	−0.407320	0.654408
C	−3.376987	−0.465480	1.370291
C	−3.190470	−1.683018	1.396297
C	−4.066247	−2.388661	0.700172
C	−4.793123	−1.597985	0.238682
C	−2.830782	−1.022917	−1.956793
C	−2.039432	−1.764391	−1.452743
C	−1.182495	−0.980907	−0.745066
C	−1.415708	0.262184	−0.819146
C	−2.458709	0.212152	−1.554627
Fe	−2.977211	−0.978202	−0.228484
H	−3.598181	−1.338821	−2.521591
H	−2.098794	−2.746543	−1.569916
H	−0.490735	−1.269883	−0.228468
H	−2.878737	0.993040	−1.758348
H	−5.523789	−1.855540	−0.330375
H	−4.698499	0.403369	0.443879
H	−2.826928	0.297343	1.776322
H	−2.482883	−1.999708	1.833422
H	−4.146251	−3.347343	0.533744
C	0.734285	1.351622	−0.187265
C	−0.734285	1.351622	−0.187265
B	1.311997	2.047716	1.149081
B	0.000000	2.629473	2.132789
B	−1.311997	2.047716	1.149081

B	1.321962	2.894172	−0.270800
B	0.844219	3.682381	1.184686
B	−0.844219	3.682381	1.184686
B	−1.321962	2.894172	−0.270800
B	0.000000	2.382840	−1.163567
B	0.000000	3.898688	−0.266638
H	0.000000	2.153295	−2.292258
H	0.000000	2.804657	3.260792
H	2.256123	1.688517	1.557704
H	1.413045	4.545933	1.698549
H	0.000000	4.893835	−0.784879
H	−2.269949	3.039389	−0.840151
H	2.269949	3.039389	−0.840151
H	−1.413045	4.545933	1.698549
H	0.000000	1.585608	1.728480
H	−2.256123	1.688517	1.557704

A.5 Zwitterionic three-dot molecule with di-anionic pentaborate counterion

Table A.5 reports the coordinates of the optimized geometry of the isolated molecule with the UKS method using CAM-B3LYP functional with def2-TZVP basis set [119]. Grimme D3 correction is applied [120, 121]. The geometry optimization is performed using the ORCA package [117, 118].

Table A.5 Coordinates of the optimized geometry of the zwitterionic three-dot molecule with di-anionic pentaborate counterion.

Atom	**x (Å)**	**y (Å)**	**z (Å)**
B	−4.050870541 1	2.226995527 4	0.000000000 0
B	−2.763068773 7	−0.130999741 5	−0.000000000 0
B	−1.230747468 4	2.292495428 6	0.000000000 0
B	−2.089784125 0	1.387304120 4	−2.148628188 0
B	−2.632375512 1	1.713296275 5	1.543191540 7

C	−5.3520195017	3.1883118428	0.0000000000
C	−6.4531917126	3.9203221867	0.0000000000
C	−7.5219760826	4.6197985839	0.0000000000
C	−7.0037778180	5.6934138471	0.0000000000
C	−8.8984413462	4.1968592127	0.0000000000
C	0.1700339006	3.2371123481	0.0000000000
C	1.1254625385	3.9691226920	0.0000000000
C	2.3561840391	4.7011330358	0.0000000000
C	1.6598548618	5.8886164211	0.0000000000
C	3.7636249159	4.3619494998	0.0000000000
C	−2.7448331523	−1.5778889481	0.0000000000
C	−2.6962519440	−3.0256426625	0.0000000000
C	−2.6800583001	−4.4083288983	−0.0000000000
C	−3.8621987306	−4.8963356099	0.0000000000
C	−1.4493366613	−5.1566060772	−0.0000000000
H	−9.2061216868	5.2704744758	0.0000000000
H	−9.7243199514	3.4485820337	0.0000000000
H	−7.8944315519	6.5230257544	0.0000000000
H	−5.7892495467	5.8723495860	0.0000000000
H	2.7610267962	6.5718262597	0.0000000000
H	0.5262954322	6.3440894625	0.0000000000
H	4.2346539234	5.3518092042	−0.0000000000
H	4.1860727151	3.6112509376	0.0000000000
H	−0.2995835532	−4.6685993656	−0.0000000000
H	−1.6598548618	−6.2627552871	−0.0000000000
H	−3.5383247461	−5.9862179846	−0.0000000000
H	−4.8500148810	−4.2781936646	0.0000000000
C	−1.9127327478	1.3253392168	−3.9186138548
C	−2.8051913624	1.7862900835	3.2561574684
N	−2.9546815133	1.9095771713	4.6673595751
N	−1.7610660536	1.1525658817	−5.2944156550

A.6 Three-dot 'Y'-shaped functionalized zwitterionic closo-carborane

Table A.6 reports the coordinates of the optimized geometry of the isolated molecule with the UKS method using CAM-B3LYP functional with def2-TZVP basis set [119]. Grimme D3 correction is applied [120, 121]. The geometry optimization is performed using the ORCA package [117, 118].

Table A.6 Coordinates of the optimized geometry of the zwitterionic three-dot 'Y'-shaped functionalized zwitterionic closo-carborane.

Atom	x (Å)	y (Å)	z (Å)
B	−3.5073000000	−0.7885000000	1.4289000000
H	−2.9688000000	−0.8285000000	2.4847000000
B	−3.3856000000	−1.9551000000	−0.0133000000
H	−2.7520000000	−2.9507000000	−0.1340000000
B	−3.5962000000	−0.5277000000	−1.1939000000
H	−3.1303000000	−0.3624000000	−2.2721000000
B	−3.6986000000	0.6431000000	0.2476000000
H	−3.3273000000	1.7659000000	0.3465000000
B	−4.8881000000	−1.8597000000	0.9815000000
H	−5.1783000000	−2.7627000000	1.7022000000
B	−4.9532000000	−1.6768000000	−0.8677000000
H	−5.2984000000	−2.4230000000	−1.7302000000
B	−5.1691000000	0.1661000000	−0.6749000000
H	−5.7146000000	0.9752000000	−1.3705000000
B	−5.1112000000	−0.0135000000	1.1630000000
H	−5.5953000000	0.6445000000	2.0364000000
B	−6.1181000000	−0.9910000000	0.1762000000
C	−2.5958000000	−0.5380000000	0.0969000000
C	−1.1883000000	−0.3675000000	0.0669000000
C	−7.6248000000	−1.0318000000	0.1805000000
C	−8.8633000000	−0.8773000000	0.1453000000
Fe	−10.5567000000	−0.1752000000	−0.0281000000
P	−9.5932000000	1.1139000000	−1.6526000000

P	−9.7412000000	1.4085000000	1.4004000000
C	−8.6353000000	2.5677000000	−0.8908000000
H	−10.3800000000	1.7728000000	−2.6570000000
H	−8.6388000000	0.4315000000	−2.4599000000
C	−8.2883000000	2.2798000000	0.5656000000
H	−10.5681000000	2.4972000000	1.8500000000
H	−9.2128000000	0.9425000000	2.6387000000
H	−7.7255000000	2.7373000000	−1.4737000000
H	−9.2757000000	3.4515000000	−0.9847000000
H	−7.4355000000	1.5991000000	0.6426000000
H	−8.0473000000	3.2005000000	1.1049000000
C	−11.7324000000	−1.6686000000	0.9519000000
C	−12.4442000000	−0.4299000000	0.9771000000
H	−11.3885000000	−2.2247000000	1.8108000000
C	−11.5185000000	−2.0249000000	−0.4130000000
C	−12.6602000000	−0.0035000000	−0.3667000000
H	−12.7576000000	0.0982000000	1.8662000000
H	−10.9770000000	−2.8909000000	−0.7613000000
C	−12.0814000000	−0.9975000000	−1.2291000000
H	−13.1936000000	0.8821000000	−0.6783000000
H	−12.0931000000	−0.9856000000	−2.3091000000
C	0.0220000000	−0.2259000000	0.0424000000
C	1.4426000000	−0.0825000000	0.0158000000
C	2.0330000000	1.1921000000	0.0084000000
C	2.2600000000	−1.2251000000	−0.0013000000
C	3.4334000000	1.3356000000	−0.0154000000
H	1.4050000000	2.0757000000	0.0227000000
C	3.6625000000	−1.1119000000	−0.0248000000
H	1.7997000000	−2.2073000000	0.0006000000
C	4.2307000000	0.1754000000	−0.0322000000
H	5.3112000000	0.2722000000	−0.0536000000
C	4.0329000000	2.6316000000	−0.0209000000
C	4.5142000000	3.7731000000	−0.0246000000
Fe	5.3162000000	5.4904000000	−0.0203000000
P	6.8241000000	4.6210000000	−1.4385000000

P	6.581 100 000 0	4.629 700 000 0	1.625 500 000 0
C	8.212 500 000 0	3.736 800 000 0	−0.468 800 000 0
H	7.607 700 000 0	5.410 900 000 0	−2.351 200 000 0
H	6.392 900 000 0	3.589 600 000 0	−2.337 600 000 0
C	7.666 400 000 0	3.261 200 000 0	0.874 100 000 0
H	7.564 500 000 0	5.394 100 000 0	2.356 500 000 0
H	5.969 700 000 0	3.938 500 000 0	2.721 100 000 0
H	8.613 800 000 0	2.904 900 000 0	−1.055 400 000 0
H	9.014 600 000 0	4.470 600 000 0	−0.327 800 000 0
H	7.000 100 000 0	2.403 000 000 0	0.744 300 000 0
H	8.470 900 000 0	2.984 800 000 0	1.562 300 000 0
C	3.776 400 000 0	6.633 500 000 0	0.837 700 000 0
C	5.006 100 000 0	7.368 200 000 0	0.886 900 000 0
H	3.175 200 000 0	6.327 300 000 0	1.680 000 000 0
C	3.485 500 000 0	6.381 800 000 0	−0.541 600 000 0
C	5.478 700 000 0	7.562 700 000 0	−0.442 000 000 0
H	5.499 100 000 0	7.712 100 000 0	1.785 600 000 0
H	2.647 900 000 0	5.812 500 000 0	−0.914 000 000 0
C	4.528 000 000 0	6.941 800 000 0	−1.330 100 000 0
H	6.369 200 000 0	8.101 400 000 0	−0.731 200 000 0
H	4.585 600 000 0	6.917 800 000 0	−2.408 600 000 0
C	4.482 400 000 0	−2.280 900 000 0	−0.040 000 000 0
C	5.194 900 000 0	−3.294 300 000 0	−0.053 800 000 0
Fe	6.204 500 000 0	−4.898 500 000 0	−0.071 200 000 0
P	4.621 200 000 0	−5.691 700 000 0	−1.456 400 000 0
P	4.829 000 000 0	−5.500 600 000 0	1.603 500 000 0
C	3.147 400 000 0	−6.380 400 000 0	−0.455 900 000 0
H	4.842 500 000 0	−6.776 000 000 0	−2.375 800 000 0
H	3.971 900 000 0	−4.767 200 000 0	−2.339 900 000 0
C	3.074 600 000 0	−5.669 900 000 0	0.892 100 000 0
H	4.960 000 000 0	−6.744 100 000 0	2.325 300 000 0
H	4.605 400 000 0	−4.617 600 000 0	2.709 000 000 0
H	2.217 800 000 0	−6.262 000 000 0	−1.020 600 000 0
H	3.330 100 000 0	−7.453 200 000 0	−0.324 000 000 0
H	2.708 300 000 0	−4.645 500 000 0	0.776 100 000 0

H	2.422 900 000 0	−6.199 800 000 0	1.593 200 000 0
C	8.019 300 000 0	−4.216 900 000 0	0.737 600 000 0
C	7.969 000 000 0	−5.647 100 000 0	0.807 800 000 0
H	8.105 800 000 0	−3.535 000 000 0	1.569 500 000 0
C	7.934 700 000 0	−3.855 300 000 0	−0.645 900 000 0
C	7.846 600 000 0	−6.168 700 000 0	−0.511 700 000 0
H	8.009 400 000 0	−6.235 000 000 0	1.714 200 000 0
H	7.902 200 000 0	−2.848 500 000 0	−1.032 800 000 0
C	7.821 800 000 0	−5.046 000 000 0	−1.415 000 000 0
H	7.809 500 000 0	−7.212 900 000 0	−0.785 400 000 0
H	7.745 200 000 0	−5.097 000 000 0	−2.491 400 000 0

A.7 Bis(trimethylsilyl) sulfide

Table A.7 reports the coordinates of the optimized geometry of the isolated molecule with the UKS method using B3LYP functional with def2-TZVP basis set [119]. Grimme D3 correction is applied [120, 121]. The geometry optimization is performed using the ORCA package [117, 118].

Table A.7 Coordinates of the optimized geometry of the bis(trimethylsilyl) sulfide.

Atom	**x (Å)**	**y (Å)**	**z (Å)**
S	−0.954 288 917 302 69	−1.239 557 588 817 14	−0.654 221 837 090 48
Si	0.717 881 014 891 63	−0.077 918 629 986 13	0.065 333 075 801 46
Si	−2.730 523 513 586 68	−0.062 132 130 097 61	−0.303 304 619 753 19
C	−2.913 346 879 186 15	1.260 164 385 786 59	−1.620 033 600 004 93
C	−2.741 640 521 479 83	0.726 684 820 868 30	1.399 528 298 409 27
C	−4.140 772 404 063 54	−1.287 808 428 219 87	−0.440 338 071 578 11
C	0.610 241 940 561 48	1.719 273 541 469 55	−0.462 355 339 639 79
C	0.843 386 483 836 41	−0.187 013 571 251 93	1.932 779 640 831 88
C	2.219 339 037 209 87	−0.883 121 067 265 22	−0.714 502 676 266 07
H	−2.905 831 379 602 04	0.812 073 759 023 80	−2.615 528 640 850 01
H	−2.104 480 058 965 03	1.990 904 808 091 22	−1.575 855 941 658 65
H	−3.859 115 920 592 59	1.795 977 973 857 16	−1.495 100 508 380 90

H	−1.953 786 036 700 91	1.471 626 098 393 99	1.518 974 898 268 83
H	−2.622 096 125 954 37	−0.024 598 849 810 18	2.181 585 486 756 27
H	−3.699 265 322 863 90	1.231 653 836 734 96	1.557 530 583 384 10
H	−4.134 093 161 933 86	−1.785 737 822 106 17	−1.412 153 472 622 63
H	−5.102 372 122 218 19	−0.778 968 062 749 47	−0.329 020 034 048 87
H	−4.070 131 401 182 95	−2.056 816 083 893 03	0.331 402 640 324 02
H	1.521 849 293 904 63	2.244 719 226 555 22	−0.162 819 603 067 73
H	−0.232 944 393 327 26	2.233 270 098 638 57	0.000 444 041 145 27
H	0.509 257 175 443 97	1.806 227 274 647 23	−1.545 500 158 842 79
H	−0.022 550 509 976 34	0.255 088 851 996 81	2.426 772 877 308 42
H	1.736 482 592 403 32	0.337 432 331 176 15	2.285 471 581 837 36
H	0.913 899 255 302 36	−1.228 809 651 273 33	2.250 807 834 714 70
H	3.134 716 480 444 31	−0.391 412 349 047 86	−0.374 015 600 211 93
H	2.180 019 792 276 84	−0.817 568 735 469 74	−1.803 578 392 941 47
H	2.282 296 385 361 61	−1.938 764 704 451 85	−0.442 302 461 923 97

A.8 Hexanedithiol bis(trimethylsilane)

Table A.8 reports the coordinates of the optimized geometry of the isolated molecule with the UKS method using CAM-B3LYP functional with def2-TZVP basis set [119]. Grimme D3 correction is applied [120, 121]. The geometry optimization is performed using the ORCA package [117, 118].

Table A.8 Coordinates of the optimized hexanedithiol bis(trimethylsilane).

Atom	**x (Å)**	**y (Å)**	**z (Å)**
S	−0.835 850 532 541 84	−1.582 075 010 050 48	−0.327 396 389 425 15
Si	9.991 958 687 037 24	−0.473 834 037 374 63	−0.102 556 078 351 01
Si	−2.622 744 118 728 35	−0.298 431 346 356 11	−0.522 745 061 155 94
C	−2.461 876 877 498 34	0.603 895 380 357 64	−2.140 348 668 384 74
C	−2.620 744 773 409 03	0.858 599 999 000 31	0.931 501 271 322 85
C	−4.023 435 201 769 48	−1.509 322 341 724 72	−0.500 692 875 954 69
C	11.392 600 185 346 78	0.737 104 787 927 17	−0.124 516 433 848 45
C	9.831 134 416 286 82	−1.376 437 664 172 07	1.514 887 119 671 75

C	9.989 745 565 945 40	−1.630 521 136 699 47	−1.557 061 497 693 50
H	−2.403 329 749 558 17	−0.087 045 074 128 34	−2.980 662 766 897 56
H	−1.588 679 267 226 57	1.255 874 895 767 56	−2.167 007 194 796 96
H	−3.343 227 998 663 15	1.233 098 047 154 49	−2.284 968 419 912 77
H	−1.762 705 686 223 00	1.530 944 877 126 23	0.922 393 503 024 76
H	−2.627 377 503 270 83	0.317 689 898 915 17	1.877 490 199 790 80
H	−3.520 529 994 544 16	1.477 072 781 859 84	0.895 404 877 663 27
H	−3.951 206 239 899 42	−2.224 913 386 929 48	−1.320 340 410 376 98
H	−4.970 708 322 057 32	−0.977 447 939 519 97	−0.609 357 833 194 76
H	−4.061 638 587 893 84	−2.065 219 099 884 18	0.436 277 579 540 51
H	12.339 896 375 901 61	0.205 222 421 774 77	−0.016 096 407 794 98
H	11.320 476 344 432 43	1.452 522 614 482 07	0.695 287 046 869 79
H	11.430 662 530 130 15	1.293 188 826 373 04	−1.061 374 316 723 01
H	9.772 757 228 852 30	−0.685 670 647 377 49	2.355 350 653 461 54
H	10.712 432 974 502 04	−2.005 767 996 613 66	1.659 271 172 909 81
H	8.957 868 550 047 62	−2.028 321 504 333 46	1.541 498 932 655 68
H	10.889 560 547 970 38	−2.248 964 628 453 33	−1.521 236 825 212 40
H	9.996 243 303 148 63	−1.089 390 738 482 28	−2.502 921 848 063 47
H	9.131 735 437 106 22	−2.302 897 259 262 87	−1.547 996 471 472 44
C	0.509 925 202 846 17	−0.392 052 223 174 57	−0.140 397 639 874 05
C	1.858 636 801 642 84	−1.050 867 813 966 77	−0.375 842 584 475 42
C	3.004 594 914 791 02	−0.065 591 058 210 17	−0.197 683 243 049 47
C	4.364 476 165 577 96	−0.706 511 983 386 65	−0.426 972 921 677 89
C	5.510 442 613 569 31	0.278 761 197 400 02	−0.248 830 435 890 70
C	6.859 138 730 083 41	−0.380 109 526 209 47	−0.484 256 479 961 61
S	8.204 973 801 041 59	0.809 859 241 448 99	−0.297 455 923 371 45
H	0.449 389 887 625 11	0.016 051 274 624 67	0.871 671 527 660 81
H	0.348 800 598 455 32	0.435 058 525 091 07	−0.833 676 907 730 73
H	1.884 111 272 865 69	−1.471 643 012 893 41	−1.383 249 349 773 42
H	1.978 287 045 127 87	−1.887 919 891 302 07	0.315 719 844 425 65
H	2.967 492 918 896 79	0.358 315 560 584 53	0.810 325 695 818 30
H	2.877 689 207 189 36	0.772 978 393 308 44	−0.888 787 381 263 93
H	4.401 571 566 040 88	−1.130 425 021 374 37	−1.434 977 731 975 58
H	4.491 384 614 876 04	−1.545 077 699 503 19	0.264 135 978 076 54
H	5.484 968 648 722 42	0.699 568 314 681 88	0.758 559 468 949 97

H	5.390 815 817 956 42	1.115 789 109 805 42	−0.940 422 074 818 80
H	6.919 651 986 681 98	−0.788 239 714 333 65	−1.496 315 960 381 19
H	7.020 258 213 985 16	−1.207 205 959 066 29	0.209 029 502 060 90

A.9 Dodecanedithiol bis(trimethylsilane)

Table A.9 reports the coordinates of the optimized geometry of the isolated molecule with the UKS method using CAM-B3LYP functional with def2-TZVP basis set [119]. Grimme D3 correction is applied [120, 121]. The geometry optimization is performed using the ORCA package [117, 118].

Table A.9 Coordinates of the optimized dodecanedithiol bis(trimethylsilane).

Atom	**x (Å)**	**y (Å)**	**z (Å)**
S	−8.646 979 943 037 81	−3.181 963 176 069 84	−0.911 611 590 350 13
Si	9.532 616 069 448 93	−0.004 218 205 379 65	0.223 771 154 886 36
Si	−10.455 391 994 131 20	−2.035 414 208 029 59	−1.017 059 664 192 52
C	−10.447 815 639 248 97	−0.933 506 414 170 57	−2.526 421 148 311 94
C	−10.653 912 515 396 37	−0.982 264 423 678 79	0.513 735 623 167 97
C	−11.819 694 140 272 15	−3.301 050 813 020 62	−1.133 051 139 329 66
C	10.894 367 372 090 92	1.263 261 146 536 29	0.349 998 519 552 32
C	9.531 618 426 309 17	−1.120 885 177 704 14	1.722 110 191 456 93
C	9.729 564 035 892 88	−1.041 085 241 418 51	−1.318 243 303 052 11
H	−11.379 536 819 692 18	−0.367 084 392 047 76	−2.591 171 667 041 96
H	−10.344 383 847 977 49	−1.522 716 558 245 95	−3.437 829 913 975 73
H	−9.628 561 883 970 92	−0.213 501 757 438 68	−2.496 756 842 257 47
H	−11.595 775 871 640 76	−0.430 491 825 894 09	0.476 309 895 468 70
H	−10.655 612 091 237 43	−1.596 804 262 578 96	1.414 236 082 195 95
H	−9.849 810 828 806 83	−0.250 891 645 811 56	0.606 503 368 892 30
H	−12.792 086 880 127 99	−2.809 615 381 770 94	−1.201 954 706 546 37
H	−11.699 208 716 520 48	−3.931 393 455 639 50	−2.014 717 386 695 93
H	−11.832 253 600 764 95	−3.948 907 071 922 75	−0.255 808 985 622 95
H	11.867 657 471 511 57	0.772 708 407 115 30	0.412 797 637 221 74
H	10.774 026 181 646 97	1.883 606 029 150 99	1.238 897 867 369 86

H	10.904 860 306 791 83	1.920 138 856 413 26	−0.520 495 619 257 44
H	9.427 231 989 863 30	−0.541 393 227 559 21	2.639 655 809 221 34
H	10.465 380 525 557 57	−1.684 605 177 493 05	1.780 054 263 633 28
H	8.715 169 195 265 33	−1.843 665 784 642 69	1.686 930 363 880 23
H	10.673 581 111 564 98	−1.589 702 918 990 21	−1.290 391 986 194 20
H	9.725 417 456 260 30	−0.417 158 473 854 50	−2.212 273 154 318 55
H	8.927 790 264 503 87	−1.774 383 964 397 24	−1.415 823 889 849 99
C	0.084 698 913 923 64	−0.502 892 375 451 18	−0.307 459 213 280 41
C	1.489 126 232 176 59	−1.084 132 450 232 35	−0.350 580 756 853 95
C	2.580 570 795 301 40	−0.039 941 479 218 91	−0.177 728 094 814 99
C	3.984 736 256 520 00	−0.623 010 254 400 02	−0.209 983 757 605 09
C	5.070 908 364 900 62	0.428 666 197 760 20	−0.041 041 018 728 88
C	6.465 157 659 697 21	−0.171 975 191 799 80	−0.055 217 520 609 31
S	7.721 164 074 260 38	1.138 851 952 107 32	0.134 418 241 730 81
H	1.635 288 194 072 53	−1.606 526 821 161 01	−1.301 672 555 598 05
H	1.589 375 463 099 46	−1.845 143 208 638 31	0.430 449 086 240 20
H	2.430 883 985 051 36	0.487 150 069 381 69	0.769 965 800 622 46
H	2.485 238 528 335 41	0.717 196 066 102 22	−0.962 814 831 362 40
H	4.134 845 328 236 77	−1.153 049 031 217 52	−1.156 058 809 793 22
H	4.081 206 171 643 52	−1.376 045 864 877 81	0.579 110 330 113 07
H	4.921 799 137 580 84	0.966 415 934 371 45	0.898 712 460 180 88
H	4.991 101 070 982 32	1.172 701 374 326 09	−0.837 979 690 802 83
H	6.635 937 263 056 19	−0.698 327 010 058 55	−0.994 311 012 230 39
H	6.567 502 759 505 35	−0.890 334 798 026 97	0.758 467 452 574 53
H	−2.557 259 768 912 21	−0.442 832 591 492 03	0.514 024 988 004 06
H	−5.056 032 889 695 86	−0.896 668 812 988 32	0.372 840 079 751 70
C	−2.411 908 446 711 42	−0.964 624 839 268 10	−0.437 529 113 107 90
C	−4.907 669 638 861 30	−1.424 621 928 728 94	−0.574 671 921 239 81
C	−7.388 507 517 179 60	−1.873 066 964 691 56	−0.724 844 499 934 62
C	−1.007 597 728 838 97	−1.546 032 095 161 63	−0.481 884 108 230 04
H	−3.407 447 929 223 25	−2.766 799 568 883 25	0.173 270 913 170 58
C	−3.503 849 363 438 74	−2.008 306 809 781 16	−0.610 364 494 544 76
H	−2.512 611 214 665 90	−0.203 006 511 216 28	−1.217 907 247 460 20
H	−5.913 785 228 883 13	−3.221 608 012 724 90	0.050 128 012 548 16
C	−5.994 971 245 586 24	−2.475 049 280 958 08	−0.744 322 724 685 95

H	−5.004 903 373 784 96	−0.669 699 787 810 54	−1.361 872 201 446 79
H	−7.492 664 227 918 70	−1.153 433 687 376 16	−1.537 178 312 776 93
H	−3.355 922 300 579 82	−2.533 804 582 759 83	−1.559 217 726 377 06
H	−5.848 558 663 776 03	−3.009 993 554 618 27	−1.686 079 402 750 40
H	−0.015 324 216 066 12	0.259 476 904 596 21	−1.087 132 320 272 83
H	−0.907 111 747 009 26	−2.308 771 724 399 46	0.297 368 917 797 58
H	−0.061 405 487 686 55	0.017 939 651 341 01	0.644 478 746 900 37
H	−0.862 170 561 892 28	−2.066 555 293 180 09	−1.434 099 352 870 87
H	−7.555 857 768 515 28	−1.347 749 775 022 03	0.215 453 595 693 36

A.10 Tridecanedithiol bis(trimethylsilane)

Table A.10 reports the coordinates of the optimized geometry of the isolated molecule with the UKS method using CAM-B3LYP functional with def2-TZVP basis set [119]. Grimme D3 correction is applied [120, 121]. The geometry optimization is performed using the ORCA package [117, 118].

Table A.10 Coordinates of the optimized tridecanedithiol bis(trimethylsilane).

Atom	**x (Å)**	**y (Å)**	**z (Å)**
S	−8.682 889 353 915 00	−3.038 009 558 870 75	−0.837 621 305 492 65
Si	10.662 543 586 430 75	1.381 749 446 683 50	−0.159 746 990 848 29
Si	−10.502 453 653 589 28	−1.803 780 236 926 50	−0.989 869 311 752 09
C	−10.378 285 468 231 84	−0.840 479 937 497 71	−2.575 941 242 317 98
C	−10.542 479 012 979 63	−0.691 474 850 838 10	0.499 311 055 510 24
C	−11.872 570 041 366 61	−3.051 124 122 029 16	−1.007 706 968 536 88
C	12.333 846 009 843 49	0.583 106 772 889 70	−0.108 055 329 356 41
C	10.361 052 272 938 56	2.337 943 628 717 20	−1.726 087 284 917 84
C	10.282 022 856 618 78	2.387 077 413 893 10	1.357 231 232 336 46
H	−11.281 709 851 763 35	−0.238 457 468 641 04	−2.698 062 863 205 25
H	−10.295 592 680 007 67	−1.498 742 297 998 44	−3.440 137 458 782 96
H	−9.528 179 007 544 08	−0.158 101 066 126 74	−2.579 175 009 522 26
H	−11.468 207 250 767 10	−0.111 779 217 217 69	0.485 949 904 037 24
H	−10.519 046 752 733 86	−1.259 803 289 483 67	1.428 834 372 208 32

H	−9.713 818 921 861 10	0.016 697 913 702 87	0.505 391 263 118 51
H	−12.833 736 165 237 54	−2.541 440 721 040 79	−1.099 031 049 831 98
H	−11.781 477 155 714 72	−3.737 665 790 036 68	−1.850 008 983 783 83
H	−11.894 884 294 582 54	−3.638 607 142 525 10	−0.089 592 905 780 30
H	13.110 129 873 667 25	1.350 627 048 624 40	−0.111 380 719 070 86
H	12.499 238 189 862 01	−0.059 129 348 041 13	−0.973 562 745 375 59
H	12.464 606 677 138 40	−0.017 724 174 230 55	0.792 231 471 029 90
H	10.515 148 077 975 97	1.719 526 315 853 33	−2.609 786 049 736 83
H	11.062 929 677 733 11	3.173 460 407 958 85	−1.774 724 929 785 86
H	9.354 540 352 194 91	2.753 524 028 714 62	−1.766 793 593 371 41
H	10.993 656 474 090 99	3.212 711 886 521 62	1.426 352 516 108 34
H	10.370 868 790 804 39	1.793 184 193 838 82	2.266 610 211 190 36
H	9.282 233 986 901 75	2.819 348 230 962 06	1.322 487 508 705 06
C	0.136 438 191 472 57	−0.664 362 485 473 39	−0.334 410 561 081 29
C	1.518 738 463 262 07	−1.292 461 622 953 71	−0.417 704 808 791 79
C	2.649 141 705 623 91	−0.289 174 365 743 21	−0.251 289 218 108 76
C	4.028 705 084 484 57	−0.923 026 682 682 02	−0.336 357 728 688 26
C	5.160 689 253 937 86	0.079 246 759 873 20	−0.172 814 766 810 29
C	6.535 353 467 962 90	−0.568 227 832 139 28	−0.257 327 790 363 76
S	9.276 211 113 647 64	−0.332 792 613 809 38	−0.173 978 786 078 38
H	1.626 725 798 062 00	−1.802 035 456 312 37	−1.380 532 499 887 75
H	1.609 831 126 692 04	−2.069 886 000 352 63	0.347 781 128 673 93
H	2.542 900 792 393 31	0.220 058 030 369 67	0.711 914 327 957 75
H	2.559 066 452 596 18	0.488 107 381 605 27	−1.017 103 807 445 31
H	4.134 386 798 962 33	−1.433 529 382 751 92	−1.298 622 132 022 03
H	4.119 558 594 965 72	−1.698 767 656 362 02	0.430 450 167 358 02
H	5.057 207 465 655 73	0.590 531 469 385 92	0.789 413 513 389 13
H	5.073 879 415 959 85	0.853 316 852 599 35	−0.942 034 539 432 61
H	−2.489 727 345 712 43	−0.538 086 392 538 05	0.536 905 855 015 64
H	−5.004 721 643 351 95	−0.925 351 623 807 89	0.432 919 776 522 25
C	−2.375 019 455 142 52	−1.046 164 774 885 04	−0.425 928 159 650 20
C	−4.883 152 031 523 03	−1.433 851 195 245 51	−0.528 644 307 612 79
C	−7.369 264 983 165 96	−1.811 019 935 480 11	−0.642 679 503 560 00
C	−0.990 755 019 571 89	−1.670 648 063 421 74	−0.504 163 976 304 47
H	−3.409 816 819 162 61	−2.831 769 832 252 54	0.168 891 146 327 19

C	−3.497 569 584 389 32	−2.057 001 135 769 75	−0.599 254 868 245 23
H	−2.465 785 664 412 77	−0.269 097 835 703 12	−1.191 884 863 599 89
H	−5.920 573 033 041 91	−3.224 370 197 312 07	0.067 070 856 067 01
C	−5.996 300 561 908 32	−2.456 281 939 591 13	−0.706 234 112 572 52
H	−4.972 527 755 911 74	−0.660 059 678 022 54	−1.297 852 428 016 24
H	−7.485 066 481 843 74	−1.055 753 873 607 73	−1.422 724 109 001 99
H	−3.380 119 292 149 78	−2.567 564 913 305 19	−1.560 130 332 187 68
H	−5.880 471 075 313 33	−2.966 433 156 791 57	−1.665 128 300 735 00
H	0.045 255 223 630 79	0.113 753 313 738 66	−1.099 326 068 136 83
H	−0.900 309 181 466 56	−2.447 607 215 310 63	0.261 865 370 896 22
H	0.026 696 786 404 00	−0.156 305 716 631 52	0.629 087 340 877 60
H	−0.878 352 734 962 34	−2.180 269 053 585 36	−1.466 465 313 130 86
H	−7.523 228 258 089 03	−1.312 493 186 888 41	0.317 283 077 267 65
C	7.648 922 006 636 61	0.450 206 972 925 29	−0.090 667 247 335 78
H	6.648 055 093 961 98	−1.073 811 734 035 80	−1.219 048 868 120 33
H	6.630 467 799 239 64	−1.337 307 649 495 72	0.512 955 914 664 39
H	7.574 817 093 796 05	0.955 082 223 030 95	0.875 228 518 616 66
H	7.597 792 506 265 43	1.219 567 958 277 08	−0.863 950 473 588 54

A.11 1,3,5benzenetrithiol linked bis(hexanedithiol)bis(trimethylsilane)

Table A.11 reports the coordinates of the optimized geometry of the isolated molecule with the UKS method using CAM-B3LYP functional with def2-TZVP basis set [119]. Grimme D3 correction is applied [120, 121]. The geometry optimization is performed using the ORCA package [117, 118].

Table A.11 Coordinates of the optimized geometry of the 1,3,5benzenetrithiol linked bis(hexanedithiol)bis(trimethylsilane).

Atom	**x (Å)**	**y (Å)**	**z (Å)**
S	−8.581 290 543 397 71	−3.352 065 212 114 45	−0.950 021 939 768 39
Si	16.223 316 369 209 07	1.131 066 379 478 43	−0.235 691 582 321 55
Si	−10.445 457 007 235 92	−2.278 585 415 670 44	−1.028 428 124 291 66

C	−10.456 045 809 841 35	−1.117 476 429 602 02	−2.490 337 960 681 27
C	−10.693 875 999 661 72	−1.306 374 097 909 43	0.546 081 617 199 78
C	−11.738 872 781 246 83	−3.604 873 158 951 50	−1.212 087 237 588 11
C	17.817 607 175 026 18	0.169 152 829 529 59	−0.239 889 414 111 93
C	16.041 598 364 967 69	2.140 336 184 720 74	−1.796 135 737 434 81
C	16.115 717 825 574 43	2.252 467 789 943 62	1.253 155 686 646 34
H	−11.413 512 487 886 33	−0.596 207 978 134 37	−2.554 574 673 232 85
H	−10.303 924 078 814 40	−1.660 749 213 933 19	−3.423 192 266 119 04
H	−9.677 183 337 750 28	−0.357 587 472 365 37	−2.410 683 806 813 33
H	−11.658 169 212 810 88	−0.794 196 258 562 19	0.526 616 006 018 34
H	−10.676 469 620 775 50	−1.961 436 795 197 38	1.417 320 495 989 36
H	−9.923 927 452 707 42	−0.545 168 626 150 87	0.679 825 529 661 89
H	−12.734 052 004 172 96	−3.159 405 978 116 96	−1.264 799 252 847 55
H	−11.584 298 889 009 33	−4.186 259 679 313 91	−2.121 601 618 564 73
H	−11.724 655 416 943 91	−4.292 074 540 944 40	−0.365 368 602 634 34
H	18.670 186 828 563 21	0.849 312 596 148 34	−0.284 286 753 591 83
H	17.876 376 047 448 20	−0.497 503 046 306 01	−1.100 878 041 169 29
H	17.918 032 913 822 72	−0.434 975 112 392 57	0.662 345 267 192 93
H	16.087 502 824 701 96	1.504 090 315 035 29	−2.680 143 563 835 65
H	16.843 748 747 632 34	2.878 142 428 013 47	−1.867 565 752 698 65
H	15.096 377 321 415 39	2.684 262 503 719 27	−1.820 129 439 090 05
H	16.919 377 527 800 29	2.991 806 962 648 56	1.230 839 487 859 70
H	16.205 238 350 677 59	1.683 571 678 812 75	2.178 795 814 895 98
H	15.171 852 497 815 40	2.798 585 538 365 95	1.282 534 288 977 04
C	6.921 066 079 378 61	−0.573 415 884 606 90	−0.120 484 071 011 51
C	8.113 073 852 001 83	0.370 882 022 670 36	−0.088 140 409 554 88
C	9.426 046 227 059 97	−0.398 606 102 594 95	−0.112 683 013 929 58
C	10.645 062 328 322 25	0.510 323 636 283 02	−0.104 131 262 133 64
C	11.951 181 045 346 57	−0.269 115 142 170 87	−0.122 786 597 517 69
S	14.687 952 856 547 86	−0.374 141 988 181 38	−0.143 631 155 968 36
H	8.066 069 089 093 26	0.991 629 142 970 98	0.809 823 302 595 74
H	8.066 742 131 437 67	1.048 236 827 845 77	−0.944 475 968 663 48
H	9.457 554 612 733 24	−1.035 823 101 530 64	−1.001 950 709 892 12
H	9.469 501 428 590 00	−1.070 776 580 175 53	0.749 991 117 044 59
H	10.613 949 008 002 86	1.152 267 919 827 96	0.781 762 477 691 27

H	10.605 030 322 743 02	1.178 603 964 279 34	−0.970 088 121 175 43
H	−2.591 179 819 390 22	−0.423 506 371 125 08	0.538 726 234 674 69
H	−5.091 587 365 636 42	−0.919 199 975 635 75	0.357 182 112 092 75
C	−2.424 235 657 578 31	−1.001 277 186 111 71	−0.373 251 121 233 82
C	−4.905 012 750 680 88	−1.493 493 557 265 00	−0.555 226 461 497 32
C	−7.375 278 421 008 44	−1.999 291 926 323 13	−0.760 765 838 275 45
C	−1.034 410 885 633 38	−1.619 362 718 728 44	−0.340 058 810 666 23
H	−3.422 562 917 088 40	−2.773 581 614 426 59	0.325 683 264 146 72
C	−3.498 497 618 017 65	−2.070 966 646 774 33	−0.509 935 041 021 03
H	−2.494 115 732 521 94	−0.301 099 437 247 21	−1.209 146 497 023 50
H	−5.901 172 504 734 20	−3.276 896 639 666 59	0.122 769 220 409 68
C	−5.969 093 090 495 25	−2.569 724 474 794 36	−0.708 075 884 230 02
H	−4.979 014 204 489 75	−0.784 498 676 343 36	−1.385 655 324 763 82
H	−7.466 192 668 402 05	−1.310 023 691 069 02	−1.600 753 174 315 35
H	−3.318 022 614 035 40	−2.652 278 845 540 30	−1.419 198 812 712 62
H	−5.783 184 538 254 00	−3.144 787 545 878 80	−1.618 826 469 683 23
H	−7.588 657 696 799 36	−1.446 452 039 097 88	0.154 341 773 515 00
C	13.170 771 393 943 11	0.634 773 850 714 54	−0.129 411 912 043 47
H	11.981 802 831 622 09	−0.916 404 304 426 12	−1.003 257 364 867 04
H	11.999 036 651 855 09	−0.928 708 970 384 27	0.747 820 101 982 29
H	13.167 330 252 398 29	1.273 303 769 815 86	0.754 396 034 345 50
H	13.152 404 761 486 65	1.277 663 552 801 41	−1.009 974 802 063 30
S	0.201 263 022 746 99	−0.314 563 835 527 80	−0.216 380 930 396 20
H	−0.840 001 801 752 56	−2.187 176 161 608 09	−1.251 343 591 483 03
H	−0.923 336 804 932 38	−2.282 689 268 587 46	0.519 293 909 886 14
S	5.395 449 077 392 87	0.385 693 584 576 92	−0.088 196 950 405 87
H	6.930 581 058 579 68	−1.238 424 555 334 01	0.744 685 254 765 03
H	6.932 278 345 825 46	−1.176 331 011 331 97	−1.029 800 428 416 56
C	1.704 605 013 776 02	−1.145 041 914 417 08	−0.219 908 528 053 45
C	4.151 062 165 662 44	−0.807 911 879 359 51	−0.159 115 748 358 52
C	2.834 870 127 675 40	−0.287 661 700 007 52	−0.156 133 265 901 87
C	1.893 251 307 884 57	−2.507 781 828 793 94	−0.280 313 829 909 71
C	3.197 176 575 168 18	−3.016 133 029 387 41	−0.277 800 561 946 65
C	4.321 338 078 623 42	−2.170 471 287 723 41	−0.218 822 249 974 28
S	3.531 137 965 361 30	−4.704 321 187 223 00	−0.346 550 235 991 43

H	2.262 469 470 992 42	−5.134 403 790 890 44	−0.389 492 856 888 45
H	1.054 707 001 743 15	−3.183 500 332 366 38	−0.328 281 863 556 33
H	2.685 542 678 356 95	0.784 277 761 514 07	−0.106 826 637 277 03
H	5.306 811 840 498 64	−2.610 496 205 994 74	−0.220 821 143 793 33

A.12 Trithiocyanuric acid linked bis(hexanedithiol)bis(trimethylsilane)

Table A.12 reports the coordinates of the optimized geometry of the isolated molecule with the UKS method using CAM-B3LYP functional with def2-TZVP basis set [119]. Grimme D3 correction is applied [120, 121]. The geometry optimization is performed using the ORCA package [117, 118].

Table A.12 Coordinates of the optimized geometry of thetrithiocyanuric acid linked bis(hexanedithiol)bis(trimethylsilane).

Atom	**x (Å)**	**y (Å)**	**z (Å)**
S	−8.346 482 087 032 03	−3.544 735 541 275 29	−0.875 717 817 578 33
Si	16.173 757 253 998 49	0.837 513 840 267 56	−0.035 212 811 563 06
Si	−10.317 848 840 785 85	−2.569 566 063 374 11	−0.815 495 576 757 02
C	−10.397 491 852 720 21	−1.377 701 539 579 80	−2.240 879 355 910 48
C	−10.455 406 485 805 94	−1.699 522 846 762 53	0.823 060 648 101 86
C	−11.506 330 801 926 91	−3.982 025 838 074 63	−0.982 848 167 738 05
C	17.676 779 247 846 72	−0.244 555 640 962 57	−0.073 511 448 974 94
C	16.048 557 535 777 10	1.974 761 491 130 14	−1.499 715 815 472 70
C	15.959 913 219 773 16	1.738 086 200 344 65	1.576 719 574 948 81
H	−11.389 094 000 467 56	−0.920 684 554 550 54	−2.269 180 551 004 78
H	−10.234 151 975 463 79	−1.878 813 801 085 39	−3.194 764 474 105 91
H	−9.669 845 249 058 52	−0.571 817 159 240 15	−2.143 783 069 397 67
H	−11.442 651 197 160 72	−1.238 419 763 891 62	0.899 716 801 319 62
H	−10.344 224 139 233 22	−2.392 968 186 936 64	1.656 070 657 498 49
H	−9.715 325 995 988 73	−0.906 802 231 594 90	0.932 577 304 070 03
H	−12.531 481 364 672 76	−3.607 673 001 374 00	−0.950 060 501 873 08
H	−11.375 550 554 626 89	−4.508 000 142 120 75	−1.928 868 129 229 40

H	−11.391 300 229 898 46	−4.703 079 529 417 23	−0.172 894 510 534 86
H	18.574 758 622 041 11	0.371 885 558 509 24	0.000 541 404 368 32
H	17.741 159 971 069 63	−0.812 867 471 702 80	−1.001 633 151 040 20
H	17.689 252 222 187 25	−0.947 936 228 688 23	0.759 585 271 460 41
H	16.081 709 591 521 35	1.426 787 597 837 16	−2.441 003 114 345 36
H	16.895 376 885 979 51	2.664 948 167 006 27	−1.485 691 032 587 53
H	15.138 596 297 457 32	2.574 346 373 078 24	−1.479 390 932 947 25
H	16.800 586 696 103 44	2.422 245 694 924 62	1.713 719 575 675 18
H	15.946 996 432 096 87	1.052 583 344 637 89	2.423 499 211 317 63
H	15.047 561 358 644 61	2.333 868 179 017 09	1.598 759 055 816 49
C	6.719 667 841 772 00	−0.228 809 995 660 73	−0.321 451 392 340 56
C	7.997 689 867 818 66	0.592 377 813 316 63	−0.316 487 477 873 72
C	9.236 250 329 530 18	−0.289 820 606 482 91	−0.276 874 091 834 45
C	10.528 592 742 905 02	0.511 593 282 140 71	−0.269 947 990 526 27
C	11.766 217 611 510 76	−0.372 864 442 963 74	−0.235 707 251 408 01
S	14.508 090 532 223 83	−0.606 191 801 103 61	−0.192 552 313 635 75
H	7.999 885 110 001 94	1.264 880 829 838 83	0.545 897 781 049 80
H	8.030 359 123 711 22	1.227 357 886 147 64	−1.206 141 785 152 49
H	9.231 096 883 105 99	−0.963 006 330 568 97	−1.139 559 194 275 92
H	9.200 332 531 290 94	−0.928 524 920 139 81	0.610 818 853 476 44
H	10.534 697 814 882 25	1.182 346 410 521 24	0.595 174 056 674 56
H	10.562 597 211 124 33	1.152 932 017 010 54	−1.156 333 564 255 99
H	−2.579 732 154 929 26	−0.073 422 893 767 98	0.234 609 958 984 52
H	−5.019 603 360 608 06	−0.784 179 662 778 52	0.116 184 408 379 18
C	−2.355 350 501 296 54	−0.733 973 744 765 47	−0.607 071 190 217 16
C	−4.783 691 578 409 76	−1.449 715 608 147 11	−0.719 702 817 965 11
C	−7.199 068 366 281 12	−2.146 317 304 312 00	−0.840 464 138 716 90
C	−0.914 751 937 414 99	−1.209 027 986 746 59	−0.517 324 695 575 55
H	−3.202 546 555 579 25	−2.490 952 813 535 99	0.295 819 811 404 15
C	−3.334 359 918 667 63	−1.898 883 967 230 85	−0.614 587 199 228 80
H	−2.489 631 249 789 29	−0.138 528 601 710 00	−1.513 983 414 192 41
H	−5.640 501 265 331 87	−3.208 519 892 996 51	0.180 361 709 875 23
C	−5.759 747 228 436 39	−2.617 465 330 998 03	−0.730 440 562 091 50
H	−4.914 362 224 580 64	−0.857 066 005 038 12	−1.630 260 686 867 20
H	−7.350 339 798 766 65	−1.568 395 834 204 30	−1.754 817 306 736 43

H	−3.099 725 894 268 56	−2.564 755 904 738 76	−1.450 179 635 397 16
H	−5.531 436 380 060 86	−3.282 338 190 404 17	−1.566 645 200 818 43
H	−7.466 100 995 123 96	−1.502 638 501 802 12	−0.000 188 942 567 00
C	13.042 408 551 709 68	0.449 422 348 558 26	−0.224 599 322 790 51
H	11.770 709 173 004 37	−1.037 654 116 093 79	−1.102 770 183 342 38
H	11.739 894 899 687 46	−1.012 692 878 576 83	0.649 402 755 129 09
H	13.079 659 843 211 57	1.107 335 148 036 19	0.646 595 847 912 97
H	13.109 257 494 825 14	1.083 170 435 054 74	−1.112 314 376 070 06
S	0.181 027 469 078 07	0.228 236 028 242 67	−0.515 240 048 005 92
H	−0.657 662 191 392 11	−1.844 024 016 634 92	−1.362 898 708 548 75
H	−0.745 133 952 029 27	−1.782 463 710 536 17	0.392 137 595 354 95
S	5.300 972 281 939 05	0.889 581 242 149 11	−0.382 542 108 514 84
H	6.643 322 244 385 41	−0.845 322 392 282 32	0.572 286 581 015 53
H	6.680 636 056 050 71	−0.891 762 057 155 41	−1.183 915 392 252 78
C	1.751 665 090 509 55	−0.515 236 616 767 19	−0.445 989 862 867 01
C	3.968 105 596 573 48	−0.227 303 235 050 68	−0.389 322 797 429 10
N	1.859 135 888 117 98	−1.841 220 908 614 91	−0.406 474 082 136 22
C	3.106 855 715 657 12	−2.286 338 670 014 50	−0.357 829 179 357 60
N	4.198 823 896 504 61	−1.535 678 304 811 77	−0.347 361 117 129 94
S	3.393 623 174 596 77	−4.008 716 894 886 62	−0.301 594 901 480 57
H	2.095 587 594 066 45	−4.336 006 845 657 36	−0.328 146 104 986 60
N	2.768 460 566 716 46	0.335 620 232 240 60	−0.438 764 137 383 57

A.13 Trithiocyanuric acid linked tris(hexanedithiol)bis(trimethylsilane)

Table A.13 reports the coordinates of the optimized geometry of the isolated molecule with the UKS method using CAM-B3LYP functional with def2-TZVP basis set [119]. Grimme D3 correction is applied [120, 121]. The geometry optimization is performed using the ORCA package [117, 118].

Table A.13 Coordinates of the optimized geometry of the trithiocyanuric acid linked tris(hexanedithiol)bis(trimethylsilane).

Atom	x (Å)	y (Å)	z (Å)
S	−7.397 523 554 197 22	−4.729 857 919 778 39	−0.536 165 450 413 44
Si	16.726 878 455 803 55	1.278 346 511 043 94	−0.165 124 864 165 05
Si	−9.432 672 401 730 60	−3.950 497 442 114 50	−0.839 468 245 684 85
C	−9.479 184 435 774 76	−3.161 527 866 883 94	−2.523 485 254 291 00
C	−9.767 816 829 198 87	−2.718 798 839 418 63	0.513 222 200 604 03
C	−10.496 273 739 620 13	−5.463 998 066 642 62	−0.721 825 903 159 62
C	18.286 196 272 729 92	0.292 631 104 514 21	0.005 016 225 859 12
C	16.518 184 226 857 16	2.034 262 436 441 76	−1.850 686 056 490 17
C	16.488 238 606 675 25	2.520 660 241 679 75	1.196 522 440 550 19
H	−10.492 958 751 493 48	−2.807 615 199 734 13	−2.723 755 744 311 98
H	−9.212 139 532 939 70	−3.871 135 349 969 46	−3.306 076 170 146 27
H	−8.813 043 959 152 15	−2.301 959 392 791 83	−2.594 068 789 593 05
H	−10.792 090 018 885 37	−2.352 015 642 806 26	0.416 750 034 211 72
H	−9.666 166 155 612 41	−3.169 335 972 938 99	1.500 296 350 004 43
H	−9.105 543 431 176 14	−1.854 869 786 537 01	0.457 285 986 332 75
H	−11.543 302 795 324 40	−5.191 866 149 972 84	−0.870 115 035 113 66
H	−10.234 007 291 824 01	−6.199 790 723 066 99	−1.482 624 834 453 39
H	−10.412 327 303 289 34	−5.939 176 830 956 42	0.255 887 605 243 35
H	19.150 509 402 021 68	0.951 739 895 051 06	−0.096 719 054 546 33
H	18.363 972 090 429 98	−0.475 940 301 740 54	−0.764 472 088 425 50
H	18.351 642 254 277 32	−0.191 555 208 138 34	0.979 487 581 518 82
H	16.577 640 493 158 61	1.284 672 537 896 75	−2.639 195 248 625 69
H	17.319 473 539 673 83	2.758 192 410 875 83	−2.016 009 062 092 86
H	15.572 048 581 600 03	2.566 143 830 034 81	−1.949 020 217 636 76
H	17.298 129 840 412 73	3.252 818 883 375 72	1.155 403 501 082 27
H	16.513 039 259 354 65	2.052 179 734 546 37	2.180 125 006 454 52
H	15.549 977 133 045 30	3.065 954 786 813 95	1.095 537 138 735 96
C	7.344 490 376 147 93	−0.287 198 046 109 15	−0.081 753 617 793 29
C	8.573 116 257 184 91	0.605 663 832 819 25	−0.063 579 812 006 76
C	9.858 817 426 217 40	−0.206 781 781 119 44	−0.032 817 699 712 61
C	11.106 021 493 360 42	0.662 813 871 081 74	−0.021 584 080 435 37
C	12.389 088 729 916 39	−0.154 747 531 875 02	0.005 357 900 705 57
S	15.139 703 770 545 32	−0.241 779 081 535 93	0.057 664 538 733 61
H	8.536 649 584 767 02	1.266 265 381 651 22	0.807 128 805 326 38

H	8.571 134 942 986 01	1.252 575 347 448 94	−0.945 297 470 523 56
H	9.888 396 650 948 85	−0.872 076 229 099 03	−0.901 080 575 462 39
H	9.859 301 319 648 07	−0.854 170 484 378 06	0.849 331 864 230 53
H	11.078 208 622 922 43	1.327 422 744 339 31	0.847 747 494 045 18
H	11.104 301 018 544 38	1.310 677 424 245 71	−0.903 952 299 339 19
H	−1.935 237 423 276 75	−0.772 493 112 838 00	0.443 179 481 779 01
H	−4.308 024 773 775 50	−1.682 303 592 405 46	0.349 172 115 151 12
C	−1.668 858 595 233 98	−1.407 842 163 503 14	−0.405 660 504 658 39
C	−4.029 791 459 897 28	−2.329 789 491 834 58	−0.487 913 451 801 00
C	−6.376 909 270 368 42	−3.236 707 320 919 33	−0.569 502 636 777 88
C	−0.193 393 845 026 72	−1.762 927 056 314 53	−0.337 491 925 731 60
H	−2.350 635 081 397 02	−3.233 207 252 210 57	0.500 264 494 171 44
C	−2.545 622 594 000 72	−2.651 593 917 680 67	−0.405 596 648 824 54
H	−1.864 934 778 745 53	−0.820 985 600 807 99	−1.306 916 321 655 30
H	−4.717 932 168 629 50	−4.147 464 679 956 65	0.438 584 179 323 31
C	−4.900 339 112 152 58	−3.578 114 293 705 25	−0.475 797 889 864 70
H	−4.226 171 761 179 07	−1.755 382 305 659 04	−1.398 370 539 236 62
H	−6.595 108 447 186 84	−2.693 895 703 543 87	−1.491 395 017 180 74
H	−2.267 082 843 587 13	−3.293 186 551 824 68	−1.246 893 796 610 19
H	−4.626 260 896 695 98	−4.229 488 326 507 32	−1.308 846 033 900 49
H	−6.684 458 118 578 29	−2.601 222 159 810 81	0.263 678 539 567 71
C	13.619 822 319 605 24	0.733 909 262 825 90	0.007 592 282 904 94
H	12.423 153 269 767 86	−0.818 775 925 430 19	−0.861 540 523 888 50
H	12.402 062 355 472 40	−0.794 675 236 372 26	0.890 818 581 062 33
H	13.624 126 430 866 76	1.396 161 563 057 70	0.876 910 931 356 17
H	13.650 504 478 643 66	1.367 096 270 763 21	−0.881 822 665 843 54
S	0.788 627 329 641 79	−0.245 625 780 450 66	−0.321 873 898 104 06
H	0.104 441 671 117 80	−2.364 579 059 885 29	−1.194 079 072 528 22
H	0.030 888 473 286 04	−2.334 432 699 991 58	0.561 273 119 718 55
S	5.861 153 324 737 17	0.743 869 843 421 25	−0.130 221 914 485 45
H	7.303 697 226 635 25	−0.920 357 026 546 09	0.802 687 380 345 55
H	7.345 003 286 031 96	−0.939 667 801 643 04	−0.952 941 072 002 85
C	2.409 893 604 783 55	−0.878 389 474 482 66	−0.253 921 396 334 29
C	4.601 374 930 023 37	−0.456 979 044 110 05	−0.170 142 835 574 85
N	2.600 090 013 433 10	−2.195 307 668 142 42	−0.237 990 336 309 41

C	3.870 577 050 124 69	−2.569 223 028 572 56	−0.185 418 872 515 12
N	4.913 900 117 671 63	−1.744 650 310 823 47	−0.149 413 829 480 24
S	4.275 451 631 818 07	−4.262 018 147 220 85	−0.159 018 262 247 69
H	−0.387 079 781 050 48	−9.061 760 799 481 64	−1.269 556 628 770 04
N	3.367 243 833 254 81	0.034 850 561 989 55	−0.221 902 459 344 97
C	2.639 801 827 419 51	−5.027 968 325 150 06	−0.232 883 784 635 30
S	−1.479 063 590 760 70	−11.592 603 229 092 30	−0.447 613 863 260 44
H	−1.141 155 805 077 00	−12.887 912 648 581 77	−0.437 154 333 140 20
C	2.775 982 164 447 95	−6.540 655 685 865 04	−0.219 821 797 377 16
H	2.056 110 219 529 88	−4.680 459 725 023 69	0.617 500 362 307 90
H	2.140 586 071 056 18	−4.688 360 399 940 48	−1.138 584 885 615 51
C	1.415 729 911 628 69	−7.218 382 692 455 12	−0.295 209 401 301 67
H	3.394 336 380 513 08	−6.864 217 383 708 62	−1.061 364 503 458 23
H	3.294 952 589 405 54	−6.857 892 857 425 49	0.688 585 254 704 67
C	1.496 150 810 404 39	−8.736 606 756 981 51	−0.284 345 750 880 42
H	0.798 202 347 231 61	−6.884 013 339 894 85	0.544 376 464 872 03
H	0.899 522 147 424 28	−6.891 104 625 767 45	−1.203 287 646 160 44
C	0.126 278 536 156 34	−9.393 571 119 890 09	−0.362 584 976 987 83
H	2.111 885 947 124 23	−9.073 863 944 501 70	−1.123 665 524 259 64
H	2.008 793 102 308 35	−9.067 084 600 238 62	0.624 187 410 388 90
C	0.203 651 909 654 37	−10.909 789 841 574 76	−0.358 342 924 338 10
H	−0.487 022 508 953 03	−9.062 190 179 982 29	0.480 210 738 346 53
H	0.688 086 499 996 88	−11.259 960 936 001 27	0.552 330 415 141 99
H	0.781 209 895 345 40	−11.260 115 803 560 57	−1.212 952 925 272 09

A.14 6-(ferrocenyl)hexanethiol cation

Table A.13 reports the coordinates of the optimized geometry of the isolated molecule with the UKS method using B3LYP functional with def2-TZVP basis set [119]. Grimme D3 correction is applied [120, 121]. The geometry optimization is performed using the ORCA package [117, 118].

Table A.14 Coordinates of the optimized geometry of the 6-(ferrocenyl)hexanethiol cation.

Atom	x (Å)	y (Å)	z (Å)
Fe	0.00000000	0.00000000	10.27544414
C	1.75741181	1.19931111	10.20897015
C	1.71406847	−0.97754321	9.51374548
C	1.73030159	0.37966955	11.36995726
C	1.70313906	−0.97742935	10.93794539
C	1.76800553	0.36878248	9.05407579
C	−1.81805619	0.52682872	9.24946272
C	−1.78035235	1.19297611	10.49807779
C	−1.75108029	−0.87044459	9.49021903
C	−1.69260774	0.21267599	11.52107193
C	−1.67593609	−1.06924566	10.89998045
H	1.75271051	2.27835367	10.19685004
H	1.67382297	−1.85221549	8.88543586
H	1.72291843	0.72432396	12.39139080
H	1.67621685	−1.84871587	11.57212586
H	−1.84691330	1.00217965	8.28195304
H	−1.77910736	2.26155943	10.64463971
H	−1.74808767	−1.64307959	8.73853645
H	−1.63721399	0.40692972	12.57996902
H	−1.62162310	−2.01972459	11.40513971
C	1.81721890	0.84228397	7.63759988
C	1.10802695	−0.04733842	6.61502470
H	1.42163781	1.85973562	7.58828306
H	2.87652122	0.92330267	7.36503746
H	0.05823055	−0.17053626	6.90232651
H	1.54964274	−1.04833471	6.62321803
C	1.18544820	0.52590366	5.20125409
H	2.23629667	0.65196415	4.92082039
H	0.74531611	1.52905982	5.19354071
C	0.48444659	−0.34244069	4.15933679
C	0.56498369	0.24709108	2.75001673
H	0.93088532	−1.34290832	4.16124239
H	−0.56688054	−0.47432003	4.44085693
H	0.11623486	1.24553697	2.74574776

H	1.61099389	0.37881021	2.46127191
C	−0.13298535	−0.62243683	1.71174449
H	−1.18586833	−0.76469807	1.96086864
H	0.32439258	−1.61333006	1.67428074
S	0.00000000	0.00000000	0.00000000
H	−0.71343658	1.12433965	0.18369314

Appendix B

BBchar code

Appendix B reports the the MATLAB code of the main scripts and functions of the Block-Based characterization (BBchar) tool.

The following code reports, as an example, the launching script for the simulation of all the input compinations and subsequent characterization of a XOR gate.

```
clear variables
close all

%% Paths definition
myDataPath = '~';
BBcharPath = fullfile(myDataPath,'BBchar');
BBcharCodePath = fullfile(BBcharPath,'Code');
thisPath = pwd;
scerpaPath = fullfile(myDataPath,'scerpa');
libraryPath = fullfile(BBcharPath, 'Lib');

outputPath = fullfile(BBcharPath,'Layouts','xor');
file = 'xor.qll';


%% Clock signal parameters

%definitions
clock_low = -2;
```

```
clock_high = +2;
clock_step = 5;

%Step simulation implementation
pSwitch =  linspace(clock_low, clock_high, clock_step);
pHold =   linspace(clock_high, clock_high, clock_step);
pRelease =  linspace(clock_high, clock_low, clock_step);
driverPara.pReset =   linspace(clock_low, clock_low, ...
    clock_step);

%Cycle to simulate
driverPara.pCycle = [pSwitch pHold pRelease ...
    driverPara.pReset];

%% Driver parameters
driverPara.doubleMolDriver = 1;
driverPara.Ninputs = 4; %Number of layout physical inputs
driverPara.driverNames = [{'Dr1'} {'Dr2'} {'DrC0'} ...
    {'DrC1'}]; %list of the drivers name as they are in
                % the .qll file
driverPara.driverModes = [{'0'} {'0'} {'1'} {'1'};
                          % Dr1 combinations
                          {'0'} {'1'} {'0'} {'1'};
                          % Dr2 combinations
                          {'0'} {'0'} {'0'} {'0'};
                          % DrC0 combinations
                          {'1'} {'1'} {'1'} {'1'}];
                          % DrC1 combinations

driverPara.sweepType = 'lin'; %sweep creation following
                              % a linspace ('lin')
                              % or a logspace ('log')
driverPara.NsweepSteps = 1;
driverPara.cycleLength = length(driverPara.pCycle);
driverPara.clockStep = clock_step;
driverPara.NclockRegions = 4; % number of clock regions in
                              % the layout
driverPara.phasesRepetition = 3; % How many time regions
```

```
                                    % repeat in the layout
driverPara.maxVoltage = 1;   % maximum voltage (absolute
                             % value) the driver will assume

%% Termination settings
%set to '1' if you want to add a termination to the layout
terminationSettings.enableTermination = 1;
%specify a custom number of cells to realize each the
% termination. Default is 8 molecules
terminationSettings.customLength = 0;
%set to 1 for bus layouts, set to 0 for single line layouts
terminationSettings.busLayout = 1;

%% SCERPA settings
%layout (MagCAD)
circuit.qllFile = fullfile(pwd,file);
circuit.magcadImporter = 1;
circuit.doubleMolDriverMode = driverPara.doubleMolDriver;
circuit.outIsPin = 0;

%algorithm settings
settings.out_path = outputPath;
settings.damping = 0.6;
settings.verbosity = 0;
settings.dumpDriver = 1;
settings.dumpOutput = 1;
settings.dumpClock = 1;
settings.dumpVout = 1;

%viewer settings
plotSettings.plot_waveform = 1;
plotSettings.plot_waveform_index = 1;
plotSettings.plot_3dfig = 0;
plotSettings.plot_1DCharge = 0;
plotSettings.plot_logic = 1;
plotSettings.plot_potential = 1;
plotSettings.plotSpan = clock_step;
plotSettings.fig_saver = 0;
```

```
plotSettings.HQimage = 0;

if isfield(settings,'out_path')
    plotSettings.out_path = settings.out_path;
end

%% Characterization settings
charSettings.LibPath = libraryPath;
charSettings.LibDeviceName = 'xor';
charSettings.out_path = outputPath;

%% Launch the BBchar software
simulate = 1;
characterize = 1;

cd(BBcharCodePath)
circuit.Values_Dr = buildDriver(driverPara);
circuit.stack_phase = buildClock(driverPara);
% if the user want the termination
if terminationSettings.enableTermination
    [circuit, terminationCircuit] = add_termination(...
        circuit,terminationSettings,driverPara.pCycle,...
        length(driverPara.pReset));
else %termination not enabled
    termination.num = 0;
end
cd(thisPath)

% launcher
if simulate
    if terminationSettings.enableTermination
        circuit.qllFile = terminationCircuit.filepath;
        settings.out_path = outputPath;
        plotSettings.out_path = settings.out_path;
    end
    cd(scerpaPath)
    diary on
    SCERPA('generateLaunchView',circuit,settings,...
```

```
        plotSettings);
    diary off
    if isfield(settings,'out_path')
        movefile('diary',fullfile(settings.out_path,...
            'logfile.log'))
    end
    cd(thisPath)
end
if characterize
    cd(BBcharCodePath)
    tic
    characterization(charSettings,terminationSettings,...
        terminationCircuit,driverPara,circuit.Values_Dr);
    charTime = toc;
    cd(thisPath)
end
```

The following function generated the driver matrix to perform a Self-Consistent ElectRostatic Potential Algorithm (SCERPA) simulation considering the user inputs.

```
function [valuesDr] = buildDriver(driverSettings)

if ~isfield(driverSettings,'sweepType')
    warning(['Missing sweep type for drivers, default' ...
        ' will be used, default value is ''lin'' '])
    driverSettings.sweepType = 'lin';
end

switch(driverSettings.sweepType)
    case 'lin'
        % from smaller to bigger value
        variation = linspace(driverSettings.maxVoltage,...
            -driverSettings.maxVoltage, ...
            driverSettings.NsweepSteps);
        %from bigger to smaller value
        not_variation = linspace(...
            -driverSettings.maxVoltage,...
            driverSettings.maxVoltage, ...
```

```
            driverSettings.NsweepSteps);
    case 'log'
        % generates NsweepSteps/2 points between decades
        %  10^-2 and 10^0. 0.01 1
        half_pos_variation = driverSettings.maxVoltage*...
            logspace(-2, 0, driverSettings.NsweepSteps/2);
        overturned_half_pos_variation = ...
            driverSettings.maxVoltage*logspace(...
            0, -2, driverSettings.NsweepSteps/2);
%1 0.01

        % Add a central '0' for compliance with odd
        % NsweepSteps
        if mod(driverSettings.NsweepSteps,2)
            variation = [ overturned_half_pos_variation...
                0  -half_pos_variation];
            not_variation = ...
                [ -overturned_half_pos_variation 0 ...
                half_pos_variation];
        else
            variation = [ overturned_half_pos_variation ...
                -half_pos_variation];
            not_variation = ...
                [-overturned_half_pos_variation ...
                half_pos_variation];
        end
    otherwise
        warning(['Sweep type for drivers not ' ...
            'recognized, default will be used, ' ...
            'default value is ''lin'' ']);
        variation = linspace(driverSettings.maxVoltage, ...
            -driverSettings.maxVoltage, ...
            driverSettings.NsweepSteps);
        not_variation = linspace(...
            -driverSettings.maxVoltage, ...
            driverSettings.maxVoltage, ...
            driverSettings.NsweepSteps);
end
```

```
Ndrivers = driverSettings.Ninputs;

% each element of variation is repeated cycleLength times
D_sweep = repelem(variation, driverSettings.cycleLength);
% each element of not_variation is repeated cycleLength
% times
D_not_sweep = repelem(not_variation, ...
    driverSettings.cycleLength);

D_one = -driverSettings.maxVoltage * ones(1, ...
    length(D_sweep));
D_zero = driverSettings.maxVoltage * ones(1, ...
    length(D_sweep));

% the number of columns of driverModes tells the number of
% driver values' combinations
[~, Ncomb] = size(driverSettings.driverModes);

%length of the values to insert to empty the pipe and make
% the last input to propagate till the end of the circuit
empty_pipe = (driverSettings.phasesRepetition)* ...
    driverSettings.cycleLength;
Dr_tot = zeros(1,length(D_sweep)*Ncomb + empty_pipe);
% + 1 for the input name, times 2 if doubleMolDriver
valuesDr = cell(Ndrivers+Ndrivers* ...
    driverSettings.doubleMolDriver,length(Dr_tot)+1);

for nDr = 1:Ndrivers      %for each input branch
    for jj = 0:Ncomb-1      % for each combination value
        currentArrayElements = ...
            (jj*length(D_sweep) + 1):(length(D_sweep)+ ...
            jj*length(D_sweep));
        switch(driverSettings.driverModes{nDr,jj+1})
            case '0'
                Dr_tot(currentArrayElements) = D_zero;
            case '1'
                Dr_tot(currentArrayElements) = D_one;
```

```
            case 'sweep'
                Dr_tot(currentArrayElements) = D_sweep;
            case 'not_sweep'
                Dr_tot(currentArrayElements) = D_not_sweep;
        end
    end

    % filling elements for the empty pipe phase looking the
    % last value of the combinations
    if strcmp(driverSettings.driverModes{nDr,end},...
            'sweep') || strcmp(...
            driverSettings.driverModes{nDr,end},'1')
        Dr_tot(currentArrayElements(end)+1:end) = ...
            -driverSettings.maxVoltage * ...
            ones(1,empty_pipe);
    else % not_sweep or '0'
        Dr_tot(currentArrayElements(end)+1:end) = ...
            driverSettings.maxVoltage * ones(1,empty_pipe);
    end

    %write dr name in row ii and column 1
    valuesDr{nDr,1} = driverSettings.driverNames{nDr};
    valuesDr(nDr,2:end) = [num2cell(Dr_tot)];
    if driverSettings.doubleMolDriver
        %write dr_c name in row ii+Ndrives and column 1,
        % so we obtain Dr1,Dr2,..,DrN,Dr1_c,Dr2_c,..,DrN_c
         valuesDr{nDr+Ndrivers,1} = ...
             [driverSettings.driverNames{nDr} '_c'];
         valuesDr(nDr+Ndrivers,2:end) = ...
             [num2cell(-Dr_tot)];
    end

end
```

The following code report the function to create the clock matrix to perform a SCERPA simulation considering the user inputs.

```
function [stack_phase] = buildClock(settings)
```

```
    [~,Ncomb] = size(settings.driverModes);
    filler = repmat(settings.pReset,1,...
        settings.NclockRegions);
    completeCycle = [repmat(settings.pCycle,1,...
        settings.NsweepSteps*Ncomb+(...
        settings.phasesRepetition-1))...
        filler];
    stack_phase = zeros(settings.NclockRegions,length(...
        completeCycle));

    for ii = 1:settings.NclockRegions
        stack_phase(ii,:) = circshift(completeCycle,...
            length(settings.pReset)*(ii-1));
    end

end
```

The following code describes the function used to attact a termination to each Device Under Test (DUT) output, creating a new MagCAD input file. It also adjust the driver and clock matrices to include the newly added termination circuit.

```
function [QCAcircuit, termination] = add_termination(...
    QCAcircuit, settings, pCycle, pResetLength)

% Read the circuit qll file and extract the name and the
% number of the independent output
CUTstruct = xmlRead(QCAcircuit.qllFile);
[outNames,indexName] = unique( CUTstruct.output.name );
Noutputs = length(outNames);

if settings.busLayout && Noutputs == length(...
        CUTstruct.output.name)
    error("Dependent output in bus layout MUST have" + ...
        " the same name. Please correct the layout!");
end

if isfield(settings,'customLength') && ...
```

```
        settings.customLength ~= 0
    termination.Length = settings.customLength;
else
    %default termination has 8 molecules (4 cells)
    termination.Length = 4;
end

termination.numOutput = Noutputs;
termination.filepath = insertBefore(QCAcircuit.qllFile,...
    '.qll','_termination');
copyfile(QCAcircuit.qllFile, termination.filepath);

%add for cycle for each output
for nOut = 1:Noutputs
    % get output info
    OUT_x = CUTstruct.output.x(indexName(nOut));
    OUT_y = CUTstruct.output.y(indexName(nOut));
    OUT_angle = CUTstruct.output.angle(indexName(nOut));

    if OUT_angle == 0
        test_x = OUT_x - 1;
    elseif OUT_angle == 90
        test_y = OUT_y - 1;
    elseif OUT_angle == 270
        test_y = OUT_y + 1;
    else
        error(['Angle not compatible with the actual' ...
            'program. Please correct the .qll and try' ...
            'again']);
    end

    %find the molecule near the output and read the phase
    if exist('test_x','var') && ...
            any([CUTstruct.molecules.x]  == test_x)
        index = find([CUTstruct.molecules(:).x] == test_x);
        nearMolPhase = CUTstruct.molecules(index(1)).phase;
    elseif exist('test_y','var') && ...
            any([CUTstruct.molecules.y] == test_y)
```

```
        index = find([CUTstruct.molecules(:).y] == test_y);
        nearMolPhase = CUTstruct.molecules(index(1)).phase;
    else
        error(['No molecule near the output: check and' ...
            'correct the layout'])
    end
    Nphases = max([CUTstruct.molecules(:).phase]) + 1;
    termination.stack(nOut).phase = ...
        mod(nearMolPhase+1,Nphases);

    % Compute every id used in the original qll to extract
    % the next one to use
    mol_id_MAX = ...
        max(str2double([CUTstruct.molecules(:).id]));
    out_id_MAX = max(str2double([CUTstruct.output(:).id]));
    drv_id_MAX = max(str2double([CUTstruct.driver(:).id]));
    id_MAX = max([mol_id_MAX out_id_MAX drv_id_MAX]);
    termination.stack(nOut).StartID = id_MAX +1;

    if settings.busLayout
        termination.stack(nOut).StartX = ...
            [CUTstruct.output.x(indexName(nOut)) ...
            CUTstruct.output.x(indexName(nOut) + 1)];
        termination.stack(nOut).StartY = ...
            [CUTstruct.output.y(indexName(nOut)) ...
            CUTstruct.output.y(indexName(nOut) + 1)];
    else
        termination.stack(nOut).StartX = ...
            CUTstruct.output.x(indexName(nOut));
        termination.stack(nOut).StartY = ...
            CUTstruct.output.y(indexName(nOut));
    end
    termination.stack(nOut).angle = OUT_angle;

    terminationFileContent = createQLLfile(...
        termination,nOut,settings.busLayout);
    fileID = fopen(termination.filepath,'w');
    fprintf(fileID,terminationFileContent);
```

```
    fclose(fileID);

end

% Update Values_Dr and stack_phase

%Evaluate the last driver value to copy it n-times
% at the end
driver_last_value = QCAcircuit.Values_Dr(:,end);
%Create the matrix of repeated values to attach at the end
% of Values_Dr
flap_matrix = repmat(driver_last_value,1,length(pCycle));
%Attach flap matrix
QCAcircuit.Values_Dr = [QCAcircuit.Values_Dr flap_matrix];

%Insert a pCycle in stack_phase in the correct position for
% each row, considering the presence of the pReset filler
newPhaseMatrix = zeros(size(QCAcircuit.stack_phase,1),...
    size(QCAcircuit.stack_phase,2) + length(pCycle));
for ii = 1:size(QCAcircuit.stack_phase,1)
    pos = [1:length(pCycle)] + pResetLength*(ii-1);
    idx = ones(1,length(newPhaseMatrix));
    idx(pos) = 0;
    newPhaseMatrix(ii,pos) = pCycle;
    newPhaseMatrix(ii,logical(idx)) = ...
        QCAcircuit.stack_phase(ii,:);
end
QCAcircuit.stack_phase = newPhaseMatrix;

end

%%% Function used to generate the new qll file with the
% termination
function [terminationFile] =  createQLLfile(...
    termination,nOut,busLayout)

    terminationFile = fileread(termination.filepath);
    molLineTemplate = fileread('molLineTemplate.qll');
```

```
    newID = termination.stack(nOut).StartID;
    newX = termination.stack(nOut).StartX;
    newY = termination.stack(nOut).StartY;

    for ii = 1:termination.Length
        strToAdd = molLineTemplate;
        strToAdd = strrep(strToAdd,"$ID$",num2str(newID));
        strToAdd = strrep(strToAdd,"$PHASE$",num2str(...
            termination.stack(nOut).phase));
        strToAdd = strrep(strToAdd,"$X$",num2str(newX(1)));
        strToAdd = strrep(strToAdd,"$Y$",num2str(newY(1)));
        terminationFile = insertBefore(terminationFile,...
            '    </layout>',strToAdd);

        if busLayout
            newID = newID + 1;
            strToAdd = molLineTemplate;
            strToAdd = ...
                strrep(strToAdd,"$ID$",num2str(newID));
            strToAdd = ...
                strrep(strToAdd,"$PHASE$",num2str(...
                termination.stack(nOut).phase));
            strToAdd = ...
                strrep(strToAdd,"$X$",num2str(newX(2)));
            strToAdd = ...
                strrep(strToAdd,"$Y$",num2str(newY(2)));
            terminationFile = ...
                insertBefore(terminationFile,...
                '    </layout>',strToAdd);
        end

        newID = newID + 1;
        if termination.stack(nOut).angle == 0
            newX = newX + 1;
        elseif termination.stack(nOut).angle == 90
            newY = newY + 1;
        elseif termination.stack(nOut).angle == 270
```

```
            newY = newY - 1;
        end

    end

end
```

The following function is responsible for the analysis of the output produced by SCERPA to extract the characterization data. It creates a new folder in the library where it places the characterization files.

```
%% VIN/VOUT - CHARACTERISTIC

function characterization(charSettings,...
    terminationSettings,terminationCircuit,...
    driverPara,drivers)

% Paths definition
if ~isfolder(charSettings.LibPath)
    % creating main Library directory if it doesn't exist
    mkdir(charSettings.LibPath);
end
% path of the directory related to the specific circuit
currentDeviceLibPath = fullfile(charSettings.LibPath,...
    charSettings.LibDeviceName);
if ~isfolder(currentDeviceLibPath)
    mkdir(currentDeviceLibPath);
end
outFolderPath = fullfile(charSettings.out_path,...
    'SCERPA_OUTPUT_FILES');

% Read simulation data
table_AI = readtable(fullfile(outFolderPath,...
    'Additional_Information.txt'),'VariableNamesLine',1);
%rename time column
table_AI.Properties.VariableNames{1} = 'Time';
availableRows = table_AI.Properties.VariableNames;
table_AI_array = table2array(table_AI);
```

```
%flag that tells whether it is a bus layout or not
bus_flag = terminationSettings.busLayout;


%% Extract output values from the table
% Evaluating the position as expressed in the qll file of
% the molecules right before the terminations and associate
% the new names for the table
for oo = 1:terminationCircuit.numOutput
    switch terminationCircuit.stack(oo).angle
        case 0
            if bus_flag
                % order output as from lowest y to the
                % highest, for bus structure H before L
                out_pos_qll((2*oo-1):(2*oo),:) = ...
                    sortrows([zeros(2,1) ...
                    terminationCircuit.stack(oo).StartY'...
                    (terminationCircuit.stack(oo).StartX...
                    -1)'],2);
                new_outNames{4*oo-3} = ...
                    sprintf('Vou_%dA_H',oo);
                new_outNames{4*oo-2} = ...
                    sprintf('Vou_%dB_H',oo);
                new_outNames{4*oo-1} = ...
                    sprintf('Vou_%dA_L',oo);
                new_outNames{4*oo} = sprintf('Vou_%dB_L',oo);
            else
                out_pos_qll(oo,:) = ...
                    sortrows([0 ...
                    terminationCircuit.stack(oo).StartY'...
                    (terminationCircuit.stack(oo).StartX...
                    -1)'],2);
                new_outNames{2*oo-1} = ...
                    sprintf('Vou_%dA',oo);
                new_outNames{2*oo} = ...
                    sprintf('Vou_%dB',oo);
            end
```

```
        case 90
            if bus_flag
                out_pos_qll((2*oo-1):(2*oo),:) = ...
                    sortrows([zeros(2,1) ...
                    (terminationCircuit.stack(oo).StartY...
                    -1)' ...
                    terminationCircuit.stack(oo).StartX'...
                    ],3);
                new_outNames{4*oo-3} = ...
                    sprintf('Vou_%dA_dH',oo);
                new_outNames{4*oo-2} = ...
                    sprintf('Vou_%dB_dH',oo);
                new_outNames{4*oo-1} = ...
                    sprintf('Vou_%dA_dL',oo);
                new_outNames{4*oo} = ...
                    sprintf('Vou_%dB_dL',oo);
            else
                out_pos_qll(oo,:) = sortrows([0 ...
                    (terminationCircuit.stack(oo).StartY...
                    -1)' ...
                    terminationCircuit.stack(oo).StartX'],...
                    3);
                new_outNames{2*oo-1} = ...
                    sprintf('Vou_%dA_d',oo);
                new_outNames{2*oo} = ...
                    sprintf('Vou_%dB_d',oo);
            end
        case 270
            if bus_flag
                out_pos_qll((2*oo-1):(2*oo),:) = ...
                    sortrows([zeros(2,1) ...
                    (terminationCircuit.stack(oo).StartY+...
                    1)' ...
                    terminationCircuit.stack(oo).StartX'],...
                    3);
                new_outNames{4*oo-3} = ...
                    sprintf('Vou_%dA_uH',oo);
                new_outNames{4*oo-2} = ...
```

```
                    sprintf('Vou_%dB_uH',oo);
                new_outNames{4*oo-1} = ...
                    sprintf('Vou_%dA_uL',oo);
                new_outNames{4*oo} = ...
                    sprintf('Vou_%dB_uL',oo);
            else
                out_pos_qll(oo,:) = sortrows([0 ...
                    (terminationCircuit.stack(oo).StartY...
                    +1)' ...
                    terminationCircuit.stack(oo).StartX']...
                    ,3);
                new_outNames{2*oo-1} = ...
                    sprintf('Vou_%dA_u',oo);
                new_outNames{2*oo} = ...
                    sprintf('Vou_%dB_u',oo);
            end
    end
end

%read the qll to extract the qll_identifier and the phase
qllFile_term = fileread(fullfile(charSettings.out_path,...
    strcat(charSettings.LibDeviceName,...
    '_termination.qll')));
abq = '([^"]+)';    % anything but quotation mark
for oo = 1:size(out_pos_qll,1)
    xpr = ['<item comp="',abq,'" id="',abq,'"( angle="',...
        abq,'")? x="',num2str(out_pos_qll(oo,3)),...
        '" y="',num2str(out_pos_qll(oo,2)),...
        '" layer="0">(\s*<property' ...
        ' name="',abq,'" value="',abq,'"/>)*'];
    tmp = regexp(qllFile_term, xpr, 'tokens');
    outID{2*oo-1} = ['Vout_' sprintf('%.4da',...
        str2double(tmp{1,1}{1,2}))];
    outID{2*oo} = ['Vout_' sprintf('%.4db',...
        str2double(tmp{1,1}{1,2}))];
    % get the phase of each output molecules
    phasecell = regexp(tmp{1,1}{1,4}, ['\s*<property ' ...
        'name="phase" value="',abq,'"/>'], 'tokens');
```

```
    outPhase(2*oo-1) = str2double(phasecell{1,1})+1;
    outPhase(2*oo) = str2double(phasecell{1,1})+1;
end
% extract the column indexes of the table where output
% voltages are stores in the correct order
[tf,loc] = ismember(availableRows,outID);
[~,p] = sort(loc(tf));
out_cols = find(tf);
out_cols = out_cols(p);

%% Get the driver values list from the driver
% values are the first occurence
[driverValues,index] = unique(cell2mat(...
    drivers(:,2:end)).','rows','stable');
in_firsthalf_col = 1:(size(driverValues,2)/2);
in_secondhalf_col = (size(driverValues,2)/2+1):size(...
    driverValues,2);
%drivers are reversed in the origianl matrix
interleaved_idx = [in_secondhalf_col;in_firsthalf_col];
interleaved_idx = repelem(interleaved_idx,1,2);
interleaved_idx = interleaved_idx(:)';
driverValues = driverValues(:,interleaved_idx).';
Ndrivers = length(driverPara.driverNames);
for dd = 1:Ndrivers
    if bus_flag
        new_driverNames{4*dd-3} = sprintf('Vin_%dA_H',dd);
        new_driverNames{4*dd-2} = sprintf('Vin_%dB_H',dd);
        new_driverNames{4*dd-1} = sprintf('Vin_%dA_L',dd);
        new_driverNames{4*dd} = sprintf('Vin_%dB_L',dd);
    else
        new_driverNames{2*dd-1} = sprintf('Vin_%dA',dd);
        new_driverNames{2*dd} = sprintf('Vin_%dB',dd);
    end
end

%% Extract the time instants (table rows) corresponding
%% with  the output in the hold phase for the selected
%% input combination
```

```
%the first time depend on the output phase and the phase
% repetition in the circuit, the others are separated by a
% cycle lenght
time_rows = index + (outPhase+1).*driverPara.clockStep ...
    + (driverPara.cycleLength * ...
    (driverPara.phasesRepetition -1));

%% Generate the lookup table and save it to the library
table_header = [new_driverNames new_outNames];
table_values = zeros(size(driverValues,2),...
    size(driverValues,1)+length(out_cols));
for comb = 1:size(driverValues,2)
    table_values(comb,:) = [driverValues(:,comb)' ...
        diag((table_AI_array(time_rows(comb,:),...
        out_cols)),0)'];
end
%creating the table containing output and drivers
T = array2table(table_values,'VariableNames',table_header);
path = fullfile(currentDeviceLibPath,'table.csv');
writetable(T,path);   %creation of the .csv file

%% Generate the additional information file and save it to
%% the library
% saving the min and max coordinates in y-axis and z-axis
% (to evaluate the number of cells)
qllFile = fullfile(charSettings.out_path,...
    strcat(charSettings.LibDeviceName,'.qll'));
copyfile(qllFile,currentDeviceLibPath)
circuit = xmlRead(qllFile);

ymin = min([circuit.molecules.y]);
ymax = max([circuit.molecules.y]);
zmin = min([circuit.molecules.x]);
zmax = max([circuit.molecules.x]);
y_cell_num = (ymax - ymin + 1);
z_cell_num = (zmax - zmin + 1);
area_cells = y_cell_num*z_cell_num;
```

```
%latency of the circuit
latency = driverPara.phasesRepetition*...
    driverPara.NclockRegions;

% writing the .txt file with the additional informations
fileid = fopen(fullfile(currentDeviceLibPath,...
    'info.txt'),'w');
fprintf(fileid,'Number of outputs\t%d\n',length(outID));
for w = 1:length(outID)
    fprintf(fileid,'%s\t',new_outNames{w});
end
fprintf(fileid,'\nLatency\t%d',latency);
fprintf(fileid,'\nNumber of clock phases\t%d',...
    driverPara.NclockRegions);
fprintf(fileid,'\nMaximum driver voltage\t%.2f V',...
    driverPara.maxVoltage);
fprintf(fileid,'\nTotal area\t%dx%d=%d',y_cell_num,...
    z_cell_num,area_cells);
fclose(fileid);

end
```

The following function is used for reading the Look-Up Table (LUT) of a device and providing the output voltages corresponding to te specified input.

```
function [Vout] = InOut_eval(LibPath,device,input)

     %open the file that contains the names of
     % the output files
    infoFile = fileread(fullfile(LibPath,device,...
        'info.txt'));
    tmp = regexp(infoFile,...
        'Number of outputs\s([0-9]+)\n','tokens');
    num_out = str2double(cell2mat(tmp{1}));

    LUTtable = readtable(fullfile(LibPath,device,...
        'table.csv'),'VariableNamesLine',1);
    availableRows = LUTtable.Properties.VariableNames;
```

```
    if isempty(regexp(availableRows{1,end},...
            'Vou_[0-9]*[A|B]_[a-z]?[H|L]', 'once'))
        busFlag = 0;
    else
        busFlag = 1;
    end
    LUT = table2array(LUTtable);
    num_in = size(LUT,2) - num_out;
    LUT_in = LUT(:,1:num_in);

    if num_in ~= size(input,1)*size(input,2)
        error("The size of the provided input " + ...
            "is not consistent with the device.")
    end

    in_total = input';
    in_total = in_total(:)';

    % calculate the norm of each row of LUT-input
    dist = vecnorm(LUT_in - in_total, 2, 2);
     %the nearest vector has the minimun norm
    [~, match] = min(dist);
    Vout = reshape(LUT(match,num_in+1:end),2,num_out/2)';

end
```